Experimental Validation of On-chip Terahertz Spoof Surface Plasmon Polariton Structures Integrated to Coplanar Strip Waveguide

by

Mohsen Haghighat

B.Sc., Shiraz University, 2013
M.Sc., Tarbiat Modares University, 2015

A Dissertation Submitted in Partial Fulfillment of the Requirements for the Degree of
DOCTOR OF PHILOSOPHY

in the
Department of Electrical and Computer Engineering

We acknowledge and respect the Lək'^{w}əŋən (Songhees and X'^{w}sepsəm/Esquimalt) Peoples on whose territory the university stands, and the Lək'^{w}əŋən and W$\underline{S}$ÁNEĆ Peoples whose historical relationships with the land continue to this day.

Experimental Validation of On-chip Terahertz Spoof Surface Plasmon Polariton Structures Integrated to Coplanar Strip Waveguide

by

Mohsen Haghighat

B.Sc., Shiraz University, 2013
M.Sc., Tarbiat Modares University, 2015

Supervisory Committee

Prof. Thomas Darcie, Co-Supervisor
(Department of Electrical and Computer Engineering)

Dr. Levi Smith, Co-Supervisor
(Department of Electrical and Computer Engineering)

Dr. Andrew MacRae, Outside Member
(Department of Physics and Astronomy)

ABSTRACT

This dissertation addresses the gap in experimental validation of Spoof Surface Plasmon Polaritons (SSPP) at Terahertz (THz) frequencies (0.3 - 3 THz), a domain extensively explored through theoretical and simulation-based research but still lacking broadband experimental validation at THz range. The SSPP structures, which mimic the behavior of optical surface plasmon polaritons at lower frequencies (e.g. microwave and THz), have unique electromagnetic properties such as strong subwavelength field confinement, flexible characteristics based on geometry, the potential for miniaturization, and ease of on-chip integration, that is beneficial for a variety of applications including, sensing, imaging, and communications.

In this work, we present the first experimental verification of SSPP characteristics at THz frequencies (beyond 300 GHz) using guided wave systems with CoPlanar Strip (CPS) feedlines. We also design and demonstrate several CPS-based SSPP structures, including two SSPP-based Low Pass Filter (LPF)s that can also be used as sensors, and two novel THz Band Pass Filter (BPF)s, all of which have potential for applications in filtering, sensing, and communication technologies. These works serve as proof of concept for filtering and also experimental validation of SSPP at THz frequencies.

Further, we investigate the use of these THz waveguides for sensing applications. For this purpose, we selected glucose, a material with a distinct absorption signature beyond 1 THz, to showcase the sensing capabilities of the waveguides. The interaction between glucose and the evanescent electromagnetic field of the waveguide is demonstrated, where CPS waveguides are preliminary used to capture the material's absorption over a broad spectral range. To enhance the sensor's sensitivity, we tune the SSPP structures to match the absorption frequency of glucose. This tuning leverages the strong field confinement properties of SSPP, as well as their band-edge sensitivity to changes in surrounding permittivity, resulting in significant improvements in sensor performance.

The experimental results presented in this dissertation not only validate the practical application of SSPP structures at THz frequencies but also introduce novel designs and techniques that enhance their capabilities in sensing applications. This work contributes to the growing field of SSPP research, providing valuable insights for the development of advanced THz technologies, including sensors, filters, and communication systems.

Contents

List of Tables

List of Figures

List of Acronyms

BPF Band Pass Filter

CPW CoPlanar Waveguide

CPS CoPlanar Strip

DFT Discrete Fourier Transform

FD Frequency Domain

HF HydroFluoric Acid

LOR Lift-Off Resist

LPF Low Pass Filter

LT-GaAs Low Temperature-grown Gallium Arsenide

MBE Molecular Beam Epitaxy

MS MicroStrip

PCS Photo-Conductive Switch

PR Photo Resist

RX Receiver

SL Slot Line

SPP Surface Plasmon Polaritons

SSPP Spoof Surface Plasmon Polaritons

TC Transition Circuit

TD Time Domain

TDS Time Domain Spectroscopy

TE Transverse Electric

TEM Transverse Electro-Magnetic

THz Terahertz

THz-TDS Terahertz Time Domain Spectroscopy

TL Transmission Line

TM Transverse Magnetic

TSoC Terahertz System on Chip

TX Transmitter

VNA Vector Network Analyzer

ACKNOWLEDGEMENTS

I would like to express my gratitude to my supervisors; Prof. Thomas Darcie and Dr. Levi Smith for providing me the opportunity to pursue PhD studies in their group, and for their invaluable guidance, support, expertise, and continuous encouragement. Their insights have been instrumental in shaping my research and overcoming challenges along the way.

I extend my sincere appreciation to Dr. Andrew McRae for accepting the be a member of the supervisory committee for the PhD candidacy exam and the final exam. I also like to thank Dr. Christopher Collier (University of British Columbia) for agreeing to review my dissertation as an external referee.

I also thank my lab colleagues and friends; Ali Dehghanian, Saeid Asadi, and Ghazal Mansouri for the wonderful time we shared in the lab during the program.

I thank 4D LABS at Simon Fraser University for the fabrication of the structures and CAMTEC at the University of Victoria for providing Nanofab facilities for the fabrication of photo-conductive devices.

Lastly and most importantly, I am grateful to my wife Sahar, my parents, and my family for their unwavering love, encouragement, and support during my PhD studies and throughout my life.

DEDICATION

This dissertation is dedicated to:
My lovely wife Sahar for her patience, love, encouragement, and support;
My kind parents and family for their unwavering love;
and to the memory of my beloved brother ...

Chapter 1

Introduction

1.1 Motivation

The concept of 'spoof' surface plasmon polariton structures that mimic the behavior of optical Surface Plasmon Polaritons (SPP) at low frequencies (e.g., microwave and THz) was introduced in 2004 [8] and rapidly gained significant research attention to this date, especially at microwave frequency range. The SSPP structures offer promising solutions due to their unique electromagnetic properties and potential for miniaturization and integration.

The increasing demand for advanced technologies in filtering, sensing, communication, and imaging has brought significant attention to SSPP structures at THz frequencies. Despite extensive research in this field, experimental validation of SSPP characteristics at THz frequencies remains scarce. Most existing studies rely on simulations or indirect verifications through device scaling to operate at microwave frequencies, where standard vector network analyzers provide convenient characterization tools. This dissertation aims to bridge this gap by presenting the first experimental verification of several SSPP structure characteristics at THz frequencies in a guided wave system, employing CPS feedlines for accurate measurement and analysis. Specifically, we have designed and demonstrated two structures with low-pass filtering characteristics and two novel THz BPFs.

This work also seeks to advance the understanding and practical application of SSPP structures in the THz regime, paving the way for innovative solutions in emerging technologies. For this purpose, we aimed to use the designed THz waveguides for sensing applications. One of the materials that shows an absorption signature at THz

frequencies beyond 1 THz is glucose. We selected glucose to showcase the sensing capabilities of our THz waveguides on a thin membrane. The thin membrane not only provides low loss but also facilitates the interaction between the material and the electromagnetic evanescent field of the waveguide. Initially, we used only the CPS waveguide to capture the absorption of the material in a wide spectral range, which was the first effort to use THz guided waves to sense anhydrous glucose. Next, we used tuned SSPP at the absorption frequency of interest to enhance the sensitivity of the sensor, owing to the strong field confinement properties of SSPP. Additionally, SSPP has a band-edge (sharp cut-off) in the spectrum which is sensitive to changes in surrounding permittivity.

What motivated the author to perform this research is that despite the extensive theoretical and simulation-based research on SSPP structures, there remains a significant lack of experimental validation at THz frequencies, particularly in guided wave systems. Furthermore, while SSPP structures are theoretically promising for sensing applications due to their strong field confinement and band-edge sensitivity, practical demonstrations of their sensing capabilities in the THz regime are non-existent. This gap in experimental research and application underscores the need for further investigation to realize the full potential of SSPP structures for advanced THz technologies in sensing and beyond.

1.2 Dissertation Format

This dissertation is written in a paper-based format, including six manuscripts. This section provides an overview of the content of the subsequent chapters. Chapter 1 is the introduction, including the motivation of the research, organization of the dissertation, list of contributions, an introduction to THz frequency range, and basics of SSPP structure which is the focus of this research. Chapter 2 presents a brief review of the literature related to this research. Chapter 3 presents the methods, including measurement setup and also the fabrication process of photoconductive devices. Chapter 4 delivers a summary of the contributions (six research articles). Finally, Chapter 5 concludes the dissertation by summarizing key findings, discussing their significance, and offering recommendations for future research directions. A copy of all of the published or submitted manuscripts in publisher formats can be found in the appendix. Through this structured arrangement, the dissertation aims to engage readers in a coherent and insightful exploration of the research topic.

1.3 List of Contributions

This section lists the author's contributions directly related to this dissertation, including published and submitted scientific journal papers, collaborations with the research group, and conference proceedings.

1.3.1 Main Contributions

This section lists my main (major) contributions (i.e. primary author, including six manuscripts). It contains three published papers with the citation in front of the title and three other works submitted to peer-reviewed journals. For cohesion of the content, the works have not been chronologically ordered (based on the date of submission or acceptance). Instead, it follows the story of the thesis, outlined in the previous section on the organization of the dissertation. Below the title of each work, the contribution of each author is stated.

1. **Demonstration of a Terahertz Coplanar Strip Spoof Surface Plasmon Polariton Low Pass Filter, *Scientific Reports* [1]**

   M.H. conducted simulations, fabricated PCS devices, performed the experiments, and prepared an early draft of the manuscript. T.D. provided guidance and advice on the concept and writing. L.S. analyzed the results, offered insights on the theory, fabrication, and experiments, and revised the writing.

2. **Demonstration of Terahertz Spoof Surface Plasmon Polariton Waveguides using Coplanar Striplines with Internal Corrugations, *Optics Express* [2]**

   M.H. conducted simulations, fabricated PCS devices, performed the experiments, and prepared an early draft of the manuscript. A.D. assisted in experimental measurements. T.D. provided guidance and advice on the concept and writing. L.S. analyzed the results, offered insights on the theory, fabrication, and experiments, and revised the writing.

3. **THz Bandpass Filter Using Single-Conductor Spoof Surface Plasmon Polariton Structure Integrated with Coplanar Stripline**

   M.H. conducted simulations, fabricated PCS devices, performed the experiments, and prepared an early draft of the manuscript. T.D. provided guidance

and advice on the concept and writing. L.S. analyzed the results, offered insights on the theory, fabrication, and experiments, and revised the writing.

4. **Terahertz Band Pass Filter based on Spoof Surface Plasmon Polariton Split Rings developed from Coplanar Strip with Internal Stubs**

   M.H. conducted simulations, fabricated PCS devices, performed the experiments, and prepared an early draft of the manuscript. T.D. provided guidance and advice on the concept and writing. L.S. analyzed the results, offered insights on the theory, fabrication, and experiments, and revised the writing.

5. **On-Chip Glucose Sensing Using Guided Waves at Terahertz Frequencies, *Scientific Reports* [3]**

   M.H. conducted the modeling and simulations, fabricated PCS devices, designed and performed the experiments, and prepared an early draft of the manuscript. T.D. provided guidance and advice on the concept and writing. L.S. offered insights on the main idea, theory, fabrication, and experiments and revised the writing.

6. **Terahertz CPS-based Spoof Surface Plasmon Polariton Permittivity and Absorption Sensor**

   M.H. conducted the modeling and simulations, fabricated PCS devices, designed and performed the experiments, and prepared an early draft of the manuscript. T.D. provided guidance and advice on the concept and writing. L.S. offered insights on the main idea, theory, fabrication, and experiments and revised the writing.

1.3.2 Collaborations

This section includes other contributions, including collaborations with others in our research group.

I have contributed to the research of our scientific group mainly by the fabrication of PCS devices for experimental measurements and also discussions about theory, simulations, and experiments, which resulted in the works published in [9, 10, 11, 12].

1.3.3 Conference Proceedings

This section lists the works presented at scientific conferences during the PhD studies, published or indexed by esteemed publishers such as the Institute of Electrical and Electronics Engineers (IEEE) and the International Society for Optics and Photonics (SPIE). Since these works form part of the main contributions discussed in the dissertation, only their citations are provided to avoid repetition, allowing readers to access the full papers through the publishers' online libraries. The conference proceedings are listed below in chronological order:

- **Terahertz CPS-based Spoof Surface Plasmon Polariton Filter on Silicon Nitride Substrate, IEEE [13]**
  Mohsen Haghighat; Thomas E. Darcie; Levi Smith, *48th International Conference on Infrared, Millimeter, and Terahertz Waves (IRMMW-THz)*, Montreal, Canada, QC, September 2023.

- **A THz Spoof Surface Plasmon Polariton Band Pass Filter for 6G Communication Applications, IEEE [14]**
  Mohsen Haghighat; Thomas E. Darcie; Levi Smith, *IEEE Pacific Rim Conference on Communications, Computers and Signal Processing (PACRIM)*, Victoria, BC, Canada, August 2024.

- **An On-chip Terahertz Glucose Sensor, IEEE [15]**
  Mohsen Haghighat; Thomas E. Darcie; Levi Smith, *49th International Conference on Infrared, Millimeter, and Terahertz Waves (IRMMW-THz), IEEE*, Perth, WA, Australia, September 2024.

- **Spoof Surface Plasmon Polariton (SSPP) Split Rings for THz Bandpass Filtering, SPIE [16]**
  Mohsen Haghighat; Thomas E. Darcie; Levi Smith, *SPIE Photonics West*, San Francisco, California, United States, January 2025.

1.4 Introduction to THz

1.4.1 THz Frequency Range

The THz frequency range also known as the 'THz gap' is the range of frequencies between microwave and infrared on the electromagnetic spectrum. There is not a single definition of this range with designated frequency limits; however, it is commonly defined from 0.1 to 10 THz [17]. Electromagnetic waves at THz frequencies have been challenging to study due to the lack of practical sources and detectors. However, recent advancements in technology have led to the development of new devices that can operate in this range, making it possible to explore its potential applications [18]. The THz frequency range has been found to have a variety of potential uses, including in imaging and sensing, communications, and spectroscopy [19]. The advantage of the THz frequencies in this application is low photon energy that results in non-ionizing radiation, unlike X-ray radiation. It also has a short penetration depth that can penetrate soft materials like clothing, paper, plastic, and exterior layers of body tissues that can be utilized for medical and security applications [20].

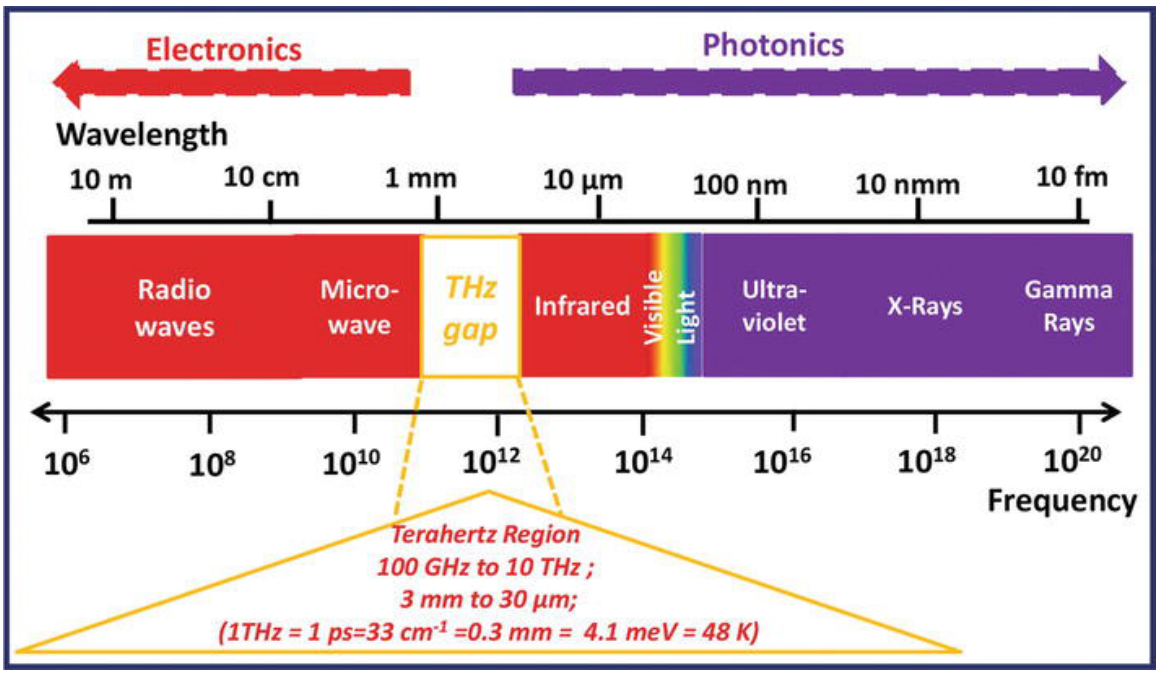

Figure 1.1: Frequency and wavelength regions of the electromagnetic spectrum, illustrating and defining the THz range, which lies between microwave and photonics ranges. Reprinted from [21] (Open access).

1.4.2 THz Generation and Detection

THz generation and detection are crucial in the exploration of the THz gap. As mentioned, sources and detectors for THz frequencies have been challenging because they lie between microwave and optical methods with a fundamental limitation that this frequency range is too high for current microwave or solid-state electronics due to high carrier transit time and parasitic effects, which cause a loss of gain and efficiency for frequencies beyond 100 GHz. Signal sources, probes, and Vector Network Analyzer (VNA)s also face bandwidth limitations at these frequencies. At the same time, the THz range is too low for optical sources and lasers, as they rely on optical materials that are inefficient at directly generating or detecting THz waves. These challenges stem from the inherent physical and material constraints that arise in this intermediate frequency range.

Fortunately, there are several methods proposed and demonstrated for generating and detecting THz radiation, including photo-conductive switching [18], photo-conductive mixing [22], optical rectification [23], microwave frequency multiplication [24], backward wave oscillators [25], free-electron lasers [26], or quantum cascade lasers [27]. In this research, we only use and discuss the details of the photo-conductive switching method which is compatible with our Terahertz System on Chip (TSoC) measurement platform.

THz-TDS method is a technique to study material properties by transmitting a radiated THz-bandwidth pulse through an unknown sample. The THz-bandwidth pulse is generated by illuminating a biased photo-conductive switch with a femtosecond optical pulse, which generates a flow of carriers that results in radiation of a THz wave.

Photo-conductive switching is particularly advantageous for generating intense and broadband THz pulses, making it suitable for applications in spectroscopy and imaging. It can also be used to demonstrate the functionality of THz waveguides for communication systems. Additionally, photo-conductive switching is relatively low-cost, which makes it accessible to a wide range of users. These advantages have made photo-conductive switching a popular choice for THz research and development.

One of the most popular semiconductors to fabricate the PCS is Low Temperature-grown Gallium Arsenide (LT-GaAs). This material is selected because of its sub-picosecond carrier lifetime. For most THz applications the LT-GaAs epilayer is grown at a low temperature ($\approx 230^{\circ}$C) via Molecular Beam Epitaxy (MBE) on a Semi-

Insulating GaAs (SI-GaAs) substrate. Low-temperature growth of GaAs results in defects (Arsenic antisites) in the crystalline structure which form midgap states that quickly trap electrons from the conduction band [28]. The un-annealed LT-GaAs has a minimal carrier lifetime ($\approx$ 0.09 ps) and substrate resistance of 3 MΩ (for a 5 μm gap) [28]. It is desirable to increase the substrate resistance to reduce the dark current, which can be achieved by thermal annealing. As a consequence, the carrier lifetime also increases. With high-temperature annealing (i.e. 600°C for 10 mins), the defect concentration reduces substantially and the carrier lifetime becomes much greater than 1 ps which is not desired. This trade-off should be optimized for THz generation. The LT-GaAs layer annealed at 450°C for 10 minutes which corresponds to the lifetime of $\approx$ 0.23 ps [28] which is effective for THz generation.

The basic principle of photo-conductive switching with LT-GaAs involves illuminating an LT-GaAs sample with a laser pulse. This creates an excess of free carriers, which are then accelerated by an applied electric field to generate a photo-current. The electric field is created by applying a bias voltage across the GaAs layer. As a result, a THz-bandwidth pulse is generated with a temporal duration on the order of a few hundred femtoseconds [7, 29, 30].

To bias the PCS utilized to generate the THz-bandwidth pulse, its metallic (gold) contacts should be connected to the bias lines that are connected to the THz waveguide so that it is biased and sources the THz pulse to the waveguide at the same time. This concept is illustrated in Fig. 1.2, which shows how the PCS is placed on the waveguide and how the laser beam is incident to the backside of the LT-GaAs layer of PCS devices for THz generation and detection. The adhesion between PCS contacts and CPS lines is created by water molecules' Van der Waals forces [31].

1.5 Introduction to SSPP

An SPP wave is a surface wave that propagates under specific excitation conditions at optical frequencies (typically the visible light and infrared spectrum) at the interface between a dielectric and metals, such as gold (Au) [19]. In this case, the metal can be called an SPP waveguide. The SPP wave involves both electron oscillations in the metal (i.e., surface plasmon) and electromagnetic waves in the dielectric (i.e., polaritons). The analysis and theory of SPP are detailed in [19].

At microwave and THz frequencies, however, the SPP cannot be excited since metals act like perfect electric conductors and do not exhibit plasmonic properties at

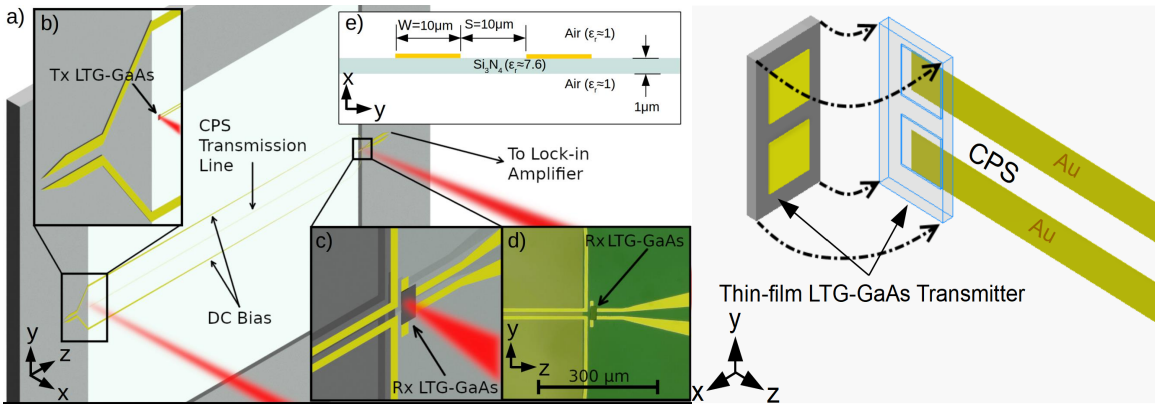

Figure 1.2: THz generation and detection using LT-GaAs PCS and pulsed laser (right), PCS placement on CPS lines (left). Reprinted with permission from [7]

lower frequencies. Interestingly, researchers found that engineered metals can mimic the behavior of the SPP waveguide. Hence, the name 'spoof' or 'designer' SPP or SSPP appeared and gained interest in the literature [8, 4, 32, 33]. SSPPs share many properties of SPPs, including dispersion characteristics, localized field confinement, low-loss, Transverse Magnetic (TM) mode support, and propagation in subwavelength scale [34]. These structures have attracted the attention of researchers over the last two decades [5].

1.5.1 Theory of SSPP

The analysis of a popular SSPP structure made of a 1D array of grooves (Fig. 1.3) is presented in [4]. Solving the equations for the incident and reflected electromagnetic waves have resulted in the SSPP dispersion relation (1.1) in the limit of $\lambda >> d, a$.

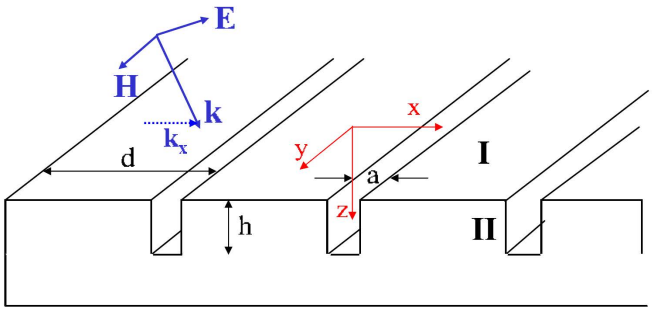

Figure 1.3: SSPP with 1D array of grooves). Reprinted from [4]

$$k_x = k_0\sqrt{1+\left(\frac{a^2}{d^2}\right)\tan^2(k_0h)} \tag{1.1}$$

where h is the depth of grooves on the metal or wire, a is the aperture width or groove width, d is the period of corrugation, and k_0 is $k_0 = \omega\sqrt{\varepsilon_r}/c = 2\pi\sqrt{\epsilon_r}/\lambda$ where ε_r is the relative permittivity of dielectric (i.e. air) and c is the speed of light in the vacuum.

Equation (1.1) shows that the behavior of SSPP structures is predominantly governed by h, especially for the band-edge frequency of the structure ($k_x d = \pi$). This can also be seen when we consider $k_0 h \to \pi/2$, leading to $k_x \to \infty$, regardless of a, d values. However, as $\lambda >> d, a$ was the basic assumption to obtain this equation, it should be considered for the design of SSPP structures. Increasing the aperture of the a/d ratio can slightly affect the dispersion relation just at low wavenumbers or low frequencies.

1.5.2 Guided wave SSPP with CPS feedlines

In this section, we explain the components of SSPP integrated with CPS feedlines to excite the SSPP with a guided wave method. Figure 1.4 shows the block diagram of this system. The system consists of the following building blocks.

1. PCS for THz generation and detection.
2. CPS feedlines for transferring the THz signal to the SSPP structure. The fundamental mode of this waveguide is Transverse Electro-Magnetic (TEM) mode.
3. Transition Circuit (TC) for the gradual introduction of SSPP for the purpose of mode conversion from TEM to TM and also to return loss.
4. SSPP which is the main structure that we want to excite with a guided THz wave. The fundamental mode of SSPP is the TM mode.

1.5.3 Analysis of CPS-SSPP

To date, no closed-form dispersion relations have been presented for a finite-thickness CPS-SSPP structure. However, if the thickness of the CPS-SSPP conductors were

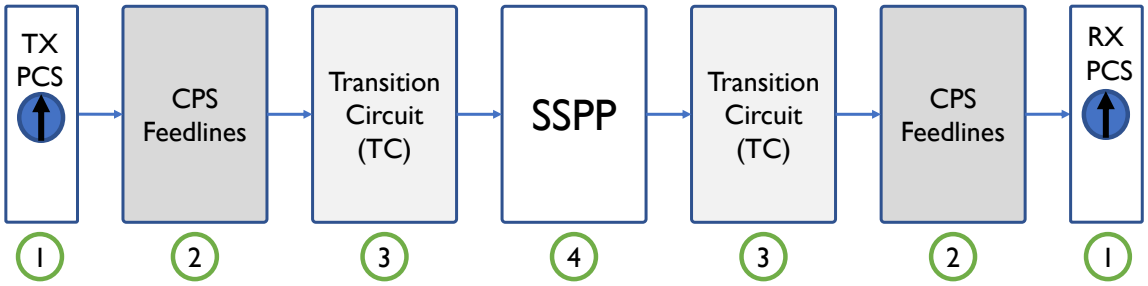

Figure 1.4: Diagram of guided wave SSPP integrated to CPS feedlines

supposed to be infinite, then the CPS-SSPP dispersion relation could be approximated by a 1D array of grooves (Fig. 1.3) [4, 33]:

$$k_z = k_{eff}\sqrt{1 + \left(\frac{a^2}{d^2}\right)\tan^2(k_{eff}H_n)}, \tag{1.2}$$

where H_n is the length of stubs (i.e. depth of grooves) in the structure shown in Fig. 1.5, $d = a + W_n$ is the period, a is the aperture or the distance between the stubs, W_n is the width of the stubs, $k_{eff} = \omega\sqrt{\varepsilon_{eff}}/c$ is the effective wavenumber, ε_{eff} is the effective relative permittivity of the substrate (i.e., a combination of thin SiN membrane and air and for CPS-SSPP device field profile $\varepsilon_{eff} \approx 1.7$ based on simulations), and c is the speed of light. We note that (4.1) is not explicitly true for a CPS-SSPP, but it provides a reasonable approximation [1]. The validity of a similar approximation is also found in [33, 35].

Investigation of (4.1) reveals that the CPS-SSPP exhibits low-pass behavior (when $k_{eff}H_n$ is small, then $k_z \approx k_{eff}$). Next, we see that the response of SSPP structures is primarily controlled by H_n. This is observed by considering $k_{eff}H_n \to \pi/2$ which results in $k_z \to \infty$. We note that this relates to the asymptotic frequency which is calculated by $f_{AS} = c/(4\sqrt{\varepsilon_{eff}}H_n)$. At frequencies below the band-edge ($k_z d = \pi$), the insertion loss will be minimal. At frequencies above the band edge, a significant insertion loss is expected. Near the band-edge, a resonance occurs which results in large field enhancement inside the CPS-SSPP grooves [36].

Figure 1.6 compares the dispersion relation obtained from eigenmode simulations on the unit cell of the CPS-SSPP structure (solid lines) with the theoretical dispersion relation (dashed lines) in (4.1), which shows a reasonable alignment for three different

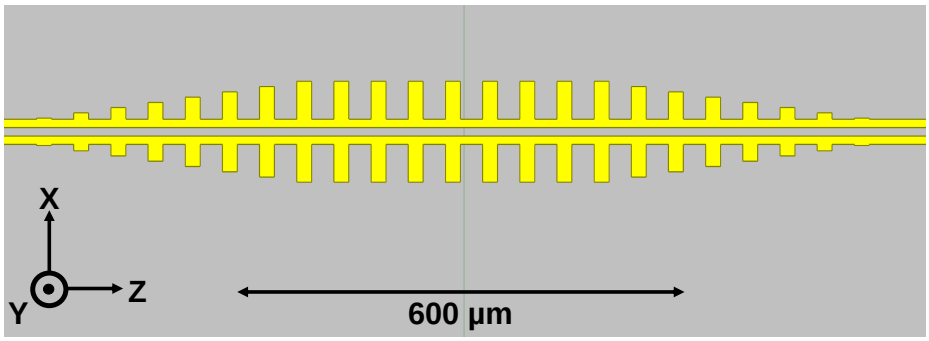

Figure 1.5: CPS-SSPP structure with external corrugations

dimensions of SSPP groove depth.

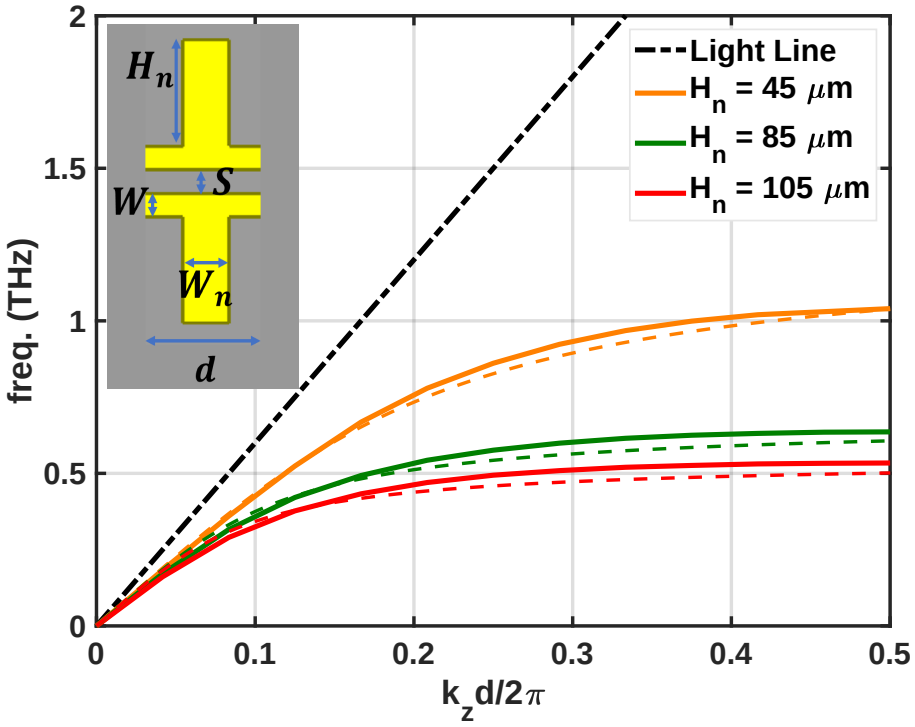

Figure 1.6: Comparison between the CPS-SSPP dispersion curves obtained from simulation and theory (equation 4.1). Reprinted from [1]

1.5.4 Applications of THz SSPP Waveguide

SSPP structures have several applications at THz frequencies, including imaging, sensing, spectroscopy, waveguiding, and communication [32, 37]. The sensing applications utilize the localized filed confinement properties of SSPPs and their slow-wave behavior [5]. Also, SSPPs can be utilized as data communication building blocks such as interconnections, antennas, power dividers, phase shifters, and filters [5, 36]. In this research, we focus on two key applications of CPS-based SSPP structures: sensing and filtering, which are described in this section.

- **Sensing Applications:**
  THz SSPPs have the capability of strong subwavelength field confinement and a flexible band-edge frequency that can be adjusted for specific materials for sensing applications. A chemical analyte or dielectric can be placed next to the area where the localized field exists [38], and the analyte will absorb the field depending on the material properties. It is worth noting that the maximum field confinement happens at frequencies slightly lower than the band-edge frequency (just before the cut-off), which can be adjusted by modifying the SSPP geometry.

- **Filtering Applications:**
  THz SSPP structures have a low-pass filtering behavior with significant roll-off rates and have a low loss (0.75 dB/mm at 300 GHz [39]) in the passband and strong stop-band rejection (more than -20 dB). These filters can be used in applications where selectivity with sharp cut-off is desired and linear phase requirement is not strict [36, 40, 41]. SSPP structures are inherently dispersive around the band-edge frequency [1], and analog methods, such as dispersion compensation techniques [42], can be used to enhance the phase response of the structure. It is worth noting that the phase response of the structure is nearly linear at passband frequencies lower than the band-edge frequency and becomes nonlinear close to the band edge.

Now that we mentioned a few potential applications, here we discuss the advantages and disadvantages of SSPPs:

A key advantage of SSPP is to create a **surface wave** with a high magnitude close to the waveguide that enables transmission with **low radiation loss** even on thick dielectric layers, which is useful for on-chip THz waveguiding without the need

for bulky cavities. Typical high-frequency waveguides such as CPW and CPS fail to guide the THz wave over a long distance when implemented on thick substrates due to significant radiation losses.

SSPPs also offer **design flexibility**, which means their properties can be tailored through the design of the sub-wavelength geometric parameters of the device and its unit cell in the periodic structure. This flexibility allows for the engineering of desired properties for filters, sensors, and other devices. By manipulating the geometry, it is possible to achieve unique and configurable capabilities that are not easily achievable with conventional filters and devices.

Another advantage of SSPP over conventional filters and sensors is propagation in **subwavelength** structures [32], where the unit cell width or corrugation period is significantly smaller than the wavelength of operation. This is important because of the following aspects:

Miniaturization: subwavelength propagation allows for the miniaturization of devices and components [41]. In conventional filters, the size of the devices is typically on the order of half-wavelength. However, by exploiting SSPPs, it is possible to design and fabricate compact devices that operate at much smaller wavelength scales.

Enhanced Field Confinement: SSPPs can confine electromagnetic fields to subwavelength dimensions, leading to enhanced field concentration. As mentioned, this property is particularly useful in applications such as waveguiding to reduce radiation loss and sensing, where higher sensitivity is desired [32, 38].

On the other hand, SSPP structures also have some disadvantages. Firstly, this structure has limited compatibility with conventional optical and electronic components. Traditional waveguides and components are designed with standard operating principles and ports, such as VNA probes. For guided-wave SSPP, a transition circuit is required for adaptation, which contributes to insertion loss. Moreover, SSPPs are inherently dispersive structures near the band-edge frequency. Although it may not pose a concern in sensing applications, it is considered a drawback for filtering and communication systems. Therefore, the design should ensure operation within the nondispersive region of the spectral response.

Chapter 2

Review of SSPP

SSPP have attracted significant attention as a class of metamaterial structures operating at microwave and THz frequencies. These structures mimic the properties of conventional SPPs, including significant electromagnetic field confinement and customizable dispersion characteristics, which can be tailored through geometric modifications, which is why it is also referred to as 'designer' surface plasmons [8]. These unique features have potentials for a wide range of applications, from sensors and communication devices to miniaturized THz components [5].

2.1 Early Development and Conceptualization

The concept of SSPP was first introduced by Pendry et al. [8] in 2004, who demonstrated that surface plasmon-like behavior could be achieved using artificial structures such as arrays of grooves or holes in a metallic surface. These geometries interact with obliquely incident light or electromagnetic waves, effectively mimicking SPPs at sub-wavelength scales [8, 4, 32]. This breakthrough established the fundamental basis for SSPP, showing that metal grating and engineering could replicate the behavior of SPPs while also offering more flexibility through geometric design.

The initial SSPP structures were designed using 3D geometries, which included arrays of grooves or holes on a metal surface. Some of these structures presented in preliminary research on SSPPs are shown in Fig. 2.1. These designs were capable of guiding electromagnetic waves in a similar manner to surface plasmons but without the need for a negative refractive index of metals at optical frequency [19]. These early SSPP designs were pivotal in demonstrating the feasibility of mimicking surface

plasmon polaritons using engineered structures [8]. Later, finite-thickness SSPP was explored especially at microwave frequencies [33, 35, 5].

2.2 Guided-wave Integration and Advancements

As research progressed, the focus shifted towards improving the integration of SSPP structures with guided-wave systems, allowing for practical applications in microwave and THz devices. The use of guided-wave SSPP structures became a key area of exploration due to their enhanced capabilities in signal transmission and compatibility with existing measurement systems.

In a guided-wave system, direct excitation of the fundamental Transverse Magnetic TM mode in an SSPP waveguide is inherently challenging. To address this, SSPP structures are typically integrated with feedlines such as CPW [37, 35, 43], MS [44], Slot Line (SL) [45], and CPS [36, 46, 40]. These feedlines primarily support quasi-TEM modes, as seen in CPW, CPS, and MS configurations, or quasi-Transverse Electric (TE) modes in the case of SL [45]. Due to the differing mode characteristics between the feedlines and SSPP structures, a TC is required for mode conversion. Figure 2.2 shows a couple of works on the integration of SSPP with CPW and MS feedlines for excitation.

One popular approach in the literature involved integrating SSPP into coplanar waveguides, as they offer ease of integration with standard VNA, commonly used for testing and characterizing microwave components [5, 35, 37]. This method allowed for efficient excitation and coupling of SSPP structures, which improved their performance and applicability in real-world systems. However, integrating SSPP with CPWs presented challenges, particularly related to coupling efficiency and the need for large flaring ground conductors at the transition between the waveguide and the plasmonic structure. This transition region often resulted in increased insertion losses and consumed valuable chip area, making the integration less efficient in some cases [37, 47]. To address these issues, further research focused on optimizing the transition design, reducing losses, and improving the coupling efficiency between the CPW and the SSPP structures [47].

Moreover, the development of transition circuits played a crucial role in improving the performance of SSPP devices. These circuits serve to match the impedance between the CPW and the SSPP structure, thereby reducing reflection and enhancing the overall signal transmission [47]. The transition circuit concept has been central

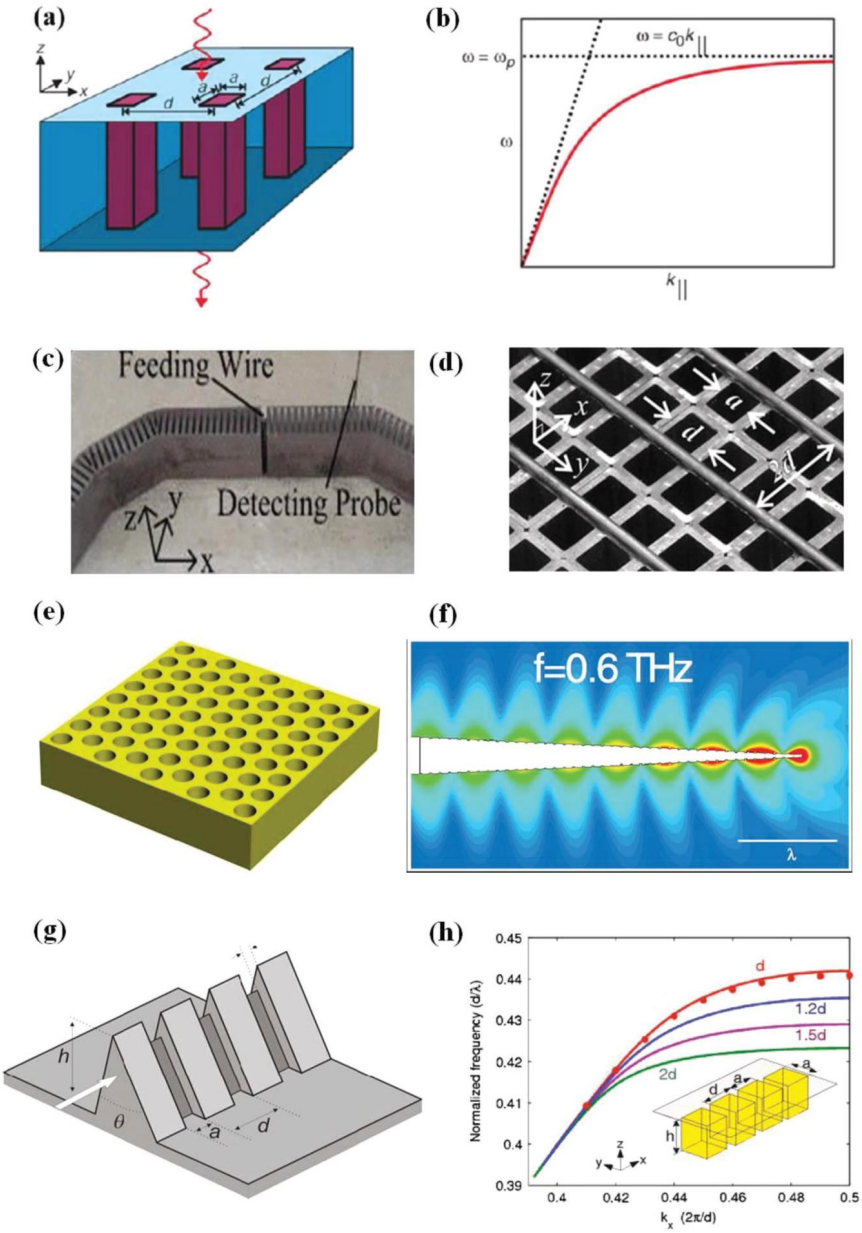

Figure 2.1: Series of preliminary 3D SSPP structures (a) Surface with holes. (b)Dispersion relation of SSPP (c) power splitter SSPP (d) Dimensions of periodic holes. (e) SSPP with radial holes. (f) Corrugations on metallic wire (conical) (g) Pyramid corrugation. (h). Flexibility of dispersion relation. Reprinted with permission from [5], Copyright 2018 WILEY-VCH Verlag GmbH & Co. KGaA, Weinheim.

to achieving efficient energy transfer and is a significant advancement in the practical implementation of SSPP devices.

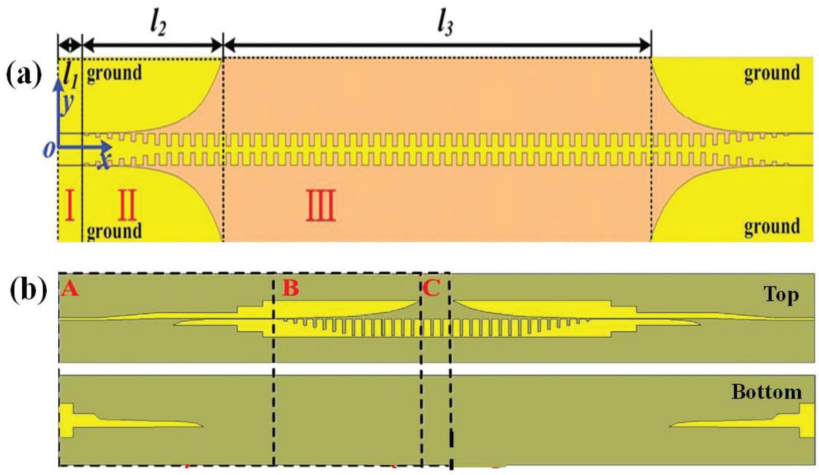

Figure 2.2: Guided-wave SSPP by integration to CPW and MS wavegides. (a) CPW to SSPP. (b) MS to SSPP. Reprinted with permission from [5], Copyright 2018 WILEY-VCH Verlag GmbH & Co. KGaA, Weinheim.

2.3 Dual-Conductor Configurations

In response to the challenges faced with CPW-based SSPP structures especially at THz frequencies, including flaring grounds loss and area consumption, dual-conductor CPS-based configurations were introduced as an efficient alternative. The dual-conductor approach enabled seamless integration with multi-conductor waveguides, eliminating the need for large matching circuits and transition regions. This innovation improved the integration of SSPP into microwave and THz systems, without the necessity of flaring grounds, enhancing their practical application in communication and sensing technologies [6, 46].

There are two approaches for the integration of SSPP into CPS. One method involves modifying the single-conductor SSPP to a dual-conductor configuration, thereby facilitating integration with a CPS, a configuration known as CPS-SSPP is presented in our works [1, 13] and also others' works in the literature [6, 46, 40]. Another approach, which has not been previously documented in the literature, entails the direct integration of a single-conductor SSPP with a CPS which necessitates the design of a transition circuit to couple CPS lines to SSPP. This approach is presented

in section 4.3.

Figure 2.3 shows the structure proposed in [6]. This structure utilizes two transitions from MS to CPS and from CPS to SSPP for demonstration at microwave frequencies. This approach was later demonstrated at THz frequencies in [1] by the author of this dissertation.

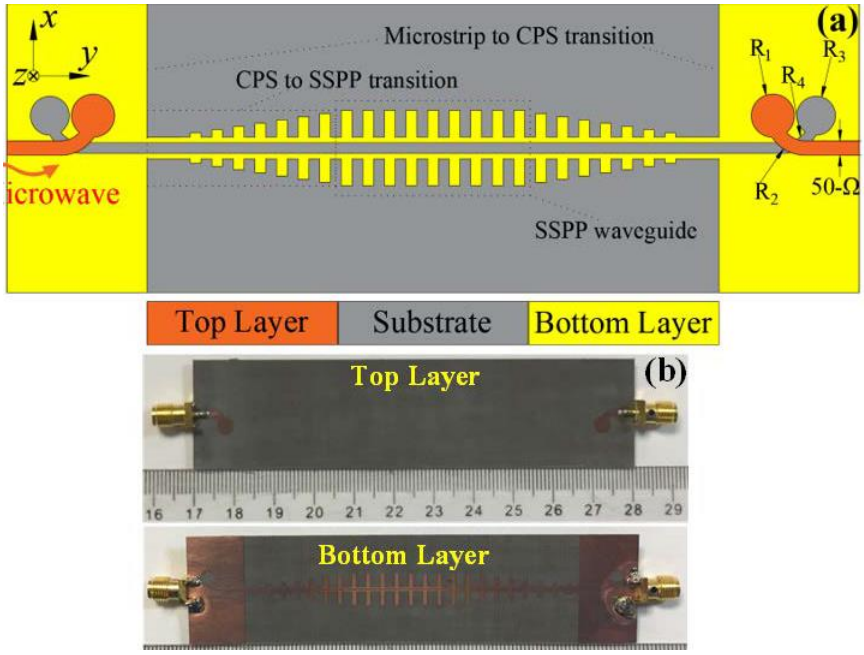

Figure 2.3: Dual conductor SSPP approach to integrate with CPS. (a) Structure diagram. (b) Fabricated structure. Reprinted from [6], copyright 2018 Optical Society of America under the terms of the OSA Open Access Publishing Agreement.

2.4 SSPP-based Filters and Frequency Selective Structures

As SSPP structures matured, research increasingly focused on their application in frequency-selective devices, such as filters. SSPP-based BPFs have emerged as an important area of interest. Early efforts demonstrated band-pass filtering with SSPP at microwave frequencies [48]. However, the development of high-performance band-pass filters remained a challenge at THz frequencies, primarily due to high losses, especially with MS waveguides [49]. Moreover, most of the traditional microwave BPF designed use a cavity-based structure to perform the filtering which poses challenges for on-chip integration of the filter.

Researchers have explored novel approaches to enhance the performance of SSPP-based filters, such as integrating different metamaterials and optimizing the geometry of the structures. These advancements have led to significant improvements in filter performance, making SSPP-based filters more competitive for applications in communication systems [50, 51, 52].

2.5 Recent Progress and Future Directions

Recent work on planar SSPP has focused on addressing the remaining challenges in integrating SSPP structures into practical systems, and design for practical applications. Researchers have continued to explore innovative solutions to reduce losses and enhance the scalability of SSPP devices. One of the most promising directions is the development of hybrid SSPP structures, which combine SSPP with other types of metamaterials to create efficient and versatile devices [48, 40]. These hybrid designs have the potential to unlock new possibilities for SSPP applications in high-performance microwave and THz systems.

Additionally, the optimization of TC and the exploration of novel materials for SSPP structures will continue to drive the field forward. As research progresses, SSPP devices are expected to play a key role in the development of compact, high-performance components for a wide range of applications, including communication, sensing, and imaging technologies.

2.6 Review Summary

SSPP has become an important area of research, offering unique capabilities for guiding electromagnetic waves at subwavelength scales. From the initial conceptualization of SSPP using metallic arrays to the recent advancements in guided-wave integration and filter and sensor design, the field has made significant strides in improving the performance and practical applicability of SSPP devices. Continued innovations in integration techniques, hybrid structures, sensors, and filter design will likely lead to further breakthroughs, opening up new possibilities for SSPP in THz communication and sensing technologies.

Chapter 3

Methods

3.1 Measurement Setup

Measurements were performed using a modified THz-TDS setup, as shown in Fig. 4.4. The basic principle of this measurement method is photoconductive sampling [53].

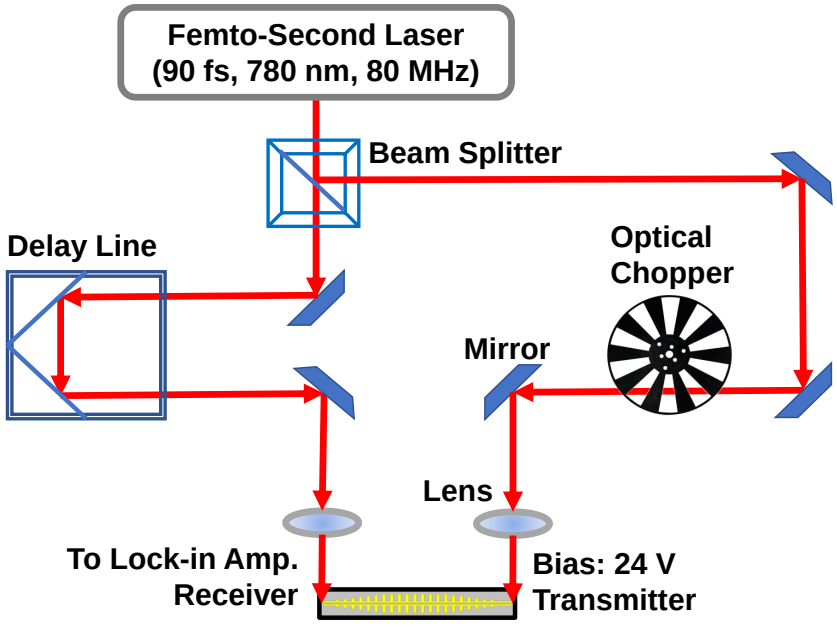

Figure 3.1: The modified THz-TDS setup used for measurements on THz circuits with PCS.

Photoconductive sampling is a widely used technique for generating and detecting THz signals because of its broadband capabilities and high temporal resolution.

It relies on PCS made from materials like LT-GaAs, which exhibit ultrafast carrier dynamics. In this method, a femtosecond pulsed laser excites the PCS, generating electron-hole pairs in the semiconductor. When a bias voltage is applied across the PCS, these carriers are rapidly accelerated, producing a transient current. This transient current generates a broadband THz pulse at the transmitter PCS. The generated THz pulse then propagates from PCS or photo-conductive antenna [54] through a communication channel, which can be free-space, a transmission line, a waveguide, or an optical fiber, depending on the application and distance. In our platform, the channel is a CPS waveguide [1, 55]. At the receiver PCS, the same laser pulse is used as a sampling gate. The incident THz pulse creates a voltage and, subsequently, a current across the PCS. The resulting current is proportional to the instantaneous electric field of the THz pulse. By varying the relative delay between the laser pulse and the THz pulse using a mechanical delay line, the time-domain waveform of the THz pulse can be reconstructed [53]. Photoconductive sampling offers several advantages, including high sensitivity, precise temporal resolution, and compatibility with broadband THz spectroscopy. This technique forms the foundation of THz-TDS systems, enabling detailed analysis of THz signals in various applications.

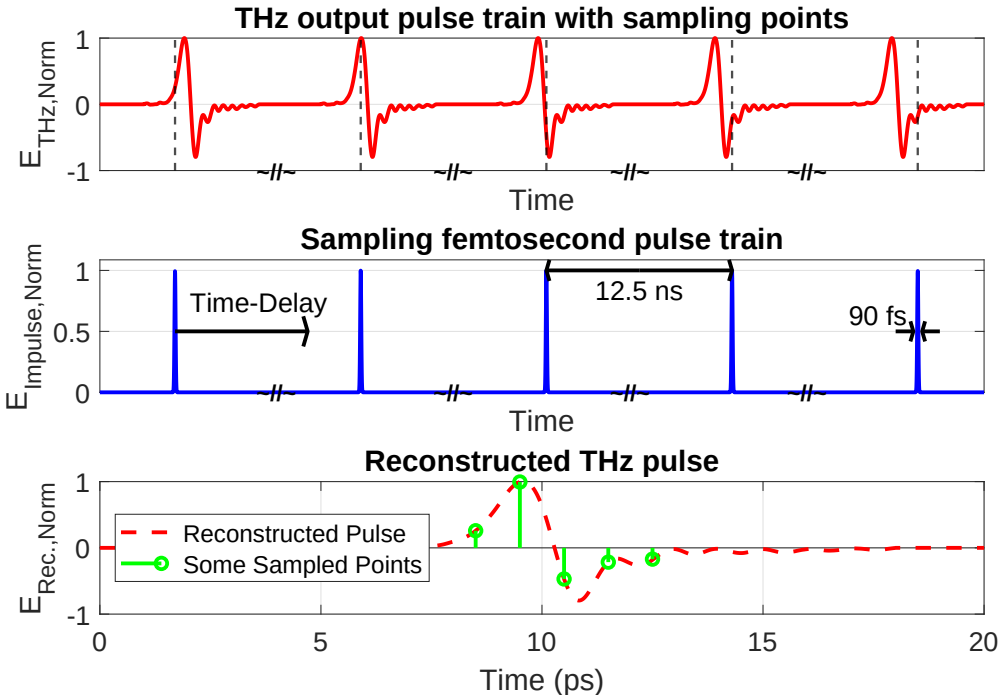

Figure 3.2: Principle of photoconductive sampling method used in the modified THz-TDS system.

The setup in Fig. 3.1 utilizes a femtosecond pulsed laser with a central wavelength of 780 nm to generate and detect broadband THz pulses. The laser beam was focused on the PCS devices integrated into the waveguide, enabling the excitation and subsequent detection of THz signals.

The measurement process involved the generation of THz pulses at the transmitter PCS, which propagated through the CPS-SSPP structure. The receiver PCS detected these pulses, reconstructing the transmitted signal. This reconstruction was achieved by translating a mechanical delay line, allowing the detection of time-resolved signals based on the receiver current. A lock-in amplifier was used to extract the signal with high sensitivity, akin to the standard THz-TDS technique [55, 56].

It is worth noting that in the upcoming measurement results shown in Chapter 4, the band-edge frequency locations (i.e., key feature in SSPP) remain consistent across multiple measurements and over extended periods. The same devices were remeasured after six months, one year, and two years following the initial characterization, yielding band-edge frequencies within 0.5% of the original values. The minor deviations observed are primarily attributed to measurement noise. These findings highlight the stability and reproducibility of the response and the band-edge frequencies.

To resolve the narrow spectral features in the measurements presented in Chapter 4, such as the band-edge frequency in SSPP [1] and the spectral absorption dip for sensors [3], it is crucial to ensure that the spectral resolution is fine enough to capture these features. The typical width of the SSPP band-edge frequency is 50 GHz [1], and the linewidth of the glucose absorption dip (at 1.4 THz) is 140 GHz [57]. The spectral resolution is determined by the temporal window length, which is approximately 100 ps for most measurements presented in Chapter 4. However, the temporal figures in the chapter show only the first 30 - 40 ps for clarity of the pulse shape. The temporal length of 100 ps in measurements implies that the spectral resolution is on the order of 10 GHz, which is sufficient to resolve both the band edges and absorption dips.

Fluctuations in the measurement results originated from various random noise sources, including laser instability, electrical noise, PCS shot noise, vibrations, and environmental factors. The dominant noise mechanism causing fluctuations is the vibration of lenses and the mechanical delay line, which consequently vibrates the focused laser beam on PCS devices, resulting in photo-current fluctuations. One common approach to mitigating these fluctuations is spectral averaging, which involves performing repeated measurements for each device to average out random noise.

3.2 Fabrication of Photo Conductive Switches

This section provides a concise overview of the fabrication process for PCS in 12 steps illustrated in Figures 3.3 - 3.7. In short, the fabrication procedure includes photolithography, gold (Au) and titanium (Ti) deposition, and wet etching of GaAs and AlAs. While the detailed process is documented in [54], a brief summary is provided here to explain some of the specific details and graphically illustrate each step of the real fabrication process performed by the author of the dissertation.

To fabricate the PCS devices, a specific multilayer wafer is required. The desired LT-GaAs layer was grown on a sacrificial AlAs layer atop a semi-insulating GaAs (SI-GaAs) substrate shown in the cross sections in Fig. 3.3. This wafer should be cleaved to facilitate the lithography process. After cleaving the wafer into small square pieces (7 mm $\times$ 7 mm), using standard photolithography and lift-off, Au contacts (200 nm thick), with a 10 nm Ti adhesion layer between Au and LT-GaAs were patterned onto the LT-GaAs surface, as shown in Fig. 3.3 for cleaving and lithography and in Fig. 3.4 for the lift-off process. In this process, a positive Photo Resist (PR) was used allowing for high resolution, and a layer of Lift-Off Resist (LOR) was employed to create undercuts shown in Fig. 3.3(right) to facilitate the lift-off process.

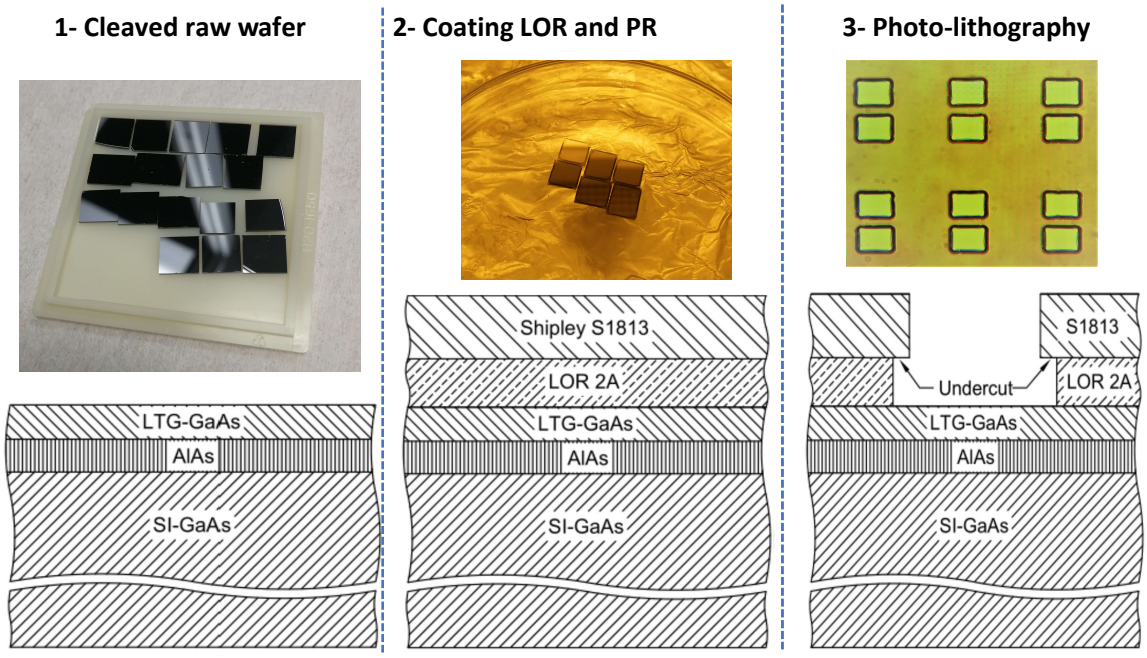

Figure 3.3: Photolithography on cleaved pieces of LTG-GaAs wafer. Cross section pictures used from [7]

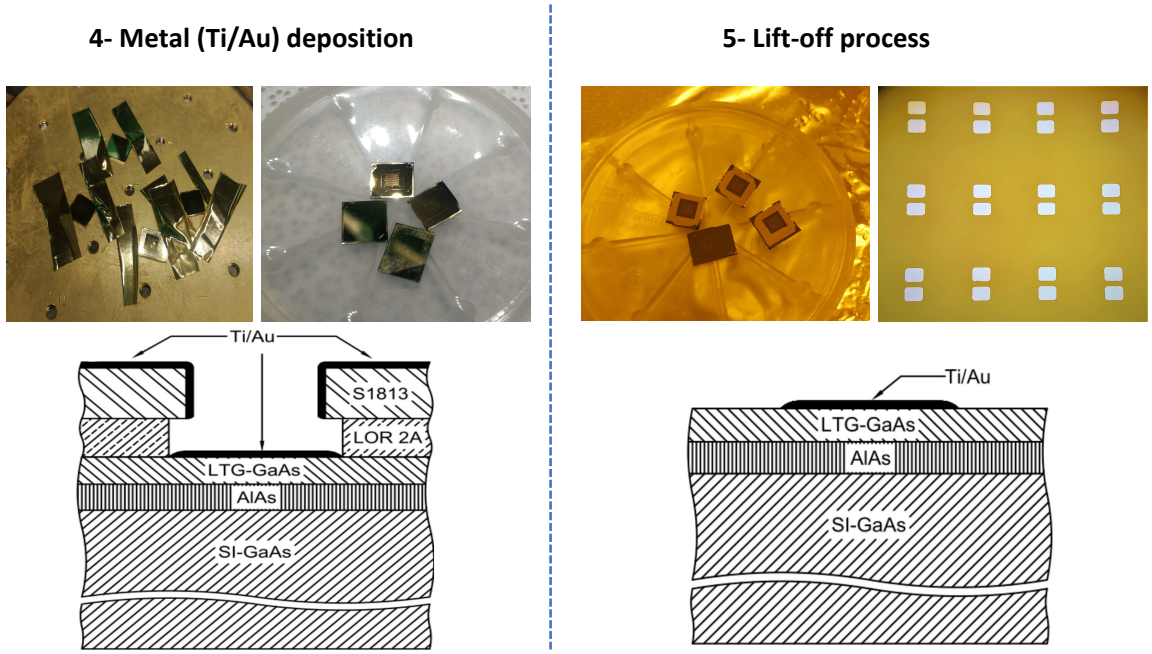

Figure 3.4: Metal sputtering and lift-off process. Cross section pictures used from [7]

Each PCS region was subsequently masked and etched with a solution of citric acid and hydrogen peroxide to define the PCS thickness, depicted in Fig 3.5, in which the profile of the sample is shown in steps 7 and 8, along the dashed redline, indicating the thickness of metal and LT-GaAs layers after cleaning in step 8. It is worth noting that the rounded shape of PCS shown in step 7 of Fig 3.5 is because the etching process was performed the next day after covering the PCS with the photoresist. This overnight delay causes the deformation of the photoresist layer from a rectangular pattern to a rounded shape. This being said the best practice is to perform etching right after the development of the photoresist or perform post-baking of the photoresist if a consecutive process is not possible.

Following this, the surface was cleaned and re-masked with an etch-resist wax shown in Fig 3.6. The LT-GaAs layer of the wafer was detached by submerging the structure in hydrofluoric acid (HF) to dissolve the AlAs layer. Further etching with citric acid and hydrogen peroxide disconnected any remaining LT-GaAs films interlinking the PCS grid [see Fig. 3.7, step 10]. Finally, the etch-resist wax was removed using trichloroethylene (TCE) [Fig. 3.7, step 11], resulting in thousands of LT-GaAs PCS active regions.

For ease of access and clarity, the brief step-by-step fabrication procedure is out-

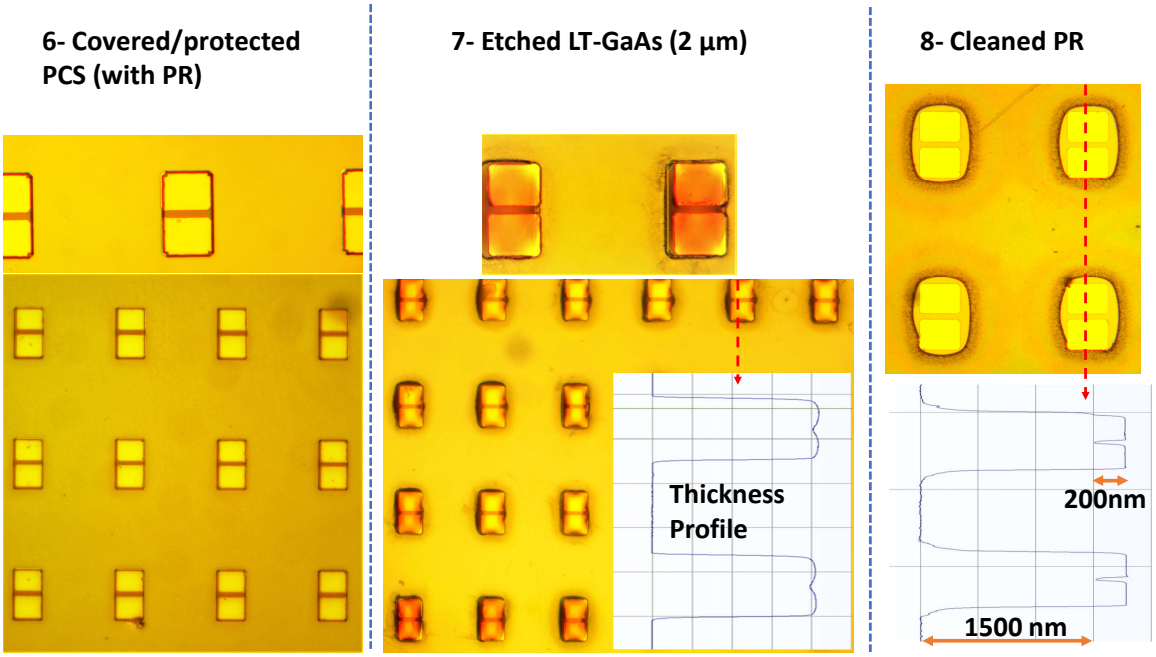

Figure 3.5: Etching process to create a thin film of LTG-GaAs attached to Gold contacts. Curves show the thickness profile of the device along the dashed red line, indicating 200 nm of Gold and 1500 nm of GaAS

lined below. For details refer to [54, 7]

1. **Prepare the wafer and cleaving:** Begin with a multilayer wafer consisting of an LTG-GaAs layer (approximately 2 m thick) grown on a sacrificial AlAs layer (approximately 200 nm thick) atop a semi-insulating GaAs substrate. Cleave the wafer into small square pieces of dimensions 7 mm by 7 mm using a diamond-tipped scribe and a breaking tool to cleave the wafer precisely along the crystal planes. [See Fig. 3.3]

2. **Photoresist coating:** Apply a uniform layer of lift-off resist (LOR 3A, thickness approximately 1.5 µm) followed by a photoresist (Shipley S1813, thickness approximately µm) to the cleaved wafer pieces. Use a spin coater at 2500 rpm (LOR) / 5000 rpm (photoresist) for 30 seconds to achieve uniform coating. Bake the wafer on a hot plate at 110°C for 3 minute (LOR) and at 170°C for 1 minute (photoresist) to ensure proper adhesion. [See Fig. 3.3]

3. **Photolithography:** Use standard photolithography techniques to pattern the desired structure onto the LT-GaAs surface. Expose the wafer under a UV lamp with an intensity of 22 mW/cm^2 for 4 seconds. Develop the exposed wafer in

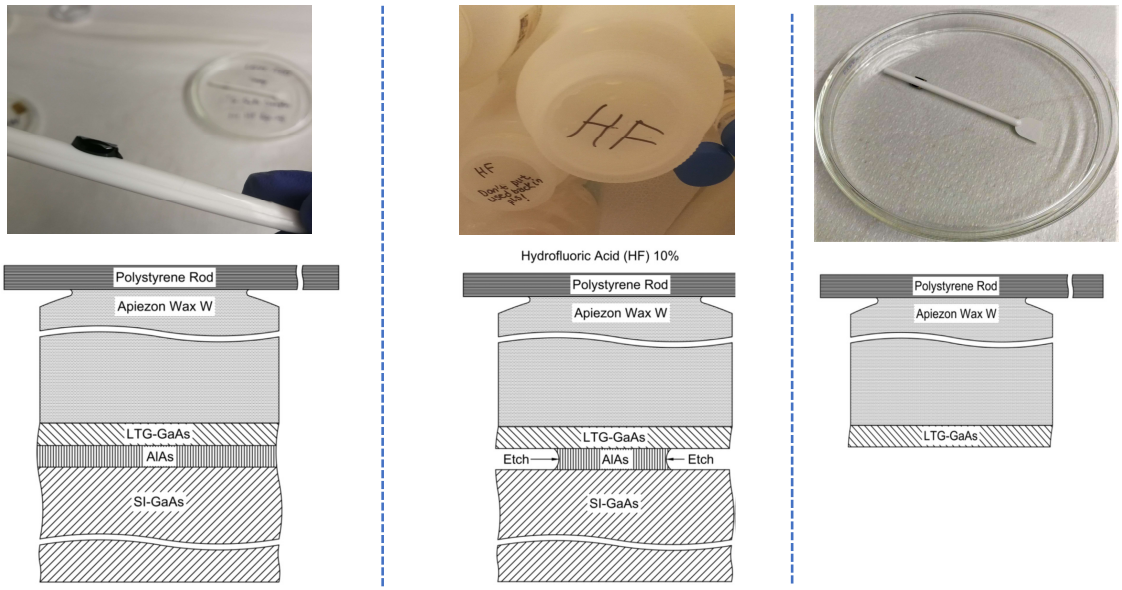

Figure 3.6: HF process to remove the AlAs sacrificial layer. Cross section pictures used from [7]

MF-319 for at least 50 seconds, to ensure undercuts for easy lift-off, followed by rinsing in DI water. Bake the wafer on a hot plate at 110°C for 1 minute to harden the resist. [See Fig. 3.3]

4. **Metal deposition:** Deposit a layer of Gold (Au, thickness approximately 200 nm) on Titanium (Ti, thickness approximately 10 nm) as the adhesion layer to form electrical contacts. [See Fig. 3.4]

5. **Lift-off:** Perform the lift-off process by submerging the wafer in warm Remover-PG (PG) (around 50-80°C) for approximately 30 minutes. Different bath beakers can be used, for example, a sequence of PG-IPA-PG baths is recommended by one of the PG producers (Kayaku). Use an ultrasonic bath to aid in the lift-off process, removing excess metal and leaving only the patterned Au contacts on the wafer surface. [See Fig. 3.4]

6. **Masking for etching:** Mask each PCS region with a photoresist (typically Shipley S1813) to prepare for etching. After development, the photoresist is recommended to be baked at 110°C for 1 minute to harden it before etching. Using a profilometer is also recommended to check the thickness of the resist.

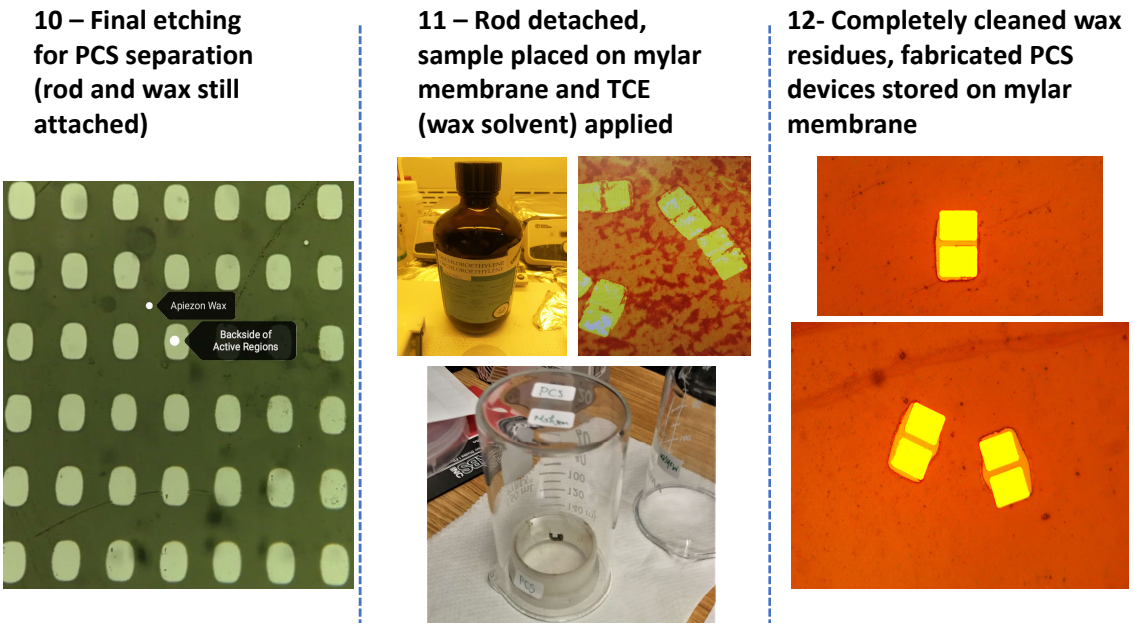

Figure 3.7: PCS device extraction from the wax, and storage of fabricated devices

Ensure the resist completely covers the areas that need to remain intact during the etching process. [See Fig. 3.5]

7. **Etching:** Define the PCS thickness by etching the LT-GaAs layer with a solution of citric acid and hydrogen peroxide. Use Monohydrous citric acid and combine it with DI water (1 gram / 1.29 ml) to make liquid citric acid. Then a combination of citric acid and hydrogen peroxide (30%) was used (5:1). This combination provides an etching rate of 200 nm/minute. Etch for approximately 5 minutes, monitoring the process to ensure the desired depth is achieved (typically around 1 µm). Conduct the etching immediately after developing the photoresist or post-bake the resist at 110°C for 1 minute to prevent deformation. [See Fig. 3.5]

8. **Cleaning:** Remove any residue left from the etching process by thoroughly cleaning the surface with warm Remover-PG, Acetone, IPA, and DI water, followed by drying with a nitrogen blower. Check for any residual photoresist or etch residue under a microscope. Inspect with profilometer [See Fig. 3.5]

9. **Removal of AlAs sacrificial layer:** Submerge the wafer structure in hydrofluoric acid (HF, concentration 10%) for approximately 2 days to dissolve the AlAs sacrificial layer, detaching the LT-GaAs layer. The LTG-GaAs layer

should remain intact in HF regardless of etching time. [See Fig. 3.6]

10. **Final etching:** Perform an additional etching step using citric acid and hydrogen peroxide to separate any remaining LTG-GaAs films interlinking the PCS grid. Etch for approximately 1 minute, until the grid-like pattern emerges, ensuring that no connections between the PCS regions remain. Wash with DI water immediately. [See Fig. 3.7]

11. **Wax removal:** Detach the wax from the rod. Place the sample with wax on top side of the mylar membrane. Apply trichloroethylene (TCE) drops to the wax at room temperature to remove the wax. Use a cleanroom cloth to gradually clean the mix of wax and TCE. Do not apply too much of TCE, since it causes the PCS to float in liquid and is difficult to bond on the mylar layer. [See Fig. 3.7]

12. **Extraction and storage:** Extract the fabricated PCS devices, ensuring that there is no residual wax, and store them appropriately on a mylar membrane. This process yields thousands of LT-GaAs PCS active regions, ready for subsequent testing and integration. [See Fig. 3.7]

The fabricated PCS devices shown in Fig. 3.7(step 12) were bonded to the structure membrane [Fig. 3.8(a)] using acupuncture needles for alignment and the water molecule Van der Waals (VDW) forces for bonding to the metal surface (the technique described in [31]). The fabricated PCS dimensions were 70 µm × 40 µm × 1.5 µm, with a 5 µm gap between the metal contacts. Placement of the PCS devices on the structure was performed using a modified probe station. A droplet of water was applied to the PCSs to ensure robust contact via Van der Waals forces.

This method of placing water droplets was traditionally used [31, 55], but the author found that it increases the probability of breaking the thin membrane, at the time of holding a needle on top of PCS and placing the droplet. The author found a novel non-invasive method by smoothly sliding the PCS to the desired location, removing the needle and simply breathing out by mouth on the membrane so that the water droplets are visible around the PCS under the microscope. This will fix the PCS in place and provide a reasonable adhesion. Most of the time it is sufficient to get a dark current and perform the measurements. Otherwise, the droplet of water can be applied, this time without any needle pressure.

Subsequently, the PCB board with the structures on membranes was mounted on a modified THz-TDS setup shown in Fig. 3.8(c,d) to measure the dark current at the ports. The device position was then aligned to focus the laser beam onto the PCS, optimizing the photo-current. The THz pulse was transmitted through the waveguide, and the received signal was measured using a lock-in amplifier. Based on the study in [58], the optical-to-THz average power conversion efficiency of the transmitter PCS, under a 24 V bias voltage, a 40 µm device width, and 7 mW of optical power, was estimated to be approximately 0.006%. This corresponds to a maximum average THz power of 0.42 µW delivered to the CPS transmission line (TL) and the subsequent CPS-SSPP structure.

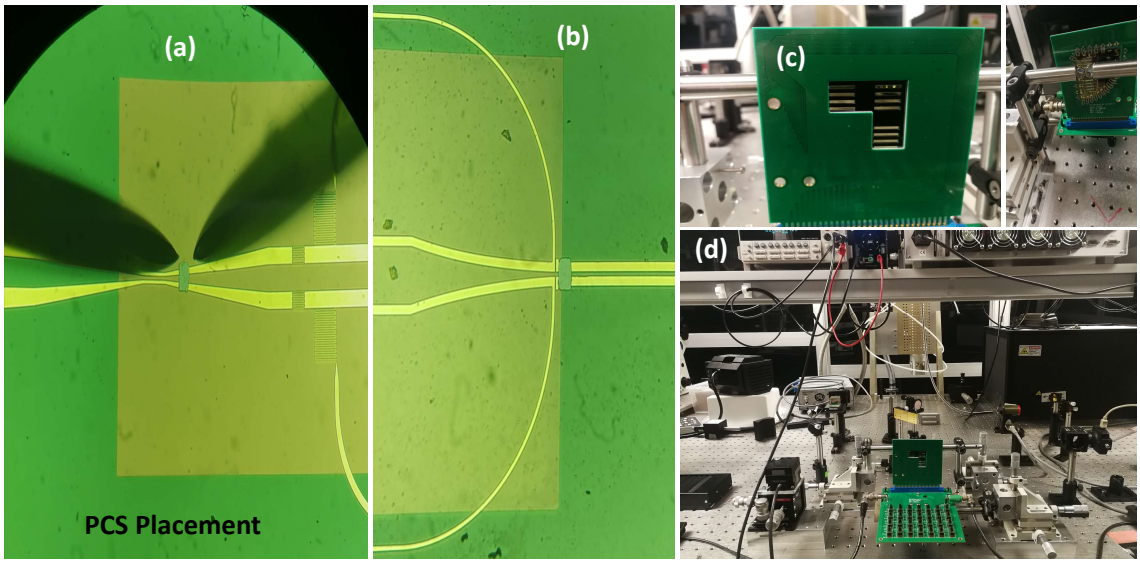

Figure 3.8: Placement of PCS devices on the structures to generate and detect THz bandwidth pulses

Chapter 4

Contributions

This chapter provides details of the primary contributions listed in chapter 1, section 1.3. The full manuscripts (published or submitted) are included in Appendices A through F in the journal's format for reference and more details about design and methods. This chapter incorporates a part of content and figures from the author's published or submitted manuscripts without alteration, in accordance with the applicable Creative Commons copyright licenses (CC BY 4.0 and CC BY-NC-ND 4.0) and the Optica Open Access Publishing Agreement. All figures are appropriately cited within their captions.

4.1 Demonstration of a Terahertz Coplanar Strip Spoof Surface Plasmon Polariton Low Pass Filter

This project presents the first experimental verification of SSPP characteristics at THz frequencies in a guided wave system using CPS feedlines, which is the preliminary work toward achieving one of the objectives of the dissertation. Specifically, we designed three SSPP structures with varying band-edge frequencies (1.04 THz, 0.63 THz, and 0.53 THz), then fabricated and verified the low-pass transmission characteristics using a modified THz-TDS system. We found strong agreement between simulation, theory, and experiment.

SSPP devices exhibit low-pass behavior with significant roll-off rates over short structure lengths. Practically, short filter lengths are desirable to minimize the necessary component area. Also, SSPPs exhibit slow-wave behavior and significant field enhancement [32].

It is not straightforward to directly excite the fundamental mode TM of an SSPP waveguide. For practical purposes, SSPP structures are typically integrated with a feedline such as a CPW [37, 35, 43], CPS, [36, 46, 40], MS [44], or SL [45]. The fundamental modes of the aforementioned waveguides are quasi-TEM (CPW, CPS, and MS) or quasi-TE for the SL[47]. Given that the feedline and SSPP have different modes, a TC is necessary to perform a mode conversion. To date, most of the research efforts have utilized a CPW feedline to excite an SSPP mode where large flaring grounds are used in the TC to aid in the mode conversion [47]. The CPW configuration is commonly used because of its compatibility with standard microwave frequency VNA probes. Alternatively, in [36], it was suggested to use a CPS feedline to excite the SSPP mode (termed CPS-SSPP). The CPS-SSPP has several benefits such as a reduced circuit size and improved lumped element compatibility. In [36], the authors designed a *THz* CPS-SSPP structure but fabricated and tested a scaled structure at microwave frequencies. The reason for the scale modification is that it is exceedingly difficult to perform device characterization at THz frequencies because there is limited or no commercial equipment available. Downshifting to GHz provides useful insight, but it negates difficulties that are expected to occur at THz frequencies such as substrate radiation and losses.

While many simulations at THz frequencies have been conducted, most of the

validation experiments have been performed at microwave frequencies by scaling the structures and implementing them on MS platforms to measure the performance up to 16 GHz [36, 46, 40, 59]. To date, experimental measurements of THz SSPPs have predominantly focused on frequencies up to approximately 300 GHz [37, 60, 61] except for our preliminary work which focused on a single CPS-SSPP configuration [13]. On the other hand, some studies have employed radiated wave approaches to investigate SSPPs at frequencies greater than 1 THz [62]; however, this work focuses on using non-radiative feedlines for their improved integration benefits such as their well-known field profiles and planar coupling efficiencies.

To verify SSPP behavior, we investigate a signal that has been transmitted through an SSPP. It is known that an SSPP behaves like a low-pass filter where the cut-off frequency is given by the band-edge associated with the periodic structure (discussed later) [4]. In this work, we integrate three different CPS-SSPP geometric configurations into our THz System-on-Chip (TSoC) platform [55] as shown in Fig. 4.1, then we verify the stop-band location at THz frequencies. The TSoC platform consists of planar conductors on a very thin (1 µm) Si_3N_4 membrane which reduces the loss and dispersion of the propagating wave along the CPS feedlines and ensures the CPS-SSPP is excited with a near-TEM field profile. This method enables us to characterize devices at THz frequencies with ease since radiative substrate losses are heavily mitigated. We find that the SSPP results from the experiments are in agreement with simulation and theory. To the best of our knowledge, this work presents the highest experimental frequency achieved for guided-wave SSPP characterization. Note that this is a proof-of-concept, and with the appropriate circuit modifications, it is possible to investigate SSPP device characteristics beyond 3 THz. The most salient feature of the presented TSoC CPS-SSPP is the ease of implementation while obtaining THz-band operation. While it is possible to use a VNA along with several extension modules as an alternative, it becomes a costly endeavor that currently cannot exceed 1.5 THz using commercially available extension modules.

One of the useful tools to analyze SSPP structures is the dispersion relation often derived from the unit cell of its periodic structure. Unfortunately, no closed-form dispersion relations have been presented for a finite-thickness CPS-SSPP structure. However, if we consider the thickness of the CPS-SSPP conductors to be infinite, then the CPS-SSPP dispersion relation can be approximated by a 1D array of grooves

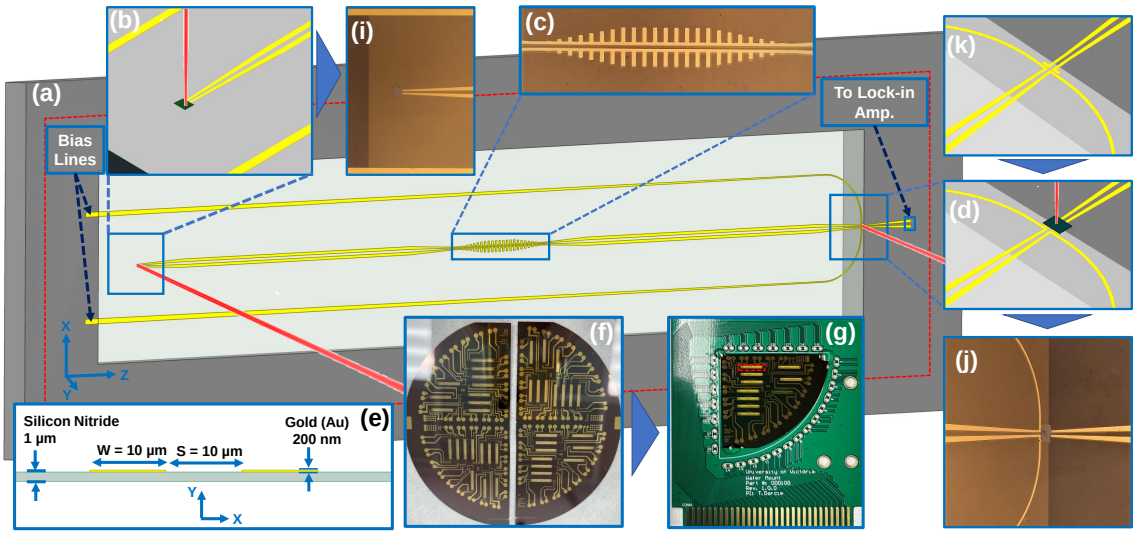

Figure 4.1: Illustration of CPS-SSPP device and measurement platform. (a) The whole structure along with tapered and bias lines on Silicon Nitride membrane. (b) Transmitter PCS and incident laser beam. (c) Main CPS-SSPP structure. (d) Receiver PCS and incident laser beam. (e) Dimensions of central reference CPS line and the membrane. (f) Fabricated circuits on Wafer. (g) Mounted Wafer quarter on PCB to connect to the measurement setup. (i) Real Transmitter PCS. (j) Real Receiver PCS. (k) Contact point for the receiver PCS on the edge of the membrane. Reprinted from [1].

[4, 33]:

$$k_z = k_{eff}\sqrt{1+\left(\frac{a^2}{d^2}\right)\tan^2(k_{eff}H_n)}, \tag{4.1}$$

where H_n is the length of stubs (i.e. depth of grooves) in the SSPP region, $d = a+W_n$ is the period, a is the aperture or the distance between the stubs, W_n is the width of the stubs, $k_{eff} = \omega\sqrt{\varepsilon_{eff}}/c$ is the effective wavenumber, c is the speed of light, and ε_{eff} is approximated by the effective relative permittivity of the CPS feedlines at THz frequencies. There are empirical models to obtain ε_{eff} [49, 63, 64], but we use numerical simulations to overcome the constraints of the empirical boundaries. We found $\varepsilon_{eff} \approx 1.7$ between 0.1 and 1.5 THz using ANSYS HFSS. We note that (4.1) is not explicitly true for a CPS-SSPP, but it provides a reasonable approximation. The validity of a similar approximation is also found in [33, 35].

To complement the theory and experiment we use ANSYS HFSS to perform eigenmode and frequency-domain (FD) full-wave simulations of the CPS-SSPP structures. We use the eigenmode simulation to obtain the dispersion diagram and band-edge

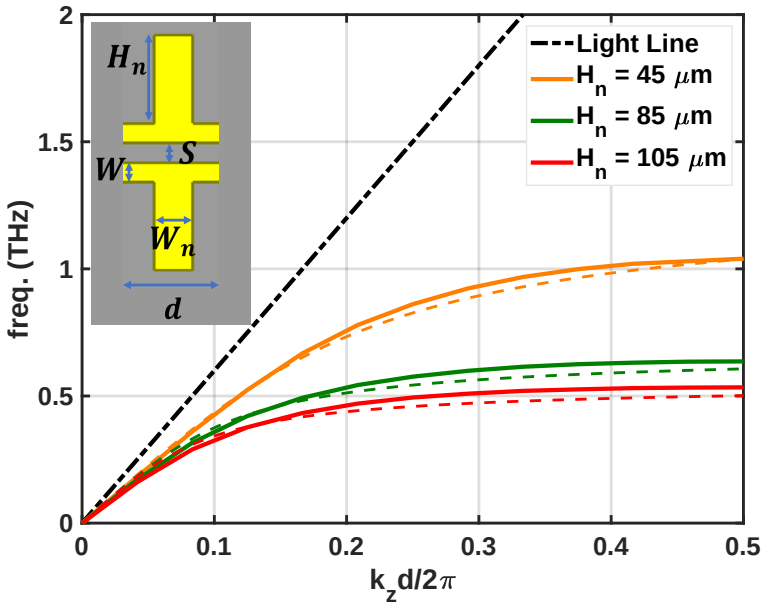

Figure 4.2: Dispersion curves obtained by eigenmode simulation (solid lines) and theory (dashed lines) on the CPS-SSPP unit cell (inset). H_n is variable as shown in the legend and fixed dimensions are d = 50 µm, W_n = 20 µm, and S = 10 µm. Reprinted from [1].

frequencies for the CPS-SSPP unit cells. Figure 4.2 plots the simulated dispersion relation (solid lines) for the three CPS-SSPP structures investigated in this work. It is possible to use (4.1) for this purpose (dashed lines), but we reiterate that (4.1) was derived for a 1D array of grooves, thus caution is required. Regardless, for each case, we see asymptotic behavior which is characteristic of SSPPs. The simulated band-edges were found to be: 1.04 THz (H_n = 45 µm), 0.63 THz (H_n = 85 µm), and 0.53 THz (H_n = 105 µm) which are in close agreement with values previously obtained from equation (4.1).

We perform FD simulations for several purposes. First, we investigate the transmission through the fabricated CPS-SSPP structures where H_n = 45, 85, and 105 µm. Figure 4.3 plots the results of these simulations. Low-pass behavior is clearly observed and the cut-off frequency aligns with the predicted band-edge frequencies.

For THz generation and detection, fabricated PCSs. After fabrication of the PCS devices and the CPS-SSPP structures, measurements were performed using the modified THz-TDS setup depicted in Fig. 4.4. The experiment involved utilizing a femtosecond pulsed laser with a wavelength of 780 nm focused on PCSs placed on the waveguide to generate and detect a broadband THz pulse signal. The transmit-

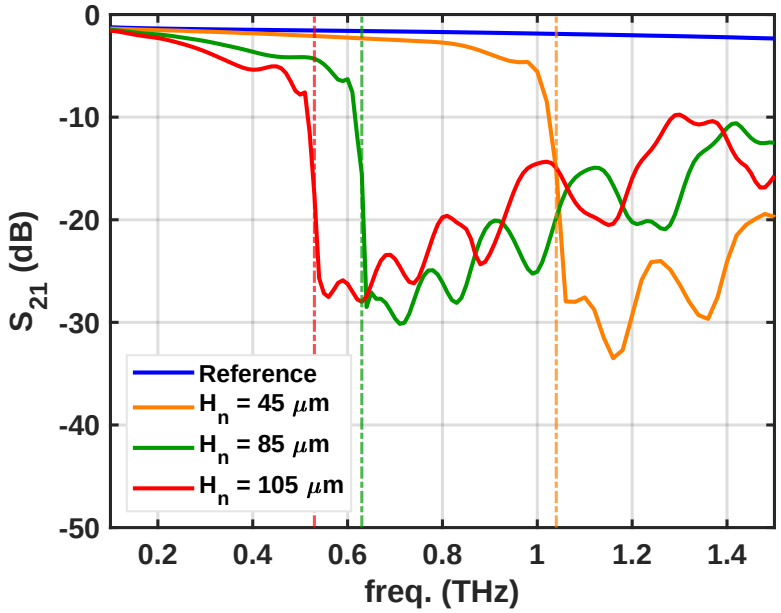

Figure 4.3: CPS-SSPP S_{21} (dB) from FEM simulation results for the structures which were experimentally tested. The vertical dashed lines indicate the simulated band-edge frequencies. Reprinted from [1].

ted signal was reconstructed by translating the mechanical delay line measuring the receiver current using a lock-in amplifier [55, 56].

The experimental results for the CPS-SSPP are displayed in Fig. 4.5 alongside a reference without stubs (i.e., $H_n = 0$).

To estimate the experimental signal transmission, it is necessary to take the difference between the respective signal ($H_n = 45$, 85, or 105 µm) and the common reference measurement. We see that as the stub length increases the cut-off frequency reduces as predicted by (4.1). Figure 4.6 plots the band-edge frequency versus H_n using simulation, theory, and experiment where reasonable agreement is observed. Next, the roll-off rate associated with the band-edge frequencies is significant and is on the order of ≈ -160 dB/Octave. As a consequence of the steep roll-off (and non-linear phase response), we see oscillations in the temporal response, which are the most significant for the $H_n = 105$ µm structure. Thus, if the CPS-SSPP structures are to be used as low-pass filters, then it is important to consider the applications' phase response requirements.

This project successfully demonstrated THz SSPPs beyond 0.5 THz. This experimental verification will enable others to investigate a multitude of other novel

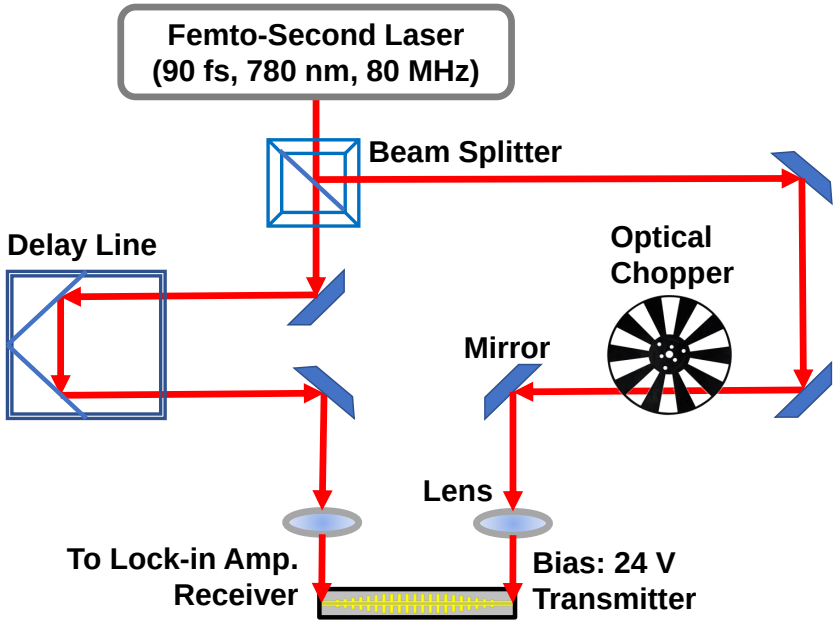

Figure 4.4: The modified THz Time Domain Spectroscopy setup for performing measurements on THz circuits with photo-conductive switches. Reprinted from [1].

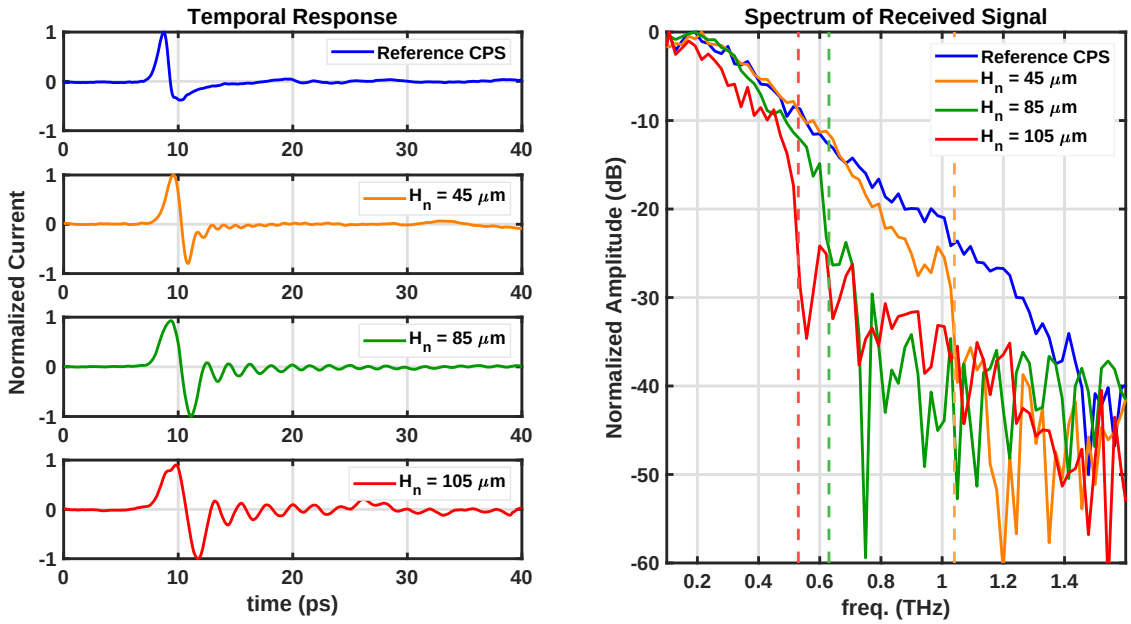

Figure 4.5: Measurement results for structures with different stub lengths. The time-domain results are obtained from the lock-in amplifier, the spectral response is obtained by applying the Discrete Fourier Transform of the temporal response. The vertical dashed lines indicate the simulated band-edge frequencies. Reprinted from [1].

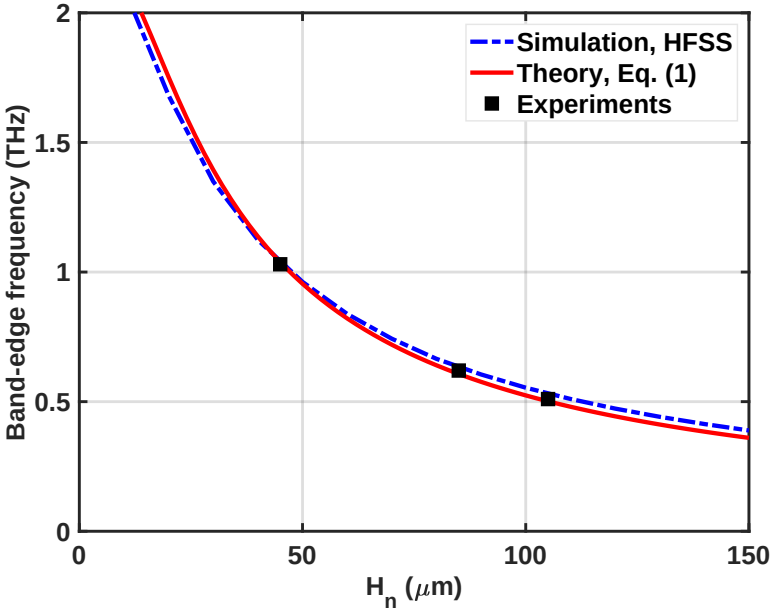

Figure 4.6: Band-edge frequency versus H_n obtained from eigenmode simulations, theoretical dispersion relation, and experiment. Reprinted from [1].

guided-wave SSPP structures for a range of applications at THz frequencies. As mentioned, the novelty of this work is the first guided-wave SSPP demonstration that confirms SSPP behavior beyond 1 THz using guided wave feedlines for excitation and ultra-thin (1 µm) Si_3N_4 substrate to significantly reduce radiation losses and dispersion (novel for SSPP devices). Additionally, this is the first work to experimentally characterize several different band-edge frequencies within the THz range, which enables the validation of simulation and theoretical models at higher frequencies. This also opens a pathway to study different SSPP structures at THz. The next work is about an investigation of another SSPP unit cell at the THz range to enhance the functionality of the structure presented in this work.

4.2 Demonstration of Terahertz Spoof Surface Plasmon Polariton Waveguides using CPS with Internal Corrugations

The previous work in section 4.1, made it possible to investigate other SSPP unit cells experimentally. One of the features of the unit cell used in previous work (section 4.1), was the small separation between CPS lines primarily created to adapt the SSPP structure with CPS configuration. From the theory of CPS waveguides and simulations, we know that this small gap contributes to the insertion loss of the feedline. This inspired us to propose a complementary SSPP structure based on CPS with internal corrugation. We increased the CPS separation to reduce the loss and transferred the grooves inside the CPS. This method also improves the mode conversion efficiency of the transition circuit.

First, we investigated the CPS feedlines without corrugations. The CPS feedlines and the membrane are suspended over the air to reduce the radiation loss into the substrate [55]. To characterize the impact of the CPS conductor separation, S, on the attenuation coefficient we perform a simulation to obtain the attenuation coefficient in dB/mm. The results are plotted in Fig. 4.7. We select the feedline width to be $W = 30$ µm which provides acceptable ohmic losses [55]. Figure 4.7 illustrates that the feedline attenuation decreases as S increases. This relationship partially motivates this study by illustrating that the CPS feedline of Unit Cell 'A' (large S) will generally exhibit lower attenuation than Unit Cell 'B' (small S). Next, for Unit Cell 'A', H is limited to be less than $S/2$. This implies that the feedline geometry impacts the viable cut-off frequency range. Fortunately, this constraint does not have a large effect on reasonable CPS configurations that exhibit low loss and dispersion at THz frequencies. Thus, we select $S = 140$ µm which limits $H < 70$ µm.

The common SSPP unit cells and an example reference can be found in Table 4.1. All of the unit cells illustrated in Table 4.1 are capable of supporting an SSPP transverse magnetic (TM) mode. The choice of the unit cell depends on integration practicality and the desired application. However, in all cases, it is desirable to reduce the passband insertion loss. Unit Cell 'A' and 'B' are both driven by a CPS feedline, but they have different attenuation coefficients. The relationship between CPS geometry and loss has been studied in the prior work and it was found that larger values of S generally result in lower attenuation [55].

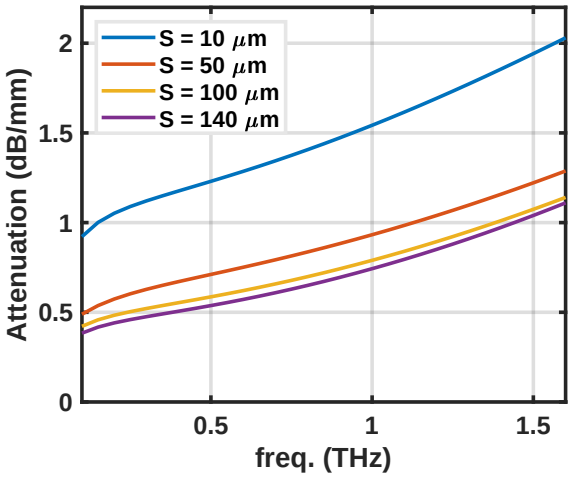

Figure 4.7: Loss of the CPS transmission lines with different S values (distance between conductor strips) from 10 µm to 140 µm and fixed strip width, $W = 30$ µm. Reprinted from [2].

Table 4.1: Unit cell illustrations, Reprinted from [2].

A (this work)	B [36]	C [35]	D [33]
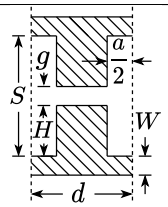	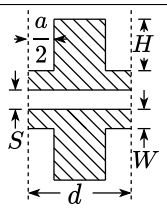	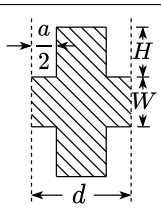	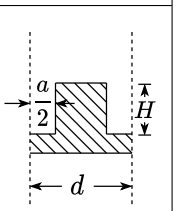

We analyze the effect of increasing CPS separation on SSPP through simulation and then experimentally confirm the excitation of the SSPP mode at two different corrugation depths, 55 µm and 65 µm. We found that the associated SSPP band-edge frequency changed from 0.89 THz to 0.72 THz which is consistent with the simulations.

Figure 4.8 illustrates the structures used in the experiment. The SSPP waveguide consists of a periodic array of Unit Cell 'A'.

We experimentally investigate Unit Cell 'A' SSPP structures with different cut-off frequencies specified by the stub height, H (see Fig. 4.8). An eigenmode simulation was performed to accurately determine the band-edge frequency (where $k_z d = \pi$) from the dispersion diagram (see Fig. 4.9) which results in cut-off frequencies of 0.72 THz (for $H = 65$ µm) and 0.89 THz (for $H = 55$ µm). Figure 4.10 plots the S-parameters

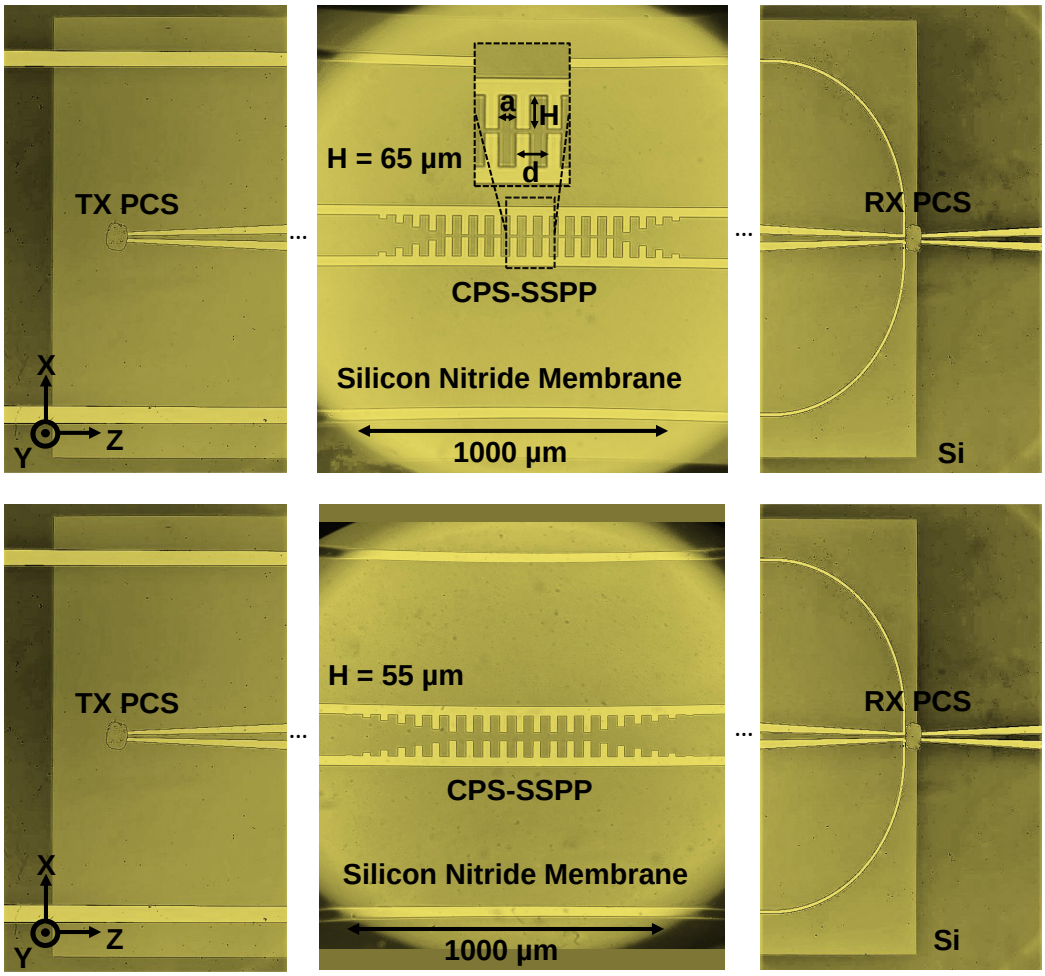

Figure 4.8: Illustration of the fabricated devices with the transmitter and receiver sections. Reprinted from [2].

for the two configurations which illustrates a sharp reduction in transmission above the band-edge frequencies which aligns with the eigenmode simulation results.

Three structures were investigated experimentally: a reference (H = 0 µm), H = 55 µm, and H = 65 µm. The reference should not experience a cut-off frequency, whereas the H = 55 µm and H = 65 µm should exhibit cut-off at 0.89 THz and 0.72 THz, respectively (see Fig. 4.10). Figure 4.11(a-c) plots the received temporal responses. The corresponding spectral responses were obtained by applying the DFT to the temporal data and are plotted in Fig. 4.11(d) Observation of the SSPP spectral traces in comparison with the reference trace illustrates a distinct transition at the predicted cut-off frequencies which demonstrates that a structure composed of Unit Cell 'A' exhibits the low-pass filter characteristics that are indicative of CPS-SSPP

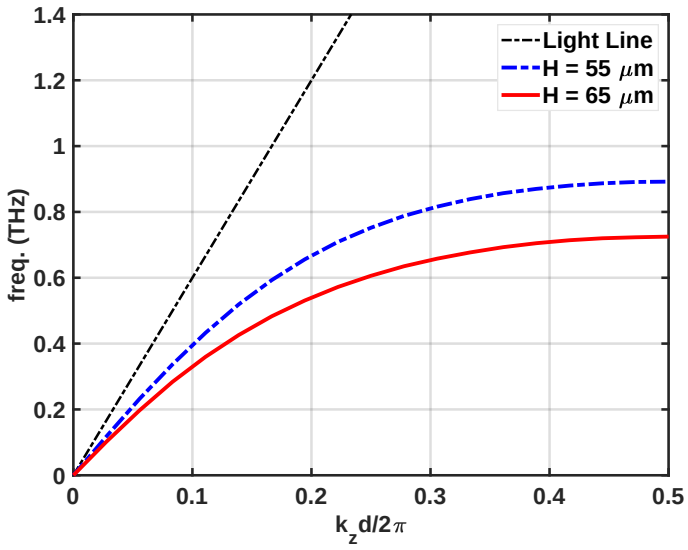

Figure 4.9: Dispersion curves of the SSPP structures with internal corrugations (Unit Cell 'A') obtained from eigenmode simulation, for $H = 55$ µm and $H = 65$ µm selected for experimental validation

excitation.

This work has illustrated the design and experimental validation of internally corrugated CPS-SSPP structures (Unit Cell 'A' in Table 4.1) operating at THz frequencies. The purpose of selecting Unit Cell 'A' is to reduce the insertion loss by two mechanisms including reducing the feedline attenuation by increasing conductor separation and also the improvement of the mode conversation efficiency between CPS and SSPP. This work investigated these two effects via simulation. Further, we experimentally confirmed that Unit Cell 'A' is capable of functioning as a CPS-SSPP waveguide which was demonstrated by the existence of low-pass behavior for different stub lengths, when $H = 55$ µm (0.89 THz), $H = 65$ µm (0.72 THz).

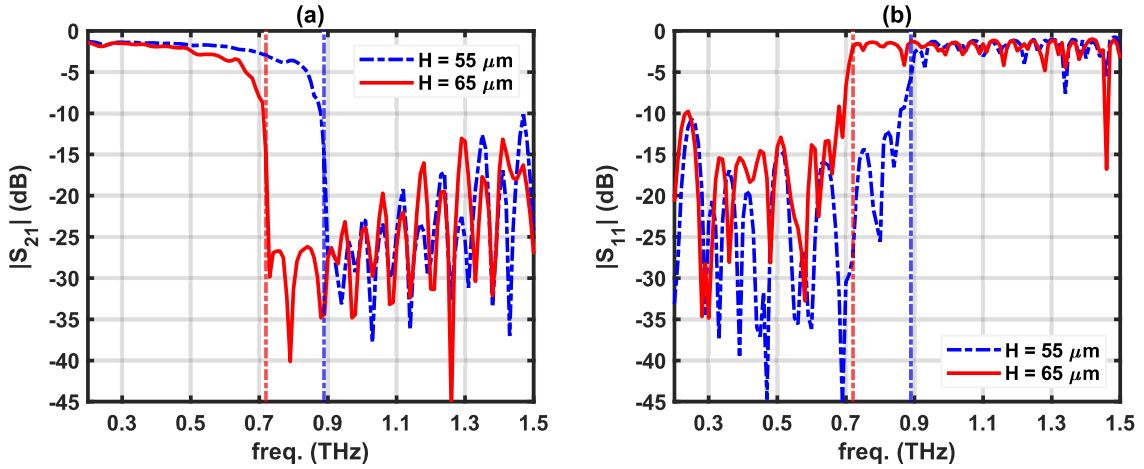

Figure 4.10: Frequency response of the proposed structure (including feedline tapering) with different stub lengths: (a) $|S_{21}|$ (dB) and (b) $|S_{11}|$ (dB) for $H = 55$ µm and $H = 65$ µm. Reprinted from [2].

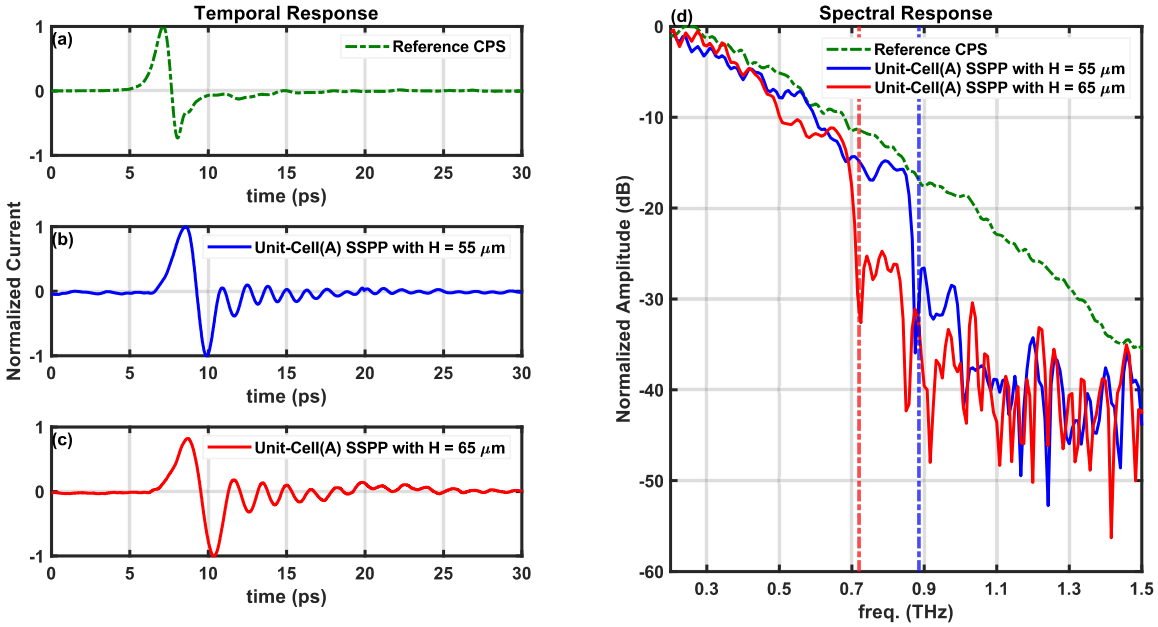

Figure 4.11: Measurement results. (a) Temporal response for the reference CPS ($H = 0$ µm). (b) Temporal response for CPS-SSPP Unit Cell 'A' with $H = 55$ µm (blue). (c) Temporal response for CPS-SSPP Unit Cell 'A' with $H = 65$ µm (blue). (d) Spectral responses are plotted by applying the DFT of the temporal responses. The vertical dashed lines indicate the simulated band-edge frequencies. Reprinted from [2].

4.3 THz Bandpass Filter Using Single-Conductor Spoof Surface Plasmon Polariton Structure Integrated with Coplanar Stripline

In the previous sections (4.1 and 4.2), we mentioned that our platform opens the pathway to validate THz SSPP structure and we adapted the SSPP to CPS. In fact, we used dual-conductor SSPP to have compatibility with CPS. However, the majority of planar SSPP literature is focused on Single-conductor SSPP and its integration to CPW [35, 37, 47]. This motivated us to integrate single-conductor SSPP with dual-conductor CPS, which was not studied in the literature. We achieved this through the design of a transition circuit that capacitively couples the signal from CPS to SSPP and performs the mode conversion at the same time to excite the SSPP mode. Obviously this capacitive coupling results in the rejection of low frequencies. With design and optimization, this structure can function as a THz bandpass filter with strong out-of-band rejection.

This work presents a novel THz BPF based on SSPP structure with experimental validation at a center frequency of 1.0 THz. To the best of the authors' knowledge, the proposed structure is the first integration of a single-conductor SSPP with a dual-conductor CPS. The measured passband transmission loss at 1.0 THz is approximately 5 dB less than a corresponding CPS with the same length. Simulated out-of-band rejection exceeds 20 dB for the lower cut-off frequency and 30 dB for the upper cut-off frequency; however, in measurements, it ranges from 15 to 30 dB as a result of having a relatively narrowband, low-power output signal, thereby lower signal-to-noise ratio with the employed pulse-based measurement method. The filter, with a center frequency of 1 THz, exhibits a 3 dB bandwidth of approximately 300 GHz, spanning from 870 GHz to 1170 GHz. Measurement results, including cut-off frequencies, align well with theoretical predictions and simulations.

As mentioned, to excite the SSPP without the use of flaring grounds utilizing CPS feedlines, one method involves modifying the single-conductor SSPP to a dual-conductor configuration, thereby facilitating integration with a CPS, a configuration known as CPS-SSPP [1, 46, 40, 13]. Another approach entails the direct integration of a single-conductor SSPP with a CPS which has not been previously documented in the literature, except our preliminary work at 300 GHz [14]. This implementation necessitates a transition between CPS and SSPP.

The transition circuit is created by gradually extending the length of SSPP stubs while tapering the CPS lines and eventually terminating the CPS conductors. This TC configuration couples the propagating wave to the SSPP and blocks the low frequencies. To operate at THz frequencies, we employed a thin 1 µm Silicon Nitride membrane, which has been demonstrated to mitigate loss and dispersion within the THz range up to 2 THz [55, 1]. Figure 4.12 illustrates the proposed SSPP-based BPF fabricated on the Silicon Nitride membrane, along with transceiver PCSs for THz generation and detection.

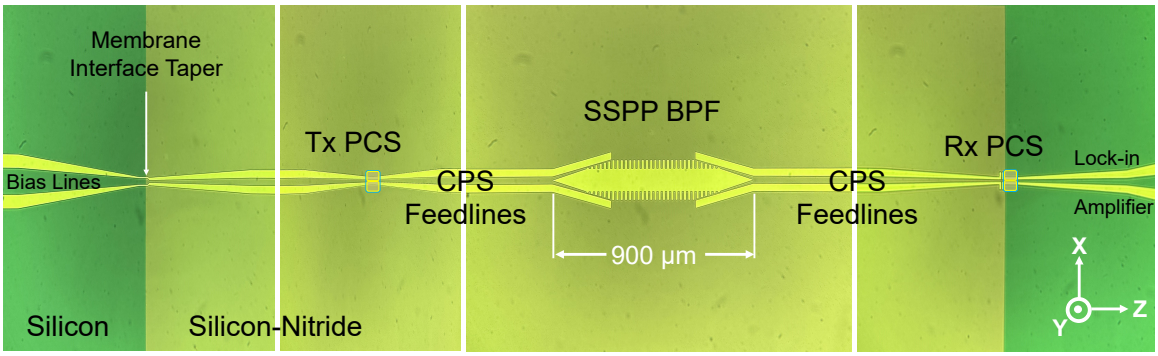

Figure 4.12: Fabricated THz SSPP Band Pass Filter on Thin Silicon Nitride Membrane with CPS feedlines and transition circuits for excitation and Tx/Rx PCS for THz generation and detection

The upper cut-off frequency can be approximated with an eigenmode simulation on the SSPP unit cell to extract the dispersion curves and the band-edge frequencies as shown in Fig. 4.13, with different trace (dashed-dotted line) for $H_n = 42$ µm which the measured structure for demonstration.

This work aims at developing a periodic SSPP-based bandpass filter. We select a subwavelength value for the period $d = 20$ µm and $a = 0.5d = 10$ µm as they must be much smaller than the wavelength [4, 32, 33]. The wavelength of the propagating wave around the center frequency (1 THz) is ≈300 µm. In this work, we selected the value for the period of corrugation, d, to be less than 10% of the wavelength; hence, the supposed subwavelength period condition is valid up to 1.5 THz. Based on the dispersion relation presented in [1] for an upper cut-off frequency of 1.2 THz, we should select $H_n = 42$ µm.

For investigation of expected band-edge locations and for simplicity we performed a simulation where the structure is modeled as a perfect electric conductor which results in the S_{21} parameters shown in Fig. 4.14 where H_n varies from 28 µm to

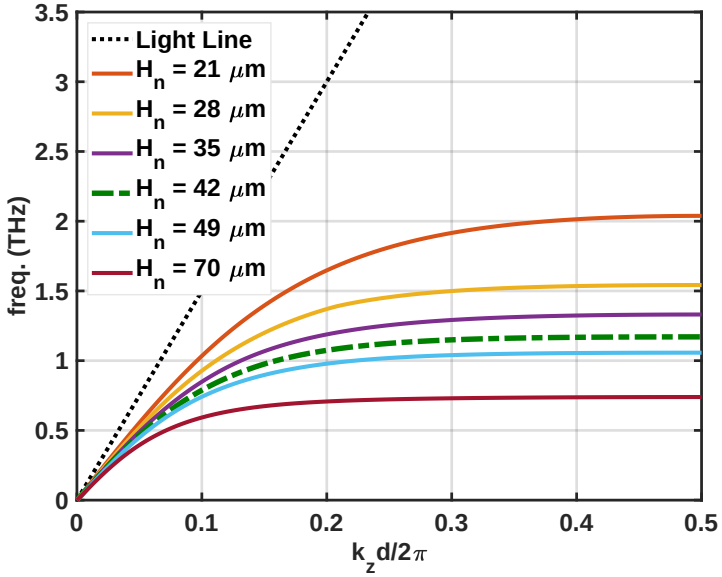

Figure 4.13: BPF Unit Cell Dispersion Curves, determining upper cut-off frequency. Unit cell dimensions: $d = 20$ µm, $a = 10$ µm, $W_0 = 90$ µm, 21 µm $\leq H_n \leq$ 70 µm.

70 µm, illustrating the bandpass filtering and variability of band-edge locations with geometry, with insertion loss of $\approx$ 0.5-2 dB in the desired passband frequencies.

For visualization of filtering operation, Fig. 4.15 illustrates the electric field plots for the structure with $H_n = 42$ µm at 1 THz in the passband, and lower/upper stopbands at 0.5 and 1.5 THz. The field plot at 1 THz also illustrates the field confinement capability of the SSPP structure in the groove areas.

The experimental results of the SSPP-based BPF structure with $H_n = 42$ µm are shown in Fig. 4.16, including the temporal responses of the BPF and a reference CPS (i.e. transient output pulses). The reference CPS is a feedline shown in Fig. 4.12 fabricated with the same length. Figure 4.16 also displays the corresponding spectral responses on a single subplot (right side) obtained from applying the Discrete Fourier Transform on the temporal responses. Since the output signal is weak, the spectral response will be a very small value in the dB scale (in the order of -30 dB to -70 dB), therefore, we normalized the data by shifting both of the spectral responses with the maximum absolute value of the reference spectrum, without changing the relative amplitude difference between the traces. The spectral response of the BPF shows steep roll-off rates at expected cut-off frequencies at 0.8 THz and 1.2 THz. The upper cut-off frequency at 1.2 THz is expected from the SSPP band-edge when H_n = 42 µm based on the dispersion curves Fig. 4.13 and S parameter simulations with

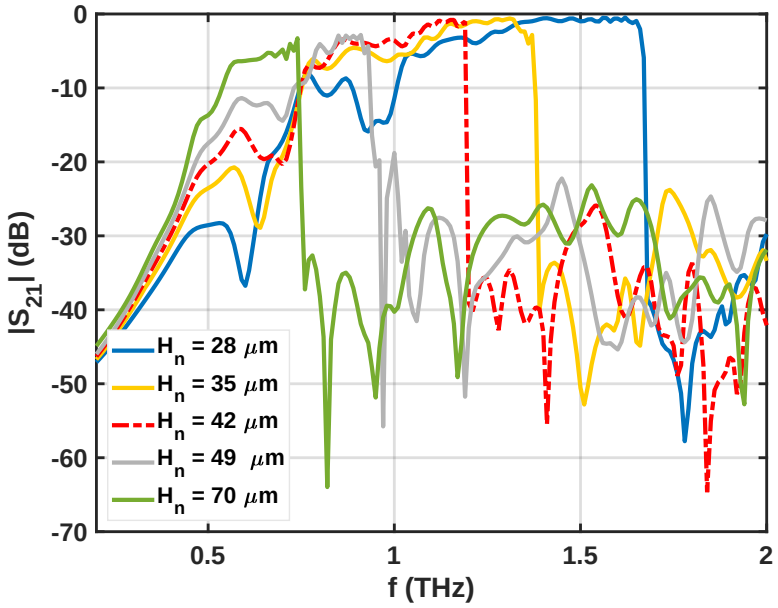

Figure 4.14: Transmission response (S_{21}) of the SSPP BPF structure with variable H_n from 28 µm to 70 µm

sharp upper-band cut-off shown in Fig. 4.14.

This project introduced a novel THz planar SSPP BPF, marking a significant milestone in SSPP-based filter structures by integrating a single-conductor SSPP to CPS. Through experimental validation, the filter demonstrates impressive performance metrics, including a low passband amplitude difference of 5 dB compared to a CPS feedline with the same length and dimensions, and out-of-band rejection surpassing 20 dB for low frequencies and about 15-20 dB for high frequencies. With a 3 dB bandwidth of approximately 0.3 THz, ranging from 0.87 to 1.17 THz, the filter exhibits robust signal transmission and rejection capabilities within its passband and stopbands, closely aligned with simulations. Notably, the integration of a single-conductor SSPP with a dual-conductor CPS feedline represents a pioneering approach.

The next work proposes another SSPP-based bandpass filter, with a different mechanism to tailor both of the filter's cut-off frequencies by design of related unit cells, using CPS and rectangular split rings created by vertical slots along an SSPP structure.

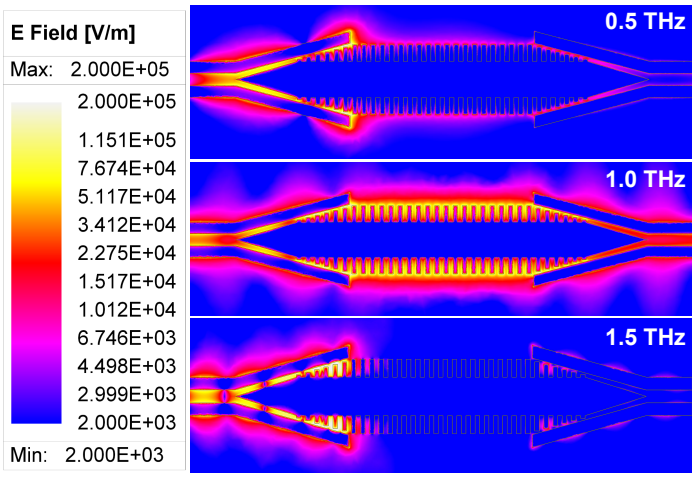

Figure 4.15: Field plots of the proposed SSPP BPF structure with $H_n = 42$ µm at 0.5 THz (lower stopband), 1 THz (passband), and 1.5 THz (upper stopband). The temperature (color) scale ranges from blue (2×10^3 V/m) to white (2×10^5 V/m) on a logarithmic scale.

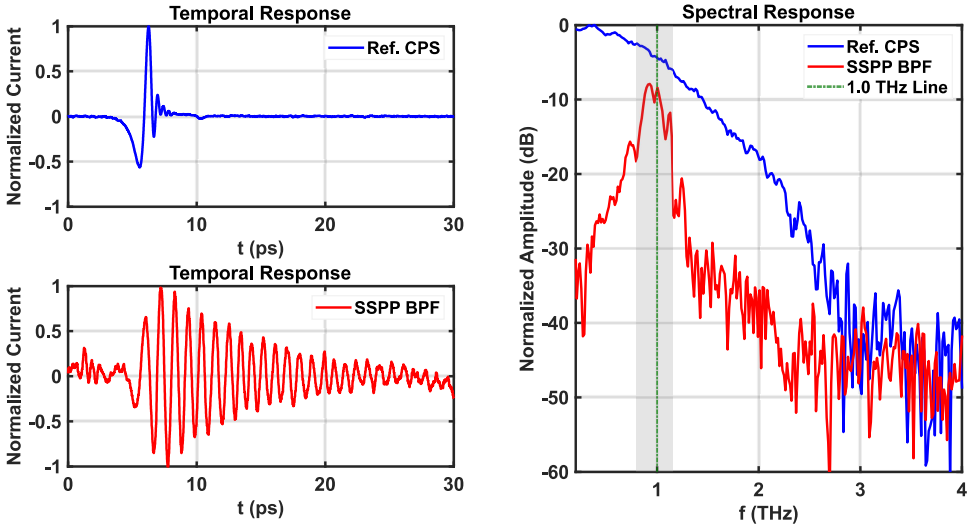

Figure 4.16: Measurement results for the proposed SSPP-based BPF and corresponding reference CPS

4.4 Terahertz Band Pass Filter based on Spoof Surface Plasmon Polariton Split Rings developed from Coplanar Strip with Internal Stubs

The previous work (section 4.3) inspired us to think of innovative band selective structures based on SSPP and capacitive coupling, where the capacitive part serves for low-frequency rejection and SSPP effectively attenuates higher frequencies. In order to implement this idea in a different form, one of the options is to utilize the CPS-SSPP with Internal corrugations, presented in 4.2. By creating narrow horizontal slots on the SSPP stubs, the structure will be able to maintain the SSPP properties for the upper stopband and also reject lower frequencies with series capacitance associated with the slots (see Fig. 4.17).

This work presents the design and experimental verification of a novel THz SSPP BPF based on CPS-SSPP with internal grooves [2] and central rectangular split rings. The proposed BPF achieves high-frequency rejection through low-pass SSPP characteristics and blocks low frequencies using gaps within the structure. Figure 4.17 shows a top view of the proposed structure. The upper and lower cut-off frequencies can be adjusted by modifying the geometries in the design stage. For demonstration, a BPF with a center frequency of approximately 1 THz was fabricated and measured using a modified THz-TDS system. The measured passband transmission around 1 THz, as well as the lower and upper 3 dB cut-off frequencies at approximately 0.8 THz and 1.2 THz, respectively, agree with the simulations. Figure 4.18 illustrates the fabricated structure used for demonstration.

As a well-known analysis of SSPP structure [6, 1], we extracted the dispersion curves of the proposed unit cell shown in Fig. 4.19, by performing an eigenmode simulation. Interestingly, dispersion curves in this figure indicate two areas with relatively small slopes and the creation of slow waves, representing the lower and upper cut-off frequency (i.e., band-edge) of a resulting periodic structure. Also, by varying just one of the dimensions (H_n) the band-edge frequency can be designed; however, to control the bandwidth, other dimensions shown in the inset of Fig. 4.19 should be tailored.

We note that the structure cannot be connected directly to the CPS feedlines shown in Fig. 4.18 for excitation since there is a tremendous mode mismatch between CPS (quasi-TEM) and SSPP (quasi-TM), and thereby significant reflections.

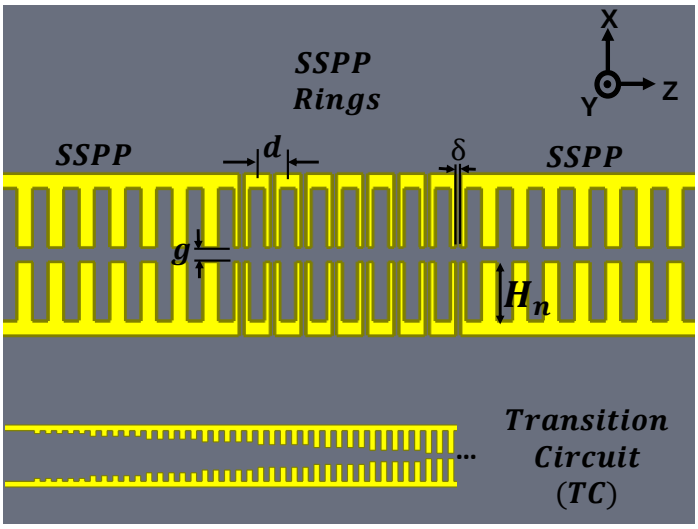

Figure 4.17: Proposed BPF structure based on SSPP rings

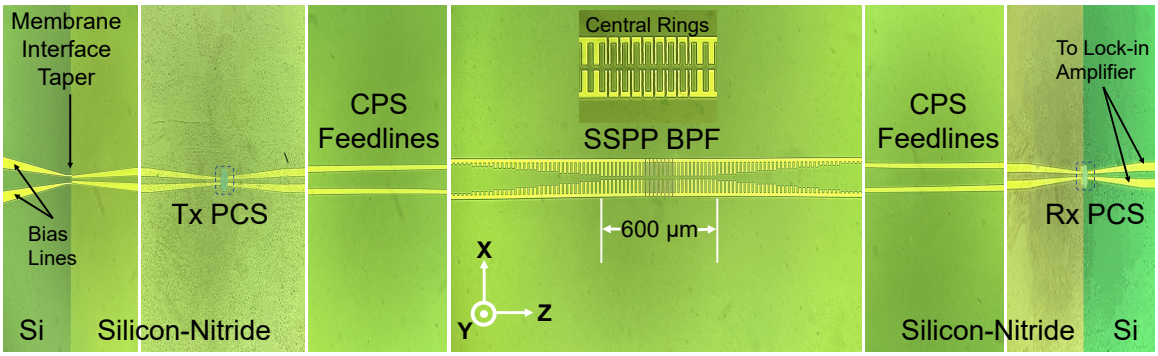

Figure 4.18: Fabricated SSPP-based BPF with central rings on a thin Silicon Nitride Membrabe excited by CPS feedlines. Key dimensions: Period $d = 20$ µm, SSPP groove width $a = 10$ µm, ring gap $\delta = 3$ µm, SSPP vertical gap $g = 10$ µm, and groove depth $H_n = 40$ µm.

Therefore a transition circuit with a gradual increase in the depth of SSPP grooves is required as detailed in [1, 2].

Frequency domain simulations were conducted on the structure using ANSYS HFSS. where the model incorporated CPS and SSPP waveguides with the following parameters: SSPP period $d = 20$ µm, SSPP stub width $W_s = 10$ µm, CPS feedline separation $S = 30$ µm, CPS transmission line width $W = 30$ µm, and a Si_3N_4 substrate with a thickness of 1 µm, relative permittivity $\varepsilon_r = 7.6$, $\sigma_{Si_3N_4} = 0$, and $\tan\delta_e = 0.00526$ [65].

The structure modeled as a gold with finite conductivity the same as CPS. This simulation revealed S_{21} parameters, demonstrating bandpass filtering behavior with

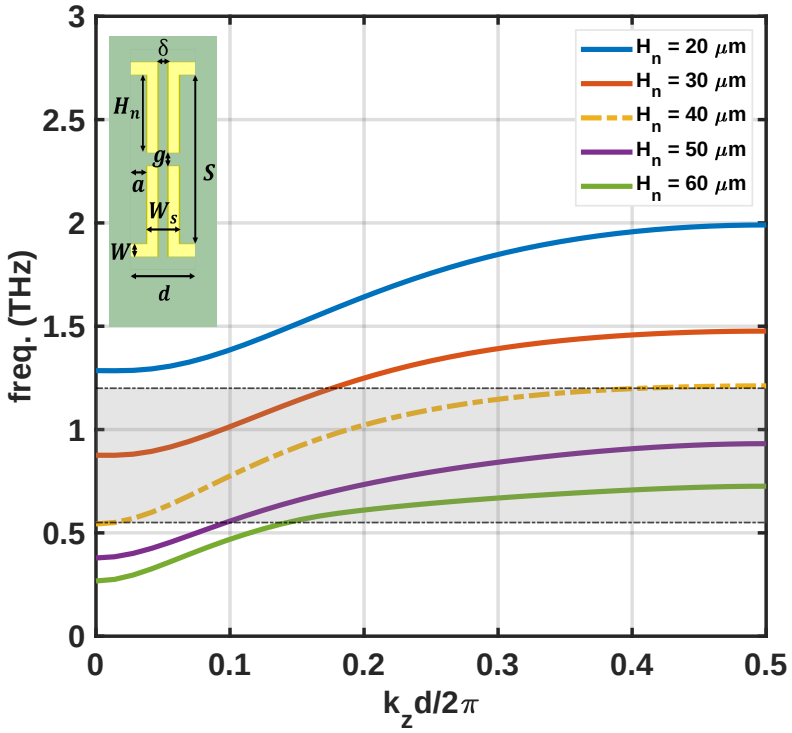

Figure 4.19: SSPP rings dispersion curves

varying band-edge locations depending on geometry, and insertion losses ranging from approximately 0.5 to 2 dB within the desired passband frequencies, shown in Fig. 4.20 for different SSPP geometries (groove depth).

To visualize the filtering operation, electric field plots for the structure with H_n = 40 µm were analyzed at 1 THz (in the passband) and at 0.5 and 1.5 THz (lower and upper stopbands, respectively), shown in Fig. 4.21. These plots also illustrate the strong field confinement capability of the proposed SSPP structure inside the SSPP rings and grooves.

The experimental results of the proposed SSPP-based BPF structure withH_n = 40 µm are presented in Fig. 4.22, showcasing both the temporal responses of the BPF and a reference CPS (transient output pulses). The reference CPS, depicted in Fig. 4.18, is a feedline with an equivalent length. The CPS temporal response exhibits an anticipated broadband Gaussian THz pulse, while the BPF response manifests as a narrow-band pulse with multiple oscillations. Notably, the oscillation period is approximately 1 ps, corresponding to 1 THz, the center frequency of the BPF structure. Additionally, Fig. 4.22 illustrates the corresponding spectral responses on a

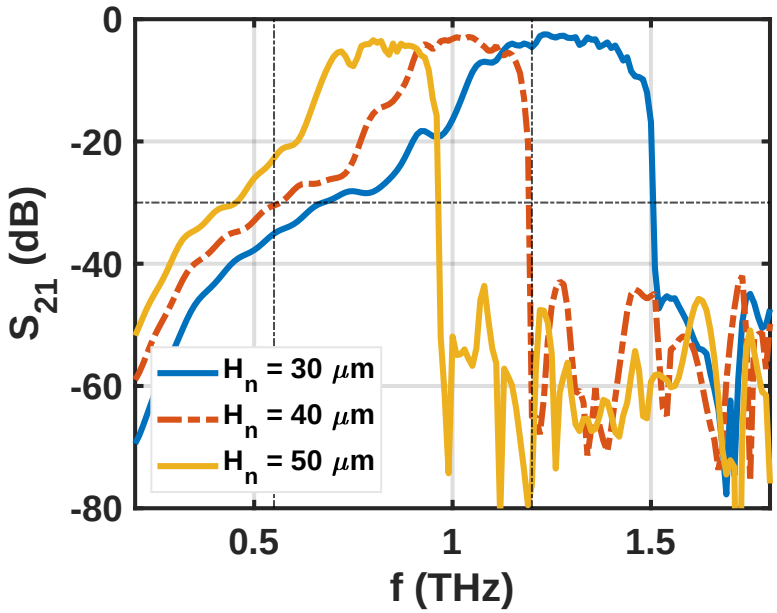

Figure 4.20: Simulated S_{21} for the BPF based on SSPP rings with H_n = 30, 40, 50 µm

single subplot (right side) derived from applying the Discrete Fourier Transform on the temporal responses. Due to the weak output signal, the spectral response registers very low values in the dB scale (ranging from -30 dB to -70 dB). To facilitate comparison, both spectral responses are normalized by aligning them with the maximum absolute value of the reference spectrum, preserving the relative amplitude difference between the traces.

The spectral response of the BPF exhibits steep roll-off rates at the expected cut-off frequencies of 0.8 THz and 1.2 THz. The upper cut-off frequency at 1.2 THz aligns with the SSPP band-edge when H_n = 40 µm, as evidenced by dispersion curves (Fig. 4.19) and S-parameter simulations with sharp upper-band cut-off (Fig. 4.20). Comparative analysis of spectral responses in Fig. 4.22 indicates a 10-20 dB out-of-band rejection for the BPF, lower than expected (more than 20 dB for low frequencies and more than 30 dB for upper band rejection) from simulation results. This discrepancy is mainly caused by noise levels and the relatively weak BPF output narrow band signal holding only a small portion of total pulse energy. Despite this, the measured out-of-band rejection remains acceptable. Another important parameter extracted from the measurement results is the amplitude difference between the BPF and CPS reference spectra in the passband, approximately 5 dB, consistent with

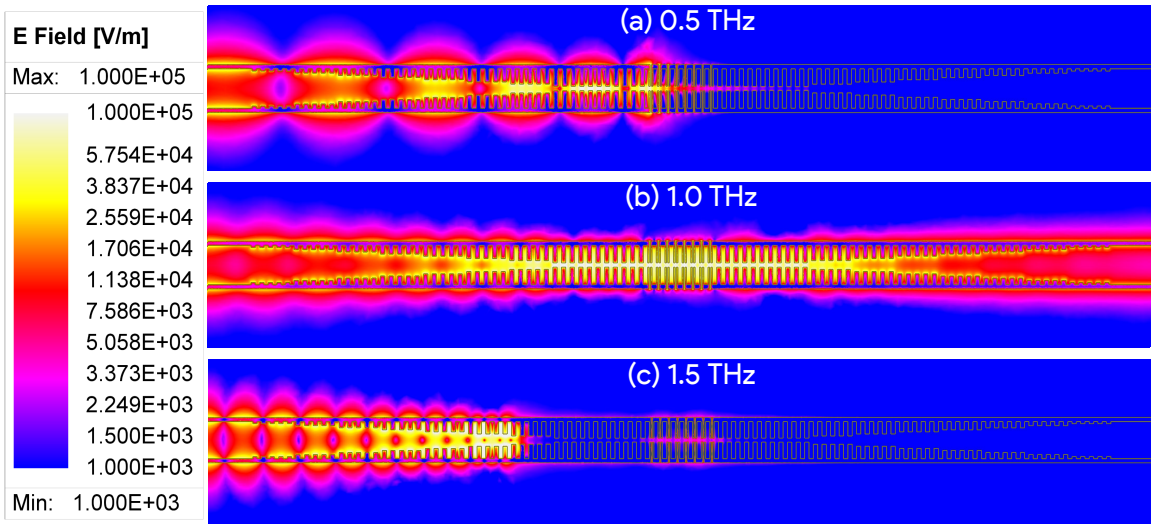

Figure 4.21: Electric field plots of the proposed THz SSPP band-pass filter with $H_n = 40$ µm at 0.5 THz (lower stopband), 1 THz (passband), and 1.5 THz (upper stopband), illustrating passband transmission and out-of-band rejection.

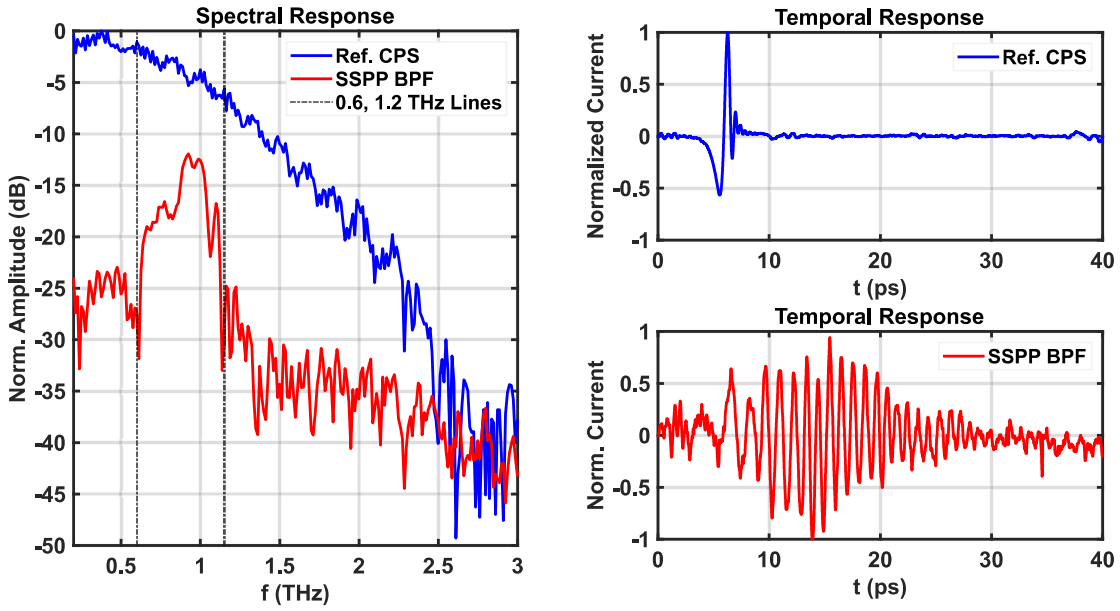

Figure 4.22: Measurement results of the proposed BPF with $H_n = 40$ µm with a center frequency around transmission along with a reference CPS with the same length

minimum insertion loss expectations from S-parameter simulations.

In this project, we introduced a novel THz SSPP BPF by leveraging CPS-SSPP integration with internal grooves and central split rings, the proposed filter achieves high-frequency rejection through low-pass SSPP characteristics while effectively blocking low frequencies using strategically positioned slots within the SSPP stubs. Furthermore, the BPF's upper and lower cut-off frequencies are tunable via geometrical modifications, offering versatility in THz frequency manipulation. Experimental validation of a fabricated BPF with a center frequency of approximately 1 THz demonstrates promising performance, with measured passband transmission agreeing with simulations, thereby highlighting the effectiveness of the introduced SSPP split rings in achieving targeted band selection functionality.

Having completed experimental measurements on the CPS and SSPP structures, we now turn our attention to exploring their practical applications. Among the mentioned applications (e.g. filtering, sensing, imaging, and communication), sensing stands out as a key application, particularly because it aligns well with our methods and approach using thin membranes. By positioning materials near -but not in direct contact with- the waveguide structure, the evanescent field generated by the waveguide can still interact with the material through the membrane. Further details will be discussed in the next section.

4.5 On-Chip Glucose Sensing Using Guided Waves at Terahertz Frequencies

Leveraging the experimental characterization of CPS and SSPP structures, we now turn our focus to their practical applications, with a particular emphasis on sensing. This section explores the development of on-chip glucose sensing using guided waves at THz frequencies. Utilizing thin membranes enables materials to interact with the evanescent field of the waveguide without direct contact, offering a precise method for detection.

Despite the main focus of the dissertation being on SSPP structures, in our preliminary sensing project, we focused on CPS structure since it provides a broadband spectrum that facilitates the study of material absorption at the THz range. Then we transition to SSPPs to seek higher sensitivity.

It is worth noting that the primary objective of this work is to demonstrate a method for on-chip THz spectroscopy, which can be applied to a variety of materials exhibiting distinct absorption signatures at THz frequencies including, but not limited to organic material like sugars [66], explosives [67], pharmaceuticals, and drugs [68]. For the purpose of this demonstration, glucose was selected as a safe representative material with unique absorption features in the THz frequency range.

This work demonstrates an on-chip anhydrous D-glucose sensor using a CPS on a thin (1 µm) silicon nitride membrane at THz frequencies for the first time. A thin layer ($\approx$ 10 µm) of D-glucose was placed in close proximity to the CPS, and the transmission response was measured using a modified THz-TDS setup. D-glucose introduces frequency-dependent changes to the effective permittivity of the CPS waveguide, resulting in a modified spectral response at the receiver. Measurement results show absorption signatures at 1.42 THz and 2.07 THz corresponding to the first two significant resonances beyond 1 THz for D-glucose allowing for label-free detection. The frequency-dependent attenuation coefficient was estimated by simulation for several D-glucose layer thicknesses using a modified Lorentz model. Measurement results align with simulations and other literature that use free-space THz radiation. This work verifies on-chip THz sensing of D-glucose and presents a pathway toward on-chip sensing of other materials at THz frequencies.

Here we briefly review the works related to glucose sensing with a focus on methods used at THz frequencies, since it has not been covered in the review chapter of the dissertation for the coherence of the review materials.

The pursuit of glucose sensing methods aligns with the objective of promoting health and well-being, either glucose detection in food, or blood glucose monitoring. Glucose sensing methods have been reviewed in [69, 70, 71] from traditional enzymatic and electrochemical methods to optical and spectroscopic techniques. Regarding in-body glucose sensing, the category of optical sensors is favorable for their non-invasive nature and potential for continuous monitoring. These methods include fluorescence, Raman spectroscopy, near-infrared (NIR), mid-infrared (MIR), and far-infrared (FIR) spectroscopy [71]. However, optical methods face challenges due to scattering [69, 72, 70] with reduced scattering coefficient of 30 - 50 cm^{-1} [73], contributing to Signal to Noise Ratio (SNR) reduction [74], relatively weak glucose absorption peaks especially in NIR range [75], and interference from surrounding light [76]. On the other hand, THz waves have less scattering compared to IR and optical beams [72, 74] with estimated reduced scattering coefficient up to 1 cm^{-1} based on analysis in [73], and have strong glucose absorption peaks [66, 77] which enables easier glucose detection with higher SNRs [70]. Moreover, THz waves penetrate into human tissue up to 300 µm [78], potentially reaching the dermis layer where blood and glucose are present whereas the MIR range only penetrates up to 100 µm, which corresponds to the thickness of the epidermis layer that lacks blood [75]. However, glucose can still be detected in the MIR and THz range within the interstitial fluid (ISF) of the epidermis, where a slight concentration of glucose is present but blood capillaries are not reached at this depth [75]. Absorption coefficients extracted from THz-TDS measurements have shown a high sensitivity to the glucose level in blood samples [79]. Additionally, THz-TDS combined with weak value amplification was demonstrated to be sensitive to small changes in concentrations of glucose both in solid and liquid samples [80]. However, challenges remain in terms of miniaturization and cost-effectiveness of THz sensors [71], which can be addressed by on-chip THz sensors, that are the focus of this research.

Glucose absorbs electromagnetic radiation at certain frequencies in the THz band. The first peak of absorption spectra for glucose beyond 1 THz occurs in the range of 1.40 - 1.44 THz [66, 81, 57, 77, 82, 83]. In literature, the majority of glucose sensing methods at THz frequencies involve directing a free-space THz beam towards a thin glucose sample [77], a metasurface [84, 85, 86, 57, 82], or nano-antennas (i.e., also a form of metasurface) [66] coated by sugar (glucose) then detecting the transmitted wave. Using metasurfaces results in strong subwavelength field concentration at a resonance frequency, making them sensitive to small features and slight variations in

the nearby environment, thereby enhancing their overall sensitivity [84]. In [86, 85] authors designed metasurface unit cells that have resonance frequencies below 0.5 THz and then measured the shift in resonance frequency in the presence of glucose or other materials. Others [66, 57] have designed the metasurface unit cell so that it targets the first THz-band absorption frequency of glucose near 1.4 THz. In [66] the authors proposed a metasurface for THz transmission by nano-slot-antennas which increases the molecular absorption cross-sections, thereby enabling the detection of sugar molecules at low concentrations. Table 4.2 provides an overview of various THz sensing methods for sugar detection including key details such as the reference source, resonance frequency in THz, frequency range covered by the sensor, structural design, mechanism of wave transmission, spectral detection method employed, and the type of sugar targeted in the respective study. Our work, highlighted as 'This Work' in Table 4.2, proposes on-chip glucose sensing operating in the broad frequency range of 0.1 - 2.2 THz, employing guided waves which as previously mentioned, is the key difference from the other works.

The aforementioned studies use free-space THz radiation for sensing which offers simplicity and flexibility in accommodating various sample geometries and configurations; however, free-space methods suffer from path loss and require bulky THz optical components [87]. Alternatively, guided-wave methods are attractive because they are compact and do not require the alignment of a THz beam. Also, a guided-wave sensor can offer lower channel loss [87] and increased sensitivity by confining the electromagnetic field within the sample region making it suitable for on-chip integrated sensors in various applications [38]. Additionally, guided-wave methods are more resilient to sample roughness and heterogeneity owing to the guided propagation of electromagnetic waves.

This work explores a unique approach for on-chip glucose sensing using guided waves via CPS on a thin silicon nitride (Si_3N_4) substrate which presents a platform that offers broadband low-loss THz-bandwidth pulse propagation [89, 55]. Also, the CPS on a thin membrane enables the interaction of the electromagnetic field with materials (such as glucose) beneath the membrane (see Fig. 4.23). Our experiments show the prominent THz-band absorption frequency of 1.42 THz measured with the fabricated sensor, which aligns with the absorption frequency reported in Table 4.2. We note that label-free sensing involves the detection of the multiple characteristic absorption signatures which occur at different frequencies and the measurement of a broad spectrum facilitates this capability. To confirm label-free sensing, we simulta-

Ref.	Resonance Freq. (THz)	Freq. Range (THz)	Structure	Wave transmission	Spectral Detection Method	Sugar type
[77]	1.43, 2.08	0.3-3.0	NA (direct exposure)	Free-Space	Absorption frequency	D-glucose
[66]	1.4, 1.7	0.5-2.5	Nano-slot antennas	Free-Space	Absorption frequency	D-glucose, Fructose, Sucrose
[57]	1.43	1.2-1.6	Metasurface	Free-Space	Absorption frequency	D-glucose
[82]	1.435	1.2-1.6	Metasurface	Free-Space	Absorption frequency	D-glucose
[85]	0.26	0.2-0.5	Metasurface	Free-Space	Resonance shift	D-glucose
[86]	0.32	0.2-0.5	Metasurface	Free-Space	Resonance shift	D-glucose
[88]	0.6	0.3-1.2	Meta-material absorber	Free-Space	Resonance shift	D-glucose
This Work	1.42, 2.07	0.1-2.2	CPS	Guided-Wave	Absorption frequency	D-glucose

Table 4.2: Summary of experimental sugar sensing methods based on THz spectroscopy

neously resolve the glucose absorption features at 1.42 THz and 2.07 THz. [77, 81].

The sensor presented in this work operates on the principle of frequency-dependent dielectric loss from a nearby material (i.e., glucose). Figure 4.24 illustrates a cross-section of the sensor geometry which is a CPS transmission line ($S = 130$ µm and $W = 30$ µm) on a suspended thin Si_3N_4 membrane ($H_1 = 1$ µm) which is in contact with a thin glucose layer ($H_2 \approx 10$ µm). The effective permittivity of the propagating wave, ε_{eff}, depends on the individual material parameters ($\varepsilon_{0,1,2}$, $\mu_{0,1,2}$, and $\sigma_{0,1,2}$) and the dimensions of the transmission line and substrate ($S, W, H_{1,2}$). Here, of primary concern, is detecting frequency-dependent variations in glucose permittivity, $\varepsilon_2(\omega)$, which can be achieved when the Si_3N_4 layer is thin $H_1 \approx 1$ µm.

The CPS sensor structure is fabricated by depositing a 1 µm Si_3N_4 layer on a 500 µm silicon substrate. Next, a rectangle of silicon with a dimension of 2 mm $\times$ 10 mm is etched under the structure where the sample material will be placed. Metallic conductors are placed using photolithography and metal deposition (Ti/Au: 10 nm/200 nm).

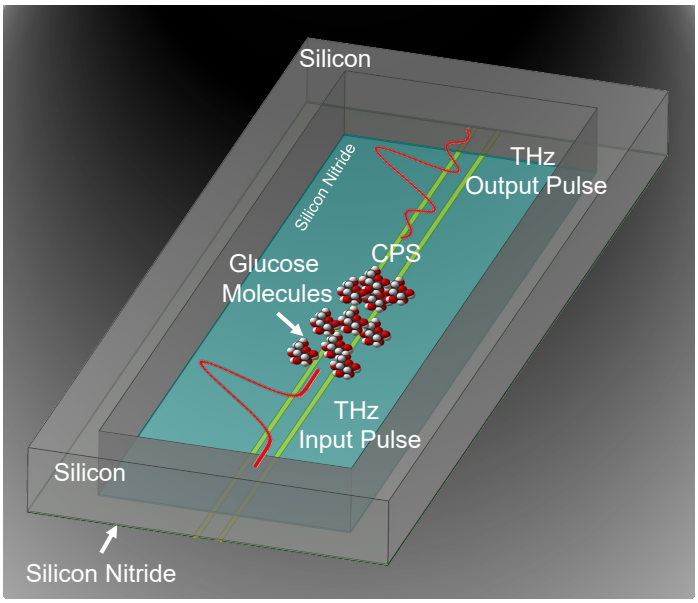

Figure 4.23: Illustration of glucose sensing by CPS waveguide on a thin Si_3N_4 membrane. Reprinted from [3].

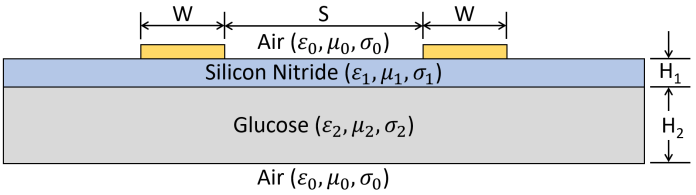

Figure 4.24: CPS sensor cross section. Reprinted from [3].

In this study, we incorporate a frequency-dependent permittivity model for glucose [82] into the existing model of a CPS that is depicted in Figure 4.24. Our objective is to obtain the attenuation coefficient of the CPS for glucose layers of varying thicknesses for frequencies ranging from 0.5 to 2.5 THz. The simulation was performed using ANSYS HFSS 2023 and characterizes the CPS behavior in the presence of glucose at different frequencies and thicknesses. The material properties of the model components include the Si_3N_4 substrate with 1 µm thickness and $\varepsilon_r = 7.6$, $\sigma_{Si_3N_4} = 0$, $\tan \delta_e = 0.00526$ [65], and gold conductors with 200 nm thickness and the conductivity of $\sigma_{Au} = 4.1 \times 10^7$ S/m. The dielectric permittivity of the glucose layer with single resonance at THz frequencies was previously modeled using the modified Lorentz model, which is widely used for modeling a single resonance in material's permittivity, as presented in [82].

Our work includes the second resonance of glucose to the glucose Lorentz model

as observed in [66] and also our experiments. Equation (4.2) shows the relation of this permittivity model with two resonances:

$$\varepsilon(\omega) = \varepsilon_\infty + \frac{\omega_p^2}{\omega_{0,1}^2 - \omega^2 + i\gamma_1\omega} + \frac{\omega_p^2}{\omega_{0,2}^2 - \omega^2 + i\gamma_2\omega} \tag{4.2}$$

where $\varepsilon_\infty = 3.231$ is the dielectric coefficient at infinite frequency [82], $\omega_{0,1} = 2\pi(1.42\,\text{THz})$ is the first resonance frequency beyond 1 THz, $\omega_{0,2} = 2\pi(2.07\,\text{THz})$ is the first resonance frequency, $\omega_p = 2\pi(0.11\,\text{THz})$ is bulk plasma frequency of the dielectric for the thin film of glucose, $\gamma_1 = 2\pi(0.04\,\text{THz})$ and $\gamma_2 = 2\pi(0.08\,\text{THz})$ represents the corresponding damping constant at the resonance frequencies.

Next, we simulated the attenuation coefficient for the CPS illustrated in Figure 4.25a with a glucose layer (ε_2 in Figure 4.24) using (4.2) for several different glucose thicknesses (H_2 = 5, 10, 15 µm). The results of this simulation are plotted in Figure 4.25b along with a reference without any glucose which has an attenuation of ≈ 0.6 dB/mm at 1.4 THz. As previously mentioned, the average thickness of glucose is ≈ 10 µm measured by a profilometer along the top CPS line depicted on the inset. According to Figure 4.25b this thickness corresponds to an attenuation depth of ≈ 4.5 dB/mm which is the height of the absorption peak at 1.42 THz and attenuation of ≈ 2.2 dB/mm at 2.07 THz.

We note that Figure 4.25a shows a section of CPS for illustration of the model layers without matching sections at the input and output where CPS is tapered to match the impedance with the transmitter and receiver sites. This tapering mitigates the reflections and prevents the appearance of standing waves.

We also conducted simulations with a non-uniform or heterogeneous layer of glucose, to investigate the effect of discontinuity in the glucose layer and found that the reflectivity (S_{11}) remains close to the reasonable value of ≈ -20 dB, while a clear resonance is still observable in the transmission response (S_{21}). Details of these simulations can be found in the Supplementary Information files.

The measurement results of unloaded (no glucose) and loaded sensor (with ≈ 10 µm glucose layer) are shown in Figure 4.26. Note that the spectral amplitude decay with increasing frequency in the experimental results is an expected consequence of applying a THz finite duration pulse as an input signal rather than an ideal THz impulse with a flat spectral response [55]. From the simulations (Figure 4.25b), the depth of peak absorption should be approximately 3 mm × 4.5 dB/mm = 13.5 dB which is observed in measurement results (spectral response in Figure 4.26).

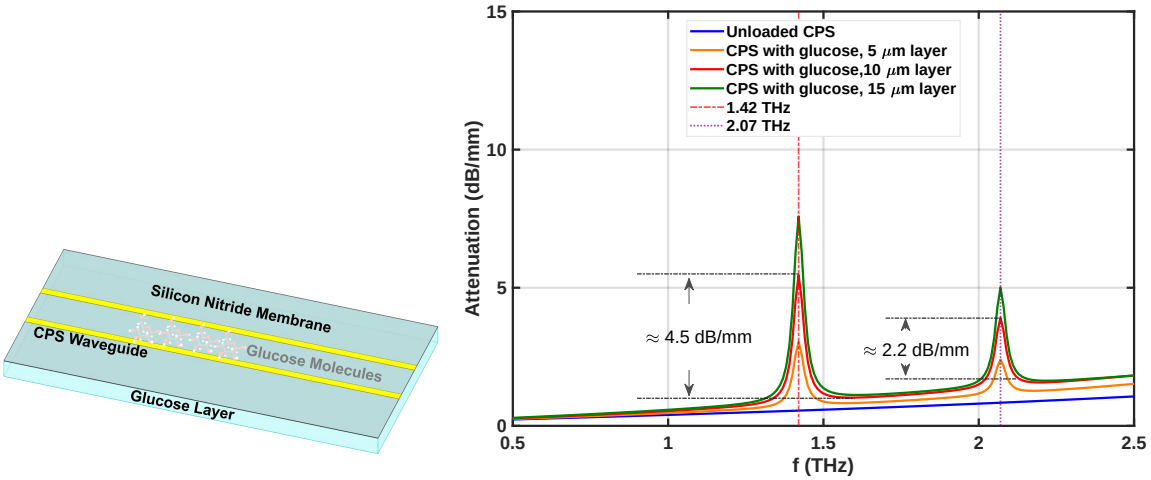

(a) (b)

Figure 4.25: (a) CPS on the thin membrane with glucose layer. (b) Attenuation of CPS with modified Lorentz model for glucose layer with different thicknesses under the sensor's thin membrane. Reprinted from [3].

The frequency-dependent absorption observed in experimental results demonstrates the sensor functionality. It is important to recognize that this work is primarily a proof-of-concept and that future methods will be developed to improve sensitivity through the optimization of sample distribution methodology and circuit topology. We note that glucose shows broad absorption starting from 1.10 THz up to around 1.28 THz [66, 81, 77]. This is observed in Figure 4.26 as a minor depression before the main peak at 1.42 THz. Moreover, another THz absorption peak of glucose at 2.07 THz is observed in the measurement results and is expected to occur at 2.05 THz - 2.10 THz[77, 81, 57, 66]. We predict the attenuation of the dip at 2.07 THz relative to the attenuation at 1.42 THz using the data from [66] which results in an expected attenuation of $\approx$ 5.8 dB at 2.10 THz. As shown in Figure 4.26 the experimental results find a depth of absorption peak is $\approx$ 6.2 dB which is within reasonable agreement with the expected value.

It is important to consider the practical aspects of sensors. The broadband nature of the received spectrum has several benefits which can reduce the probability of false positives and false negatives. First, the absorption at 1.42 THz can be measured relative to the adjacent region of the spectrum (i.e., 1.5 THz), but this method would be susceptible to false positives since other materials, such as sucrose, exhibit weak absorption characteristics near 1.4 THz. However, since the presented sensor is ca-

pable of resolving broad spectral information that corresponds to two signatures for glucose (1.42 THz and 2.07 THz) it becomes straightforward to reduce the probability of false positives by verifying that both signatures exist simultaneously with the appropriate relative magnitudes. Next, the sensor can exhibit false negatives if the glucose film is poorly distributed away from the CPS. Our proof-of-concept sensor is susceptible to this issue due to our current drop-coating method; however, we have begun investigating microfluidic methods to address this issue which are beyond the scope of this work.

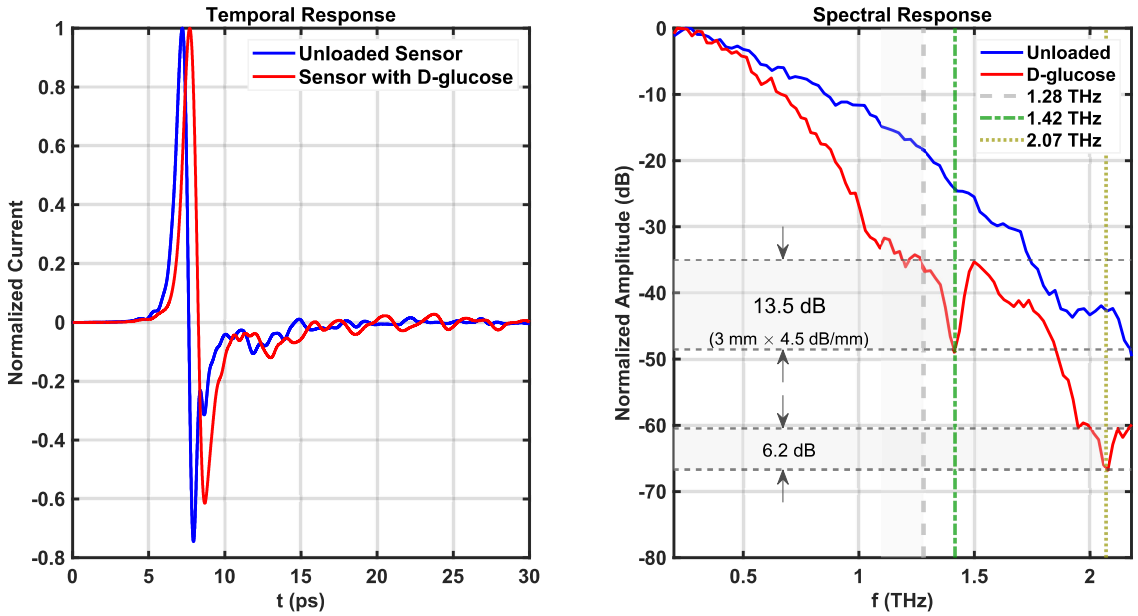

Figure 4.26: Measurement results of the proposed CPS-based glucose sensor. Reprinted from [3].

This project demonstrated an on-chip glucose sensor using a CPS waveguide at THz frequencies on a thin Si_3N_4 membrane. The sensor is based on the interaction between the propagating electromagnetic waves at THz frequencies and a thin layer of glucose placed in close proximity to a transmission line which results in frequency-dependent notches in the received spectrum. Our experiments reveal a resonance at 1.42 THz and 2.07 THz which aligns with findings in existing literature. The novelty of our approach is its guided-wave nature and on-chip integration potential. This work demonstrates pathways towards on-chip label-free sensing of glucose and other materials with applications such as the food industry and healthcare.

Now that we have the foundation of membrane-based sensing with CPS, in the next work, we will focus on SSPP guided-wave sensors with their unique capability

of strong field confinement which results in effective interaction with materials and more sensitivity.

4.6 A Terahertz Spoof Surface Plasmon Polariton Permittivity and Absorption Sensor

After utilizing a CPS waveguide on a thin membrane for glucose sensing in [1], we are now prepared to investigate structures with higher sensitivity leveraging a similar approach.

This work introduced a novel on-chip THz sensor based on SSPP structures. The proposed sensor shows a low-pass behavior with a band edge at 1.7 THz and strong field confinement in the 1.0-1.6 THz range. This confined field is capable of effectively interacting with surrounding materials. Absorption signatures in this frequency range sensitively absorb the power. We used Glucose as an example for a demonstration of this effect in which intermolecular resonances result in absorption at $\approx$ 1.4 THz. Using the same device, the thickness of the glucose film (or the effective mass of glucose at the sensing area) alters the permittivity of the dielectric, leading to a shift in the band edge of the spectrum. This change results in time-delay variations in the temporal response, which we demonstrate experimentally. Additionally, we employed another sensor with a band-edge frequency at 0.72 THz, where glucose exhibits a relatively constant permittivity, to examine the effect of band-edge variation with the material's average thickness, which is correlated to the effective permittivity. This work introduces the first THz sensing method based on SSPP, combining both resonance shift and absorption sensing mechanisms simultaneously.

THz sensors have gained significant attention for their potential in highly sensitive non-invasive sensing applications based on THz spectroscopy [84, 5]. Among these, sensors based on SSPP offer unique advantages, including strong field confinement and enhanced interaction with the target analyte [66]. SSPPs enable the design of versatile and miniaturized THz systems, making them suitable for applications in healthcare, food safety, and chemical analysis. Several previous studies have investigated free space SSPP excitations or guided wave methods at the microwave range [66, 88, 86, 84]. Yet there is a gap in the investigation of on-chip guided-wave SSPP sensing methods. This work focuses on the development of SSPP-based on-chip THz sensors for glucose detection as a proof-of-concept material, which has not been investigated by SSPP-based sensors already proposed in the literature [38, 5].

Glucose sensing is essential in various industries, including the medical and food sectors. Escalating sugar consumption in modern diets has been linked to chronic health issues such as cardiovascular diseases, diabetes, and obesity [90, 91]. This

necessitates accurate and reliable glucose detection methods. In this study, glucose is chosen as the model analyte due to its widespread significance in both health monitoring and food quality control.

Traditional glucose detection methods, including enzymatic and electrochemical techniques, have limitations such as short lifespan, complex handling, and limited portability [69]. Recent advancements have explored optical methods such as fluorescence, Raman spectroscopy, and infrared spectroscopy, which are non-invasive but face challenges like scattering, weak absorption peaks, and interference from ambient light [71, 72]. THz sensing, particularly with SSPP structures, addresses these challenges by providing strong glucose absorption peaks and reduced scattering [77, 73].

SSPP-based sensors leverage the interaction between electromagnetic waves and engineered periodic structures to confine and enhance the electric field near the sensor surface. This feature makes SSPP structures highly sensitive to small variations in the dielectric properties of the target analyte, such as glucose [66]. Additionally, SSPP-based sensors are compatible with on-chip fabrication technologies, enabling integration with electronic systems for portable and real-time glucose monitoring.

Glucose serves as a proof-of-concept material to validate the performance of SSPP-based sensors due to its well-characterized dielectric properties and strong absorption in the THz range [79]. In the THz range, glucose exhibits distinct absorption peaks, facilitating its detection even at low concentrations [80]. Moreover, its relevance to both healthcare and food safety ensures the practical applicability of SSPP-based sensing technologies.

This paper presents the design and experimental validation of an SSPP-based on-chip THz sensor for glucose detection. The sensor demonstrates high sensitivity and selectivity, paving the way for broader applications in material sensing. Figure 4.27 shows the fabricated sensor structure, and Figure 4.28 depicts the filed plot of the structure indicating strong confined filed at the central area of the sensor, which is beneficial for effective interaction with surrounding materials.

Two approaches can be employed for designing SSPP-based sensors. The first approach, which is relatively underexplored in the literature, involves leveraging the confined field within the transmission band of the structure to target the absorption frequency peak or vibrational resonance of the material. The second approach focuses on identifying a frequency range where the permittivity of the sample remains relatively constant and detecting shifts in the band-edge frequency (resonance frequency) of the SSPP structure, which vary depending on the concentration or thickness of the

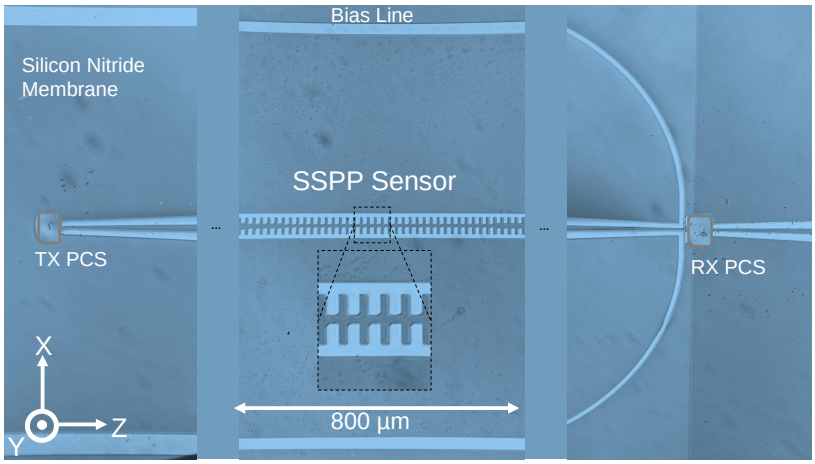

Figure 4.27: Fabricated SSPP sensor based on CPS with internal corrugations

target substance.

In order to seek the first approach, We design the proposed SSPP unit cell, such that it has a specific band-edge frequency as we know the field confinement is maximum at that frequency, depending on the material under test. This can be achieved using the dispersion relation of the SSPP. As presented in [2, 1] the dispersion relation can be approximated by (for a surface wave propagating along the Z-direction): $k_z = k_{eff}\sqrt{1 + (a^2/d^2)\tan^2(k_{eff}H)}$, where H is the length of SSPP stubs inside of the CPS (i.e. depth of grooves), d is the period of corrugation, W_s is the width of the stubs, $a = d - W_s$ is the aperture or the width of grooves, $k_{eff} = \omega\sqrt{\varepsilon_{eff}}/c$ is the effective wavenumber, ε_{eff} is the effective relative permittivity (for the CPS feedlines on thin Silicon Nitride membrane $\varepsilon_{eff} \approx 1.9$ based on the simulations at THz frequencies), and c is the speed of light. This dispersion relation shows that the band-edge and asymptotic frequency of SSPP structures is mainly controlled by H and provides a reasonable approximation to the design of SSPP made by rectangular grooves [33, 35].

Now that we have an approximation of the dispersion relation at our disposal, suppose that we want the structure to have band-edge frequencies at about 1.7 THz for the first approach and 0.7 THz for the second approach, given the glucose permittivity model [1].

We fix the values of d = 20, 50 µm and a =10, 30 µm as they should be much smaller than the wavelength of operation [4, 32, 33]. Then, we numerically solve the dispersion relation to find the value of H. The calculation results in rounded values of H = 22 µm and 65 µm for the band-edge frequency at 1.7 THz and 0.7 THz,

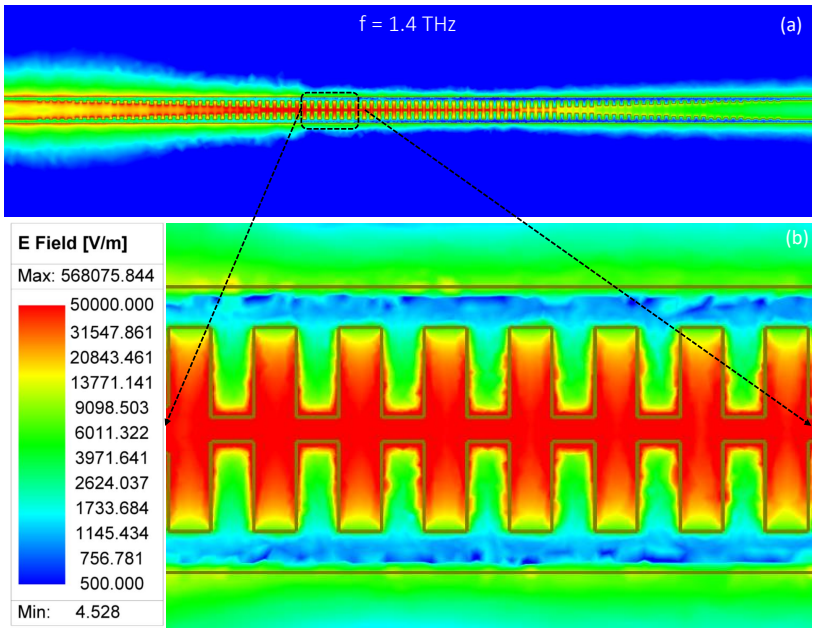

Figure 4.28: Electric field plots of the structure showing strong field confinement at the central area of the SSPP sensor. (a) Entire structure. (b) Zoomed on the central area.

respectively. The gap between the internal stub tips is fixed to be 10 µm for both of the sensors. Smaller gaps can slightly affect the band edge as a result of creating shunt capacitance between the mutual stubs [2].

Based on the simulations, increasing the number of SSPP stubs, N, enhances the slope of the band-edge, however, there are only moderate improvements in roll-off rates for $N > 9$ [36]. Large N values can guarantee a sharp band-edge, but in practice, it can increase the insertion loss as the length of the SSPP waveguide increases. For the lower bound, $N < 5$ decreases the slope of roll-off and reduces the area with enhanced field confinement which are the primary benefits of SSPP [1, 2].

Next, we design a transition circuit (TC) to minimize the return loss and effectively convert the TEM mode in CPS to TM mode in SSPP. This is achieved by gradually increasing the stub length. Here we selected a linear growth of stubs. The values of stubs are shown in Table 4.3 and 4.4.

Table 4.3: Stub lengths for the TC (Units: µm), for the sensor with H= 20 µm

H	H_1	H_2	H_3	H_4	H_5	H_6	H_7
20	2.5	5.0	7.5	10.0	12.5	15.0	17.5

Table 4.4: Stub lengths for the TC (Units: µm), for the sensor with H= 65 µm

H	H_1	H_2	H_3	H_4	H_5	H_6
65	5.0	15.0	25.0	35.0	45.0	55.0

ANSYS HFSS was used to perform eigenmode and frequency-domain (FD) simulations on the proposed structures. We aim to replicate the real devices in the simulations, hence, the model includes the Si_3N_4 substrate as 1 µm thick and ε_r = 7.6, $\sigma_{Si_3N_4} = 0$, and tan $\delta_e = 0.00526$ [65]. The gold (Au) thickness is 200 nm and the conductivity is $\sigma_{Au} = 4.1 \times 10^7$ S/m. All simulations use d =20, 50 µm, W_s =10, 20 µm, S_{CPS} =90, 140 µm, and W =10, 30 µm, where the first and second number are related to two different structures.

We use the eigenmode simulation to obtain the dispersion diagram and band-edge frequencies for the fabricated CPS-SSPP unit cells [2]. We also used FD simulation to study the transmission of the structure comparing unloaded and loaded conditions with glucose layer under the sensor's membrane. Figure 4.29 shows the S_{21} of the structure when the glucose layer thickness varies from 0 (unloaded) to 5µm, showing both absorption at 1.4 THz and band edge shift mechanism. Additionally, Fig. 4.30 illustrates a comparison between proposed SSPP sensor and CPS sensor presented in [1], with the same glucose layer thickness when loaded. The comparison of the unloaded and loaded responses of each sensor at the absorption frequency of 1.4 THz shows a 25 dB difference which is significant in terms of sensitivity. Also, the depth of absorption is 2 dB higher in the SSPP case.

Regarding the SSPP sensing at lower frequencies (0.7 THz), where the permittivity of glucose is relatively constant, we performed an eigenmode simulation in Fig. 4.31 showing that effective permittivity of the dielectric directly affects the band edge frequency. From the Kraszewski [92] dielectric model, the effective permittivity of dielectric is also a function of the thickness of the material and is not merely limited to chemical properties. Therefore, we can compare simulations, measurements, and a modified Kraszewski model [92] in Fig. showing a good agreement. The sensor's field plot is shown in Fig. 4.28, illustrating that this structure confines the field inside the corrugations and between the mutual stubs.

The measurements are carried out using a modified THz-TDS setup [55, 2] presented in Chapter 3. The results from the SSPP sensor measurements for different glucose samples are presented and discussed here. The first measurement, shown in

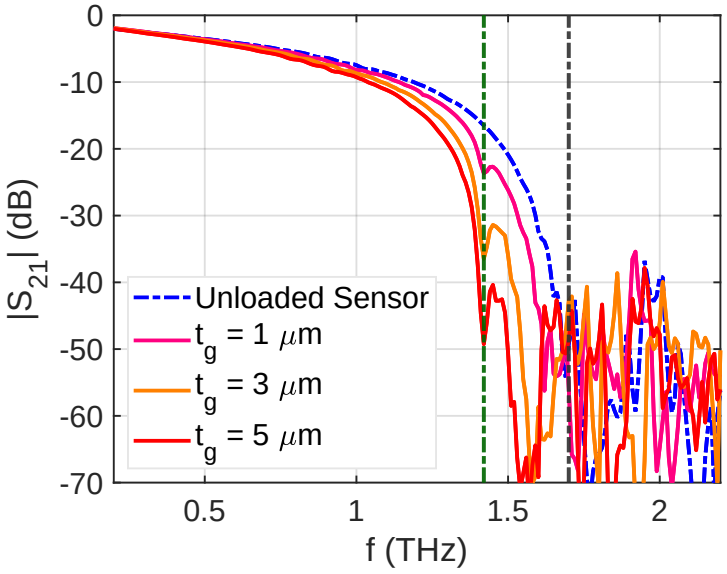

Figure 4.29: Simulated S_{21} of the SSPP structure holding band-edge at 1.7 THz (dashed grey line) with different glucose thicknesses, showing both absorption at 1.42 THz (dashed green line, modeled) and band-edge frequency shift as a result of effective permittivity variation

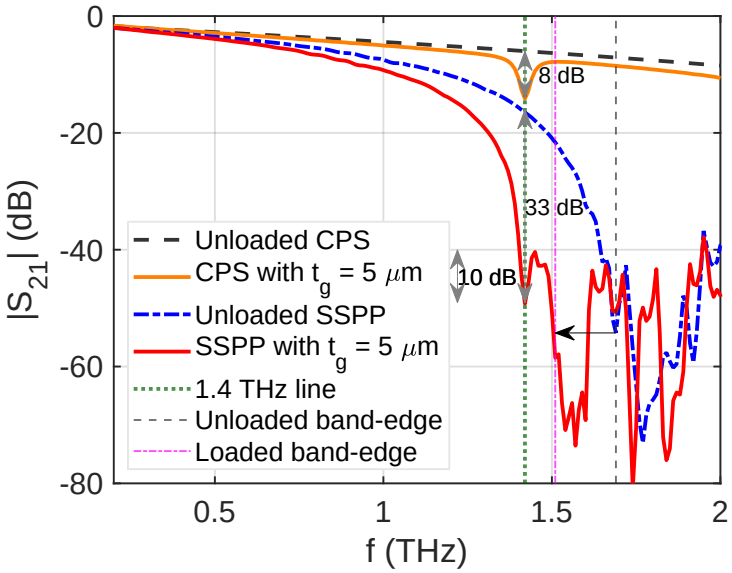

Figure 4.30: Simulated S_{21} of the SSPP vs CPS sensors with the same glucose thickness, showing a significantly larger difference with the unloaded response at 1.4 THz for the SSPP sensor

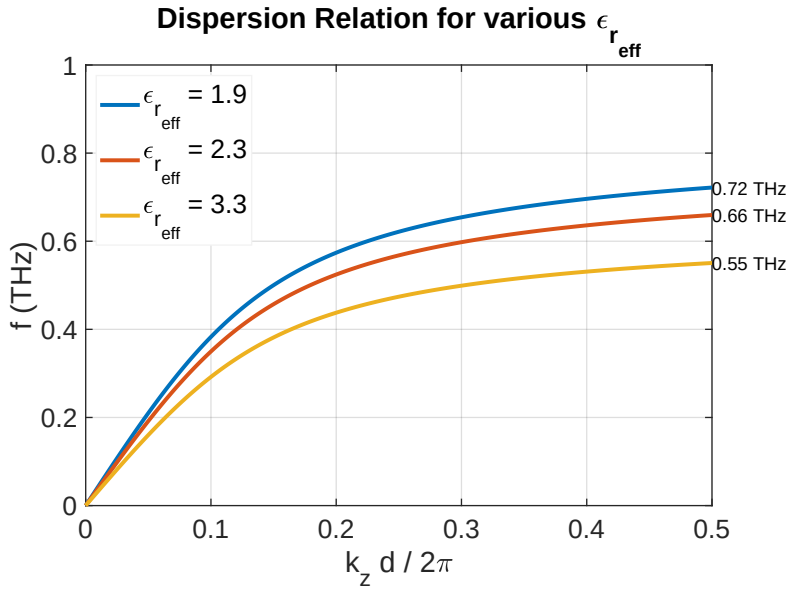

Figure 4.31: Dispersion curves of the Proposed SSPP for the measured dimensions obtained from eigenmode simulation

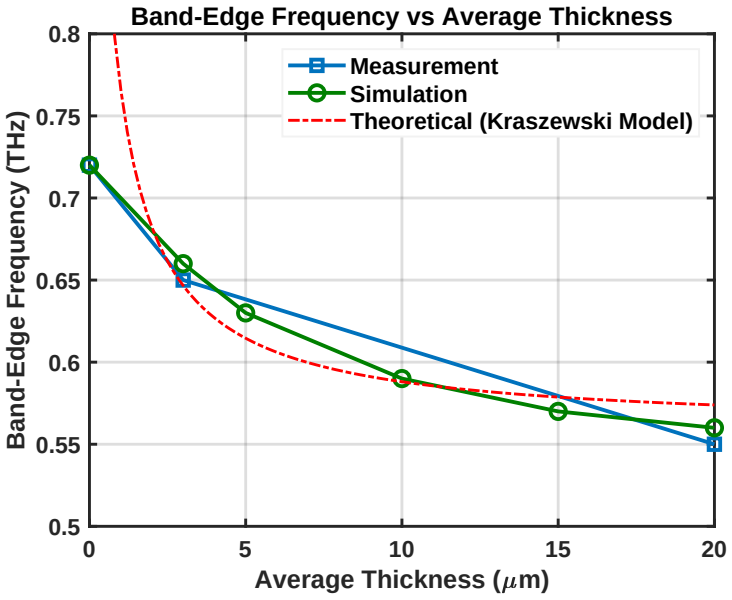

Figure 4.32: Band-edge frequency variations (Simulated, Measured, Theoretical based on dispersion relation of SSPP and modified Kraszewski effective permittivity model) versus the thickness of the glucose layer with bulk permittivity of 3.2 at the frequency range of 0.5-0.8 THz.

Figure 4.34, depicts the sensor response for a dehydrated, thin film of glucose powder. This measurement demonstrates the sensor's ability to detect absorption in the THz range, where a significant absorption peak appears around 1.4 THz, corresponding to the glucose intermolecular resonances. This observation highlights the sensor's sensitivity to material properties in the THz domain.

In Figure 4.35, the SSPP sensor response for a dried 250 mmol/L glucose solution is shown. Similar absorption behavior is observed, confirming the sensitivity and robustness of the sensor. The peak absorption slightly shifts due to the higher effective permittivity of the substrate, and the sensor's ability to detect subtle variations in the glucose concentration is clearly evident, showcasing the potential of the SSPP sensor for quantitative analysis.

Further, Fig. 4.36 presents the SSPP sensor measurements for glucose distribution and mass variations on the membrane of the sensor structure. The left column illustrates the different distributions of glucose, while the middle column shows the resulting time delays in the temporal pulse. The right column highlights the spectral variations in the band edge location and the consistent absorption peak around 1.4 THz. We note that the absorption frequency is slightly shifted to 1.35 THz due to higher field confinement of SSPP and, consequently, higher effective permittivity. The strong absorption of water molecules in the range of 1-1.2 THz can also contribute to this drift of absorption frequency. Since no other known material in the sample (i.e., glucose, isopropanol, water, SiN) exhibits absorption at 1.35 THz, this is solely related to glucose molecules.

The results in Fig. 4.36 emphasize the sensor's capability to measure the material's concentration, which directly influences both the temporal and the spectral response, including the shift in temporal pulse, the band-edge, and the intensity of the absorption peak.

Finally, in Figure 4.33, the experimental measurement results are compared with simulation results for the SSPP sensor response. The comparison reveals excellent agreement between the measured and simulated data, with a slight offset in the spectral response due to experimental conditions. This validates the sensor's performance and demonstrates that the SSPP-based sensor can be accurately designed for different sensing applications.

Overall, the SSPP sensor shows significant potential to improve sensitivity to lower concentrations compared to the CPS-based sensor [1]. Also, the combination of absorption sensing and resonance shift detection mechanisms further enhances the

sensor's sensitivity and makes it a promising tool for label-free sensing applications in biomedical and material analysis.

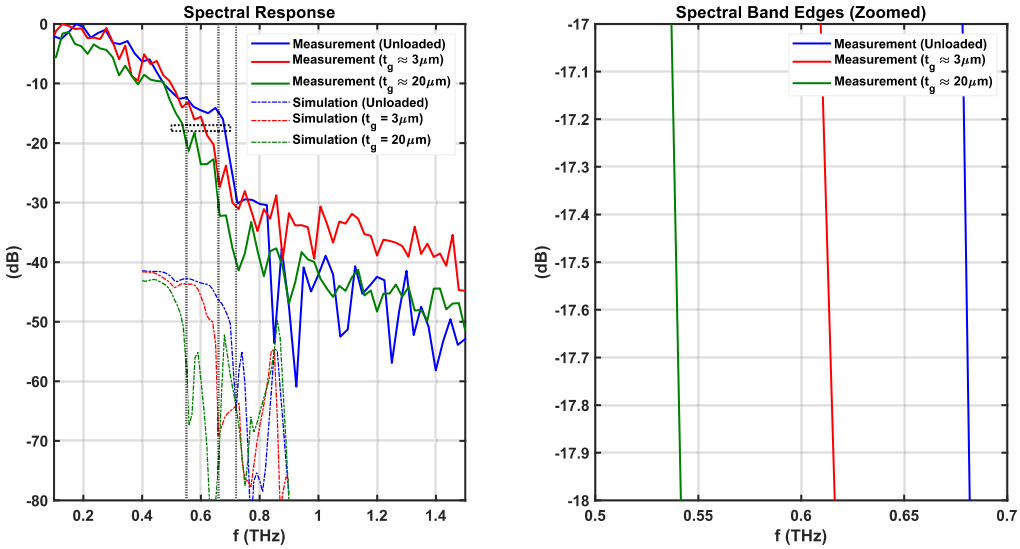

Figure 4.33: SSPP Sensor Measurement Results along with simulation results for comparison (offset of -40 dB on the Spectral Response).

We note that in the study presented in Section 4.5 and also here in Section 4.6, we encountered limitations in controlling the concentration of grains and molecules within the sensing area (waveguide), because of having a relatively large window at the back of the membrane, preventing us from quantifying the sensor's detection limit. However, we have demonstrated that the SSPP sensor exhibits superior sensitivity compared to the CPS sensor, both through simulations (showing a 25 dB higher absorption depth in SSPP when compared to unloaded sensor in Fig. 4.30) and experimental measurements (where an absorption dip was observed even without the presence of large grains in the sensing area in Fig. 4.36). Future work will focus on developing a smaller sample area or a microfluidic channel to better control the molar concentration of material at the sensing region.

This study presents a pioneering on-chip THz sensor based on the SSPP waveguide, demonstrating its potential for highly sensitive material characterization. By exploiting both resonance shifts and absorption mechanisms, the sensor effectively captures subtle changes in the dielectric properties of materials, such as glucose, in the THz frequency range. The observed shift in the band edge and its correlation with material thickness provide a novel approach for precise sensing and measurement. This work opens new avenues for THz sensing applications, offering enhanced

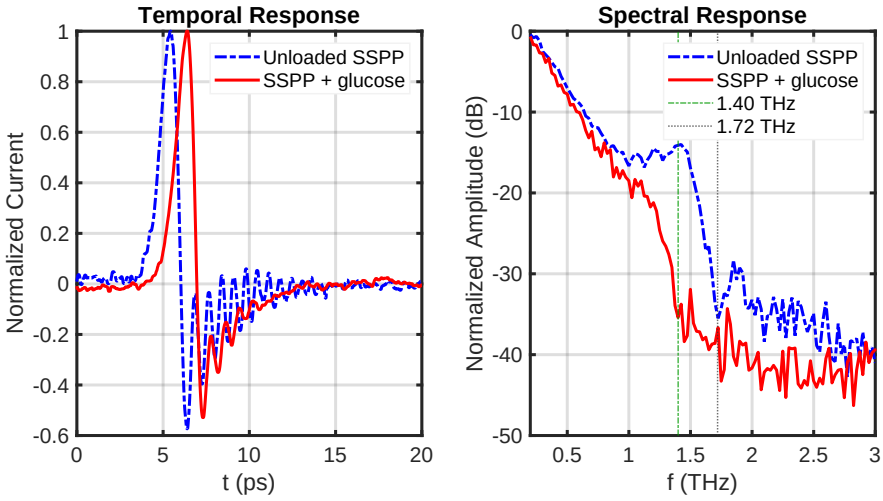

Figure 4.34: SSPP Sensor Measurement Results for a dried thin film of glucose powder.

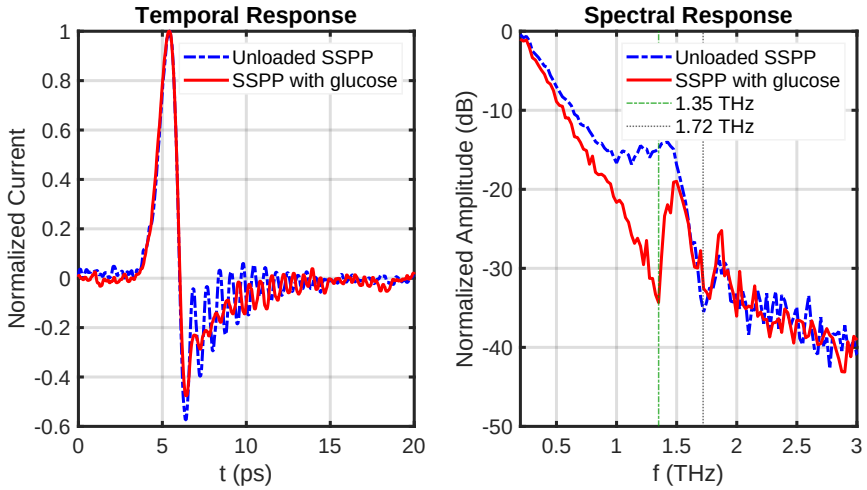

Figure 4.35: SSPP Sensor Measurement Results for dried 250 mmol/L glucose solution.

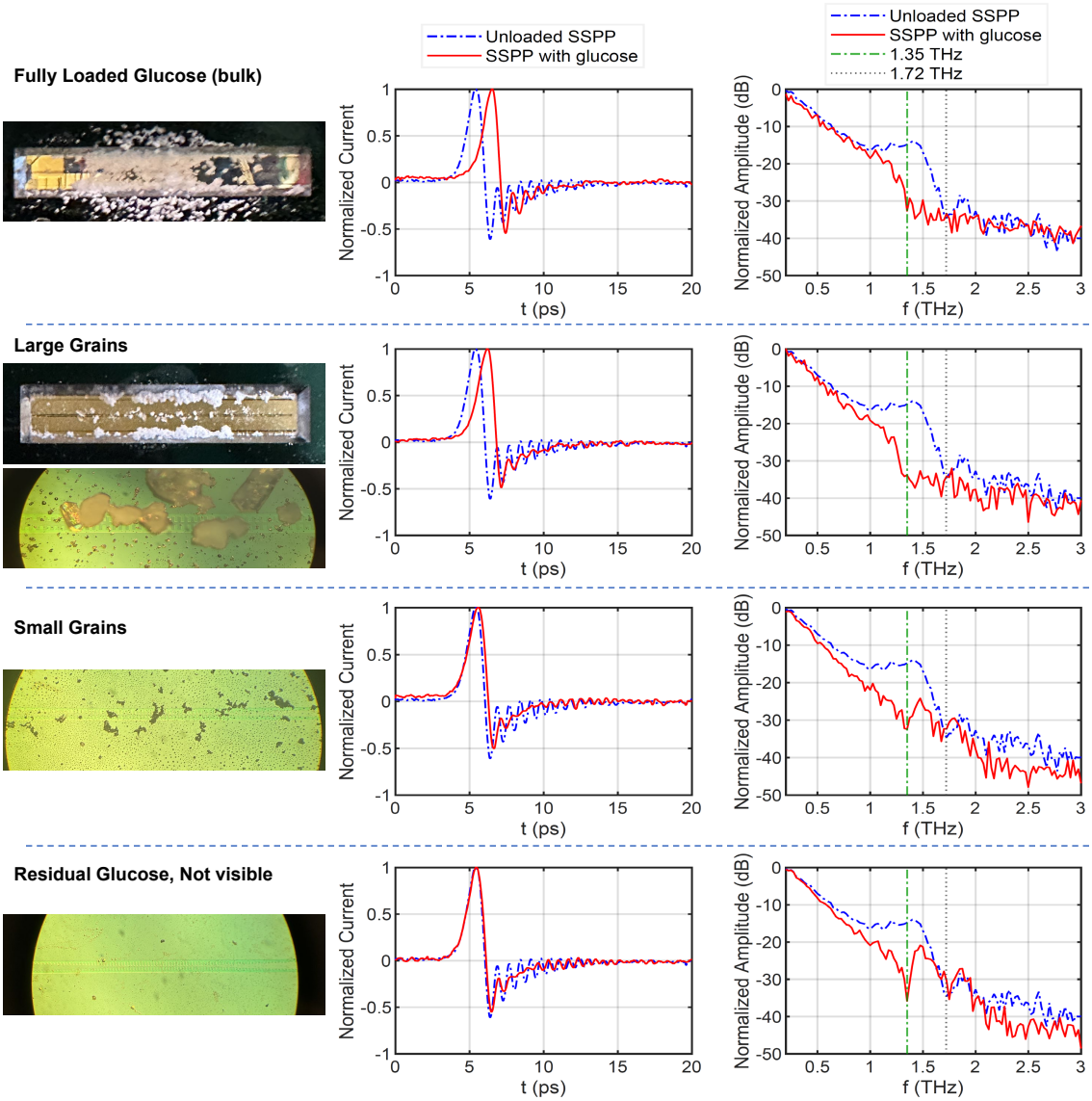

Figure 4.36: SSPP Sensor Measurement Results for different distribution and mass of glucose on the membrane of the sensor structure (left column), showing the different delays in the temporal pulse (middle column) and spectral variations in the band edge location and also a consistent absorption peak (right column).

sensitivity and versatility in detecting a wide range of substances, paving the way for future advancements in biomedical diagnostics and material analysis.

Chapter 5

Conclusion and Future Works

5.1 Conclusion

This dissertation successfully addresses the gap in the experimental validation and practical application of Spoof Surface Plasmon Polaritons (SSPP) at terahertz (THz) frequencies. By leveraging coplanar strip (CPS) feedlines, we have provided the first broadband experimental verification of SSPP characteristics at THz frequencies, extending the domain of SSPP research beyond theoretical and simulation-based studies. The development of SSPP-based low-pass and bandpass filters not only demonstrates their feasibility in advanced filtering applications but also establishes their potential for integration into future THz systems.

Additionally, the dissertation showcased the use case of CPS and SSPP structures in material sensing applications, with glucose detection serving as a proof of concept. The CPS resolves the absorption frequencies of the surrounding material film (e.g. glucose) or dielectric. Through precise tuning of SSPP structures to have field confinement and transmission at the absorption frequency of glucose, we achieved significant enhancements in sensing performance, enabled by the strong field confinement and band-edge sensitivity of SSPP waveguides. These advancements highlight the versatility of SSPP structures for emerging THz sensing technologies.

Table 5.1 provides a comparative overview of experimentally studied THz devices presented in Chapter 4, outlining their structures, key features, and operating frequencies to highlight the diversity of designs and their suitability for different filtering and sensing applications.

The findings presented in this dissertation provide a solid foundation for further

Table 5.1: Comparative overview of the experimentally studied devices based on structure type and application

Device Type	**Structure, Mechanism**	**Key Features, Innovation, Advantage, Disadvantage**	**Experimental Operating frequencies**
LPF, Waveguide	CPS-SSPP with external corrugations	dual-conductor SSPP implementation; simple fabrication, already demonstrated in microwave range	Band-edge frequencies: 0.53, 0.63, 1.04 THz
LPF, Waveguide	CPS-SSPP with internal corrugations	reduced insertion loss, improved and localized field confinement, enhanced mode conversion efficiency	Band-edge frequencies: 0.72, 0.89 THz
BPF	single-conductor SSPP integrated to CPS	High selectivity; compact single-line structure, complicated TC design	Center frequency: 1 THz
BPF	CPS with internal stubs and split-ring concept	flexible design of both lower and upper cut-offs within the unit cell, Miniaturized filter, strong out of band rejection ($\leq$ 30 dB)	Center frequency: 1 THz
Sensor	CPS on a thin membrane	on-chip (guided-wave) THz glucose sensing, easy design, broadband response, relatively low sensitivity	Measurement Range 0-2.2 THz, absorption frequencies ($\approx$ 1.4 THz, 2.1 THz)
Sensor	Guided-wave SSPP Sensor	High sensitivity to small concentration owing to field confinement, tunability for different materials	Measurement Range 0-2.0 THz, absorption frequencies ($\approx$ 1.4 THz)

exploration of SSPP structures at THz frequencies, including their optimization for specific applications in filtering, sensing, and communication. Future work can expand upon these results to explore additional materials, more complex SSPP geometries, and integrated solutions for real-world THz devices. This research contributes significantly to the growing field of THz technology, offering insights and methodologies that pave the way for innovative advancements in SSPP-based systems.

5.2 Future Works

Building upon the research presented in this dissertation, future studies can be directed toward three broad areas: the exploration of novel THz SSPP structures, the

advancement of on-chip guided-wave THz SSPP for sensing applications, and the development of THz SSPP for communication applications. This section outlines some of the potential ideas.

5.2.1 Novel THz SSPP Structures

Slow Wave CPS by Miniaturized Built-in SSPP

This structure is compact and eliminates the need for additional stubs in CPS [3]. However, the width of the CPS poses a limitation, making it challenging to design the band edge at lower frequencies. Shallow corrugations suffice for band edge frequencies above 1.5 THz, and no issues arise. At lower frequencies, a one-sided corrugation approach can be employed to effectively double the groove depth while maintaining the same CPS width.

Figure 5.1 and 5.2 illustrate the proposed CPS with built-in SSPP structure and corresponding field plots.

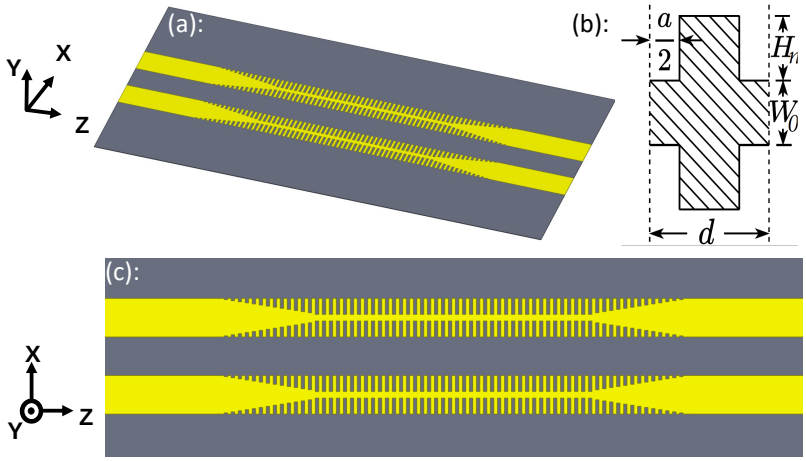

Figure 5.1: Built-in SSPP on CPS lines

This structure was already fabricated, but not yet measured. Therefore it is a quick and readily available future work. The structure has potential in sensing with higher sensitivity similar to [3].

5.2.2 Advancement of THz SSPP for Sensing Applications

This novel area of research utilizes guided-wave SSPP for on-chip sensing, based on the implementation of the structure on a thin membrane. Future advancements

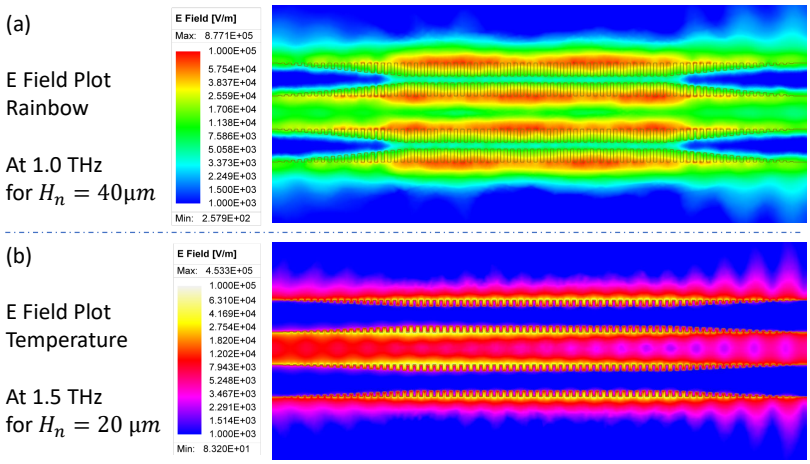

Figure 5.2: Electric Filed plots of Built-in SSPP on CPS lines with different dimensions and different color scales to illustrate field confinement at the groove areas

in this direction can include the design of various structures with field confinement capabilities and low-pass or band-pass characteristics to target frequencies of interest. This can be either an experimental work with different structures and different analyte types or more about the design and optimization of SSPP-based sensors to enhance the THz field and sensitivity. On the other hand, the usage of microfluidic channels can be investigated for liquid materials.

Here we list some possible future directions in this regard:

- Design and optimization of guided-wave SSPP sensors for maximum filed confinement and sensitivity.
- Experimental testing with glucose on various sensing structures to investigate measurement sensitivity.
- Investigation of CPS sensor response presented in [3] with various sugar types such as lactose and fructose.
- Investigation of microfluidic channel usage on the membrane-based sensor for liquid materials to reduce the THz absorption by water.

Tapered SSPP for THz field focusing

One of the structures that holds potential for SSPP-based sensing is tapered SSPP. It was first introduced in [32] as corrugations on a conical wire. We have implemented this idea in a planar structure and observed a similar behavior.

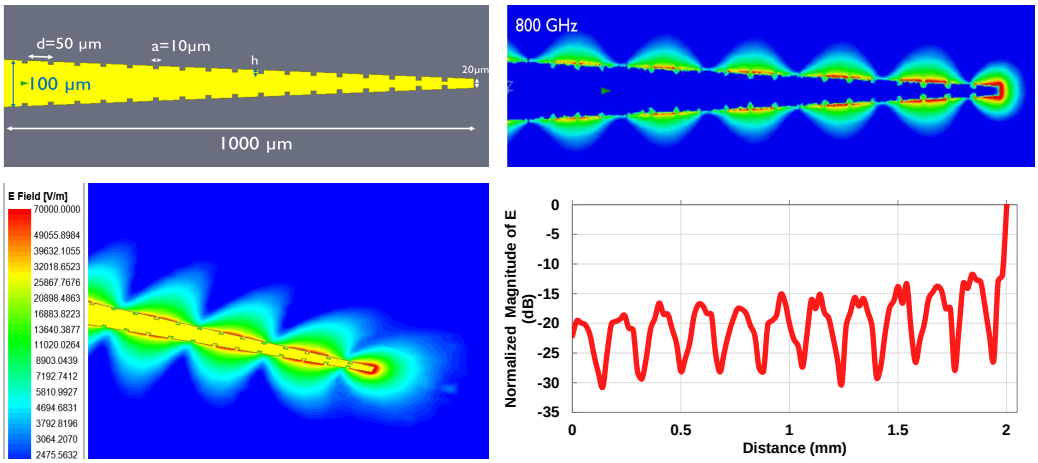

Figure 5.3: Tapered planer SSPP for THz field focusing

In this structure, we expect field focusing as long as the angle of corrugation is equal to or larger than the angle of tapering. In other words, the depth of grooves must be uniform or ascending along the structure toward the narrow end.

Figure 5.3 shows this effect with field plots and an E field magnitude curve along the top edge of the structure. This geometry has great promise for channeling THz radiation to micron-scale volumes for near-field imaging, spectroscopy, and sensing applications [32].

SSPP with incremental groove depth along the waveguide for THz field enhancement

A similar concept can be expanded to a structure with incremental corrugation depth, as shown in Fig. 5.4. At the end of the structure, the E field is concentrated in a region much smaller than the wavelength (period: d = 50 µm, aperture: a = 10 µm, wavelength: λ = 500 µm) on the surface of the structure and in the groove areas.

5.2.3 Development of THz SSPP for Waveguiding and Communication Applications

THz SSPP Waveguide with Thick Substrate: Conventional planar transmission lines such as CPS and CPW suffer from significant radiation losses at THz frequencies [55] when implemented on thick substrates ($\geq$ 10 µm). This issue originates from the weak confinement of the field, which extends beyond the metal-dielectric interface

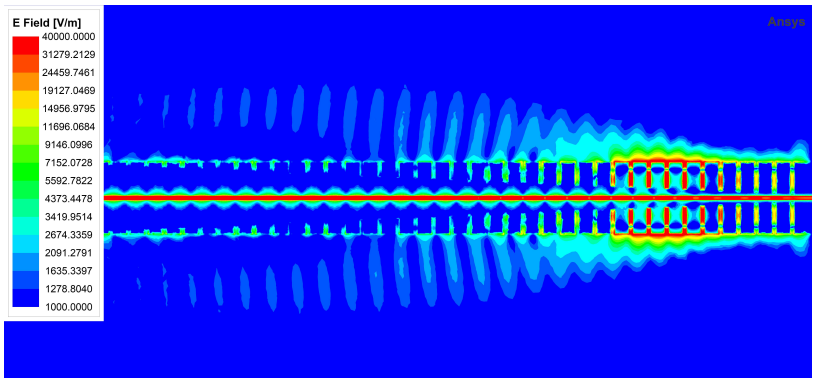

Figure 5.4: SSPP with incremental groove depth along the waveguide for THz field enhancement

and increasingly leaks into the substrate as its thickness grows. For CPS and CPW, the field distribution relies on dielectric contrast to maintain guidance, but when the substrate becomes comparable to or larger than the guided wavelength, higher-order substrate modes and leaky waves are easily excited, resulting in substantial power loss. The reduced effective permittivity and the expansion of field profiles into the air-dielectric boundary further degrade the confinement, especially at mm-wave and THz frequencies. In contrast, SSPPs leverage engineered periodic surface structures to reshape the dispersion relation and create tightly confined, non-radiative surface-bound modes. The EM fields in SSPP structures exhibit an evanescent exponential decay away from the structured metal interface, providing strong localization and confinement regardless of substrate thickness. This decouples the wave confinement from the bulk dielectric and suppresses radiation loss even on thick membranes, making SSPPs a robust solution where CPS and CPW fail to maintain low-loss propagation.

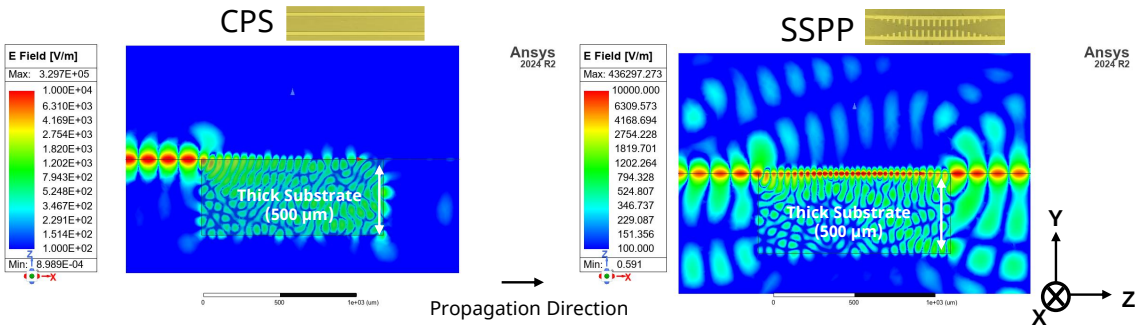

Figure 5.5: CPS vs SSPP (with internal corrugation) cross-section field plots with a thick substrate and the same dimensions (width/length of CPS lines, and width and thickness of substrate)

Figure 5.5 shows field plots of cross-sections of a CPS compared to an SSPP with the same dimensions at 1.0 THz, indicating the capability of SSPP to confine and guide the wave. This shows promising results in short distances (1 mm), which is beneficial for future miniaturized THz integrated circuits. In the future, the SSPP structure should be optimized to exhibit the lowest loss possible at a maximum length of propagation.

THz SSPP for Communication Application: THz frequencies hold significant promise for broadband communication due to their vast bandwidth availability. Despite challenges such as short transmission range and high signal attenuation, the potential of large bandwidth continues to drive research and industrial efforts to overcome these limitations [93].

A notable step in THz standardization for 6G communication is the IEEE 802.15.3 standard, which initially focused on the 300 GHz band, covering frequencies from 253 GHz to 322 GHz [94]. This standard was later revised to include frequencies up to 425 GHz [95]. With such wide bandwidth availability around the 300 GHz range, 6G communication is envisioned for applications requiring short-range, high-speed, high-throughput, and low-latency data transfer. These applications include wireless data centers, immersive virtual reality, 3D UHD video streaming, and mission-critical use cases like remote robotic surgery, autonomous systems, and self-driving vehicles [96].

This frequency range presents an excellent opportunity to leverage Spoof Surface Plasmon Polaritons (SSPP) for various components, such as waveguides [37, 47], phase shifters [97], filters [6, 1, 14], antennas [98], and other devices.

In our work, we have already developed and demonstrated a proof-of-concept bandpass filter designed for 6G communication at the 300 GHz band [14]. A promising future direction involves designing additional SSPP-based components for this frequency range, focusing on the communication channel. Verification of two-port components for proof-of-concept designs is already feasible. Furthermore, SSPP-based antennas offer remarkable potential for achieving high gain and directivity [98]. To advance these developments, we aim to realign the setup and adapt designs, enabling precise return loss measurements for various components. This paves the way to design and experimentally investigate a variety of SSPP-based antennas at THz frequencies.

Bibliography

[1] M. Haghighat, T. Darcie, and L. Smith, "Demonstration of a terahertz coplanar-strip spoof-surface-plasmon-polariton low-pass filter," *Scientific Reports*, vol. 14, 2024.

[2] M. Haghighat, A. Dehghanian, T. Darcie, and L. Smith, "Demonstration of terahertz spoof surface plasmon polariton waveguides using coplanar striplines with internal corrugations," *Optics Express*, 2024.

[3] M. Haghighat, T. Darcie, and L. Smith, "On chip glucose sensing using guided waves at terahertz frequencies," *Scientific Reports*, vol. 14, 2024.

[4] F. J. Garcia-Vidal, L. Martín-Moreno, and J. B. Pendry, "Surfaces with holes in them: new plasmonic metamaterials," *Journal of Optics A: Pure and Applied Optics*, vol. 7, no. 2, p. S97, 2005.

[5] W. X. Tang, H. C. Zhang, H. F. Ma, W. X. Jiang, and T. J. Cui, "Concept, theory, design, and applications of spoof surface plasmon polaritons at microwave frequencies," *Advanced Optical Materials*, vol. 7, no. 1, p. 1800421, 2019.

[6] Y. J. Guo, K. D. Xu, Y. Liu, and X. Tang, "Novel Surface Plasmon Polariton Waveguides with Enhanced Field Confinement for Microwave-Frequency Ultra-Wideband Bandpass Filters," *IEEE Access*, vol. 6, pp. 10 249–10 256, 2018.

[7] R. L. Smith, "Experimental evaluation of low-loss/non-dispersive terahertz waveguides," PhD dissertation, University of Victoria, 2019.

[8] J. B. Pendry, L. Martín-Moreno, and F. J. Garcia-Vidal, "Mimicking surface plasmons with structured surfaces," *Science*, vol. 305, no. 5685, pp. 847–848, 2004.

[9] A. Dehghanian, W. Gomaa, M. Haghighat, T. Darcie, and L. Smith, "Demonstration of an integrated terahertz band-stop filter using an apodized bragg grating," *Optics Express*, vol. 31, p. 32582, 2023.

[10] A. Dehghanian, M. Haghighat, T. Darcie, and L. Smith, "Demonstration of a terahertz integrated planar network synthesis filter," *Optics Continuum*, vol. 3, p. 71, 2024.

[11] S. Asadi, M. Haghighat, A. Dehghanian, T. Darcie, and L. Smith, "Terahertz bandstop filter using varying radii split-ring resonators," *Opt. Express*, vol. 33, no. 3, pp. 6421–6430, 2025.

[12] A. Dehghanian, M. Haghighat, T. Darcie, and L. Smith, "Demonstration of a planar multimodal periodic filter at thz frequencies," arXiv preprint arXiv:2502.10611, 2025.

[13] M. Haghighat, T. E. Darcie, and L. Smith, "Terahertz cps-based spoof surface plasmon polariton filter on silicon nitride substrate," in *2023 48th International Conference on Infrared, Millimeter, and Terahertz Waves (IRMMW-THz)*, 2023, pp. 1–2.

[14] M. Haghighat, T. Darcie, and L. Smith, "A thz spoof surface plasmon polariton band pass filter for 6g communication applications," in *2024 IEEE Pacific Rim Conference on Communications, Computers and Signal Processing (PACRIM)*, 2024, pp. 1–4.

[15] M. Haghighat, T. E. Darcie, and L. Smith, "An on-chip terahertz glucose sensor," in *2024 49th International Conference on Infrared, Millimeter, and Terahertz Waves (IRMMW-THz)*, 2024, pp. 1–2.

[16] M. Haghighat, T. Darcie, and L. Smith, "Spoof surface plasmon polariton (sspp) split rings for thz bandpass filtering," in *Terahertz, RF, Millimeter, and Submillimeter-Wave Technology and Applications*, 2025.

[17] R. Han, Z. Hu, C. Wang, J. Holloway, X. Yi, M. Kim, and J. Mawdsley, "Filling the gap: Silicon terahertz integrated circuits offer our best bet," *IEEE Microwave Magazine*, vol. 20, no. 4, pp. 80–93, 2019.

[18] N. T. Yardimci, S. Cakmakyapan, S. Hemmati, and M. Jarrahi, "A High-Power Broadband Terahertz Source Enabled by Three-Dimensional Light Confinement in a Plasmonic Nanocavity," *Scientific Reports*, vol. 7, no. 1, p. 4166, Jun. 2017.

[19] S. A. Maier *et al.*, *Plasmonics: fundamentals and applications*. Springer, 2007, vol. 1.

[20] S. S. Dhillon, M. S. Vitiello, E. H. Linfield, A. G. Davies, M. C. Hoffmann, J. Booske, C. Paoloni, M. Gensch, P. Weightman, G. P. Williams, E. Castro-Camus, D. R. S. Cumming, F. Simoens, I. Escorcia-Carranza, J. Grant, S. Lucyszyn, M. Kuwata-Gonokami, K. Konishi, M. Koch, C. A. Schmuttenmaer, T. L. Cocker, R. Huber, A. G. Markelz, Z. D. Taylor, V. P. Wallace, J. Axel Zeitler, J. Sibik, T. M. Korter, B. Ellison, S. Rea, P. Goldsmith, K. B. Cooper, R. Appleby, D. Pardo, P. G. Huggard, V. Krozer, H. Shams, M. Fice, C. Renaud, A. Seeds, A. Stöhr, M. Naftaly, N. Ridler, R. Clarke, J. E. Cunningham, and M. B. Johnston, "The 2017 terahertz science and technology roadmap," *Journal of Physics D: Applied Physics*, vol. 50, no. 4, p. 043001, Feb. 2017.

[21] W. Ghann and J. Uddin, *Terahertz (THz) Spectroscopy: A Cutting-Edge Technology*, J. Uddin, Ed. Rijeka: IntechOpen, 2017.

[22] E. R. Brown, K. A. McIntosh, K. B. Nichols, and C. L. Dennis, "Photomixing up to 3.8 thz in low-temperature-grown gaas," *Applied Physics Letters*, vol. 66, no. 3, pp. 285–287, 1995.

[23] A. Nahata, A. S. Weling, and T. F. Heinz, "A wideband coherent terahertz spectroscopy system using optical rectification and electro-optic sampling," *Applied Physics Letters*, vol. 69, no. 16, pp. 2321–2323, 1996.

[24] J. Ward, E. Schlecht, G. Chattopadhyay, A. Maestrini, J. Gill, F. Maiwald, H. Javadi, and I. Mehdi, "Capability of thz sources based on schottky diode frequency multiplier chains," in *2004 IEEE MTT-S International Microwave Symposium Digest (IEEE Cat. No.04CH37535)*. IEEE, 2004.

[25] A. Dobroiu, M. Yamashita, Y. N. Ohshima, Y. Morita, C. Otani, and K. Kawase, "Terahertz imaging system based on a backward-wave oscillator," *Applied Optics*, vol. 43, no. 30, p. 5637, 2004.

[26] B. Knyazev, G. Kulipanov, and N. Vinokurov, "Novosibirsk terahertz free electron laser: instrumentation development and experimental achievements," *Measurement Science and Technology*, vol. 21, no. 5, p. 054017, 2010.

[27] B. S. Williams, "Terahertz quantum-cascade lasers," *Nature Photonics*, vol. 1, no. 9, pp. 517–525, 2007.

[28] I. S. Gregory, C. Baker, W. Tribe, M. Evans, H. Beere, E. Linfield, A. Davies, and M. Missous, "High resistivity annealed low-temperature gaas with 100 fs lifetimes," *Applied Physics Letters*, vol. 83, no. 20, pp. 4199–4201, 2003.

[29] B. Heshmat, H. Pahlevaninezhad, Y. Pang, M. Masnadi-Shirazi, R. Burton Lewis, T. Tiedje, R. Gordon, and T. E. Darcie, "Nanoplasmonic terahertz photoconductive switch on gaas," *Nano Letters*, vol. 12, no. 12, pp. 6255–6259, 2012.

[30] M. Tani, M. Herrmann, and K. Sakai, "Generation and detection of terahertz pulsed radiation with photoconductive antennas and its application to imaging," *Measurement Science and Technology*, vol. 13, no. 11, p. 1739, oct 2002.

[31] E. Yablonovitch, D. M. Hwang, T. J. Gmitter, L. T. Florez, and J. P. Harbison, "Van der Waals bonding of GaAs epitaxial liftoff films onto arbitrary substrates," *Applied Physics Letters*, vol. 56, no. 24, pp. 2419–2421, 06 1990.

[32] S. A. Maier, S. R. Andrews, L. Martín-Moreno, and F. J. García-Vidal, "Terahertz Surface Plasmon-Polariton Propagation and Focusing on Periodically Corrugated Metal Wires," *Physical Review Letters*, vol. 97, no. 17, p. 176805, Oct. 2006.

[33] X. Shen, T. J. Cui, D. Martin-Cano, and F. J. Garcia-Vidal, "Conformal surface plasmons propagating on ultrathin and flexible films," *Proceedings of the National Academy of Sciences*, vol. 110, no. 1, pp. 40–45, 2013.

[34] P. A. Huidobro, A. I. Fernández-Domínguez, J. B. Pendry, L. Martín-Moreno, and F. J. Garcia-Vidal, *Spoof Surface Plasmon Metamaterials*, ser. Elements in Emerging Theories and Technologies in Metamaterials. Cambridge University Press, 2018.

[35] H. F. Ma, X. Shen, Q. Cheng, W. X. Jiang, and T. J. Cui, "Broadband and high-efficiency conversion from guided waves to spoof surface plasmon polaritons," *Laser Photonics Rev.*, vol. 8, no. 1, pp. 146–151, Jan. 2014.

[36] Y. J. Guo, K. Da Xu, and X. Tang, "Spoof plasmonic waveguide developed from coplanar stripline for strongly confined terahertz propagation and its application in microwave filters," *Optics Express*, vol. 26, no. 8, p. 10589, Apr. 2018.

[37] M. A. Unutmaz and M. Unlu, "Terahertz Spoof Surface Plasmon Polariton Waveguides: A Comprehensive Model with Experimental Verification," *Scientific Reports*, vol. 9, no. 1, p. 7616, May 2019.

[38] S. P. Singh, N. K. Tiwari, and M. J. Akhtar, "Spoof surface plasmon-based coplanar waveguide sensor for dielectric sensing applications," *IEEE Sensors Journal*, vol. 20, no. 1, pp. 193–201, 2020.

[39] M. A. Unutmaz and M. Unlu, "Spoof surface plasmon polariton delay lines for terahertz phase shifters," *J. Lightwave Technol.*, 2021.

[40] K.-D. Xu, F. Zhang, Y. Guo, L. Ye, and Y. Liu, "Spoof Surface Plasmon Polaritons Based on Balanced Coplanar Stripline Waveguides," *IEEE Photonics Technology Letters*, vol. 32, no. 1, pp. 55–58, Jan. 2020.

[41] B. Mazdouri, M. M. Honari, and R. Mirzavand, "Miniaturized spoof SPPs filter based on multiple resonators or 5G applications," *Scientific Reports*, vol. 11, no. 1, p. 22557, Nov. 2021.

[42] "Dispersion compensation for spoof plasmonic circuits," *Progress In Electromagnetics Research*, vol. 179, pp. 95–100, 2024.

[43] Y. Cinar, S. Yildirim, G. Ozsahin, M. Unutmaz, and M. Unlu, "Modelling Terahertz Spoof Surface Plasmon Polariton Waveguides Using a Circuit Model," *IEEE Transactions on Terahertz Science and Technology*, vol. 11, no. 5, pp. 557–565, Sep. 2021.

[44] A. Kianinejad, Z. N. Chen, and C.-W. Qiu, "Design and modeling of spoof surface plasmon modes-based microwave slow-wave transmission line," *IEEE Transactions on Microwave Theory and Techniques*, vol. 63, no. 6, pp. 1817–1825, 2015.

[45] D. Cao, Y. Li, and J. Wang, "Wideband compact slotline-to-spoof-surface plasmon-polaritons transition for millimeter waves," *IEEE Antennas and Wireless Propagation Letters*, vol. 16, pp. 3143–3146, 2017.

[46] K.-D. Xu, Y. J. Guo, and X. Deng, "Terahertz broadband spoof surface plasmon polaritons using high-order mode developed from ultra-compact split-ring grooves," *Optics Express*, vol. 27, no. 4, p. 4354, Feb. 2019.

[47] M. A. Unutmaz, G. Ozsahin, T. Abacilar, and M. Unlu, "Investigation of the Transitions for Coplanar Waveguide to Terahertz Spoof Surface Plasmon Polariton Waveguides," *IEEE Transactions on Antennas and Propagation*, vol. 70, no. 4, pp. 3002–3010, Apr. 2022.

[48] Y. J. Guo, K. D. Xu, Y. Liu, and X. Tang, "Novel surface plasmon polariton waveguides with enhanced field confinement for microwave-frequency ultra-wideband bandpass filters," *IEEE Access*, vol. 6, pp. 10 249–10 256, 2018.

[49] I. Bahl, M. Bozzi, and R. Garg, *Microstrip Lines and Slotlines*, 3rd ed. Artech House, 2013.

[50] J. Wang, L. Zhao, and Z.-C. Hao, "A band-pass filter based on the spoof surface plasmon polaritons and cpw-based coupling structure," *IEEE Access*, vol. 7, pp. 35 089–35 096, 2019.

[51] Y. Wei, Y. Wu, W. Wang, L. Pan, Y. Yang, and Y. Liu, "Double-sided spoof surface plasmon polaritons- line bandpass filter with excellent dual-band filtering and wide upper band suppressions," *IEEE Transactions on Plasma Science*, vol. 48, no. 12, pp. 4134–4143, 2020.

[52] Y. Liu, K.-D. Xu, J. Li, Y.-J. Guo, A. Zhang, and Q. Chen, "Millimeter-wave e-plane waveguide bandpass filters based on spoof surface plasmon polaritons," *IEEE Transactions on Microwave Theory and Techniques*, vol. 70, no. 10, pp. 4399–4409, 2022.

[53] W. G. A. Abdelmouty, "Terahertz system-on-chip using coplanar stripline transmission line on thin membrane," Ph.D. dissertation, University of Victoria, January 2021.

[54] R. D. V. Ríos, S. Bikorimana, M. A. Ummy, R. Dorsinville, and S.-W. Seo, "A bow-tie photoconductive antenna using a low-temperature-grown gaas thin-film on a silicon substrate for terahertz wave generation and detection," *Journal of Optics*, vol. 17, no. 12, p. 125802, 2015.

[55] L. Smith and T. Darcie, "Demonstration of a low-distortion terahertz system-on-chip using a cps waveguide on a thin membrane substrate," *Optics Express*, vol. 27, no. 10, pp. 13 653–13 663, May 2019.

[56] W. Gomaa, L. Smith, V. Shiran, and T. Darcie, "Terahertz low-pass filter based on cascaded resonators formed by CPS bending on a thin membrane," *Optics Express*, vol. 28, no. 21, p. 31967, Oct. 2020.

[57] A. Jaber, M. Reitz, A. Singh, A. Maleki, Y. Xin, B. T. Sullivan, K. Dolgaleva, R. W. Boyd, C. Genes, and J. Ménard, "Hybrid architectures for terahertz molecular polaritonics," *Nature Communications*, vol. 15, 2024.

[58] N. Khiabani, Y. Huang, Y.-C. Shen, and S. Boyes, "Theoretical modeling of a photoconductive antenna in a terahertz pulsed system," *IEEE Transactions on Antennas and Propagation*, vol. 61, no. 4, pp. 1538–1546, 2013.

[59] R. K. Jaiswal, N. Pandit, and N. P. Pathak, "Spoof surface plasmon polaritons based reconfigurable band-pass filter," *IEEE Photonics Technology Letters*, vol. 31, no. 3, pp. 218–221, 2019.

[60] M. A. Unutmaz, G. Ozsahin, and M. Unlu, "Optimization of terahertz spoof surface plasmon polariton waveguides for maximum °/db performance," *Journal of Lightwave Technology*, vol. 39, no. 17, pp. 5508–5515, 2021.

[61] Y. Liang, H. Yu, J. Wen, A. A. A. Apriyana, N. Li, Y. Luo, and L. Sun, "On-chip sub-terahertz surface plasmon polariton transmission lines with mode converter in cmos," *Scientific Reports*, vol. 6, no. 1, p. 30063, 07 2016.

[62] C. R. Williams, S. R. Andrews, S. A. Maier, A. I. Fernández-Domínguez, L. Martín-Moreno, and F. J. García-Vidal, "Highly confined guiding of terahertz surface plasmon polaritons on structured metal surfaces," *Nature Photonics*, vol. 2, no. 3, pp. 175–179, 03 2008.

[63] W. Knox, J. Henry, K. Goossen, K. Li, B. Tell, D. Miller, D. Chemla, A. Gossard, J. English, and S. Schmitt-Rink, "Femtosecond excitonic optoelectronics," *IEEE Journal of Quantum Electronics*, vol. 25, no. 12, pp. 2586–2595, 1989.

[64] G. Hasnain, A. Dienes, and J. Whinnery, "Dispersion of picosecond pulses in coplanar transmission lines," *IEEE Transactions on Microwave Theory and Techniques*, vol. 34, no. 6, pp. 738–741, 1986.

[65] G. Cataldo, J. A. Beall, H.-M. Cho, B. McAndrew, M. D. Niemack, and E. J. Wollack, "Infrared dielectric properties of low-stress silicon nitride," *Optics Letters*, vol. 37, no. 20, pp. 4200–4202, Oct 2012.

[66] D. Lee, J. Kang, J. H. Lee, H. Kim, C. Kim, J. Kim, T. Lee, J. Son, Q. Park, and M. Seo, "Highly sensitive and selective sugar detection by terahertz nano-antennas," *Scientific Reports*, vol. 5, 2015.

[67] Y.-S. Lee, *Principles of Terahertz Science and Technology.* Springer, 2009.

[68] A. G. Davies, A. D. Burnett, W. Fan, E. H. Linfield, and J. E. Cunningham, "Terahertz spectroscopy of explosives and drugs," *Materials Today*, vol. 11, no. 3, pp. 18–26, 2008.

[69] N. S. Oliver, C. Toumazou, A. E. G. Cass, and D. G. Johnston, "Glucose sensors: a review of current and emerging technology," *Diabetic Medicine*, vol. 26, no. 3, pp. 197–210, 2009.

[70] Y. Li and Y. Chen, "Review of noninvasive continuous glucose monitoring in diabetics," *ACS Sensors*, vol. 8, pp. 3659–3679, 2023.

[71] D. Di Filippo, F. N. Sunstrum, J. U. Khan, and A. W. Welsh, "Non-invasive glucose sensing technologies and products: A comprehensive review for researchers and clinicians," *Sensors*, vol. 23, no. 22, 2023.

[72] E. Pickwell and V. P. Wallace, "Biomedical applications of terahertz technology," *Journal of Physics D: Applied Physics*, vol. 39, no. 17, p. R301, aug 2006.

[73] S. L. Jacques, "Optical properties of biological tissues: a review," *Physics in Medicine and Biology*, vol. 58, no. 11, p. R37, may 2013.

[74] N. C. D. Truong, S. Shahdadian, S. Kang, X. Wang, and H. Liu, "Influence of the signal-to-noise ratio on variance of chromophore concentration quantification in broadband near-infrared spectroscopy," *Frontiers in Photonics*, vol. 3, 2022.

[75] J. Kottmann, J. M. Rey, J. Luginbühl, E. Reichmann, and M. W. Sigrist, "Glucose sensing in human epidermis using mid-infrared photoacoustic detection," *Biomed. Opt. Express*, vol. 3, no. 4, pp. 667–680, Apr 2012.

[76] M. H. Hassan, C. Vyas, B. Grieve, and P. Bartolo, "Recent advances in enzymatic and non-enzymatic electrochemical glucose sensing," *Sensors*, vol. 21, no. 14, 2021.

[77] H.-B. Liu and X.-C. Zhang, "Dehydration kinetics of d-glucose monohydrate studied using thz time-domain spectroscopy," *Chemical Physics Letters*, vol. 429, no. 1, pp. 229–233, 2006.

[78] Z. Vilagosh, A. Lajevardipour, and A. W. Wood, "Computational phantom study of frozen melanoma imaging at 0.45 terahertz," *Bioelectromagnetics*, vol. 40, pp. 118–127, 2019.

[79] H. Chen, X. Chen, S. Ma *et al.*, "Quantify glucose level in freshly diabetic's blood by terahertz time-domain spectroscopy," *J Infrared Milli Terahz Waves*, vol. 39, pp. 399–408, 2018. [Online]. Available: https://doi.org/10.1007/s10762-017-0462-2

[80] X. Lu, L. Xu, L. Luo, Z. Li, T. Chang, D. Wei, and H.-L. Cui, "Weak value amplified precision terahertz spectroscopic detection of solid and liquid glucose samples," *ACS Photonics*, vol. 10, no. 9, pp. 3149–3160, sep 2023. [Online]. Available: https://doi.org/10.1021/acsphotonics.3c00525

[81] C. Song, W. Fan, L. Ding, C. Xu, Z. Chen, and K. Wang, "Terahertz and infrared characteristic absorption spectra of aqueous glucose and fructose solutions," *Scientific Reports*, vol. 8, 2018.

[82] G. Lee, Y. Cho, and G. Ok, "Improved analysis of thz metamaterials for glucose sensing based on modified lorentz dispersion model," *Spectrochimica Acta Part A: Molecular and Biomolecular Spectroscopy*, vol. 293, p. 122519, 2023.

[83] H. Huang, S. Shao, G. Wang, B. Su, and C. Zhang, "Terahertz spectral properties of glucose and two disaccharides in solid and liquid states," *iScience*, vol. 25, p. 104102, 2022.

[84] M. Beruete and I. Jáuregui-López, "Terahertz sensing based on metasurfaces," *Advanced Optical Materials*, vol. 8, 2019.

[85] J. Yang, L. Qi, B. Li, L. Wu, D. Shi, J. A. Uqaili, and X. Tao, "A terahertz metamaterial sensor used for distinguishing glucose concentration," *Results in Physics*, vol. 26, p. 104332, 2021.

[86] K. Serita, H. Murakami, I. Kawayama, and M. Tonouchi, "A terahertz-microfluidic chip with a few arrays of asymmetric meta-atoms for the ultra-trace sensing of solutions," *Photonics*, vol. 6, p. 12, 2019.

[87] H. Zeng, S. Gong, L. Wang, T. Zhou, Y. Zhang, F. Lan, X. Cong, L. Wang, T. Song, Y. Zhao, Z. Yang, and D. M. Mittleman, "A review of terahertz phase modulation from free space to guided wave integrated devices," *Nanophotonics*, vol. 11, no. 3, pp. 415–437, 2022.

[88] X. Hu, G. Xu, L. Wen, H. Wang, Y. Zhao, Y. Zhang, D. R. S. Cumming, and Q. Chen, "Metamaterial absorber integrated microfluidic terahertz sensors," *Laser Amp; Photonics Reviews*, vol. 10, pp. 962–969, 2016.

[89] H. Cheng, J. Whitaker, T. Weller, and L. Katehi, "Terahertz-bandwidth pulse propagation on a coplanar stripline fabricated on a thin membrane," *IEEE microwave and guided wave letters*, vol. 4, no. 3, pp. 89–91, 1994.

[90] D. Mozaffarian, "Dietary and policy priorities for cardiovascular disease, diabetes, and obesity," *Circulation*, vol. 133, no. 2, pp. 187–225, 2016.

[91] E. E. Ventura, J. N. Davis, and M. I. Goran, "Sugar content of popular sweetened beverages based on objective laboratory analysis: Focus on fructose content," *Obesity*, vol. 19, no. 4, pp. 868–874, 2011.

[92] A. Kraszewski, "Prediction of the dielectric properties of two-phase mixtures," *Journal of Microwave Power*, vol. 12, no. 3, pp. 216–222, 1977.

[93] H.-J. Song and N. Lee, "Terahertz communications: Challenges in the next decade," *IEEE Transactions on Terahertz Science and Technology*, vol. 12, no. 2, pp. 105–117, 2022.

[94] V. Petrov, T. Kurner, and I. Hosako, "Ieee 802.15.3d: First standardization efforts for sub-terahertz band communications toward 6g," *IEEE Communications Magazine*, vol. 58, no. 11, pp. 28–33, 2020.

[95] IEEE, "IEEE Standard for Wireless Multimedia Networks: IEEE 802.15.3-2023," 2023.

[96] C.-X. Wang, X. You, X. Gao, X. Zhu, Z. Li, C. Zhang, H. Wang, Y. Huang, Y. Chen, H. Haas, J. S. Thompson, E. G. Larsson, M. D. Renzo, W. Tong, P. Zhu, X. Shen, H. V. Poor, and L. Hanzo, "On the road to 6g: Visions, requirements, key technologies, and testbeds," *IEEE Communications Surveys Tutorials*, vol. 25, no. 2, pp. 905–974, 2023.

[97] M. A. Unutmaz and M. Unlu, "Spoof surface plasmon polariton delay lines for terahertz phase shifters," *J. Lightwave Technol.*, 2021.

[98] J. J. Sheng, C. J. You, Q. Yu Li, X. H. Liu, H. L. Peng, and X. Y. Zhu, "Broadband planar filtering antenna with high out-of-band suppression based on spoof surface plasmon polariton," *IEEE Antennas and Wireless Propagation Letters*, pp. 1–5, 2024.

Appendix A

Demonstration of a Terahertz Coplanar Strip Spoof Surface Plasmon Polariton Low Pass Filter, Copy of [1]

scientific reports

Check for updates

OPEN

Demonstration of a terahertz coplanar-strip spoof-surface-plasmon-polariton low-pass filter

Mohsen Haghighat[1,2], Thomas Darcie[1] & Levi Smith[1,2]✉

There is a growing interest in spoof surface plasmon polariton (SSPP) structures at terahertz (THz) frequencies for applications such as filtering, sensing, and communications. However, to date, there are limited experiments that confirm SSPP characteristics at THz frequencies. The majority of literature focuses on simulation or verification by device scaling to Gigahertz (GHz) frequencies where standard vector network analyzers are readily available. This paper presents the first experimental verification of SSPP characteristics at THz frequencies in a guided wave system using coplanar strip (CPS) feedlines. Specifically, we design three SSPP structures with varying band-edge frequencies (1.04 THz, 0.63 THz, and 0.53 THz), then fabricate and verify the low-pass transmission characteristics using a modified THz-time-domain spectrometer (THz-TDS) system. We find strong agreement between simulation, theory, and experiment.

Terahertz (THz) systems and devices have garnered extensive research attention over the past few decades due to their attractive applications in sensing, imaging, data communication transceivers, and biomedicine[1–3]. This research has also sparked significant interest in spoof surface plasmon polaritons (SSPP) structures which mimic the behavior of conventional surface plasmon polaritons (SPP)[4,5]. SSPPs differ from conventional SPPs in that their dispersion characteristics are primarily determined by geometry as opposed to material parameters which enable SSPPs to exist at sub-optical frequencies. We note that both SSPPs and SPPs are capable of supporting surface-wave propagation and sub-wavelength field localization. SSPPs can be used for several applications, but the standard use cases are filtering, sensing, and communications[3]. Regarding filtering, SSPP devices exhibit low-pass behavior with significant roll-off rates over short structure lengths. Practically, short filter lengths are desirable to minimize the necessary component area. For sensing, SSPPs exhibit slow-wave behavior and significant field enhancement near the component[6]. The combination of these effects in the presence of an unknown sample can be used for material parameter identification[7]. Lastly, for communications, SSPPs have a relatively low loss (0.75 dB/mm at 0.22–0.32 THz[8]) and are resilient to bend losses[9]. This is an important advantage because bend losses limit the practicality of other single conductor waveguides such as the Goubau line[10] or single wire waveguide[11].

It is not straightforward to directly excite the fundamental mode transverse magnetic (TM) of an SSPP waveguide. For practical purposes, SSPP structures are typically integrated with a feedline such as a coplanar waveguide (CPW)[12–14], coplanar strip (CPS)[15–17], microstrip (MS)[18], or slotline (SL)[19]. The fundamental modes of the aforementioned waveguides are quasi-transverse electromagnetic (TEM) (CPW, CPS, and MS) or quasi-transverse electric (TE) for the SL[20]. Given that the feedline and SSPP have different modes, a transition circuit (TC) is necessary to perform a mode conversion. To date, most of the research efforts have utilized a CPW feedline to excite an SSPP mode where large flaring grounds are used in the TC to aid in the mode conversion[20]. The CPW configuration is commonly used because of its compatibility with standard microwave frequency vector network analyzers (VNA) probes. Alternatively, in[15], it was suggested to use a CPS feedline to excite the SSPP mode (termed CPS-SSPP). The CPS-SSPP has several benefits such as a reduced circuit size and improved lumped element compatibility. In[15], the authors designed a *THz* CPS-SSPP structure but fabricated and tested a scaled structure at *GHz* frequencies. The reason for the scale modification is that it is exceedingly difficult to perform device characterization at THz frequencies because there is limited or no commercial equipment available. Downshifting to GHz provides useful insight, but it negates difficulties that are expected to occur at THz

[1]Department of Electrical and Computer Engineering, University of Victoria, Victoria, BC V8P 5C2, Canada. [2]Centre for Advanced Materials and Related Technology (CAMTEC) at the University of Victoria, 3800 Finnerty Rd, Victoria, BC V8P 5C2, Canada. ✉email: levismith@uvic.ca

frequencies such as substrate radiation and extraneous resonances. Also, if the proposed application of an SSPP is a chemical sensor, then it is of the utmost importance that the device operates where the molecular absorption signatures reside, for vibrational resonances it is typically at THz frequencies[21].

While many simulations at THz frequencies have been conducted, most of the validation experiments have been performed at GHz frequencies by scaling the structures and implementing on MS platforms to measure the performance up to 16 GHz[15–17,22]. To date, experimental measurements of THz SSPPs have predominantly focused on frequencies up to approximately 300 GHz[8,12,23] except for our preliminary work which focused on a single CPS-SSPP configuration[24]. On the other hand, some studies have employed radiated wave approaches to investigate SSPPs at frequencies greater than 1 THz[25]; however, this work focuses on using non-radiative feedlines for their improved integration benefits such as their well-known field profiles and planar coupling efficiencies.

To verify SSPP behavior, we investigate a signal that has been transmitted through an SSPP. It is known that an SSPP behaves like a low-pass filter where the cut-off frequency is given by the band-edge associated with the periodic structure (discussed later)[5]. In this work, we integrate three different CPS-SSPP geometric configurations into our THz System-on-Chip (TSoC) platform[26] as shown in Fig. 1, then we verify the stop-band location at THz frequencies. The TSoC platform consists of planar conductors on a very thin (1 μm) Si_3N_4 membrane which reduces the loss and dispersion of the propagating wave along the CPS feedlines and ensures the CPS-SSPP is excited with a near-TEM field profile. This method enables us to characterize devices at THz frequencies with ease since radiative substrate losses are heavily mitigated. We find that the SSPP results from the experiments are in agreement with simulation and theory. To the best of our knowledge, this work presents the highest experimental frequency achieved for guided-wave SSPP characterization. Note that this is a proof-of-concept, and with the appropriate circuit modifications, it is possible to investigate SSPP device characteristics beyond 3 THz. The most salient feature of the presented TSoC CPS-SSPP is the ease of implementation while obtaining THz-band operation. While it is possible to use a VNA along with several extension modules as an alternative, it becomes a costly endeavor which currently cannot exceed 1.5 THz using commercially available extension modules.

Results

Theory of the CPS-SSPP and dispersion characteristics

The analysis and modeling of several SSPP structures have been investigated in prior work[27]. Unfortunately, to our knowledge, no closed-form dispersion relations have been presented for a finite-thickness CPS-SSPP structure. However, if the thickness of the CPS-SSPP conductors were to become infinite, then the CPS-SSPP dispersion relation can be approximated by a 1D array of grooves[5,9]:

$$k_z = k_{eff}\sqrt{1+\left(\frac{a^2}{d^2}\right)\tan^2(k_{eff}H_n)}, \tag{1}$$

where H_n is the length of stubs (i.e. depth of grooves) in the SSPP region (see Fig. 2), $d = a + W_n$ is the period, a is the aperture or the distance between the stubs, W_n is the width of the stubs, $k_{eff} = \omega\sqrt{\varepsilon_{eff}}/c$ is the effective

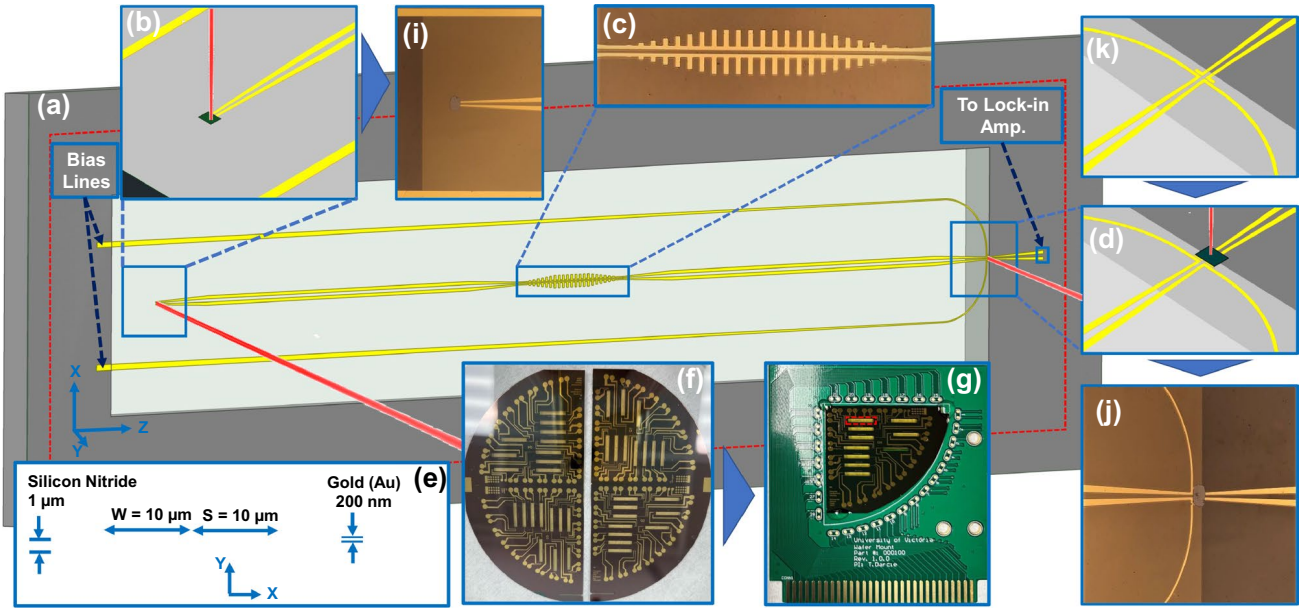

Figure 1. Illustration of CPS-SSPP device and measurement platform. (**a**) The whole structure along with tapered and bias lines on Silicon Nitride membrane. (**b**) Transmitter PCS and incident laser beam. (**c**) Main CPS-SSPP structure. (**d**) Receiver PCS and incident laser beam. (**e**) Dimensions of central reference CPS line and the membrane. (**f**) Fabricated circuits on Wafer. (**g**) Mounted Wafer quarter on PCB to connect to the measurement setup. (**i**) Real transmitter PCS. (**j**) Real receiver PCS. (**k**) Contact point for the receiver PCS on the edge of the membrane.

wavenumber, c is the speed of light, and ε_{eff} is approximated by the effective relative permittivity of the CPS feedlines at THz frequencies. There are empirical models to obtain ε_{eff}[28–30], but we use numerical simulations to overcome the constraints of the empirical boundaries. For the CPS TLs in this work, we find $\varepsilon_{eff} \approx 1.7$ between 0.1 and 1.5 THz using ANSYS HFSS. We note that (1) is not explicitly true for a CPS-SSPP, but it provides a reasonable approximation. The validity of a similar approximation is also found in[9,13].

Investigation of (1) reveals that the CPS-SSPP exhibits low-pass behavior (when $k_{eff}H_n$ is small, then $k_z \approx k_{eff}$). Next, we see that the response of SSPP structures is primarily controlled by H_n. This is observed by considering $k_{eff}H_n \rightarrow \pi/2$ which results in $k_z \rightarrow \infty$. We note that this relates to the asymptotic frequency which is calculated by $f_{AS} = c/(4\sqrt{\varepsilon_{eff}}H_n)$. At frequencies below the band-edge ($k_z d = \pi$), the insertion loss will be minimal. At frequencies above the band edge, a significant insertion loss is expected. Near the band-edge, a resonance occurs which results in large field enhancement inside the CPS-SSPP grooves[15].

Design of the CPS-SSPP structure

This paper complements the CPS-SSPP proposed in[15] and thus our design was influenced by their work. Our primary goal is to demonstrate low-pass behavior for several different CPS-SSPP configurations at THz frequencies. Fortunately, the theory presented in the previous section provides a reasonable estimate of the expected band-edge frequency. As noted, H_n is the main parameter that controls the band-edge frequency. In this work, we fabricate three different CPS-SSPP structures where $H_n = 45\,\mu m$, $85\,\mu m$, and $105\,\mu m$. Inserting these values (1), then numerically solving predicts band-edge frequencies to be 1.04 THz ($H_n = 45\,\mu m$), 0.63 THz ($H_n = 85\,\mu$m), and 0.53 THz ($H_n = 105\,\mu m$). Here, we specified the geometric parameters, and then calculated the frequency response, however, the converse could also have been performed to obtain a desired band-edge frequency. Next, the period of corrugation, d, and aperture, a, should be subwavelength[5,6]. To retain a level of comparability amongst other SSPP literature, we selected to use $d = 50\,\mu m$ and $a = 0.6d = 30\,\mu m$[5,6]. The designer can select $0.1 \leq a/d \leq 0.9$ depending on the desired dispersion characteristics given by (1). For filtering applications where a sharp roll-off is desired, a larger value of a/d is preferred since the dispersion curve approaches the asymptotic frequency more rapidly, however, this will impact the phase response and pulse shape. Also recognize that increasing a/d results in narrow stubs which can result in poor stop-band rejection. Note that a/d does not affect the asymptotic frequency and it has negligible impact on the band-edge frequency based on (1).

The transition circuit (TC) shown in Fig. 2 is required to provide the gradient momentum matching between the CPS feedlines quasi-TEM mode and the SSPP TM mode[13,15]. This concept can be described using (1) and observing two cases: $H_n = 0$ and $H_n \neq 0$. When $H_n = 0$ the CPS-SSPP is equivalent to a typical CPS TL and $k_z/k_{eff} = 1$ suggesting the momentum is matched which results in no reflections. Alternatively, when $H_n \neq 0$, then $k_z/k_{eff} > 1$ which implies a discontinuity in momentum which results in mode conversion. The gradual introduction of the CPS-SSPP stubs (i.e., the TC) reduces the discontinuity and improves the mode conversion efficiency. Supplementary Material (S1) illustrates the impact of negating the TC on the transmission. The CPS feedline dimensions were selected to be $S = W = 10\,\mu m$ to ensure the SSPP dimensions could remain on a sub-wavelength scale. Table 1 tabulates the dimensions for the TC and CPS-SSPP. The number of SSPP stubs is $N = 9$, although it can be higher with no significant impact on the frequency response[15].

This work performs the verification of SSPP behavior using our TSoC platform. Regarding the CPS-SSPP, key design considerations are TSoC material and geometric parameters. The TSoC uses 1 μm thick Si_3N_4 membrane substrate to minimize loss and dispersion of the feedlines required to drive the CPS-SSPP[26]. The conductors are 210 nm (10 nm Ti, 200 nm Au) and are defined by photolithography. The transmitter and receiver are thin-film

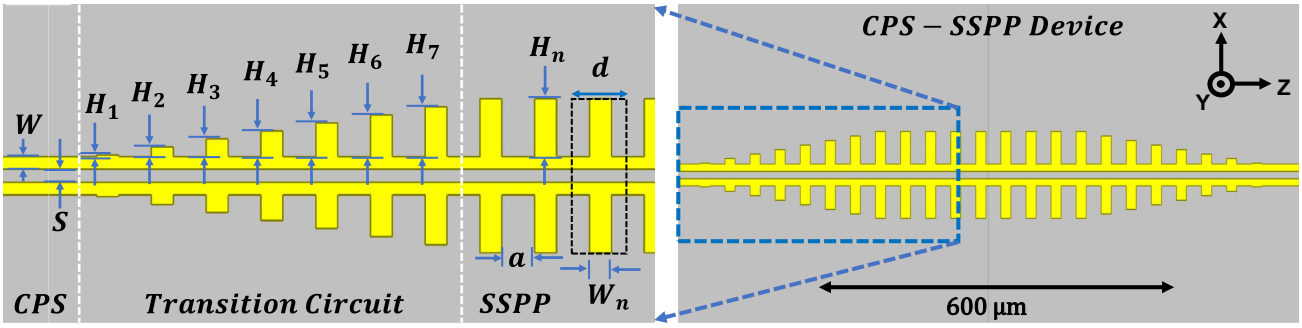

Figure 2. Transition circuit (TC) connected to the CPS-SSPP structure. $W_n = 20\,\mu m$, $a = 30\,\mu m$, $W = 10\,\mu m$, and $S = 10\,\mu m$. See Table 1 for stub height dimensions.

H_n	H_1	H_2	H_3	H_4	H_5	H_6	H_7
45	1	8	14	20	26	33	39
85	6	18	29	40	51	63	74
105	9	23	36	50	64	78	91

Table 1. Stub lengths for the TC (units: μm).

photo-conductive switches (PCSs) made from LT-GaAs. The average optical power on the transmitter is 7 mW, and the average optical power on the receiver is 14 mW. More details are provided in the Fabrication section.

Eigenmode and frequency domain simulations

To complement the theory and experiment we use ANSYS HFSS to perform eigenmode and frequency-domain (FD) full-wave simulations of the CPS-SSPP structures. In all simulations we aim to replicate the real devices, thus we model the Si_3N_4 substrate as 1 μm thick and $\varepsilon_r = 7.6$, $\sigma_{Si_3N_4} = 0$, and $\tan\delta_e = 0.00526$[31]. The gold thickness is 200 nm and the conductivity is $\sigma_{Au} = 4.1 \times 10^7$ S/m. All simulations use $d = 50$ μm, $W_n = 20$ μm, $S = 10$ μm, and $W = 10$ μm. The stub dimensions are found in Table 1.

We use the eigenmode simulation to obtain the dispersion diagram and band-edge frequencies for the CPS-SSPP unit cells. Figure 3 plots the simulated dispersion relation (solid lines) for the three CPS-SSPP structures investigated in this work. It is possible to use (1) for this purpose (dashed lines), but we reiterate that (1) was derived for a 1D array of grooves, thus caution is required. Regardless, for each case, we see asymptotic behavior which is characteristic of SSPPs. The simulated band-edges were found to be: 1.04 THz ($H_n = 45$ μm), 0.63 THz ($H_n = 85$ μm), and 0.53 THz ($H_n = 105$ μm) which are in close agreement with values previously obtained from (1).

We perform FD simulations for several purposes. First, we investigate the transmission through the fabricated CPS-SSPP structures where $H_n = 45$, 85, and 105 μm. Figure 4 plots the results of these simulations. Low-pass behavior is clearly observed and the cut-off frequency aligns with the predicted band-edge frequencies. Next, we use FD simulations for illustrative purposes. Figure 5 shows the electric field at frequencies below cut-off (0.8 THz), near cut-off (1.0 THz), and above cut-off (1.2 THz). As expected, near cut-off, a large localized field is

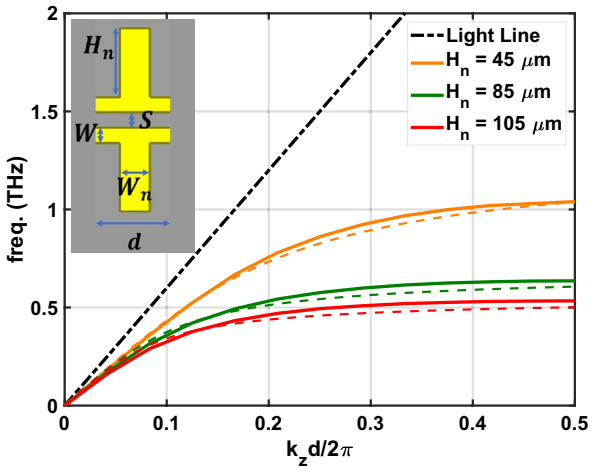

Figure 3. Dispersion curves obtained by eigenmode simulation (solid lines) and theory (dashed lines) on the CPS-SSPP unit cell (inset). H_n is variable as shown in the legend and fixed dimensions are $d = 50$ μm, $W_n = 20$ μm, and $S = 10$ μm.

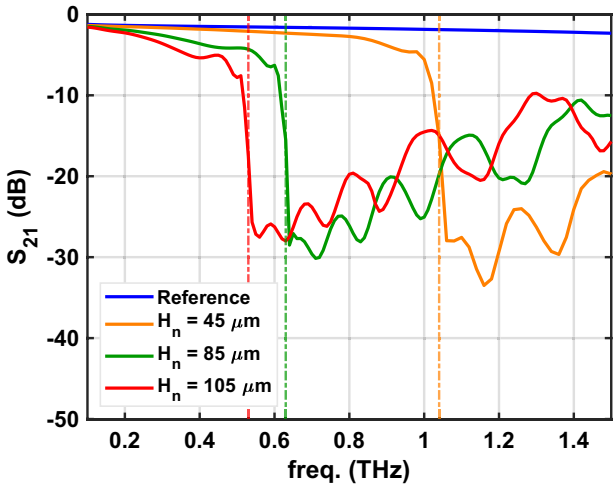

Figure 4. CPS-SSPP S_{21} (dB) from FEM simulation results for the structures which were experimentally tested. The vertical dashed lines indicate the simulated band-edge frequencies.

observed in the SSPP grooves. Lastly, Supplementary Material (S2) presents the impact of using another substrate for literary comparison with[15] and demonstrates the impact on the band-edge frequency.

Measurement results of the CPS-SSPP

The experimental results for the CPS-SSPP are displayed in Fig. 6 alongside a reference without stubs (i.e., $H_n = 0$). We note a discrepancy between the experimental results (Fig. 6) and simulated results (Fig. 4) which originates from different incident signals. For the experiment, the incident signal is a sub-picosecond time-domain pulse which has an inherent roll-off whose spectral response resembles the Reference signal in Fig. 6. To estimate the experimental signal transmission, it is necessary to take the difference between the respective signal (H_n = 45, 85, or 105 µm) and the common reference measurement. Alternatively, for the frequency-domain simulation (Fig. 4), the incident signal is frequency-independent and well-known thus the simulation

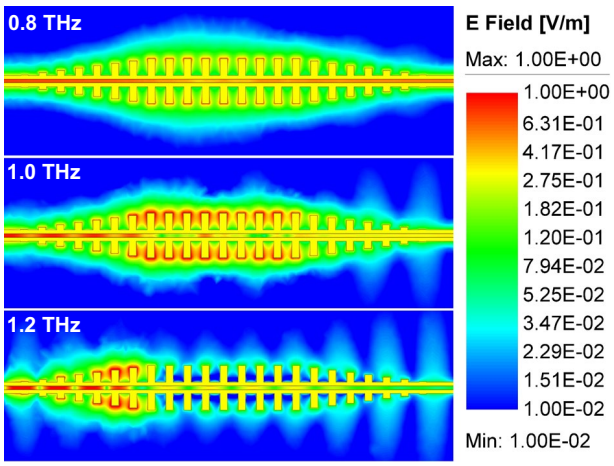

Figure 5. Field plots of CPS-SSPP at different frequencies on the structure with H_n = 45 µm. (**a**) 0.8 THz, on pass band. (**b**) 1.0 THz on the pass band, below the band-edge frequency, with maximized field confinement in the grooves. (**c**) 1.2 THz, on stop band. (The color scale is logarithmic and normalized between 0.01 and 1.00).

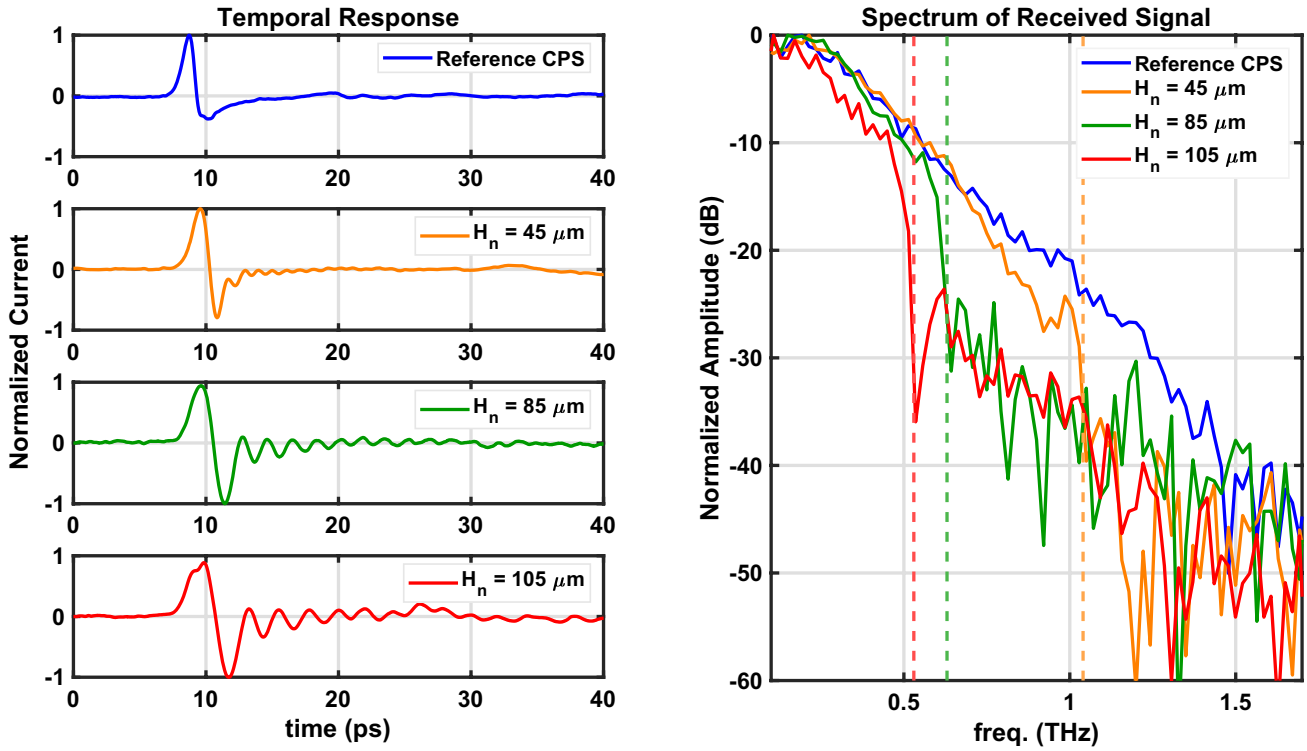

Figure 6. Measurement results for structures with different stub lengths. The time-domain results are obtained from the lock-in amplifier, the spectral response is obtained by applying the Discrete Fourier Transform of the temporal response. The vertical dashed lines indicate the simulated band-edge frequencies.

directly outputs the transmission. The vertical dashed lines in Fig. 6 indicate the simulated band-edge frequencies which align the transmission cut-off as predicted in Fig. 4. We see that as the stub length increases the cut-off frequency reduces as predicted by (1). Figure 7 plots the band-edge frequency versus H_n using simulation, theory, and experiment where reasonable agreement is observed. Next, the roll-off rate associated with the band-edge frequencies is significant and is on the order of ≈ -160 dB/Octave. As a consequence of the steep roll-off (and non-linear phase response), we see oscillations in the temporal response which are the most significant for the H_n = 105 μm structure. Thus, if the CPS-SSPP structures are to be used as low-pass filters, then it is important to consider the applications' phase response requirements.

The results presented in Fig. 6 validate the CPS-SSPP structure proposed in[15] at THz frequencies. Also, to the authors' knowledge, this work presents the first demonstration of the SSPP phenomenon using a thin Si_3N_4 substrate which enables measurements at THz frequencies. There are many opportunities for optimizing CPS-SSPP devices for novel sensing, filtering, and waveguiding applications which we hope to explore in the future.

Conclusion

This paper presented the experimental verification of several CPS-SSPP structures at THz frequencies using our TSoC platform. Specifically, we fabricated three CPS-SSPP devices on a thin Si_3N_4 membrane and observed agreement of the band-edge frequencies when H_n = 45 μm (1.04 THz), H_n = 85 μm (0.63 THz), and H_n = 105 μm (0.53 THz). This experimental verification will enable others to investigate a multitude of other novel guided-wave SSPP structures for a range of applications at THz frequencies. As previously noted, the majority of SSPP literature focuses on simulation or GHz scaling for verification. At GHz frequencies, the ability to investigate the vibrational resonances of molecules is limited, and thus a primary sensing application (i.e. THz spectroscopy) is not viable. The methods used in this paper require no device (or frequency) scaling and thus provide a clear path toward integrated SSPP sensors.

Regarding novelty, to the authors' knowledge, this work demonstrates the first experimental results that confirm SSPP behavior beyond 1 THz using guided wave feedlines for excitation. This capability is possible because the TSoC platform uses an ultra-thin (1 μm) Si_3N_4 substrate to significantly reduce radiation losses and dispersion (novel for SSPP devices). Lastly, this is the first work to experimentally characterize several different band-edge frequencies within the THz gap which enables the validation of simulation and theoretical models.

Methods

Fabrication

The fabrication of the SSPP structures was performed on a Silicon wafer with 1 μm Silicon Nitride coated layer and selectively etched the Silicon from the structure areas to make the thin membrane as illustrated in Fig. 1.

The fabrication of photo-conductive switches (PCSs) and the measurement process are presented in this section. PCSs are used for THz signal generation and detection. These components were fabricated using a multi-step process involving photolithography, gold (Au) sputtering, and wet-etching. The process is detailed in other works[32], but we summarize it here for completeness. The desired LT-GaAs layer is grown on a sacrificial AlAs layer on a semi-insulating GaAs substrate. The LT-GaAs surface is patterned with Au contacts using standard photolithography. Afterward, each PCS region is masked and wet-etched using Citric Acid and Hydrogen Peroxide (this defines the PCS thickness). Next, the surface is cleaned and re-masked with an etch-resist wax and then submerged in hydrofluoric acid (HF) to detach the LT-GaAs layer by dissolving the AlAs layer. Next, the LT-GaAs film is re-submerged in Citric Acid and Hydrogen Peroxide to disconnect the remaining LT-GaAs film which interconnects a grid of PCSs. Lastly, the etch-resistant wax is removed using trichloroethylene (TCE), resulting in thousands of LT-GaAs PCS active regions. Subsequently, two PCS active regions (transmitter and

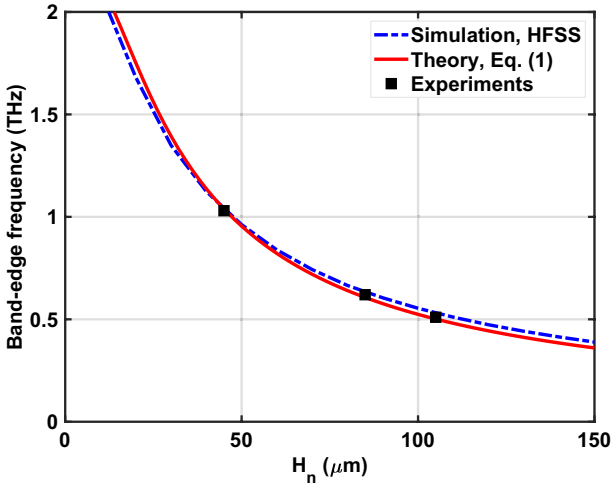

Figure 7. Band-edge frequency versus H_n obtained from eigenmode simulations, theoretical dispersion relation, and experiment.

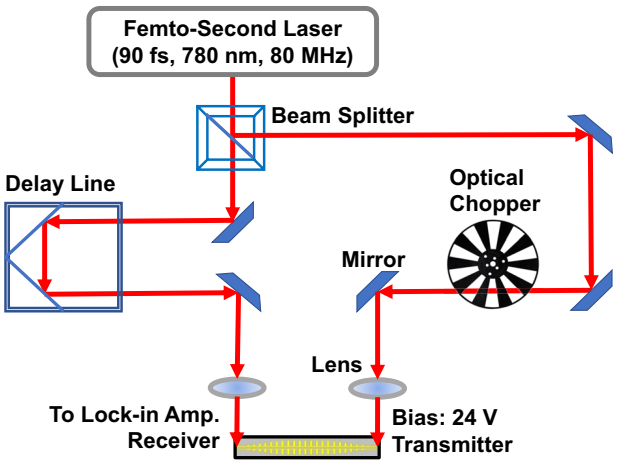

Figure 8. The modified THz time domain spectroscopy setup for performing measurements on THz circuits with photo-conductive switches.

receiver) were bonded to the TSoC using the Van der Waals (VDW) technique, as explained in[33]. The dimensions of the fabricated PCS are 70 μm × 40 μm × 1.8 μm, with 5 μm gap between the metal contacts. The placement of the PCS devices on the structure was performed using a modified probe station. Next, a droplet of water was placed on the PCSs to make robust contact with Van-der-Waals forces. Subsequently, the wafer was mounted on the modified THz-TDS setup to measure the dark current at the ports and then aligned the device position to focus the laser beam on the PCS and achieve the maximum photo-current. Afterward, the THz pulse traveled through the waveguide, and the received signal was measured using a lock-in amplifier. We estimate the optical-to-THz average power conversion efficiency based on the study in[34]. The conversion efficiency of the transmitter PCS considering 24 V bias voltage, 40 μm width of the device, and 7 mW of optical power to be approximately 0.006% which corresponds to a maximum average THz power of 0.42 μW delivered to the CPS TL and subsequent CPS-SSPP.

Measurement

After fabrication of the PCS devices and the CPS-SSPP structures, measurements were performed using the modified THz Time-domain Spectroscopy (THz-TDS) setup depicted in Fig. 8. The experiment involved utilizing a femtosecond pulsed laser with a wavelength of 780 nm focused on PCSs placed on the waveguide to generate and detect a broadband THz pulse signal. The transmitted signal was reconstructed by translating the mechanical delay line measuring the receiver current using a lock-in amplifier (alike THz-TDS)[26,35]. The fluctuations in the measurement are the result of uncorrelated system noise sources (laser, electric, environmental, etc.). A straightforward method to reduce these fluctuations is to perform spectral averaging by measuring each device many times. We note that we did not perform any spectral averaging in this work.

Data availability

All data generated or analyzed during this study are included in this published article and its supplementary information files.

Received: 18 July 2023; Accepted: 21 December 2023
Published online: 02 January 2024

References

1. Song, H.-J. & Lee, N. Terahertz communications: Challenges in the next decade. *IEEE Trans. Terahertz Sci. Technol.* **12**, 105–117 (2022).
2. Hillger, P., Grzyb, J., Jain, R. & Pfeiffer, U. R. Terahertz imaging and sensing applications with silicon-based technologies. *IEEE Trans. Terahertz Sci. Technol.* **9**, 1–19 (2019).
3. Tang, W. X., Zhang, H. C., Ma, H. F., Jiang, W. X. & Cui, T. J. Concept, theory, design, and applications of spoof surface plasmon polaritons at microwave frequencies. *Adv. Opt. Mater.* **7**, 1800421 (2019).
4. Pendry, J. B., Martín-Moreno, L. & Garcia-Vidal, F. J. Mimicking surface plasmons with structured surfaces. *Science* **305**, 847–848 (2004).
5. Garcia-Vidal, F. J., Martín-Moreno, L. & Pendry, J. B. Surfaces with holes in them: New plasmonic metamaterials. *J. Opt. A: Pure Appl. Opt.* **7**, S97 (2005).
6. Maier, S. A., Andrews, S. R., Martín-Moreno, L. & García-Vidal, F. J. Terahertz surface plasmon-polariton propagation and focusing on periodically corrugated metal wires. *Phys. Rev. Lett.* **97**, 176805 (2006).
7. Singh, S. P., Tiwari, N. K. & Akhtar, M. J. Spoof surface plasmon-based coplanar waveguide sensor for dielectric sensing applications. *IEEE Sens. J.* **20**, 193–201 (2020).
8. Unutmaz, M. A., Ozsahin, G. & Unlu, M. Optimization of terahertz spoof surface plasmon polariton waveguides for maximum ° /db performance. *J. Lightw. Technol.* **39**, 5508–5515 (2021).
9. Shen, X., Cui, T. J., Martin-Cano, D. & Garcia-Vidal, F. J. Conformal surface plasmons propagating on ultrathin and flexible films. *Proc. Natl. Acad. Sci.* **110**, 40–45 (2013).
10. Akalin, T., Treizebre, A. & Bocquet, B. Single-wire transmission lines at terahertz frequencies. *IEEE Trans. Microw. Theory Tech.* **54**, 2762–2767 (2006).

11. Astley, V., Scheiman, J., Mendis, R. & Mittleman, D. M. Bending and coupling losses in terahertz wire waveguides. *Opt. Lett.* **35**, 553–555 (2010).
12. Unutmaz, M. A. & Unlu, M. Terahertz spoof surface plasmon polariton waveguides: A comprehensive model with experimental verification. *Sci. Rep.* **9**, 7616 (2019).
13. Ma, H. F., Shen, X., Cheng, Q., Jiang, W. X. & Cui, T. J. Broadband and high-efficiency conversion from guided waves to spoof surface plasmon polaritons. *Laser Photon. Rev.* **8**, 146–151 (2014).
14. Cinar, Y., Yildirim, S., Ozsahin, G., Unutmaz, M. & Unlu, M. Modelling terahertz spoof surface plasmon polariton waveguides using a circuit model. *IEEE Trans. Terahertz Sci. Technol.* **11**, 557–565 (2021).
15. Guo, Y. J., Da Xu, K. & Tang, X. Spoof plasmonic waveguide developed from coplanar stripline for strongly confined terahertz propagation and its application in microwave filters. *Opt. Express* **26**, 10589 (2018).
16. Xu, K.-D., Guo, Y. J. & Deng, X. Terahertz broadband spoof surface plasmon polaritons using high-order mode developed from ultra-compact split-ring grooves. *Opt. Express* **27**, 4354 (2019).
17. Xu, K.-D., Zhang, F., Guo, Y., Ye, L. & Liu, Y. Spoof surface plasmon polaritons based on balanced coplanar stripline waveguides. *IEEE Photon. Technol. Lett.* **32**, 55–58 (2020).
18. Kianinejad, A., Chen, Z. N. & Qiu, C.-W. Design and modeling of spoof surface plasmon modes-based microwave slow-wave transmission line. *IEEE Trans. Microw. Theory Tech.* **63**, 1817–1825 (2015).
19. Cao, D., Li, Y. & Wang, J. Wideband compact slotline-to-spoof-surface plasmon-polaritons transition for millimeter waves. *IEEE Antennas Wirel. Propag. Lett.* **16**, 3143–3146 (2017).
20. Unutmaz, M. A., Ozsahin, G., Abacilar, T. & Unlu, M. Investigation of the transitions for coplanar waveguide to terahertz spoof surface plasmon polariton waveguides. *IEEE Trans. Antennas Propag.* **70**, 3002–3010 (2022).
21. Jepsen, P., Cooke, D. & Koch, M. Terahertz spectroscopy and imaging—modern techniques and applications. *Laser Photon. Rev.* **5**, 124–166 (2011).
22. Jaiswal, R. K., Pandit, N. & Pathak, N. P. Spoof surface plasmon polaritons based reconfigurable band-pass filter. *IEEE Photon. Technol. Lett.* **31**, 218–221 (2019).
23. Liang, Y. *et al.* On-chip sub-terahertz surface plasmon polariton transmission lines with mode converter in cmos. *Sci. Rep.* **6**, 30063 (2016).
24. Haghighat, M., Darcie, T. & Smith, L. *Terahertz CPS-based Spoof Surface Plasmon Polariton Filter on Silicon Nitride Substrate, 48th IRMMW-THz* (Montreal, Canada, 2023).
25. Williams, C. R. *et al.* Highly confined guiding of terahertz surface plasmon polaritons on structured metal surfaces. *Nat. Photon.* **2**, 175–179 (2008).
26. Smith, L. & Darcie, T. Demonstration of a low-distortion terahertz system-on-chip using a cps waveguide on a thin membrane substrate. *Opt. Express* **27**, 13653–13663 (2019).
27. Huidobro, P. A., Fernández-Domínguez, A. I., Pendry, J. B., Martín-Moreno, L. & Garcia-Vidal, F. J. *Spoof Surface Plasmon Metamaterials. Elements in Emerging Theories and Technologies in Metamaterials* (Cambridge University Press, 2018).
28. Bahl, I., Bozzi, M. & Garg, R. *Microstrip Lines and Slotlines* 3rd edn. (Artech House, 2013).
29. Knox, W. *et al.* Femtosecond excitonic optoelectronics. *IEEE J. Quantum Electron.* **25**, 2586–2595 (1989).
30. Hasnain, G., Dienes, A. & Whinnery, J. Dispersion of picosecond pulses in coplanar transmission lines. *IEEE Trans. Microw. Theory Tech.* **34**, 738–741 (1986).
31. Cataldo, G. *et al.* Infrared dielectric properties of low-stress silicon nitride. *Opt. Lett.* **37**, 4200–4202 (2012).
32. Ríos, R. D. V., Bikorimana, S., Ummy, M. A., Dorsinville, R. & Seo, S.-W. A bow-tie photoconductive antenna using a low-temperature-grown gaas thin-film on a silicon substrate for terahertz wave generation and detection. *J. Opt.* **17**, 125802 (2015).
33. Yablonovitch, E., Hwang, D. M., Gmitter, T. J., Florez, L. T. & Van der Harbison, J. P. Waals bonding of GaAs epitaxial liftoff films onto arbitrary substrates. *Appl. Phys. Lett.* **56**, 2419–2421 (1990).
34. Khiabani, N., Huang, Y., Shen, Y.-C. & Boyes, S. Theoretical modeling of a photoconductive antenna in a terahertz pulsed system. *IEEE Trans. Antennas Propag.* **61**, 1538–1546 (2013).
35. Gomaa, W., Smith, L., Shiran, V. & Darcie, T. Terahertz low-pass filter based on cascaded resonators formed by CPS bending on a thin membrane. *Opt. Express* **28**, 31967 (2020).

Acknowledgements

This work was supported by an NSERC Discovery Grant (Natural Sciences and Engineering Research Council of Canada, RGPIN-2022-03277). The authors would like to thank 4D LABS at Simon Fraser University for the fabrication of the SSPP structures and also the Centre for Advanced Materials and Related Technology (CAMTEC) at the University of Victoria for providing Nanofab facilities for the fabrication of PCS devices.

Author contributions

M.H. conducted simulations, fabricated PCS devices, performed the experiments, and prepared an early draft of the manuscript. T.D. provided guidance and advice on the concept and writing. L.S. analyzed the results, offered insights on the theory, fabrication, and experiments, and revised the writing. All authors have reviewed the manuscript.

Competing interests

The authors declare no competing interests.

Additional information

Supplementary Information The online version contains supplementary material available at https://doi.org/10.1038/s41598-023-50599-y.

Correspondence and requests for materials should be addressed to L.S.

Appendix B

Demonstration of Terahertz Spoof Surface Plasmon Polariton Waveguides using Coplanar Striplines with Internal Corrugations, Copy of [2]

Research Article Vol. 32, No. 27 / 30 Dec 2024 / Optics Express 48803
Optics EXPRESS

Demonstration of terahertz spoof surface plasmon polariton waveguides using coplanar striplines with internal corrugations

MOHSEN HAGHIGHAT,[1,2] ALI DEHGHANIAN,[1,2] THOMAS DARCIE,[1] AND LEVI SMITH[1,2,*]

[1] Department of Electrical and Computer Engineering, University of Victoria, Victoria, British Columbia V8P 5C2, Canada
[2] Centre for Advanced Materials and Related Technology (CAMTEC), University of Victoria, Victoria, British Columbia V8W 2Y2, Canada
[*] levismith@uvic.ca

Abstract: This paper presents the design and experimental verification of a terahertz (THz) spoof surface plasmon polariton (SSPP) waveguide using a coplanar stripline (CPS) with internal corrugations and is compared against an external corrugation configuration. Internal corrugations are selected to reduce the insertion loss by improving the mode conversion efficiency of the transition circuit. We examine this effect using simulation and then experimentally confirm that the SSPP mode was excited for two different corrugation depths, 55 µm, and 65 µm. We found that the associated SSPP band-edge frequency changed from 0.89 THz to 0.72 THz which is consistent with the simulations.

1. Introduction

Spoof Surface Plasmon Polariton (SSPP) waves have attracted significant research interest due to their unique capabilities derived from traditional Surface Plasmon Polaritons (SPP). SPPs are known for their ability to confine electromagnetic fields at subwavelength scales, a property that is desirable for applications in sensing, imaging, and communication technologies [1,2]. Structures that support SSPPs are created by engineering a guiding conductor's geometry to include corrugations to obtain propagation characteristics that mimic SPPs but at lower frequencies (i.e., GHz and THz). Early studies by Pendry et al. (2004) [3] and Garcia-Vidal et al. (2005) [4] laid the groundwork by mimicking the behavior of SPPs at microwave frequencies using structured surfaces. Subsequent research has expanded on these concepts, exploring planar SSPP devices [5–7]. On-chip excitation of planar SSPP-waveguides require the integration with conventional waveguides such as a coplanar waveguide (CPW) or coplanar stripline (CPS). The most common method is integration with CPW [6,8–10] which requires flared ground planes to achieve mode conversion that can result in elevated insertion losses [10]. Another method involves the integration of SSPP with CPS to avoid flaring grounds where the CPS conductors are used to guide the SSPP field [7,11–14].

In the aforementioned literature, there are several common SSPP unit cells that form the sub-wavelength grating needed for SSPP functionality. We review the most common unit cells that are integrated with planar guided wave systems at THz frequencies (0.3 – 10 THz). The terminology used to describe the various SSPP unit cells is not standardized, thus, for clarity, we illustrate each common unit cell in Table 1. The majority of literature examining SSPPs at THz frequencies are simulated studies and experimental verification is performed by scaling the device into the microwave region so that standard vector network analyzers (VNAs) can be used to characterize the SSPP scattering parameters. For these experiments, it is most common to use Unit Cells 'C' and 'D' (Table 1). The devices in this work are designed to operate at THz

#542756 https://doi.org/10.1364/OE.542756
Journal © 2024 Received 20 Sep 2024; revised 23 Nov 2024; accepted 1 Dec 2024; published 23 Dec 2024

Optics EXPRESS

frequencies as a proof-of-concept which could be used for material sensing applications. We forgo the use of a VNA when characterizing devices at THz frequencies. The optoelectronic method discussed in Section 3 is capable of broadband characterization up-to 2 THz without the need of multiple extension modules and the THz source and detector are directly coupled to the transmission lines.

Table 1. Unit cell illustrations

A (this work)	B [7]	C [6]	D [5]
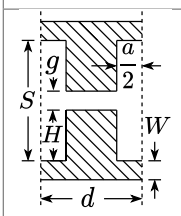	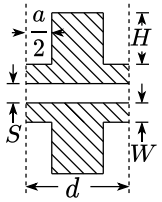	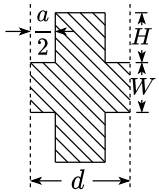	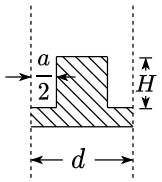

A key issue for characterizing devices at THz frequencies is selecting an appropriate feedline with low loss and dispersion. Typical feedlines used at GHz frequencies are not suitable at THz frequencies because of large substrate radiation losses and dispersion [15]. A proven method to overcome this issue is to use an ultra-thin (1 μm) Si_3N_4 substrate to support a transmission line or waveguide so that the majority of the field is in the surrounding air [15,16]. When the transmitter and receiver are photoconductive switches (PCSs), as in this work, a CPS is an appropriate feedline because it is compatible with the sliding contact excitation and detection methods [17]. Unit Cell 'B' was proposed in [7] and is compatible with CPS feedlines; however, like other THz-SSPP studies, experimental validation at THz frequencies was not reported. In [13,14], we performed the first validation of a CPS-SSPP at THz frequencies and observed the low-pass filtering characteristics which supported simulation results [7,12]. This work, compared with our previous work in [13], uses similar experimental methodology, but proposes a novel unit cell, Unit Cell 'A' compared to Unit Cell 'B' with the goal of improving the insertion loss and mode conversion efficiency.

All of the unit cells illustrated in Table 1 are capable of supporting an SSPP transverse magnetic (TM) mode. The choice of the unit cell depends on integration practicality and the desired application. However, in all cases, it is desirable to reduce the passband insertion loss. Unit Cell 'A' and 'B' are both driven by a CPS feedline, but they have a different attenuation coefficients. The relationship between CPS geometry and loss has been studied in the prior work and it was found that larger values of S generally result in lower attenuation [16]. Thus, it is expected that Unit Cell 'A' should exhibit a lower insertion loss – this will be quantified in Section 2. Also, a transition circuit (TC) is required at the interface between the feedline and SSPP to excite the SSPP TM mode. For all unit cells this is achieved by gradually increasing (or decreasing) the length of the corrugations, H, along the propagation direction [7,10]. The transverse field profiles of feedlines that drive Unit Cell 'A' and 'B' are similar, but not identical. We investigate the difference in mode conversion efficiency of internal corrugations (Unit Cell 'A') and external corrugations (Unit Cell 'B') via simulation. The motivation of this manuscript is to compare the insertion loss between the CPS-driven Unit Cells 'A' and 'B'. We find that Unit Cell 'A' has a lower insertion loss due to the lower CPS attenuation coefficient and the improved mode conversation efficiency.

2. Design and simulations

This work investigates the viability of Unit Cell 'A' to function as an SSPP waveguide that could be used as a low-pass filter or material sensor at THz frequencies. As mentioned, the motivation

Optics EXPRESS

to select Unit Cell 'A' (as opposed to Unit Cell 'B') is to reduce the overall insertion loss by using low-loss feedlines which also exhibit improved CPS-to-SSPP mode conversion efficiency.

The design procedure is supported by the use of full-wave simulations using ANSYS HFSS 2023. We aim to replicate the real devices in the simulations, including a 1 μm thick Si_3N_4 membrane where $\varepsilon_r = 7.6$, $\sigma_{Si_3N_4} = 0$, and $\tan \delta_e = 0.00526$ [18]. The gold conductors have a thickness of 200 nm and conductivity of $\sigma_{Au} = 4.1 \times 10^7$ S/m.

First, we investigate the CPS feedlines without corrugations. The CPS feedlines and the 1 μm thick Si_3N_4 membrane are suspended over the air to reduce the radiation loss into the substrate [16]. To characterize the impact of the CPS conductor separation, S, on the attenuation coefficient we perform a simulation to obtain the attenuation coefficient in dB/mm. The results are plotted in Fig. 1. We select the feedline width to be $W = 30$ μm which provides acceptable ohmic losses [16]. Figure 1 illustrates that the feedline attenuation decreases as S increases. This relationship partially motivates this study by illustrating that the CPS feedline of Unit Cell 'A' (large S) will generally exhibit lower attenuation than Unit Cell 'B' (small S). Next, for Unit Cell 'A', H is limited to be less than $S/2$. This implies that the feedline geometry impacts the viable cut-off frequency range. Fortunately, this constraint does not have a large effect on reasonable CPS configurations that exhibit low loss and dispersion at THz frequencies. Thus, we select $S = 140$ μm which limits $H < 70$ μm. We investigate the impact of varying g on the band-edge frequency in Appendix A.

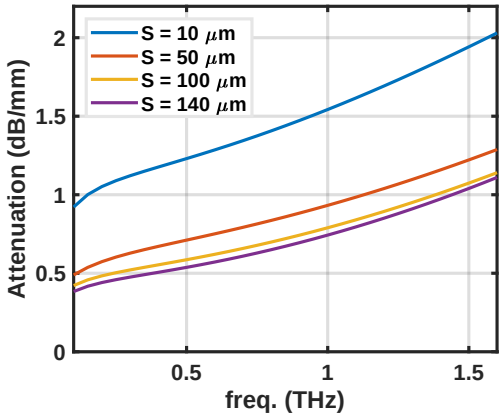

Fig. 1. Loss of the CPS transmission lines with different S values (distance between conductor strips) from 10 μm to 140 μm and fixed strip width, $W = 30$ μm

Figure 2 illustrates the structures used in the experiment. The SSPP waveguide consists of a periodic array of Unit Cell 'A'. A TC which consists of increasing/decreasing stub heights, H_{1-6}, is placed between the feedline and SSPP waveguide to introduce a gradual change in momentum which excites the SSPP TM mode. The final stub height, H, is selected to achieve the desired band-edge frequency. The grating period, d, and aperture, a, were selected to be sub-wavelength and comparable with previous work: $d = 50$ μm and $a = 30$ μm [13]. We clarify that d (and a) do not have a large impact on the band-edge frequency presuming $d \ll \lambda$ [4,19]. As reported in [13], a characteristic of an SSPP waveguide is low-pass behavior where the cut-off frequency in spectral response is given by the band-edge frequency in dispersion curves [13]. We note that analyzing a SSPP like a periodic filter (or Bragg grating) with alternating characteristic impedances can result in incorrect results due to the different field profiles. Also, while lumped-element models can be used to model the passband characteristics of an SSPP waveguide over a narrow bandwidth [9], this work uses full-wave simulations as we have found it to accurately align with experiments over large bandwidths [13].

Optics EXPRESS

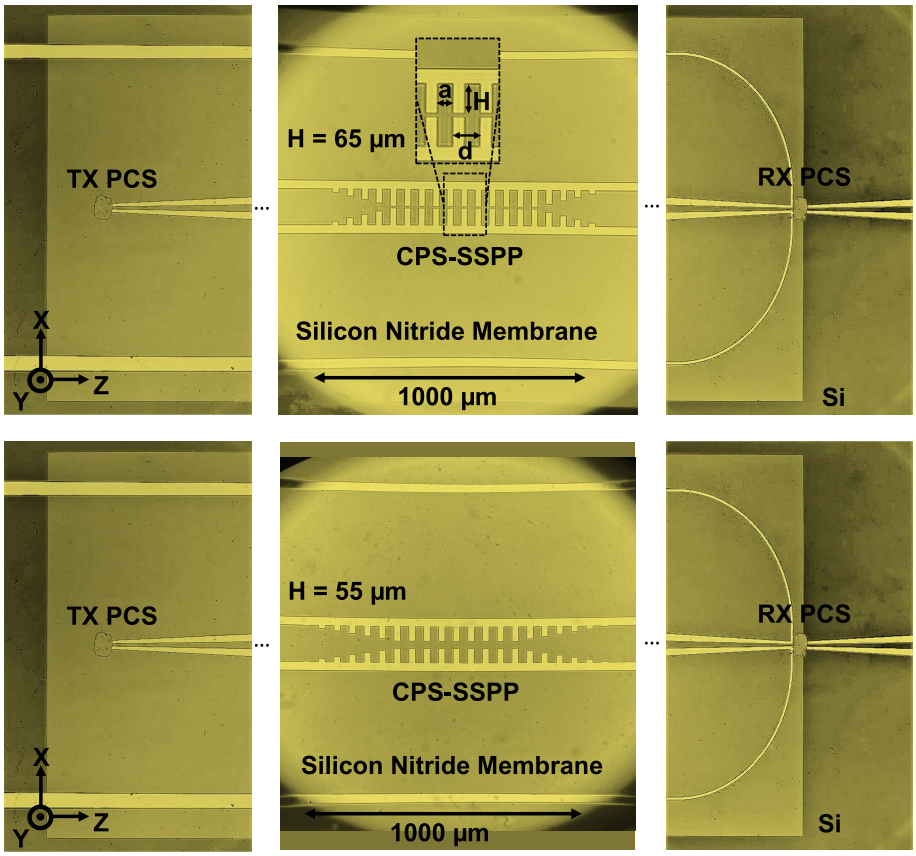

Fig. 2. Illustration of the fabricated devices with the transmitter and receiver sections. The values of stubs are shown in Table 2.

Table 2. Stub lengths for the TC in the fabricated structures (see Fig. 2) (Units: μm)

H	H_1	H_2	H_3	H_4	H_5	H_6
55	1	10	19	28	37	46
65	5	15	25	35	45	55

We experimentally investigate two Unit Cell 'A' SSPP structures with different cut-off frequencies specified by the stub height, H (see Fig. 2). An eigenmode simulation was performed to accurately determine the band-edge frequency (where $k_z d = \pi$) from the dispersion diagram (see Fig. 3(a)) which results in cut-off frequencies of 0.72 THz (for H = 65 μm) and 0.89 THz (for H = 55 μm). Also, the SSPP TM mode exhibits dispersion which is plotted as a frequency-dependent effective relative permittivity in Fig. 3(b) where it is observed that higher frequencies exhibit slow-wave propagation [20]. Figure 4 plots the S-parameters for the two configurations which illustrates a sharp reduction in transmission above the band-edge frequencies which aligns with the eigenmode simulation results. For illustrative purposes, Fig. 5 plots the magnitude of the electric field around the cut-off frequency for the structure with H = 65 μm. We note that if a thicker substrate was used (such as 20 μm polyimide [7]), then the increased

Optics EXPRESS

dielectric loading would result in a reduced band-edge frequency (Supplementary Information [13]). We also simulate the impact of varying the substrate thickness in Appendix B.

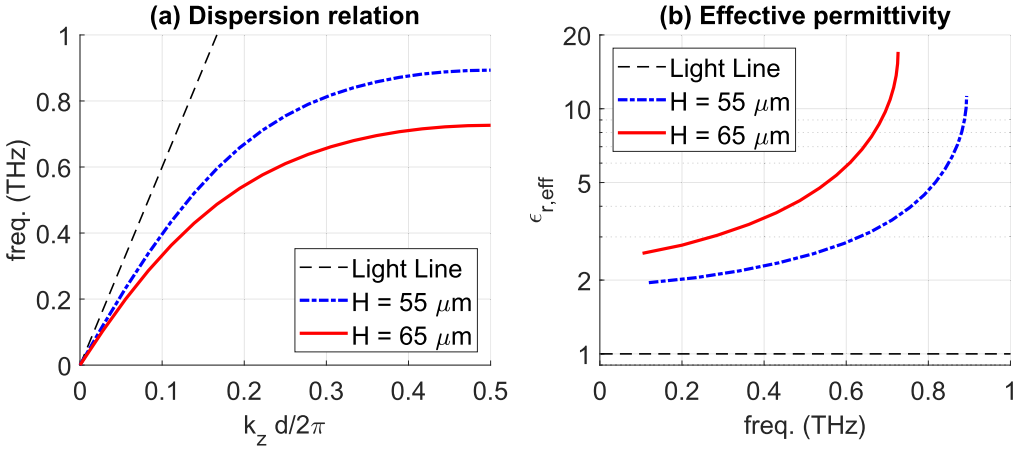

Fig. 3. (a) Dispersion curves of the SSPP structures with internal corrugations (Unit Cell 'A') obtained from eigenmode simulation, for H = 55 µm and H = 65 µm selected for experimental validation. (b) The effective relative permittivity for the SSPP modes.

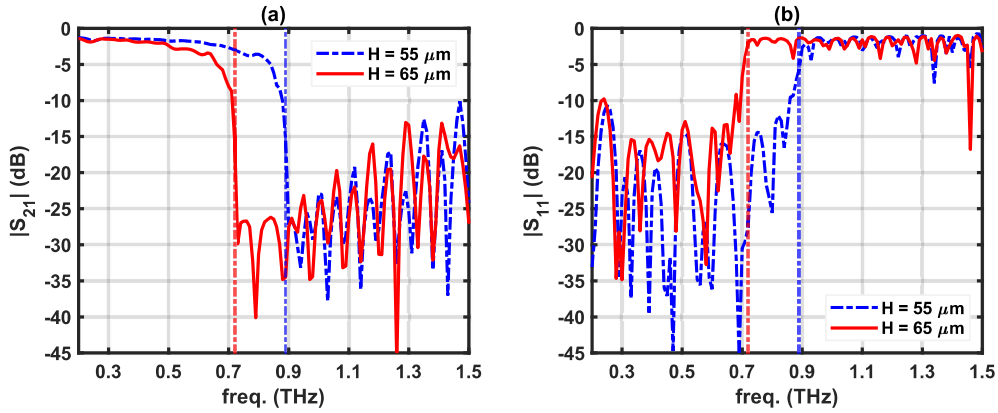

Fig. 4. Frequency response of the proposed structure (including feedline tapering) with different stub lengths: (a) $|S_{21}|$ (dB) and (b) $|S_{11}|$ (dB) for H = 55 µm and H = 65 µm.

2.1. *Unit cell comparison*

We now compare Unit Cell 'A' and Unit Cell 'B' via simulation. The two structures are illustrated in Fig. 6. We investigate the differences between the two structures by comparing their low-pass filtering performance. The number of CPS-SSPP stubs, N, impacts the maximum signal rejection above the cut-off frequency, but when N>9 there is only moderate improvements [7], thus we select N = 9. The number of TC stubs, M, is of primary interest in this study. If a structure exhibits better low-pass filtering characteristics for a lower values of M then that configuration has superior mode conversion efficiency. We note that the values for M = 2 and N = 3 in Fig. 6 were only selected as an example for illustrative clarity.

As mentioned, the TC is required to convert the quasi-TEM mode in CPS to SSPP TM mode [10,13]. This is achieved by gradually tapering the stub height. Here, we compare the mode

Optics EXPRESS

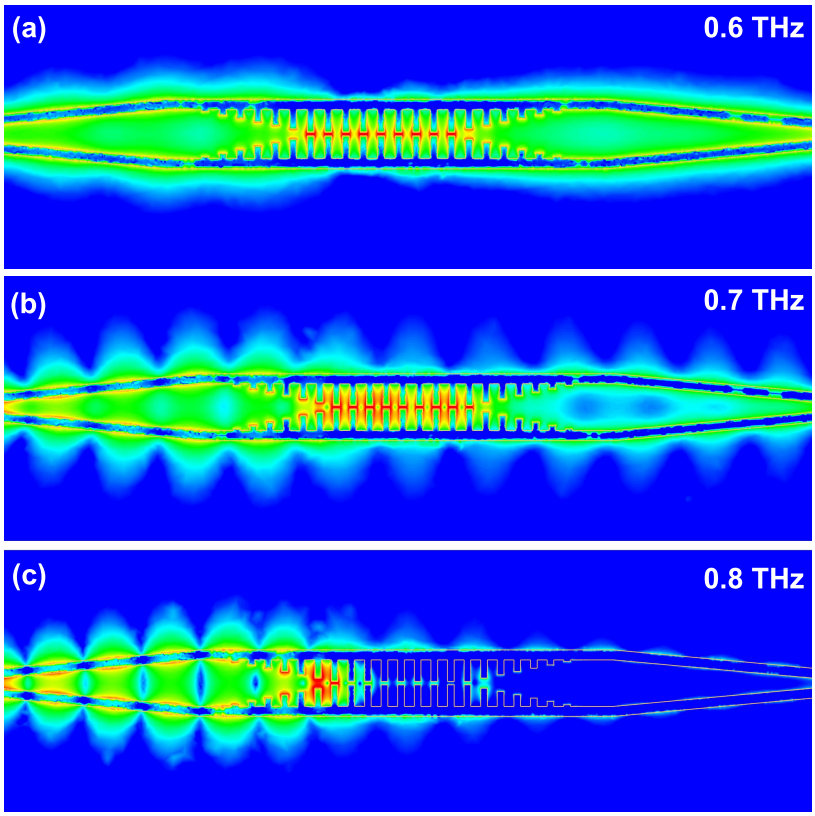

Fig. 5. Field magnitude inside of the H = 65 µm structure. The color scale (logarithmic): red = 10^5 and blue = 10^3 V/m. (a) Below cut-off: 0.6 THz. (b) Near cut-off: 0.7 THz. (c) Above cut-off: 0.8 THz.

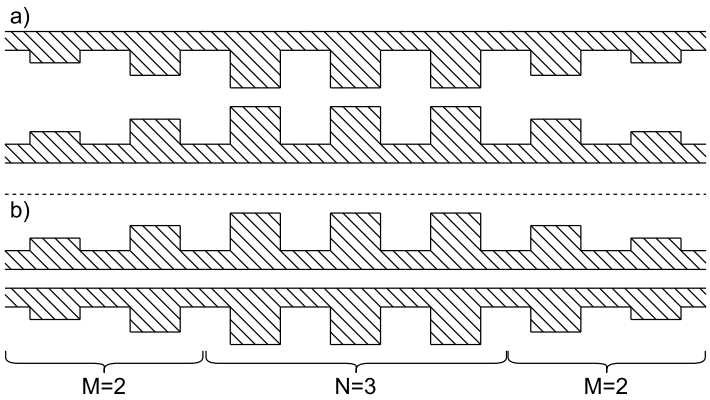

Fig. 6. Transition circuit geometry definitions for M elements in the TC and N elements in CPS-SSPP. Note that M = 2 and N = 3 were selected for illustrative clarity. a) Unit Cell 'A'. b) Unit Cell 'B'.

Optics EXPRESS

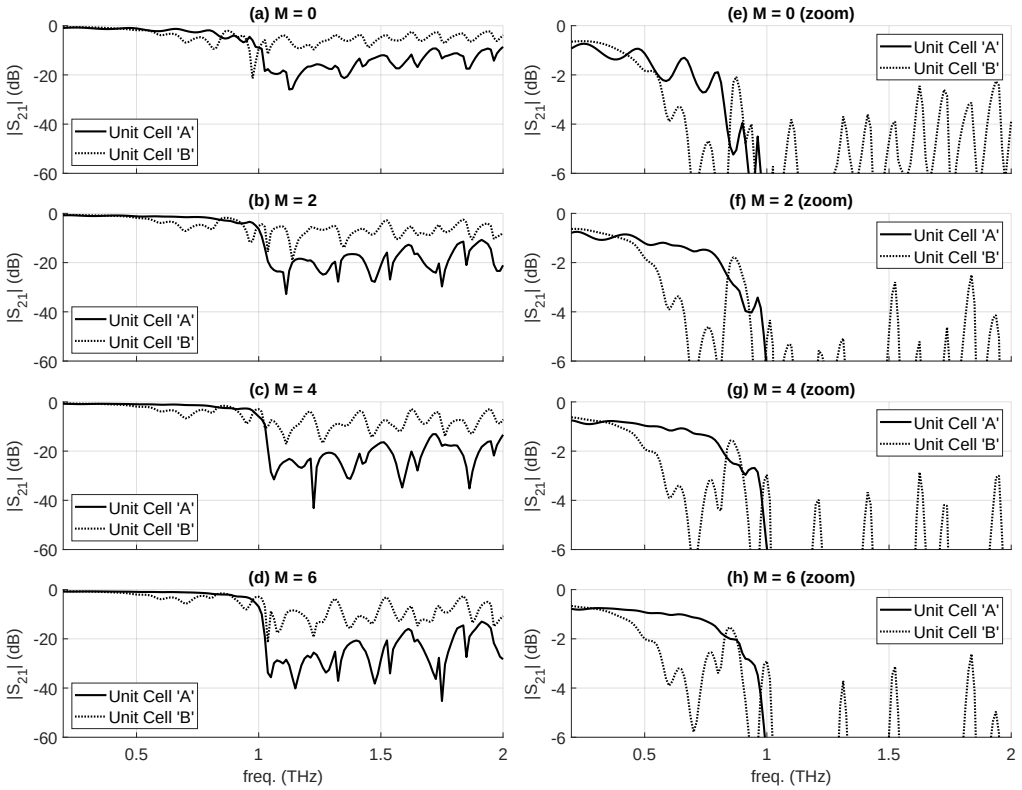

Fig. 7. Transition circuit length investigation for the both Unit Cells with $W = 30$ µm, $H = 55$ µm, $d = 50$ µm, and $a = 30$ µm. Both Unit Cells have the same cross-section length of 200 µm which requires $g = 30$ µm for Unit Cell 'A' and $S = 30$ µm for Unit Cell 'B'. (a) No TC: $M = 0$. (b) $M = 2$. (c) $M = 4$. (d) $M = 6$. (e-h) Zoomed view of (a-d) to highlight the insertion loss.

conversion efficiency (i.e, low-pass filtering performance) of the TC's between Unit Cell 'A' and Unit Cell 'B'. To illustrate the difference in the mode conversion efficiency between Unit Cell 'A' and Unit Cell 'B', we simulate $|S_{21}|^2$ for a different number of TC stubs ($M = 0, 2, 4, 6$). For both Unit Cells we have defined $H = 55$ µm, $W = 30$ µm, $d = 50$ µm, and $a = 30$ µm. Also, we have defined that the total cross-section of both Unit Cells is the same. Specifically, from Table 1, $g + 2(H + W) = 200$ µm for Unit Cell 'A', and $S + 2(H + W) = 200$ µm for Unit Cell 'B' – this condition results in $S = g = 30$ µm. Figure 7 plots the results of these simulations where Fig. 7(a-d) correspond to $M = 0, 2, 4, 6$, respectively. Figure 7(e-h), again, correspond to $M = 0, 2, 4, 6$, respectively, but have a reduced y-axis to better show the pass band characteristics. First, Fig. 7(a,e) illustrate the condition without a TC ($M = 0$) where poor mode conversion efficiency is observed for both Unit Cells by the absence of a sharp roll-off above the cut-off frequency (≈ 1 THz). However, the structure developed from Unit Cell 'A' exhibits some stop-band rejection which is not visible with Unit Cell 'B'. This can be interpreted as an improved mode conversion efficiency for Unit Cell 'A'. Next, Fig. 7(b,f) illustrate the condition where $M = 2$ which results in better mode conversion efficiency for Unit Cell 'A', whereas Unit Cell 'B' does not exhibit a clear low-pass behaviour. Similarly, Fig. 7(c,g) illustrate the condition where $M = 4$ which, again, results in a better mode conversion efficiency for Unit Cell 'A' than Unit Cell 'B'. Lastly, Fig. 7(d,h) illustrate the condition where $M = 6$ where Unit Cell 'A' now behaves like a low-pass filter with good insertion loss and stopband rejection characteristics,

Optics EXPRESS

whereas Unit Cell 'B' still does not behave alike a good low-pass filter. In all cases, Unit Cell 'A' outperforms Unit Cell 'B' which supports the motivation to design a CPS-SSPP structures using Unit Cell 'A' instead of Unit Cell 'B'.

3. Methods

In this section, we present the process of fabricating photo-conductive switches (PCSs) and conducting measurements. The PCSs are used for the generation and detection of THz signals. The PCSs are placed on the CPS feedlines when the cross-section is smaller (S = 10 μm and W = 10 μm) to reduce radiation into free-space and improve the coupling the transmission line. The transmission lines are then slowly tapered to the desired cross-section (S = 140 μm and W = 30 μm) to excite the SSPP structure. A multi-step process was performed to fabricate these devices involving photolithography, gold (Au) sputtering, and wet-etching. The detailed process can be found in other Refs. [21], but we provide a summary here for completeness. First, a low-temperature grown GaAs (LT-GaAs) layer is grown on a sacrificial AlAs layer situated on a semi-insulating GaAs substrate. The LT-GaAs surface is then patterned using standard photolithography to create Au contacts. Subsequently, each PCS region is masked and wet-etched using citric acid and hydrogen peroxide, which determines the thickness of the PCS. Next, the surface is cleaned and re-masked using an etch-resist wax. The LT-GaAs layer is then dissolved by immersing it in hydrofluoric acid (HF), detaching it from the AlAs layer. To disconnect the remaining LT-GaAs film, which interconnects a grid of PCSs, the LT-GaAs film is submerged

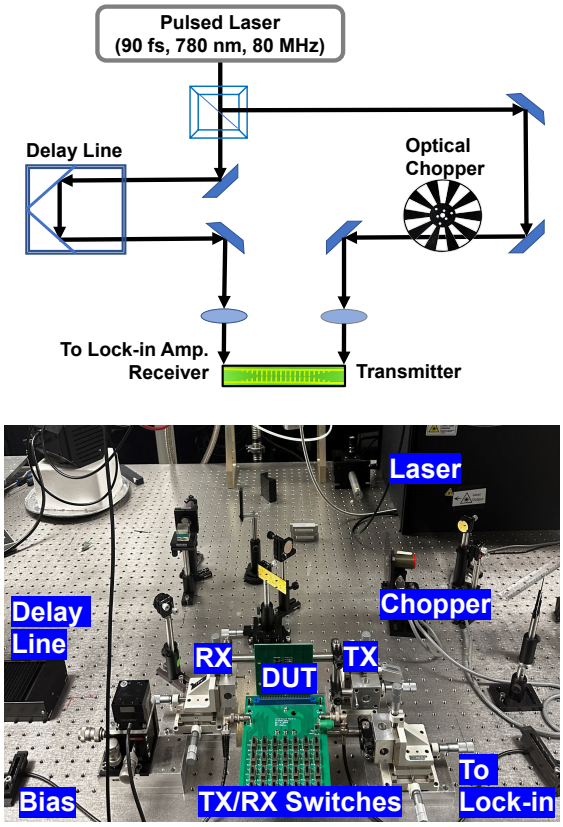

Fig. 8. The modified THz-TDS measurement setup.

Optics EXPRESS

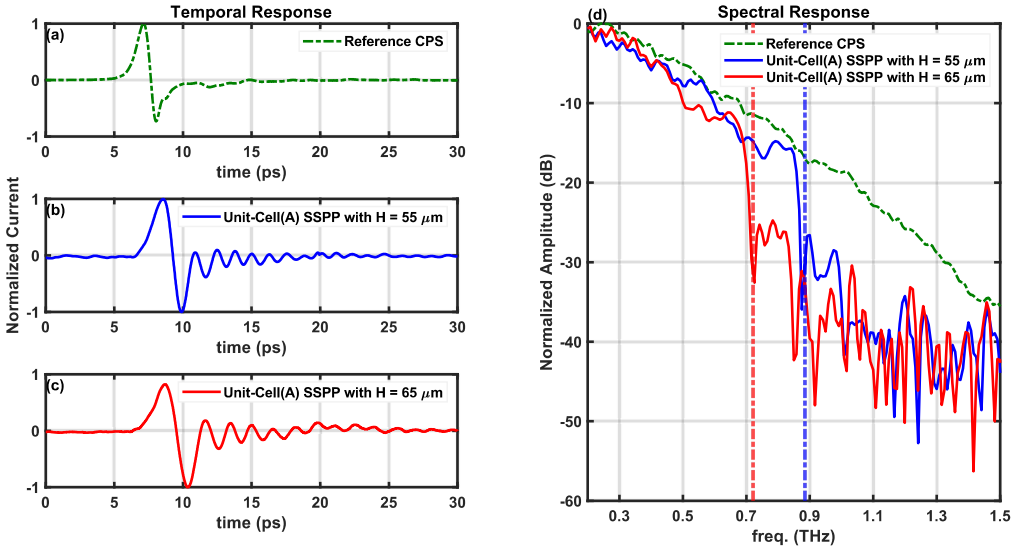

Fig. 9. Measurement results. (a) Temporal response for CPS reference (H = 0 μm). (b) Temporal response for CPS-SSPP Unit Cell 'A' with H = 55 μm (blue). (c) Temporal response for CPS-SSPP Unit Cell 'A' with H = 65 μm (blue). (d) Spectral responses are plotted by applying the DFT of the temporal responses. The vertical dashed lines indicate the simulated band-edge frequencies.

again in citric acid and hydrogen peroxide. Finally, the etch-resistant wax is removed using trichloroethylene (TCE), resulting in numerous active regions of LT-GaAs PCSs.

Next, two PCSs are placed on the designated spots (transmitter and receiver) on the membrane (as shown in Fig. 2) and bonded using a droplet of water with the Van der Waals (VDW) forces, as explained in [22]. The dimensions of the fabricated PCS are 70 μm × 40 μm × 1.8 μm, with a 5 μm gap between the PCS's gold contacts.

The measurements are carried out using a modified THz time-domain Spectroscopy (THz-TDS) setup, as illustrated in Fig. 8 [16]. The experiment involves a femtosecond pulsed laser with a wavelength of 780 nm, 90 fs pulse width, pulse rate of 80 MHz, and 28 mW average output power, focused on PCSs placed on the waveguide, to generate and detect a broadband THz pulse signal. Signal generation and detection arise from the rapid production and recombination of charge carriers in LT-GaAs PCSs which have a subpicosecond carrier lifetime that is dependent on the growth and annealing conditions. When a DC-biased (24V) PCS is illuminated by a femtosecond laser, the transient photoconductivity in the LT-GaAs transmit produces a pulse of current which drives the transmission line. At the receiver, these same dynamics allow detection of the incident THz current except that the 'bias field' is replaced by the transient incident THz voltage. The transmitted signal is reconstructed by translating the mechanical delay line and measuring the receiver current using a lock-in amplifier similar to THz-TDS techniques [16,23].

4. Results and discussion

Three structures were investigated experimentally: a reference (H = 0 μm), H = 55 μm, and H = 65 μm. The reference should not experience a cut-off frequency, whereas the H = 55 μm and H = 65 μm should exhibit cut-off at 0.89 THz and 0.72 THz, respectively (see Fig. 4). Figure 9(a-c) plot the received temporal responses that were obtained by using the setup illustrated in Fig. 8. The corresponding spectral responses were obtained by applying the Discrete Fourier Transform (DFT) to the temporal data and are plotted in Fig. 9(d). Observation of the SSPP spectral traces

Optics EXPRESS

in comparison with the reference trace illustrate a distinct transition at the predicted cut-off frequencies which demonstrates that a structure composed of Unit Cell 'A' exhibits the low-pass filter characteristics that are indicative of CPS-SSPP excitation. These results are the first to demonstrate that CPS-SSPP constructed from Unit Cell 'A' are viable SSPP waveguides at THz frequencies. We note that the spectral plots in Fig. 9(d) have inherent magnitude decay which is an expected consequence of the experimental method which uses sub-picosecond electrical pulses for excitation. The bandwidth of these pulses are finite and decay in the THz region but they provide sufficient dynamic range to observe characteristics up-to 1.5 THz. To be explicit, the dependent variable of Fig. 9(d), does not represent $|S_{21}|^2$, but is scaled by it. The amplitude difference between the reference and SSPP results in the passband, as shown in Fig. 9(d), approximates the insertion loss; however, is not exact because the receiver and transmitter photoconductive switches are not identical.

In this work, we compared Unit Cell 'A' and Unit Cell 'B' and found the improved mode conversion efficiency of Unit Cell 'A' enables the use of shorter TCs which allows for the development of compact low loss devices. Also, the larger CPS conductor separation of Unit Cell 'A' results in lower conductor losses. Together, these two effects reduce the total insertion loss of Unit Cell 'A' which enables the usage in on-chip sensor or THz communication applications.

5. Conclusion

This work has illustrated the design and experimental validation of internally corrugated CPS-SSPP structures (Unit Cell 'A' in Table 1) operating at THz frequencies. The purpose of selecting Unit Cell 'A' as opposed to Unit Cell 'B' is to reduce the insertion loss by two mechanisms. First, the reduction of the feedline attenuation by increasing conductor separation. Second, the improvement of the mode conversation efficiency between CPS and SSPP. This document investigated these two effects via simulation. Lastly, we experimentally confirmed that Unit Cell 'A' is capable of functioning as a CPS-SSPP waveguide which was demonstrated by the existence of low-pass behavior for different stub lengths, when H = 55 µm (0.89 THz), H = 65 µm (0.72 THz).

Appendix A - impact of gap size

Figure 10 plots the impact of varying g on the band-edge frequency. Reducing g results in a decrease in the band-edge frequency since a larger portion of the field becomes contained in the substrate. We note that there are practical limitations when reducing g since the transmitters biasing electric field would become maximal at a location other than the transmitter PCS which has implications on the breakdown voltage location. In short, g should be greater than S at the transmitter (g> 10 µm) to ensure our experimental method is not negatively impacted.

Optics EXPRESS

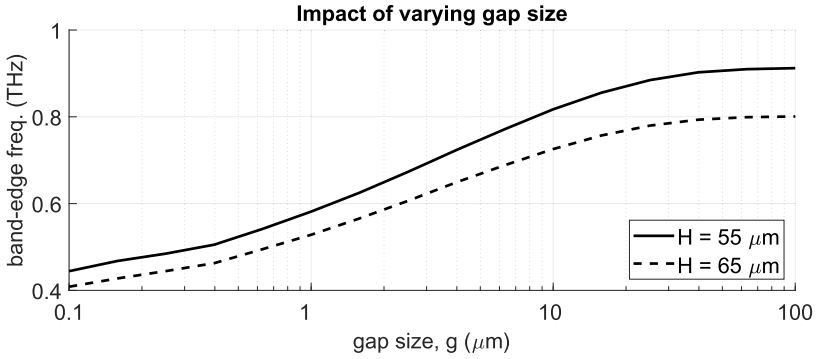

Fig. 10. Simulated impact of the gap size on the band-edge frequency for the two structures (H = 55 µm and H = 65 µm) experimentally investigated in this work.

Appendix B - impact of substrate thickness

The substrate thickness impacts the effective permittivity of the SSPP which changes the band-edge frequency. This dependency is simulated and plotted in Fig. 11. It is observed that as the substrate thickness increases, the band-edge decreases since a larger position of the field is contained within the substrate which increases the effective permittivity. We note that the band-edge will be aligned in broadband measurements (similar to Fig. 4), but other effects, such as substrate radiation, will impact the S-parameters.

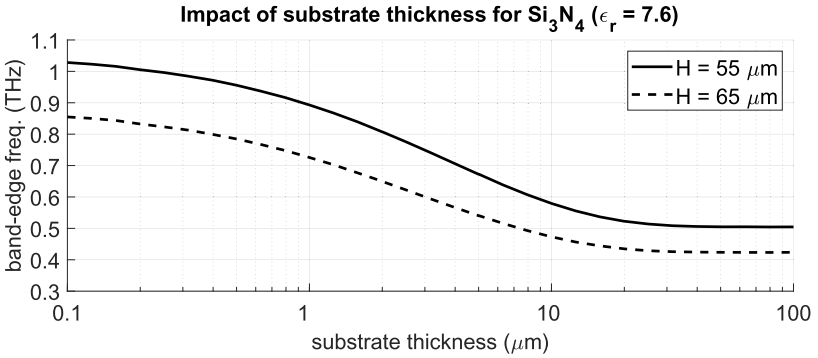

Fig. 11. Simulated impact of the substrate thickness on the band-edge frequency for the two structures (H = 55 µm and H = 65 µm) experimentally investigated in this work.

Funding. Natural Sciences and Engineering Research Council of Canada (RGPIN-2022-03277).

Acknowledgments. This work was supported by an NSERC Discovery Grant. The authors thank 4D LABS at Simon Fraser University for the fabrication of the CPS waveguides and the thin membrane, and also the Centre for Advanced Materials and Related Technology (CAMTEC) at the University of Victoria for providing Nanofab facilities for the fabrication of the PCS devices.

Disclosures. The authors declare that there are no conflicts of interest related to this article.

Data availability. Data underlying the results presented in this paper are not publicly available at this time but may be obtained from the authors upon reasonable request.

References

1. S. A. Maier, *Plasmonics: Fundamentals and Applications*, vol. 1 (Springer, 2007).
2. W. X. Tang, H. C. Zhang, H. F. Ma, *et al.*, "Concept, theory, design, and applications of spoof surface plasmon polaritons at microwave frequencies," Adv. Opt. Mater. **7**(1), 1800421 (2019).

Optics EXPRESS

3. J. B. Pendry, L. Martín-Moreno, and F. J. Garcia-Vidal, "Mimicking surface plasmons with structured surfaces," Science **305**(5685), 847–848 (2004).
4. F. J. Garcia-Vidal, L. Martín-Moreno, and J. B. Pendry, "Surfaces with holes in them: new plasmonic metamaterials," J. Opt. A: Pure Appl. Opt. **7**(2), S97–S101 (2005).
5. X. Shen, T. J. Cui, D. Martin-Cano, *et al.*, "Conformal surface plasmons propagating on ultrathin and flexible films," Proc. Natl. Acad. Sci. **110**(1), 40–45 (2013).
6. H. F. Ma, X. Shen, Q. Cheng, *et al.*, "Broadband and high-efficiency conversion from guided waves to spoof surface plasmon polaritons," Laser Photonics Rev. **8**(1), 146–151 (2014).
7. Y. Guo, K. D. Xu, and X. Tang, "Spoof plasmonic waveguide developed from coplanar stripline for strongly confined terahertz propagation and its application in microwave filters," Opt. Express **26**(8), 10589 (2018).
8. M. A. Unutmaz and M. Unlu, "Terahertz Spoof Surface Plasmon Polariton Waveguides: A Comprehensive Model with Experimental Verification," Sci. Rep. **9**(1), 7616 (2019).
9. Y. Cinar, S. Yildirim, G. Ozsahin, *et al.*, "Modelling Terahertz Spoof Surface Plasmon Polariton Waveguides Using a Circuit Model," IEEE Trans. Terahertz Sci. Technol. **11**(5), 557–565 (2021).
10. M. A. Unutmaz, G. Ozsahin, T. Abacilar, *et al.*, "Investigation of the Transitions for Coplanar Waveguide to Terahertz Spoof Surface Plasmon Polariton Waveguides," IEEE Trans. Antennas Propag. **70**(4), 3002–3010 (2022).
11. K.-D. Xu, Y. J. Guo, and X. Deng, "Terahertz broadband spoof surface plasmon polaritons using high-order mode developed from ultra-compact split-ring grooves," Opt. Express **27**(4), 4354 (2019).
12. K.-D. Xu, F. Zhang, Y. Guo, *et al.*, "Spoof Surface Plasmon Polaritons Based on Balanced Coplanar Stripline Waveguides," IEEE Photonics Technol. Lett. **32**(1), 55–58 (2020).
13. M. Haghighat, T. Darcie, and L. Smith, "Demonstration of a terahertz coplanar-strip spoof-surface-plasmon-polariton low-pass filter," Sci. Rep. **14**(1), 182 (2024).
14. M. Haghighat, T. E. Darcie, and L. Smith, "Terahertz cps-based spoof surface plasmon polariton filter on silicon nitride substrate," in *2023 48th International Conference on Infrared, Millimeter, and Terahertz Waves (IRMMW-THz)*, (2023), pp.1–2.
15. H. Cheng, J. Whitaker, T. Weller, *et al.*, "Terahertz-bandwidth pulse propagation on a coplanar stripline fabricated on a thin membrane," IEEE Microw. Guid. Wave Lett. **4**(3), 89–91 (1994).
16. L. Smith and T. Darcie, "Demonstration of a low-distortion terahertz system-on-chip using a cps waveguide on a thin membrane substrate," Opt. Express **27**(10), 13653–13663 (2019).
17. D. Grischkowsky, M. Ketchen, C.-C. Chi, *et al.*, "Capacitance free generation and detection of subpicosecond electrical pulses on coplanar transmission lines," IEEE J. Quantum Electron. **24**(2), 221–225 (1988).
18. G. Cataldo, J. A. Beall, H.-M. Cho, *et al.*, "Infrared dielectric properties of low-stress silicon nitride," Opt. Lett. **37**(20), 4200–4202 (2012).
19. S. A. Maier, S. R. Andrews, L. Martín-Moreno, *et al.*, "Terahertz Surface Plasmon-Polariton Propagation and Focusing on Periodically Corrugated Metal Wires," Phys. Rev. Lett. **97**(17), 176805 (2006).
20. M. A. Unutmaz and M. Unlu, "Spoof surface plasmon polariton delay lines for terahertz phase shifters," J. Lightwave Technol. **39**(10), 3187–3192 (2021).
21. R. D. V. Ríos, S. Bikorimana, M. A. Ummy, *et al.*, "A bow-tie photoconductive antenna using a low-temperature-grown gaas thin-film on a silicon substrate for terahertz wave generation and detection," J. Opt. **17**(12), 125802 (2015).
22. E. Yablonovitch, D. M. Hwang, T. J. Gmitter, *et al.*, "Van der Waals bonding of GaAs epitaxial liftoff films onto arbitrary substrates," Appl. Phys. Lett. **56**(24), 2419–2421 (1990).
23. W. Gomaa, L. Smith, V. Shiran, *et al.*, "Terahertz low-pass filter based on cascaded resonators formed by CPS bending on a thin membrane," Opt. Express **28**(21), 31967 (2020).

Appendix C

THz Bandpass Filter Using Single-Conductor Spoof Surface Plasmon Polariton Structure Integrated with Coplanar Stripline

THz Band Pass Filter with Integration of Single-Conductor Spoof Surface Plasmon Polariton Waveguide to Coplanar Stripline

Mohsen Haghighat[1,2], *Student Member*, Thomas Darcie[1], *Fellow*, Levi Smith[1,2,*], *Member*, IEEE

***Abstract*—This paper presents a novel terahertz (THz) band-pass filter (BPF) based on a Spoof Surface Plasmon Polariton (SSPP) structure with experimental validation at a center frequency of 1 THz. To the authors' knowledge, the proposed structure is the first integration of a single-conductor SSPP with a dual-conductor coplanar stripline (CPS) and also the first experimental validation of SSPP-based BPF at 1 THz. The measured passband transmission loss at 1.0 THz is approximately 5 dB less than a corresponding CPS with the same length. Simulated out-of-band rejection exceeds 20 dB for the lower cut-off frequency and 30 dB for the upper cut-off frequency; however, in measurements, it ranges from 15 to 30 dB as a result of having a relatively narrowband, low-power output signal, thereby lower signal-to-noise ratio with the employed pulse-based measurement method. The filter, with a center frequency of 1 THz, exhibits a 3 dB bandwidth of approximately 0.3 THz, spanning from 0.87 THz to 1.17 THz. Measurement results, including cut-off frequencies, align well with theoretical predictions and simulations.**

***Index Terms*—Terahertz, Coplanar Strip (CPS), Spoof Surface Plasmon Polaritons (SSPP), Band Pass Filter (BPF), Thin Membrane, Silicon Nitride**

I. Introduction

SPOOF surface plasmon polaritons (SSPP) devices operating at microwave and terahertz (THz) frequencies have enticed notable research attention [1]–[3], primarily owing to their inheritable capabilities from typical surface plasmon polaritons (SPP), such as significant field confinement, and dispersion properties which can be customized through geometric modifications [4], [5].

SSPP structures were initially introduced by 3D geometries like an array of holes or grooves in a piece of metal that interacted with oblique incident light or waves [1], [2]. Since then, the use of guided waves for SSPP excitation has been pursued for their improved integration capabilities [3]. A common guided-wave SSPP structure consists of a corrugated single-conductor; therefore, to interface with standard multi-conductor waveguides a matching or transition circuit is required. The majority of the literature focuses on integrating SSPP into coplanar waveguides (CPW) [6]–[11] due to compatibility with standard vector network analyzer probes. This involves connecting the signal line of the CPW to the SSPP and flaring the ground lines upon gradually increasing the SSPP stub length [9]. This configuration needs large areas of flaring ground conductors at the transition circuit which consumes the chip area and also increases coupling loss and insertion loss consequently [9].

An alternative method to exciting the SSPP without the use of flaring grounds involves utilizing CPS feedlines. One method involves modifying the single-conductor SSPP to a dual-conductor configuration, thereby facilitating integration with a CPS, a configuration known as CPS-SSPP [12]–[15]. Another approach, which has not been previously documented in the literature, entails the direct integration of a single-conductor SSPP with a CPS.

The majority of the SSPP literature is focused on either SSPP waveguiding with low loss throughout a limited bandwidth alike [7] or showcased its low pass filtering owing to slow-wave properties such as [16]. There are limited SSPP-based band-pass filters (BPF) reported at microwave and mm-wave frequencies [17]–[21]; however, these structures generally use microwave cavities which are difficult to integrate on a chip. Also, there is a lack of SSPP-based BPF research validated at THz frequencies mainly due to a shortage of equipment and waveguiding challenges such as different sources of loss at these frequencies [3], [22].

This paper presents the experimental demonstration of a novel THz SSPP-based BPF structure by introducing the integration of CPS feedlines to a single conductor SSPP for the first time. It has been presented with simulation in our preliminary work in [23] at 300 GHz band. For the integration of SSPP to CPS, a transition circuit (TC) is proposed to convert CPS quasi-TEM mode to SSPP TM mode [9], [12], and also to minimize reflections in the passband. This is achieved through gradually extending the length of SSPP stubs while tapering the CPS lines and eventually terminating the CPS conductors. This TC configuration couples the propagating wave to the SSPP and blocks the low frequencies. To operate at THz frequencies, we employed a thin 1 μm Silicon Nitride membrane, which has been demonstrated to mitigate loss and dispersion within the THz range up to 2 THz [12], [24]. Figure 1 illustrates the proposed SSPP-based bandpass filter fabricated on the Silicon Nitride membrane, along with transceiver photoconductive switches (PCS) for THz generation and detection.

Figure 2 shows the cross-section of CPS feedlines on the Silicon Nitride membrane.

[1]Department of Electrical and Computer Engineering, University of Victoria, Victoria, BC, V8P 5C2 Canada

[2]Centre for Advanced Materials and Related Technology (CAMTEC), University of Victoria, 3800 Finnerty Rd, Victoria, BC, V8P 5C2, Canada.

*Corresponding author: levismith@uvic.ca

This work was supported by a Discovery Grant from the Natural Sciences and Engineering Research Council of Canada (NSERC) .

This work made use of the 4D LABS at Simon Fraser University.

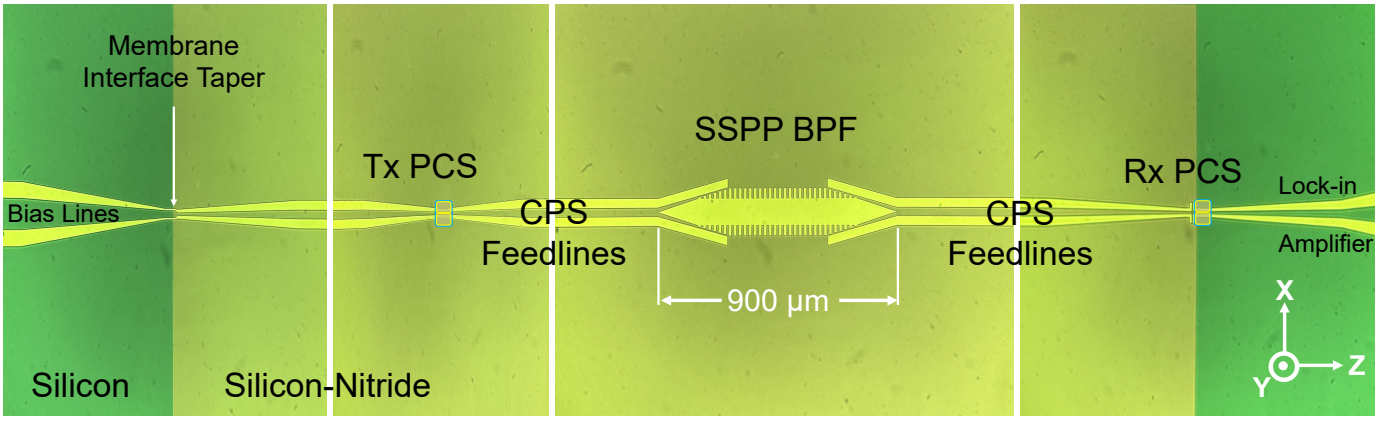

Fig. 1: Fabricated THz SSPP Band Pass Filter on Thin Silicon Nitride Membrane with CPS feedlines and transition circuits for excitation and Tx/Rx PCS for THz generation and detection

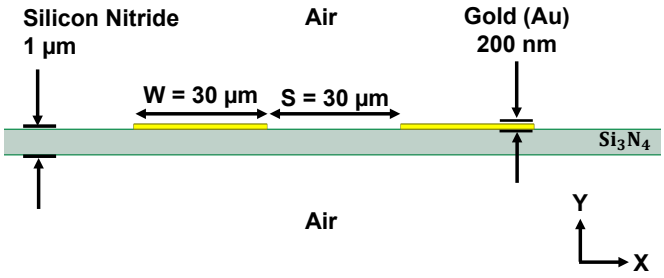

Fig. 2: Cross section of CPS feedlines on the thin membrane

II. Design

In this work, we integrate an SSPP with a CPS using a transition circuit (TC) shown in Figure 3. Ideally, the TC acts as a high-pass filter to create lower stopband rejection and also performs mode conversion between CPS TEM mode and SSPP TM mode. The gap between the CPS conductors and TC stubs creates series capacitance coupling as presented in the SSPP circuit model in [25], [26], which rejects low frequencies in the proposed configuration. A dditionally, t he g radual increment of SSPP stub height in TC provides mode conversion as explained in [6], [12]. The central SSPP waveguide [See Fig.3] acts as a low-pass filter by suppressing frequencies above the band-edge frequency [12]. By combining these elements, a band-pass filter is created that only allows a desired frequency range.

The lower cut-off frequency is primarily determined by the transition circuit (TC) geometry, the number of stubs, and the gap between the coplanar strips (CPS) and stubs, denoted as g, as illustrated in Fig. 3. The operation can be intuitively understood using the circuit model presented in [25], [26]. Reducing the gap between the flared CPS and TC stubs increases the series capacitance on the signal path, thereby lowering the cut-off frequency, and affecting low-frequency rejection. Additionally, it affects the rejection of high frequencies, since larger series capacitances exhibit lower impedance and higher transmission. Conversely,

TABLE I: Stub lengths for the TC (Units: µm)

H_n	H_1	H_2	H_3	H_4	H_5	H_6
21	3	6	9	12	15	18
28	4	8	12	16	20	24
35	5	10	15	20	25	30
42	**6**	**12**	**18**	**24**	**30**	**36**
49	7	14	21	28	35	42
70	10	20	30	40	50	60

increasing the gap decreases the capacitance, which increases the series impedance and dielectric loss, thereby contributing to the insertion loss in the passband. We selected $g = 4$ µm to overcome this trade-off by achieving acceptable insertion loss in simulation (i.e., 1.5 dB) and also a relatively strong low-frequency rejection. The investigation and optimization of the CPS to SSPP transition can be explored in future works using the circuit model for design and inside and variable TC geometry analysis, similar to the research presented in [9] on the transition from CPW to SSPP.

Besides blocking low frequencies, the transition circuit also converts the quasi-TEM mode in CPS to TM mode in SSPP. Mode conversion is achieved by gradually increasing the SSPP stub length which produces electric field components in the propagation direction. The stub lengths are tapered linearly and are tabulated in Table I. The first row is related to the measured structure with H_n = 42 µm.

The upper cut-off frequency can be approximated with an eigenmode simulation on the SSPP unit cell to extract the dispersion curves and the band-edge frequencies as shown in Fig. 4, with different trace (dashed-dotted line) for H_n = 42 µm which the measured structure for demonstration.

It can also be calculated by an analytical dispersion expression assuming that the SSPP shown in Fig. 3 is modeled like a symmetric (y-z plane) 1D array of grooves with finite thickness [2], [27]. Hence, the dispersion relation is approximated by the analysis given in [2], with surface wave propagating along the z-direction:

$$k_z = k_{eff}\sqrt{1 + k^2 \tan^2(k_{eff} H_n)}, \tag{1}$$

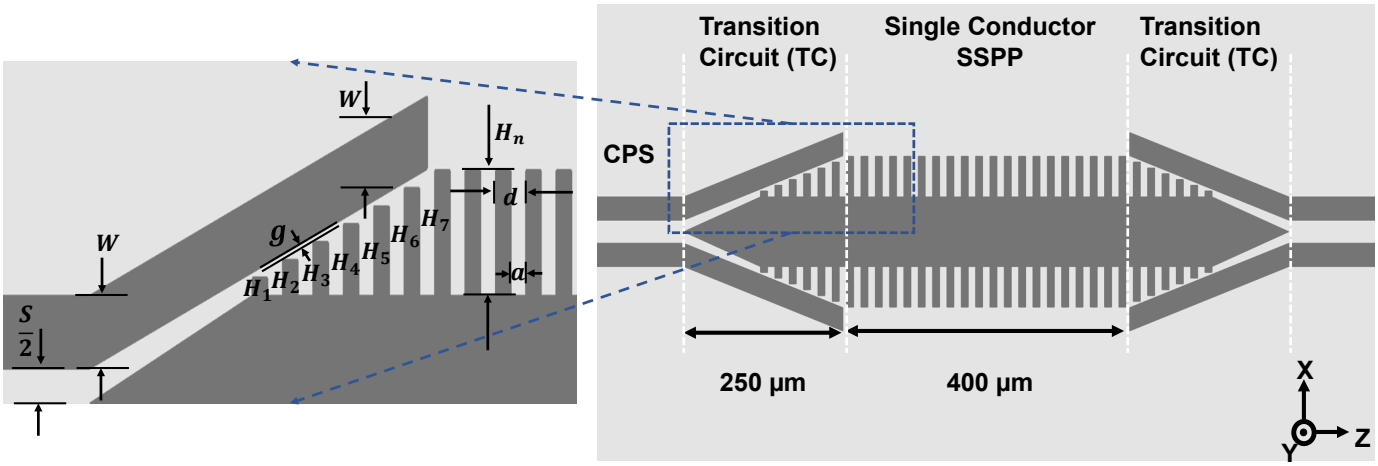

Fig. 3: CPS to SSPP transition circuit dimensions for the proposed BPF

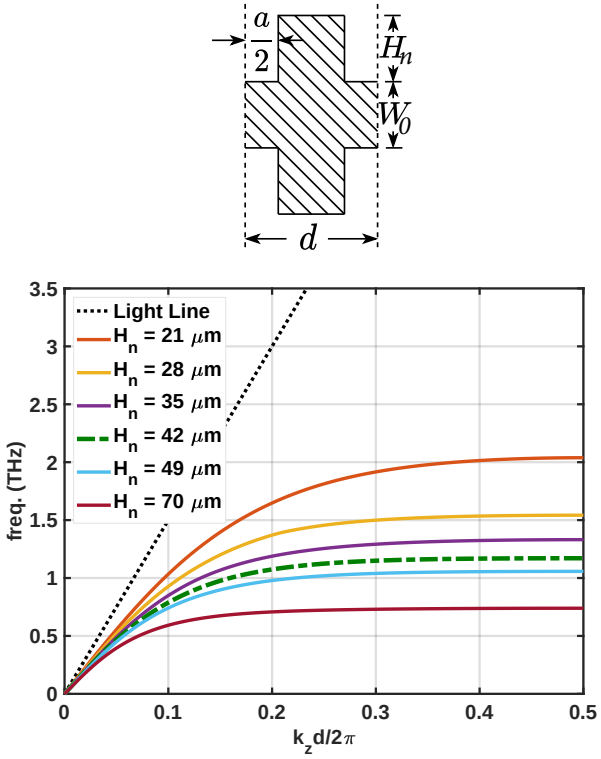

Fig. 4: BPF Unit Cell Dispersion Curves, determining upper cut-off frequency. Unit cell dimensions: d = 20 µm, a = 10 µm, W_0 = 90 µm, 21 µm $\leq H_n \leq$ 70 µm.

where H_n is the length of SSPP stubs (i.e. depth of grooves), d is the period of corrugation, W_s is the width of the stubs, $a = d - W_s$ is the aperture or the width of grooves, $k_{eff} = \omega\sqrt{\varepsilon_{eff}}/c$ is the effective wavenumber, ε_{eff} is the effective relative permittivity (for the CPS feedlines and SSPP BPF on thin Silicon Nitride membrane $\varepsilon_{eff} \approx 1.7$ based on the eigenmode simulations on SSPP unit cell at THz frequencies, particularly around 1 THz), and c is the speed of light. The dispersion relation (1) shows that the band-edge (upper cut-off frequency) of SSPP structures is mainly controlled by H_n and provides a theoretical aid in the design of SSPP filters [6], [16]. We design the SSPP waveguide using eigenmode simulations and the aforementioned theory to obtain the upper cut-off frequency similar to the analysis in [12].

This work aims at developing an SSPP-based bandpass filter. Referring to Fig. 3, we select a subwavelength value for d = 20 µm and $a = 0.5d$ = 10 µm as they must be much smaller than the wavelength [2], [27], [28]. The wavelength of the propagating wave around the center frequency (1 THz) is ≈300 µm. In this work, we selected the value for the period of corrugation, d to be less than 10% of the wavelength, hence, the supposed subwavelength period condition is valid up to 1.5 THz. Lastly, we solve Eq. (1) for an upper cut-off frequency of 1.2 THz which results in H_n = 42 µm.

We used 1 µm thick Si_3N_4 substrate which has been selected to minimize loss and dispersion [24], however, other substrates can be used to implement this structure, expecting higher loss at THz frequencies. Note that using other substrates changes the effective permittivity and the band-edge locations, hence the relation between the geometry and the band-edge should be recalculated.

III. Simulations

ANSYS HFSS was used to perform eigenmode and frequency-domain (FD) simulations on the structure. The eigenmode simulations are performed on the SSPP unit cell and reported in section II, Fig. 4, to utilize in the design procedure. The FD simulation model includes the CPS and SSPP waveguides with period of SSPP d = 20 µm, the width of SSPP stubs W_s = 10 µm, the distance between CPS conductors S = 30 µm, and the width of each CPS strip W = 30 µm, the Si_3N_4 substrate with 1 µm thickness and ε_r = 7.6, $\sigma_{Si_3N_4} = 0$, and tan δ_e = 0.00526 [29]. For investigation of expected band-edge locations and for simplicity we performed a simulation where the structure is modeled as a perfect electric conductor which results in the S_{21} parameters shown in Fig. 5 where H_n varies from 28 µm to 70 µm, illustrating the bandpass filtering and variability of band-edge locations with geometry, with insertion loss of ≈ 0.5-2 dB in the desired passband frequencies.

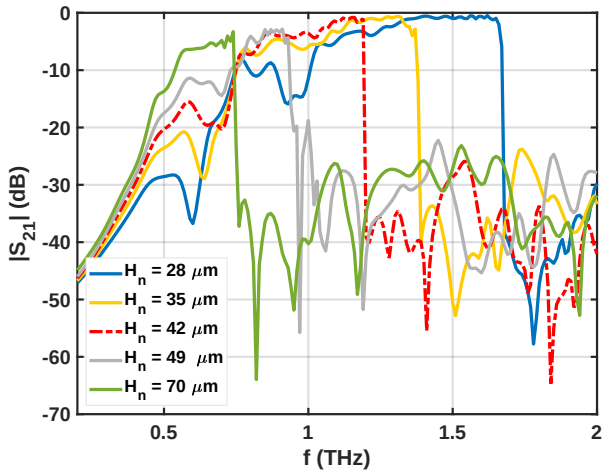

Fig. 5: Transmission response (S_{21}) of the SSPP BPF structure with variable H_n from 28 µm to 70 µm when the conductor is modeled as PEC.

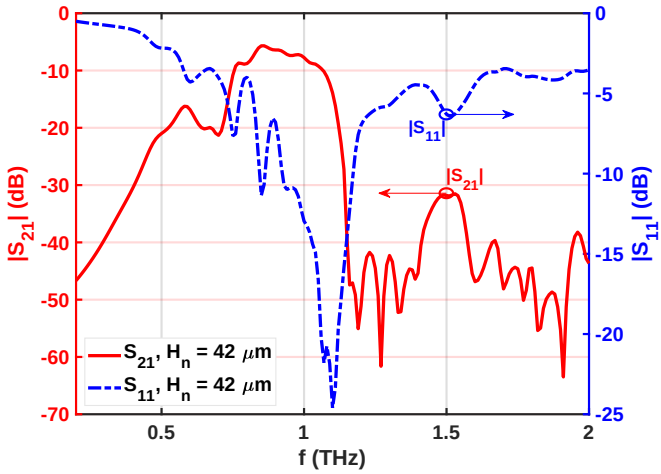

Fig. 6: S_{21} and S_{11} of the BPF structure with H_n = 42 µm considering dielectric and conductor losses.

In another simulation, the structure is modeled as Gold (Au) with 200nm thickness and the conductivity of $\sigma_{Au} = 4.1\times10^7$ S/m, which aims to replicate the measured device with H_n = 42 µm. The S_{21} and S_{11} responses of this structure are shown in Fig. 6, depicting the minimum insertion loss of $\approx$ 5 dB (average $\approx$ 6-7 dB) with maximum return loss of 24 dB in the pass band and return loss of $\approx$ 14 dB at 1 THz.

For visualization of filtering operation, Fig. 7 illustrates the electric field plots for the structure with H_n = 42 µm at 1 THz in the passband, and lower/upper stopbands at 0.5 and 1.5 THz. The field plot at 1 THz also illustrates the field confinement capability of the SSPP structure in the groove areas.

IV. Experiment

The experimental setup for the measurements is a modified THz Time-domain Spectroscopy (THz-TDS) setup presented in [24], as depicted in Fig. 8. This setup utilizes a femtosecond pulsed laser with specific parameters: a wavelength of 780 nm, a pulse width of 90 fs, a pulse rate of 80 MHz, and an average output power of 10 mW. The laser beam is precisely focused onto the photoconductive switches (PCS) placed on the designated Tx and Rx spots on a membrane [see Fig. 1], serving as the transmitter and receiver, to generate and detect THz pulses with photoconductive switching and electro-optic sampling method [24].

The PCSs, with dimensions of 70 µm $\times$ 40 µm $\times$ 1.5 µm and a 5 µm gap between the PCS metal (gold) contacts, are bonded using water droplets with Van der Waals (VDW) forces, as explained in [30]. The transmitted signal is then reconstructed by adjusting a mechanical delay line and measuring the receiver current using a lock-in amplifier, following techniques similar to those employed in conventional THz-TDS setups [24], [31].

The fabrication of photoconductive switches (PCSs) involves a multi-step process conducted as part of this research. Initially, a low-temperature grown gallium arsenide (LT-GaAs) layer is deposited on a sacrificial aluminum arsenide (AlAs) layer, which is situated on a semi-insulating GaAs substrate. Subsequently, the LT-GaAs surface undergoes photolithography to establish gold (Au) contacts. Each PCS region is then masked and subjected to wet etching using citric acid and hydrogen peroxide to define the PCS thickness. After cleaning and re-masking with etch-resist wax, the LT-GaAs layer is dissolved in hydrofluoric acid (HF), separating it from the AlAs layer. Additional steps are undertaken to disconnect the remaining LT-GaAs film, resulting in the formation of multiple active regions of LT-GaAs PCSs [32].

V. Measurement Results and Discussion

The experimental results of the SSPP-based BPF structure with H_n = 42 µm are shown in Fig. 9, including the temporal responses of the BPF and a reference CPS (i.e. transient output pulses). The reference CPS is a feedline shown in Fig. 1 fabricated with the same length. The temporal response of CPS is an expected broadband Gaussian THz pulse, and the temporal response of BPF is a narrow-band pulse with multiple oscillations. As expected, the period of oscillations is $\approx$ 1 ps which corresponds to 1 THz which is the center frequency of the BPF structure under test. Figure 9 also displays the corresponding spectral responses on a single subplot (right side) obtained from applying the Discrete Fourier Transform on the temporal responses. Since the output signal is weak, the spectral response will be a very small value in the dB scale (in the order of -30 dB to -70 dB), therefore, we normalized the data by shifting both of the spectral responses with the maximum absolute value of the reference spectrum, without changing the relative amplitude difference between the traces. The spectral response of the BPF shows steep roll-off rates at expected cut-off frequencies at 0.8 THz and 1.2 THz. The upper cut-off frequency at 1.2 THz is expected from the SSPP band-edge when H_n = 42 µm based on the dispersion curves Fig. 4 and S parameter simulations with sharp upper-band cut-off shown in Fig. 5. The lower cut-off frequency is directly controlled by the geometries of TC and indirectly by H_n

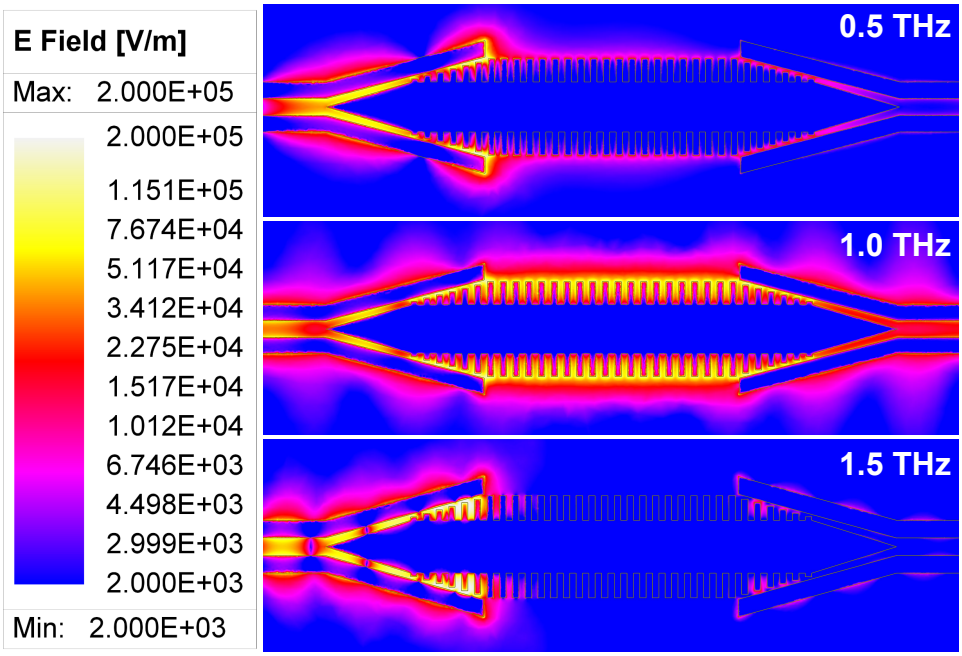

Fig. 7: Field plots of the proposed SSPP BPF structure with $H_n = 42$ µm at 0.5 THz (lower stopband), 1 THz (passband), and 1.5 THz (upper stopband). The temperature (color) scale ranges from blue (2×10^3 V/m) to white (2×10^5 V/m) on a logarithmic scale.

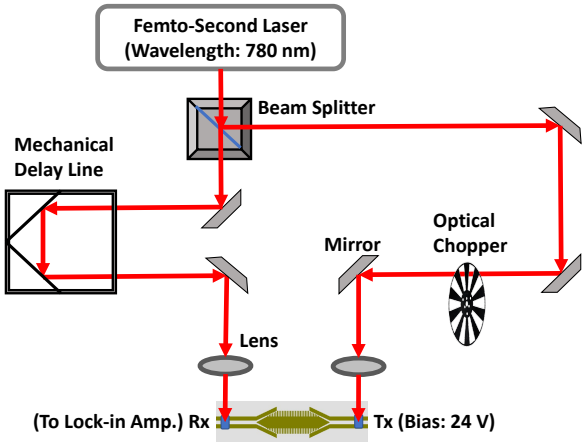

Fig. 8: BPF measurement setup based on modified THz Time Domain Spectroscopy

because this configuration holds a fixed number of TC stubs and the the dimensions of these stubs are a function of H_n. Overall, the initial low-frequency rejection up to 0.65 THz and a lower cut-off frequency before the passband at 0.8 THz (with steep roll-off) is expected from the simulation [see Fig. 6] and observed in measurement results.

The comparison of spectral responses in Fig. 9 shows 15-20 dB out-of-band rejection for BPF, which is lower than expected which should be more than 20 dB for low frequencies and more than 30 dB for upper band rejection. This is primarily because of noise levels and the weakness of BPF output since it is a relatively narrow band signal and holds only a small portion of total pulse energy. Thus, the low signal-to-noise ratio disrupts the resolution of real out-of-band rejection of the filter. Despite the weakness of the signal power, the measured out-of-band rejection is acceptable. Another important parameter to be extracted from the measurement results is the difference between the amplitude of spectrum between the BPF and CPS reference in the passband which is $\approx$ 5 dB that aligns with the minimum insertion loss expectations from S-parameters simulations [see Fig. 6].

It is worth mentioning that the spectral responses have inherent amplitude decay because these are Fourier transforms of finite-duration transient pulses rather than impulses with a flat spectrum [12], [24]. Therefore, the spectrum of BPF has a baseline that resembles the reference spectral curve. The fluctuations in the measurement are attributed to uncorrelated system noise sources, including those from the laser, equipment, and environment, as well as fluctuations in the PCS photo-current due to fabrication imperfections. These effects were also observed in the measurement of the CPS reference where we expect a much smoother spectral response based on simulations.

VI. Conclusion

This paper introduces a novel terahertz (THz) spoof surface plasmon polariton (SSPP) bandpass filter, marking a significant milestone in SSPP-based filter structures by integrating a single-conductor SSPP to CPS. Through experimental validation, the filter demonstrates impressive performance metrics, including a low passband amplitude difference of 5 dB compared to a CPS feedline with the same length and dimensions, and out-of-band rejection surpassing 20 dB for low frequencies and about 15-20 dB for high frequencies. With a 3 dB bandwidth of approximately 0.3 THz, ranging

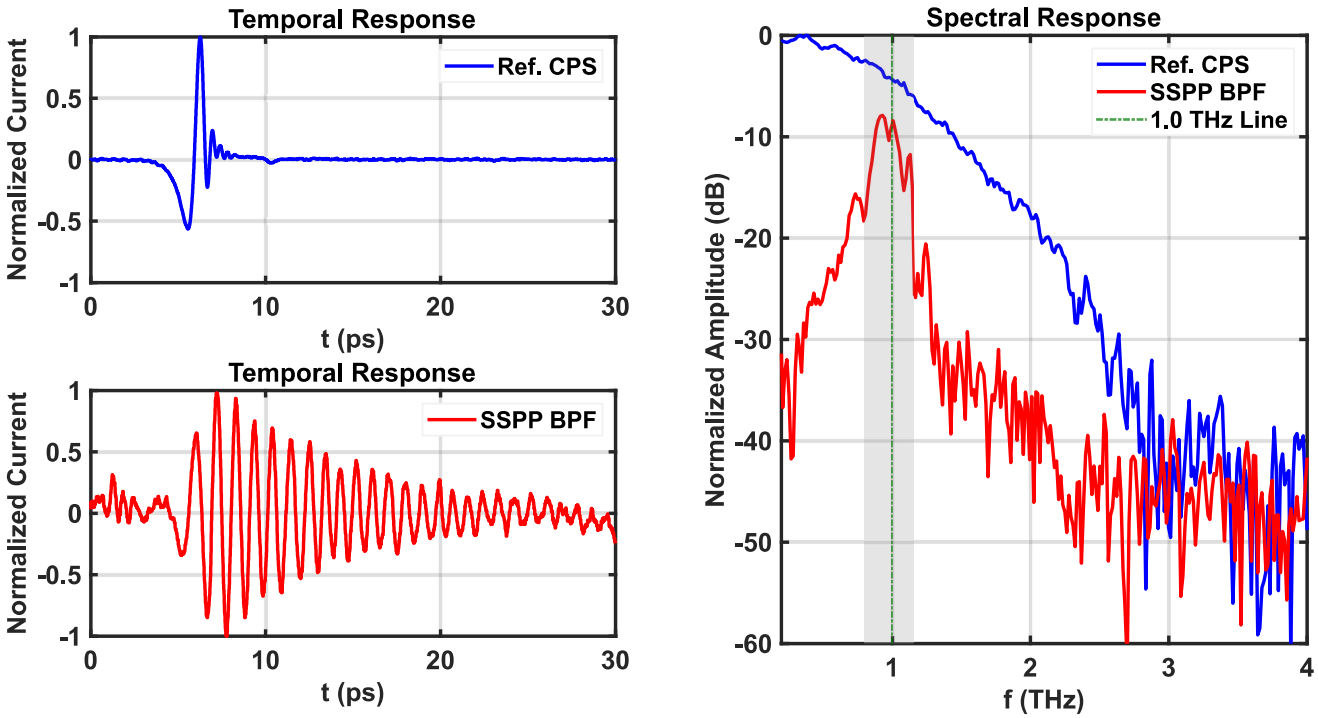

Fig. 9: Measurement results for the proposed SSPP-based BPF and corresponding reference CPS

from 0.87 to 1.17 THz, the filter exhibits robust signal transmission and rejection capabilities within its passband and stopbands, closely aligned with simulations. Notably, the integration of a single-conductor SSPP with a dual-conductor CPS feedline represents a pioneering approach. The guided-wave transmission of the THz signal was enabled by the use of a thin 1 µm Silicon Nitride membrane to mitigate loss and dispersion within the THz range. This study holds promise for a wide range of applications in next-generation communication systems, interconnects, and material sensing, highlighting the significance of planar SSPP structures in advancing THz technologies.

Acknowledgements

The research presented in this manuscript was conducted on the traditional territory of the Lək̓ʷəŋən (Songhees and Esquimalt) Peoples. We deeply respect this opportunity and the welcoming accommodations which the Lək̓ʷəŋən and W̱SÁNEĆ Peoples provided.

This work was supported by an NSERC Discovery Grant. The authors thank 4D LABS at Simon Fraser University for the fabrication of the CPS waveguides and the thin membrane, and also the Centre for Advanced Materials and Related Technology (CAMTEC) at the University of Victoria for providing Nanofab facilities for the fabrication of the PCS devices.

References

[1] J. B. Pendry, L. Martín-Moreno, and F. J. Garcia-Vidal, "Mimicking surface plasmons with structured surfaces," *Science*, vol. 305, no. 5685, pp. 847–848, 2004.

[2] F. J. Garcia-Vidal, L. Martín-Moreno, and J. B. Pendry, "Surfaces with holes in them: new plasmonic metamaterials," *Journal of Optics A: Pure and Applied Optics*, vol. 7, no. 2, p. S97, 2005.

[3] W. X. Tang, H. C. Zhang, H. F. Ma, W. X. Jiang, and T. J. Cui, "Concept, theory, design, and applications of spoof surface plasmon polaritons at microwave frequencies," *Advanced Optical Materials*, vol. 7, no. 1, p. 1800421, 2019.

[4] S. A. Maier *et al.*, *Plasmonics: fundamentals and applications*. Springer, 2007, vol. 1.

[5] P. A. Huidobro, A. I. Fernández-Domínguez, J. B. Pendry, L. Martín-Moreno, and F. J. Garcia-Vidal, *Spoof Surface Plasmon Metamaterials*, ser. Elements in Emerging Theories and Technologies in Metamaterials. Cambridge University Press, 2018.

[6] H. F. Ma, X. Shen, Q. Cheng, W. X. Jiang, and T. J. Cui, "Broadband and high-efficiency conversion from guided waves to spoof surface plasmon polaritons," *Laser Photonics Rev.*, vol. 8, no. 1, pp. 146–151, Jan. 2014.

[7] M. A. Unutmaz and M. Unlu, "Terahertz Spoof Surface Plasmon Polariton Waveguides: A Comprehensive Model with Experimental Verification," *Scientific Reports*, vol. 9, no. 1, p. 7616, May 2019.

[8] ——, "Fixed physical length spoof surface plasmon polariton delay lines for a 2-bit phase shifter," *J. Opt. Soc. Am. B*, vol. 37, no. 4, pp. 1116–1121, Mar. 2020.

[9] M. A. Unutmaz, G. Ozsahin, T. Abacilar, and M. Unlu, "Investigation of the Transitions for Coplanar Waveguide to Terahertz Spoof Surface Plasmon Polariton Waveguides," *IEEE Transactions on Antennas and Propagation*, vol. 70, no. 4, pp. 3002–3010, Apr. 2022.

[10] B. Mazdouri, M. M. Honari, and R. Mirzavand, "Miniaturized spoof SPPs filter based on multiple resonators or 5G applications," *Scientific Reports*, vol. 11, no. 1, p. 22557, Nov. 2021.

[11] W. X. Tang, H. C. Zhang, H. F. Ma, W. X. Jiang, and T. J. Cui, "Concept, Theory, Design, and Applications of Spoof Surface Plasmon Polaritons at Microwave Frequencies," *Advanced Optical Materials*, vol. 7, no. 1, p. 1800421, Jan. 2019.

[12] M. Haghighat, T. Darcie, and L. Smith, "Demonstration of a terahertz coplanar-strip spoof-surface-plasmon-polariton low-pass filter," *Scientific Reports*, vol. 14, 2024.

[13] K.-D. Xu, Y. J. Guo, and X. Deng, "Terahertz broadband spoof surface plasmon polaritons using high-order mode developed from ultra-compact split-ring grooves," *Optics Express*, vol. 27, no. 4, p. 4354, Feb. 2019.

[14] K.-D. Xu, F. Zhang, Y. Guo, L. Ye, and Y. Liu, "Spoof Surface Plasmon Polaritons Based on Balanced Coplanar Stripline Waveguides," *IEEE Photonics Technology Letters*, vol. 32, no. 1, pp. 55–58, Jan. 2020.

[15] M. Haghighat, T. E. Darcie, and L. Smith, "Terahertz cps-based spoof surface plasmon polariton filter on silicon nitride substrate," in *2023 48th International Conference on Infrared, Millimeter, and Terahertz Waves (IRMMW-THz)*, 2023, pp. 1–2.
[16] Y. J. Guo, K. Da Xu, and X. Tang, "Spoof plasmonic waveguide developed from coplanar stripline for strongly confined terahertz propagation and its application in microwave filters," *Optics Express*, vol. 26, no. 8, p. 10589, Apr. 2018.
[17] Y. J. Guo, K. D. Xu, Y. Liu, and X. Tang, "Novel surface plasmon polariton waveguides with enhanced field confinement for microwave-frequency ultra-wideband bandpass filters," *IEEE Access*, vol. 6, pp. 10 249–10 256, 2018.
[18] J. Wang, L. Zhao, and Z.-C. Hao, "A band-pass filter based on the spoof surface plasmon polaritons and cpw-based coupling structure," *IEEE Access*, vol. 7, pp. 35 089–35 096, 2019.
[19] Y. Wei, Y. Wu, W. Wang, L. Pan, Y. Yang, and Y. Liu, "Double-sided spoof surface plasmon polaritons- line bandpass filter with excellent dual-band filtering and wide upper band suppressions," *IEEE Transactions on Plasma Science*, vol. 48, no. 12, pp. 4134–4143, 2020.
[20] Y. Liu, K.-D. Xu, J. Li, Y.-J. Guo, A. Zhang, and Q. Chen, "Millimeter-wave e-plane waveguide bandpass filters based on spoof surface plasmon polaritons," *IEEE Transactions on Microwave Theory and Techniques*, vol. 70, no. 10, pp. 4399–4409, 2022.
[21] Y. Feng, K.-D. Xu, Z. Niu, B. Zhang, L. Liu, and Y. Fan, "Ka-band waveguide bandpass filters using double-layer grounded spoof surface plasmon polaritons," *IEEE Transactions on Microwave Theory and Techniques*, pp. 1–11, 2024.
[22] H.-J. Song and N. Lee, "Terahertz communications: Challenges in the next decade," *IEEE Transactions on Terahertz Science and Technology*, vol. 12, no. 2, pp. 105–117, 2022.
[23] M. Haghighat, T. Darcie, and L. Smith, "A thz spoof surface plasmon polariton band pass filter for 6g communication applications," in *2024 IEEE Pacific Rim Conference on Communications, Computers and Signal Processing (PACRIM)*, 2024, pp. 1–4.
[24] L. Smith and T. Darcie, "Demonstration of a low-distortion terahertz system-on-chip using a cps waveguide on a thin membrane substrate," *Optics Express*, vol. 27, no. 10, pp. 13 653–13 663, May 2019.
[25] A. Kianinejad, Z. N. Chen, and C.-W. Qiu, "Design and modeling of spoof surface plasmon modes-based microwave slow-wave transmission line," *IEEE Transactions on Microwave Theory and Techniques*, vol. 63, no. 6, pp. 1817–1825, 2015.
[26] Y. Cinar, S. Yildirim, G. Ozsahin, M. Unutmaz, and M. Unlu, "Modelling Terahertz Spoof Surface Plasmon Polariton Waveguides Using a Circuit Model," *IEEE Transactions on Terahertz Science and Technology*, vol. 11, no. 5, pp. 557–565, Sep. 2021.
[27] X. Shen, T. J. Cui, D. Martin-Cano, and F. J. Garcia-Vidal, "Conformal surface plasmons propagating on ultrathin and flexible films," *Proceedings of the National Academy of Sciences*, vol. 110, no. 1, pp. 40–45, 2013.
[28] S. A. Maier, S. R. Andrews, L. Martín-Moreno, and F. J. García-Vidal, "Terahertz Surface Plasmon-Polariton Propagation and Focusing on Periodically Corrugated Metal Wires," *Physical Review Letters*, vol. 97, no. 17, p. 176805, Oct. 2006.
[29] G. Cataldo, J. A. Beall, H.-M. Cho, B. McAndrew, M. D. Niemack, and E. J. Wollack, "Infrared dielectric properties of low-stress silicon nitride," *Optics Letters*, vol. 37, no. 20, pp. 4200–4202, Oct 2012.
[30] E. Yablonovitch, D. M. Hwang, T. J. Gmitter, L. T. Florez, and J. P. Harbison, "Van der Waals bonding of GaAs epitaxial liftoff films onto arbitrary substrates," *Applied Physics Letters*, vol. 56, no. 24, pp. 2419–2421, 06 1990.
[31] W. Gomaa, L. Smith, V. Shiran, and T. Darcie, "Terahertz low-pass filter based on cascaded resonators formed by CPS bending on a thin membrane," *Optics Express*, vol. 28, no. 21, p. 31967, Oct. 2020.
[32] R. D. V. Ríos, S. Bikorimana, M. A. Ummy, R. Dorsinville, and S.-W. Seo, "A bow-tie photoconductive antenna using a low-temperature-grown gaas thin-film on a silicon substrate for terahertz wave generation and detection," *Journal of Optics*, vol. 17, no. 12, p. 125802, 2015.

Appendix D

Terahertz Band Pass Filter based on Spoof Surface Plasmon Polariton Split Rings developed from Coplanar Strip with Internal Stubs

Terahertz Band Pass Filter based on Spoof Surface Plasmon Polariton Split Rings developed from Coplanar Strip with Internal Stubs

Mohsen Haghighat[1,2], *Student Member*, Thomas Darcie[1], *Fellow*,
Levi Smith[1,2,*], *Member*, IEEE

***Abstract*—This paper presents the experimental verification of a Terahertz (THz) Spoof Surface Plasmon Polariton (SSPP) Bandpass Filter (BPF) based on Coplanar Stripline (CPS)-SSPP with internal grooves and central split rings. The proposed BPF achieves high-frequency rejection through low-pass SSPP characteristics and blocks low frequencies using gaps within the structure. The upper and lower cut-off frequencies can be adjusted by modifying the geometries in the design stage. For demonstration, a BPF with a center frequency of approximately 1 THz was fabricated and measured using a modified THz time-domain spectroscopy system. The measured passband transmission around 1 THz, as well as the lower and upper 3 dB cut-off frequencies at approximately 0.8 THz and 1.2 THz, respectively, agree with the simulations.**

***Index Terms*—Terahertz (THz), Band Pass Filter (BPF), Coplanar Strip (CPS), Spoof Surface Plasmon Polaritons (SSPP), CPS-SSPP, SSPP Rings, Field Confinement, Thin Membrane, Silicon Nitride**

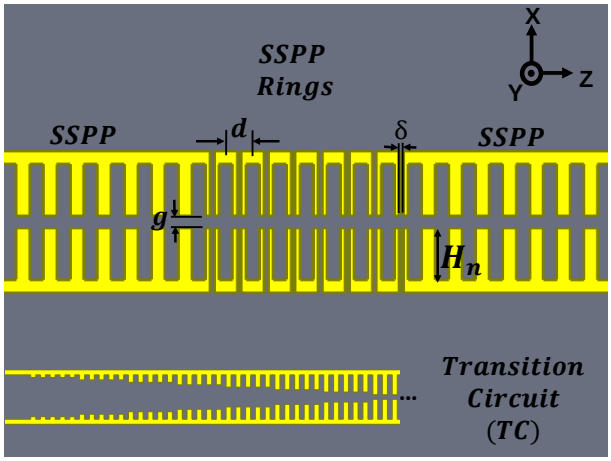

Fig. 1: Proposed BPF structure based on SSPP rings

I. Introduction

METAMATERIAL plasmonic structures operating at microwave and terahertz (THz) frequencies, known as spoof surface plasmon polariton (SSPP) devices, have garnered substantial research interest. This attention is primarily due to their inherited properties from conventional surface plasmon polaritons (SPP), including significant field confinement and customizable dispersion characteristics through geometric modifications [1]–[16].

Initially, SSPP structures were introduced using 3D geometries, such as arrays of holes or grooves in a metal surface, interacting with obliquely incident light or waves [1], [2]. Subsequently, the use of guided waves for SSPP excitation has been explored due to their enhanced integration capabilities [8]. A typical guided-wave SSPP structure comprises a corrugated single-conductor, necessitating a matching or transition circuit for interfacing with standard multi-conductor waveguides. Much of the existing literature focuses on integrating SSPP into coplanar waveguides (CPW) [11], [13], [17]–[20], given their compatibility with standard vector network analyzer probes. This integration involves connecting the CPW signal line to the SSPP and flaring the ground lines while gradually increasing the SSPP stub length [19]. However, this configuration demands large flaring ground conductor areas at the transition circuit, which consumes chip area and increases coupling and insertion losses [19].

Most SSPP research has concentrated on either SSPP waveguiding with low loss over a limited bandwidth [11] or demonstrating its low-pass filtering capabilities due to slow-wave properties [5]. There are few reported SSPP-based bandpass filters (BPF) at microwave and millimeter-wave frequencies [21]–[25]. However, these structures often use microwave cavities, making on-chip integration challenging. Additionally, there is limited research on SSPP-based BPFs validated at THz frequencies, mainly due to a lack of equipment and waveguiding challenges, such as various loss sources at these frequencies [8], [26].

To excite the SSPP with low loss at THz frequencies without using flaring grounds in the aforementioned CPW integration [19], utilizing CPS feedlines demonstrated to be a viable alternative [14], [27], [28]. Given that SSPP is essentially a single conductor, one method involves modifying the SSPP to a dual-conductor configuration by creating a slot in the metal, facilitating integration with a CPS transmission line (TL), known as CPS-SSPP [9], [10], [14].

This paper introduces a novel THz SSPP-based BPF structure based on CPS-SSPP with internal corrugation, featuring SSPP rings for the first time. To excite the device with CPS,

[1]Department of Electrical and Computer Engineering, University of Victoria, Victoria, BC V8P 5C2, Canada
[2]Centre for Advanced Materials and Related Technology (CAMTEC), University of Victoria, 3800 Finnerty Rd, Victoria, BC V8P 5C2, Canada.
[*]Corresponding author: levismith@uvic.ca
This work was supported by an NSERC Discovery Grant.
This work made use of the 4D LABS at Simon Fraser University.

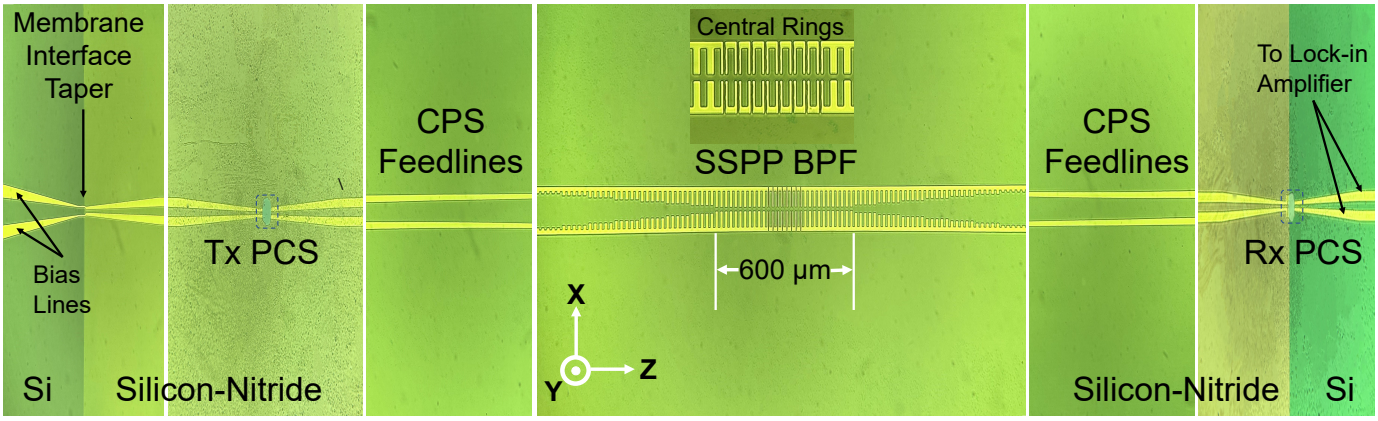

Fig. 2: Fabricated SSPP-based BPF with central rings on a thin Silicon Nitride Membrabe excited by CPS feedlines. Key dimensions: Period d = 20 μm, SSPP groove width a = 10 μm, ring gap δ = 3 μm, SSPP vertical gap g = 10 μm, and groove depth H_n = 40 μm.

we propose a transition circuit (TC) to convert the CPS quasi-TEM mode to SSPP TM mode [14], [19] and to minimize reflections in the passband. This is achieved by gradually extending the length of SSPP stubs to the maximum SSPP groove depth. We employed a thin 1 μm Silicon Nitride membrane, which has been shown to reduce loss and dispersion in the THz range up to 2 THz [14], [27]. Figure 1 depicts the proposed structure with SSPP rings and TC for SSPP excitation. Figure 2 shows the fabricated SSPP-based bandpass filter on the Silicon Nitride membrane, along with transceiver photo-conductive switches (PCS) for THz generation and detection.

II. Design

In this section, we discuss the design of the proposed SSPP BPF, based on the analysis of the Unit cell of the periodic structure that builds the main part of the filter, controlling its bandpass operation. As a well-known analysis of SSPP structure, we extracted the dispersion curves of the proposed unit cell shown in Fig. 3, by performing an eigenmode simulation. The dispersion curves in this figure indicate two areas with relatively small slopes and the creation of slow waves, representing the lower and upper cut-off frequency (i.e., band-edge) of a resulting periodic structure. Also, by varying just one of the dimensions (H_n) the band-edge frequency can be designed; however, to control the bandwidth, other dimensions shown in the inset of Fig. 3 should be tailored.

The design procedure involves eigenmode simulation of the unit cell to achieve desired band-edge frequencies by calculating the unit cell dimensions including; period d = 20 μm is set to be much smaller than wavelength of operation [2], [14], SSPP groove width a = 10 μm, ring gap δ = 3 μ, SSPP vertical gap g = 10 μm, and groove depth 20 μm $\leq H_n \leq$ 60 μm.

Upon completing the design of the unit cell, we should opt for a number of periods that we want to extend the SSPP rings. We found that there is a trade-off between stopband roll-off rates and passband insertion loss when we simulate the entire structure to obtain S parameters. In other words, as we increase

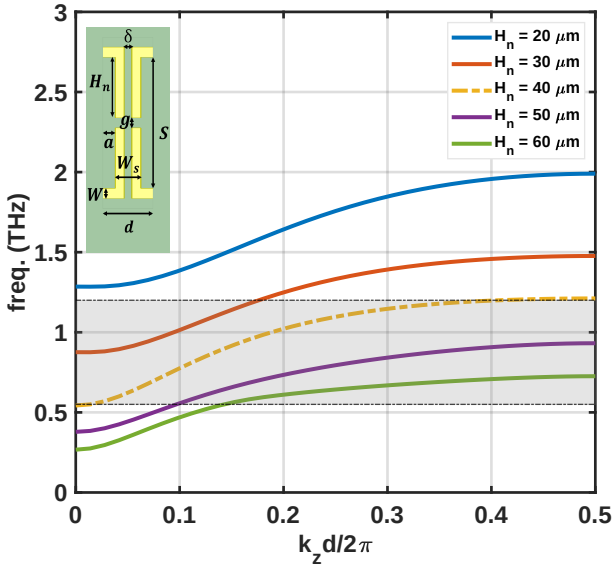

Fig. 3: SSPP rings dispersion curves

the number of rings the roll-off will be sharper; however, the baseband loss increases due to the increased number of gaps between the rings. One possible way is to reduce the gap ($\delta \leq$ 3 μ) to be able to increase the number of rings, but we found that it weakens low-frequency rejection. By the way, our lithography minimum feature size was 3 μfor this project. To alleviate this trade-off, we decided to use a minimal number of rings (i.e., 7) to get the band-pass filtering and resolved the roll-off rate issue by extending SSPP without gaps on both sides of the central rings, as shown in Fig. 1.

The structure cannot be connected directly to the CPS feedlines shown in Fig. 2 for excitation, since there is a huge mode mismatch between CPS (quasi TEM) and SSPP (quasi TM), and thereby significant reflections. Therefore a transition circuit (TC) with a gradual increase in the depth of SSPP grooves is required as detailed in [14]. In this work, we used a TC with stepped linear growth of H_n, where

TABLE I: Stub lengths for the TC (Units: μm)

H_n	H_1	H_2	H_3	H_4	H_5	H_6	H_7
30	4	8	11	15	19	23	26
40	5	10	15	20	25	30	35
50	6	13	19	25	31	38	44

each TC stub with height of H_i ($1 \leq i \leq 7$) is repeated 5 times to create a short SSPP structure and H_i increases in each section [see Fig. 1] to reach the maximum SSPP depth (i.e., H_n). The values of H_i are depicted in Table I for three selected H_n values for further frequency domain simulations and H_n = 40 μm for experimental validation. It is also possible to linearly ramp up the stub height without repetition or stepped configuration, however, the stopband S_{21} will have an increasing transmission for higher frequencies as in [14]. Also, the number of variables will be limited with stepped configuration which can be beneficial for optimization purposes and to opt for a non-linear growth.

III. Simulations

Eigenmode simulation and frequency-domain (FD) simulations were conducted on the structure using ANSYS HFSS. The eigenmode simulations, performed on the SSPP unit cell, are discussed in section II (Fig. 3). The FD simulation model incorporated CPS and SSPP waveguides with the following parameters: SSPP period $d = 20$ μm, SSPP stub width $W_s = 10$ μm, CPS feedline separation $S = 30$ μm, CPS transmission line width $W = 30$ μm, and a Si_3N_4 substrate with a thickness of 1 μm, relative permittivity $\varepsilon_r = 7.6$, $\sigma_{Si_3N_4} = 0$, and $\tan\delta_e = 0.00526$ [29]. For simplicity and to investigate expected band-edge locations, a simulation was conducted with the structure modeled as a perfect electric conductor. This simulation revealed S_{21} parameters, demonstrating bandpass filtering behavior with varying band-edge locations depending on geometry, and insertion losses ranging from approximately 0.5 to 2 dB within the desired passband frequencies.

To visualize the filtering operation, electric field plots for the structure with $H_n = 40$ μm were analyzed at 1 THz (in the passband) and at 0.5 and 1.5 THz (lower and upper stopbands, respectively), shown in Fig. 6. These plots also illustrate the strong field confinement capability of the proposed SSPP structure inside the SSPP rings and grooves.

IV. Experimental Setup and Fabrication of PCS

The experimental setup used for the measurements is based on a modified THz time-domain spectroscopy (THz-TDS) system, as outlined in [27]. This system features a femtosecond pulsed laser operating at a wavelength of 780 nm, with a pulse width of 90 fs, a repetition rate of 80 MHz, and an average output power of 10 mW. The laser beam is precisely directed onto photoconductive switches (PCS) located at the transmitter (Tx) and receiver (Rx) spots on a membrane [see Fig. 2]. These switches function as the sources and detectors of THz pulses through the processes of photoconductive switching and electro-optic sampling [27].

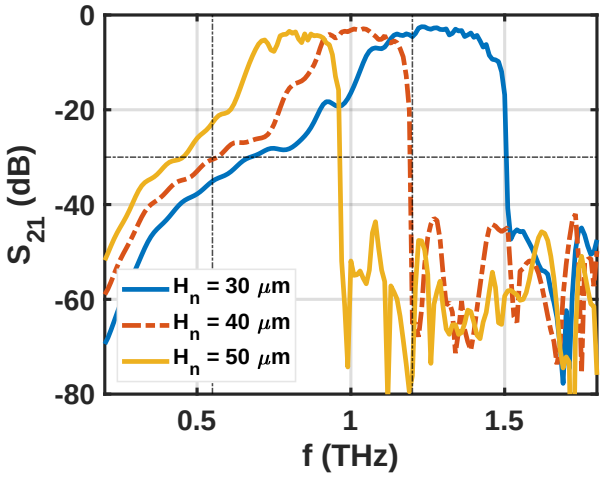

Fig. 4: Simulated S_{21} for the BPF based on SSPP rings with H_n = 30, 40, 50 μm

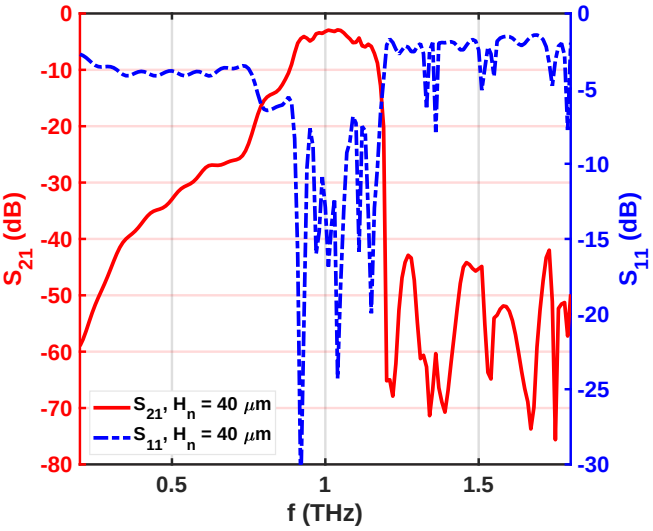

Fig. 5: Simulated S_{11} and S_{21} of the proposed BPF based on SSPP rings for the fabricated structure with H_n = 40 μm for demonstration

The PCSs measure 70 μm × 40 μm × 1.5 μm, with a 5 μm gap between the gold contacts. They are bonded using water droplets through Van der Waals (VDW) forces, as detailed in [30]. The transmitted signal is reconstructed by adjusting a mechanical delay line and measuring the receiver current with a lock-in amplifier, following the methods used in standard THz-TDS setups [14], [27].

The fabrication process for the photoconductive switches (PCSs) involves several steps. First, a low-temperature grown gallium arsenide (LT-GaAs) layer is deposited on a sacrificial aluminum arsenide (AlAs) layer, which rests on a semi-insulating GaAs substrate. Next, photolithography is applied to the LT-GaAs surface to create gold (Au) contacts. Each PCS region is masked and subjected to wet etching with citric acid and hydrogen peroxide to define the PCS thickness. After

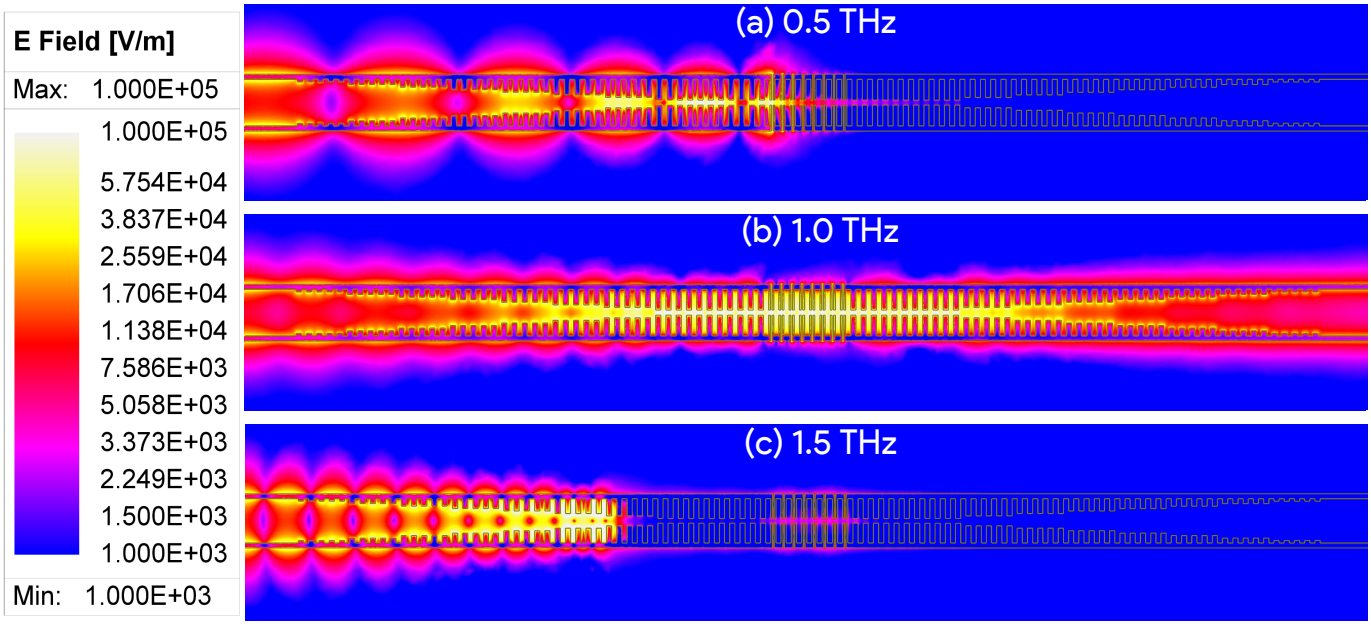

Fig. 6: Electric field plots of the proposed THz SSPP band-pass filter with H_n = 40 µm at 0.5 THz (lower stopband), 1 THz (passband), and 1.5 THz (upper stopband), illustrating passband transmission and out-of-band rejection.

cleaning and re-masking with etch-resist wax, the LT-GaAs layer is dissolved in hydrofluoric acid (HF), separating it from the AlAs layer. Further steps are taken to detach the remaining LT-GaAs film, resulting in multiple active regions of LT-GaAs PCSs [31].

V. Experimental Results and Discussion

The experimental results of the proposed SSPP-based BPF structure withH_n = 40 µm are presented in Fig. 7, showcasing both the temporal responses of the BPF and a reference CPS (transient output pulses). The reference CPS, depicted in Fig. 2, is a feedline with an equivalent length. The CPS temporal response exhibits an anticipated broadband Gaussian THz pulse, while the BPF response manifests as a narrow-band pulse with multiple oscillations. Notably, the oscillation period is approximately 1 ps, corresponding to 1 THz, the center frequency of the BPF structure. Additionally, Fig. 7 illustrates the corresponding spectral responses on a single subplot (right side) derived from applying the Discrete Fourier Transform on the temporal responses. Due to the weak output signal, the spectral response registers very low values in the dB scale (ranging from -30 dB to -70 dB). To facilitate comparison, both spectral responses are normalized by aligning them with the maximum absolute value of the reference spectrum, preserving the relative amplitude difference between the traces.

The spectral response of the BPF exhibits steep roll-off rates at the expected cut-off frequencies of 0.8 THz and 1.2 THz. The upper cut-off frequency at 1.2 THz aligns with the SSPP band-edge when H_n = 40 µm, as evidenced by dispersion curves (Fig. 3) and S-parameter simulations with sharp upper-band cut-off (Fig. 4). The lower cut-off frequency is directly influenced by the TC geometries and indirectly by H_n, as the configuration maintains a fixed number of TC stubs, with stub dimensions varying with H_n. The initial low-frequency rejection up to 0.65 THz and a lower cut-off frequency before the passband at 0.8 THz (with steep roll-off) align with simulation expectations (Fig. 5) and are observed in the measurement results.

Comparative analysis of spectral responses in Fig. 7 indicates a 10-20 dB out-of-band rejection for the BPF, lower than expected (more than 20 dB for low frequencies and more than 30 dB for upper band rejection) from simulation results. This discrepancy is mainly caused by noise levels and the relatively weak BPF output narrow band signal holding only a small portion of total pulse energy. Despite this, the measured out-of-band rejection remains acceptable. Another important parameter extracted from the measurement results is the amplitude difference between the BPF and CPS reference spectra in the passband, approximately 5 dB, consistent with minimum insertion loss expectations from S-parameter simulations (Fig. 5).

It is essential to note that spectral responses inherently exhibit amplitude decay due to the Fourier transform of finite-duration transient pulses rather than impulses with a flat spectrum [14], [27]. Thus, the BPF spectrum features a baseline resembling the reference spectral curve. Fluctuations in the measurement stem from uncorrelated system noise sources, including those from the laser, equipment, environment, and fluctuations in the PCS photo-current.

VI. Conclusion

In this work, we introduce a novel Terahertz (THz) Band Pass Filter (BPF) based on Spoof Surface Plasmon Polariton (SSPP) Split Rings, developed from Coplanar Strips (CPS) with Internal Stubs. This BPF design marks the first implementation of SSPP split rings, contributing to enhanced filtering capabilities. By leveraging CPS-SSPP integration with internal grooves and central split rings, the proposed filter achieves

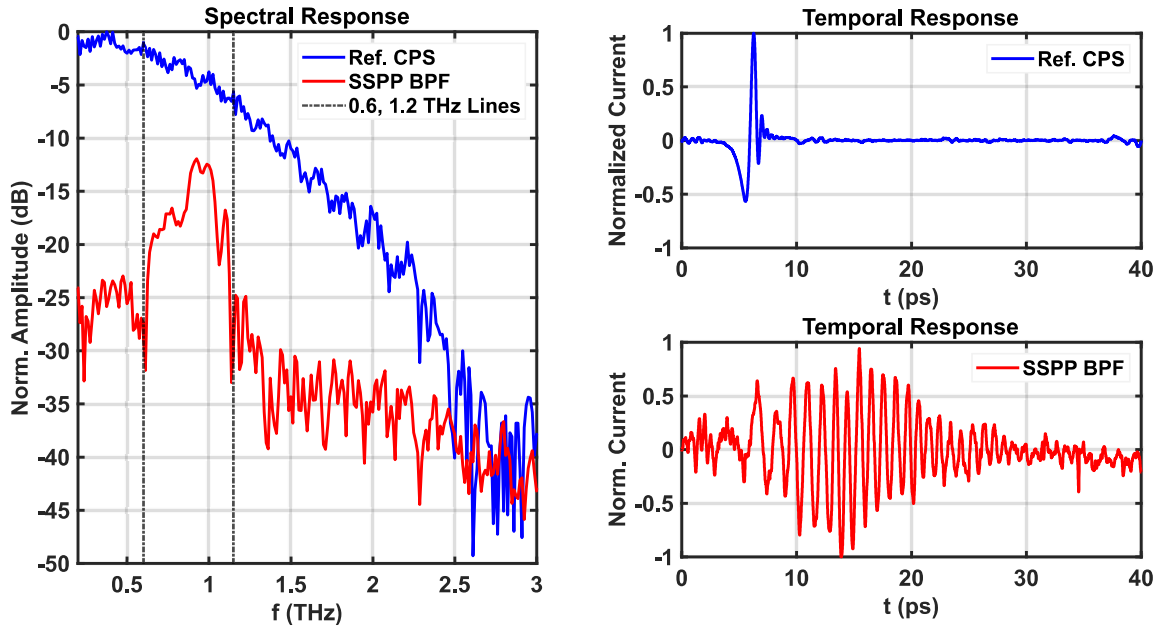

Fig. 7: Measurement results of the proposed BPF with H_n = 40 µm with a center frequency around transmission along with a reference CPS with the same length

high-frequency rejection through low-pass SSPP characteristics while effectively blocking low frequencies using strategically positioned gaps within the structure. Furthermore, the BPF's upper and lower cut-off frequencies are tunable via geometrical modifications, offering versatility in THz frequency manipulation. Experimental validation of a fabricated BPF with a center frequency of approximately 1 THz demonstrates promising performance, with measured passband transmission agreeing with simulations, thereby highlighting the effectiveness of the introduced SSPP split rings in achieving targeted filtering functionality.

REFERENCES

[1] J. B. Pendry, L. Martín-Moreno, and F. J. Garcia-Vidal, "Mimicking surface plasmons with structured surfaces," *Science*, vol. 305, no. 5685, pp. 847–848, 2004.

[2] F. J. Garcia-Vidal, L. Martín-Moreno, and J. B. Pendry, "Surfaces with holes in them: new plasmonic metamaterials," *Journal of Optics A: Pure and Applied Optics*, vol. 7, no. 2, p. S97, 2005.

[3] X. Shen, T. J. Cui, D. Martin-Cano, and F. J. Garcia-Vidal, "Conformal surface plasmons propagating on ultrathin and flexible films," *Proceedings of the National Academy of Sciences*, vol. 110, no. 1, pp. 40–45, 2013.

[4] S. A. Maier, S. R. Andrews, L. Martín-Moreno, and F. J. García-Vidal, "Terahertz Surface Plasmon-Polariton Propagation and Focusing on Periodically Corrugated Metal Wires," *Physical Review Letters*, vol. 97, no. 17, p. 176805, Oct. 2006.

[5] Y. J. Guo, K. Da Xu, and X. Tang, "Spoof plasmonic waveguide developed from coplanar stripline for strongly confined terahertz propagation and its application in microwave filters," *Optics Express*, vol. 26, no. 8, p. 10589, Apr. 2018.

[6] S. P. Singh, N. K. Tiwari, and M. J. Akhtar, "Spoof surface plasmon-based coplanar waveguide sensor for dielectric sensing applications," *IEEE Sensors Journal*, vol. 20, no. 1, pp. 193–201, 2020.

[7] X. Gao, L. Zhou, and T. J. Cui, "Odd-mode surface plasmon polaritons supported by complementary plasmonic metamaterial," *Scientific Reports*, vol. 5, no. 1, p. 9250, 03 2015.

[8] W. X. Tang, H. C. Zhang, H. F. Ma, W. X. Jiang, and T. J. Cui, "Concept, theory, design, and applications of spoof surface plasmon polaritons at microwave frequencies," *Advanced Optical Materials*, vol. 7, no. 1, p. 1800421, 2019.

[9] K.-D. Xu, Y. J. Guo, and X. Deng, "Terahertz broadband spoof surface plasmon polaritons using high-order mode developed from ultra-compact split-ring grooves," *Optics Express*, vol. 27, no. 4, p. 4354, Feb. 2019.

[10] K.-D. Xu, F. Zhang, Y. Guo, L. Ye, and Y. Liu, "Spoof Surface Plasmon Polaritons Based on Balanced Coplanar Stripline Waveguides," *IEEE Photonics Technology Letters*, vol. 32, no. 1, pp. 55–58, Jan. 2020.

[11] M. A. Unutmaz and M. Unlu, "Terahertz Spoof Surface Plasmon Polariton Waveguides: A Comprehensive Model with Experimental Verification," *Scientific Reports*, vol. 9, no. 1, p. 7616, May 2019.

[12] Y. Cinar, S. Yildirim, G. Ozsahin, M. Unutmaz, and M. Unlu, "Modelling Terahertz Spoof Surface Plasmon Polariton Waveguides Using a Circuit Model," *IEEE Transactions on Terahertz Science and Technology*, vol. 11, no. 5, pp. 557–565, Sep. 2021.

[13] B. Mazdouri, M. M. Honari, and R. Mirzavand, "Miniaturized spoof SPPs filter based on multiple resonators or 5G applications," *Scientific Reports*, vol. 11, no. 1, p. 22557, Nov. 2021.

[14] M. Haghighat, T. Darcie, and L. Smith, "Demonstration of a terahertz coplanar-strip spoof-surface-plasmon-polariton low-pass filter," *Scientific Reports*, vol. 14, 2024.

[15] S. A. Maier *et al.*, *Plasmonics: fundamentals and applications*. Springer, 2007, vol. 1.

[16] P. A. Huidobro, A. I. Fernández-Domínguez, J. B. Pendry, L. Martín-Moreno, and F. J. Garcia-Vidal, *Spoof Surface Plasmon Metamaterials*, ser. Elements in Emerging Theories and Technologies in Metamaterials. Cambridge University Press, 2018.

[17] H. F. Ma, X. Shen, Q. Cheng, W. X. Jiang, and T. J. Cui, "Broadband and high-efficiency conversion from guided waves to spoof surface plasmon polaritons," *Laser Photonics Rev.*, vol. 8, no. 1, pp. 146–151, Jan. 2014.

[18] M. A. Unutmaz and M. Unlu, "Fixed physical length spoof surface plasmon polariton delay lines for a 2-bit phase shifter," *J. Opt. Soc. Am. B*, vol. 37, no. 4, pp. 1116–1121, Mar. 2020.

[19] M. A. Unutmaz, G. Ozsahin, T. Abacilar, and M. Unlu, "Investigation of the Transitions for Coplanar Waveguide to Terahertz Spoof Surface Plasmon Polariton Waveguides," *IEEE Transactions on Antennas and Propagation*, vol. 70, no. 4, pp. 3002–3010, Apr. 2022.

[20] W. X. Tang, H. C. Zhang, H. F. Ma, W. X. Jiang, and T. J. Cui, "Concept, Theory, Design, and Applications of Spoof Surface Plasmon Polaritons at Microwave Frequencies," *Advanced Optical Materials*, vol. 7, no. 1, p. 1800421, Jan. 2019.

[21] Y. J. Guo, K. D. Xu, Y. Liu, and X. Tang, "Novel surface plasmon polariton waveguides with enhanced field confinement for microwave-frequency ultra-wideband bandpass filters," *IEEE Access*, vol. 6, pp. 10 249–10 256, 2018.
[22] J. Wang, L. Zhao, and Z.-C. Hao, "A band-pass filter based on the spoof surface plasmon polaritons and cpw-based coupling structure," *IEEE Access*, vol. 7, pp. 35 089–35 096, 2019.
[23] Y. Wei, Y. Wu, W. Wang, L. Pan, Y. Yang, and Y. Liu, "Double-sided spoof surface plasmon polaritons- line bandpass filter with excellent dual-band filtering and wide upper band suppressions," *IEEE Transactions on Plasma Science*, vol. 48, no. 12, pp. 4134–4143, 2020.
[24] Y. Liu, K.-D. Xu, J. Li, Y.-J. Guo, A. Zhang, and Q. Chen, "Millimeter-wave e-plane waveguide bandpass filters based on spoof surface plasmon polaritons," *IEEE Transactions on Microwave Theory and Techniques*, vol. 70, no. 10, pp. 4399–4409, 2022.
[25] Y. Feng, K.-D. Xu, Z. Niu, B. Zhang, L. Liu, and Y. Fan, "Ka-band waveguide bandpass filters using double-layer grounded spoof surface plasmon polaritons," *IEEE Transactions on Microwave Theory and Techniques*, pp. 1–11, 2024.
[26] H.-J. Song and N. Lee, "Terahertz communications: Challenges in the next decade," *IEEE Transactions on Terahertz Science and Technology*, vol. 12, no. 2, pp. 105–117, 2022.
[27] L. Smith and T. Darcie, "Demonstration of a low-distortion terahertz system-on-chip using a cps waveguide on a thin membrane substrate," *Optics Express*, vol. 27, no. 10, pp. 13 653–13 663, May 2019.
[28] M. Haghighat, T. E. Darcie, and L. Smith, "Terahertz cps-based spoof surface plasmon polariton filter on silicon nitride substrate," in *2023 48th International Conference on Infrared, Millimeter, and Terahertz Waves (IRMMW-THz)*, 2023, pp. 1–2.
[29] G. Cataldo, J. A. Beall, H.-M. Cho, B. McAndrew, M. D. Niemack, and E. J. Wollack, "Infrared dielectric properties of low-stress silicon nitride," *Optics Letters*, vol. 37, no. 20, pp. 4200–4202, Oct 2012.
[30] E. Yablonovitch, D. M. Hwang, T. J. Gmitter, L. T. Florez, and J. P. Harbison, "Van der Waals bonding of GaAs epitaxial liftoff films onto arbitrary substrates," *Applied Physics Letters*, vol. 56, no. 24, pp. 2419–2421, 06 1990.
[31] R. D. V. Ríos, S. Bikorimana, M. A. Ummy, R. Dorsinville, and S.-W. Seo, "A bow-tie photoconductive antenna using a low-temperature-grown gaas thin-film on a silicon substrate for terahertz wave generation and detection," *Journal of Optics*, vol. 17, no. 12, p. 125802, 2015.

Appendix E

On-Chip Glucose Sensing Using Guided Waves at Terahertz Frequencies, Copy of [3]

scientific reports

Check for updates

OPEN

On chip glucose sensing using guided waves at terahertz frequencies

Mohsen Haghighat[1,2], Thomas Darcie[1] & Levi Smith[1,2]✉

This paper demonstrates an on-chip anhydrous D-glucose sensor using a coplanar stripline (CPS) on a thin (1 μm) silicon nitride membrane at terahertz (THz) frequencies. A thin layer (≈ 10 μm) of D-glucose was placed in close proximity to the CPS and the transmission response was measured using a modified THz-TDS setup. The D-glucose introduces frequency-dependent changes to the effective permittivity of the CPS resulting in a modified spectral response at the receiver. Measurement results show absorption signatures at 1.42 THz and 2.07 THz corresponding to the first two significant resonances beyond 1 THz for D-glucose allowing for label-free detection. The frequency-dependent attenuation coefficient was estimated by simulation for several D-glucose layer thicknesses using a modified Lorentz model. Measurement results align with simulations and other literature that use free-space THz radiation. This work verifies on-chip THz sensing of D-glucose and presents a pathway toward on-chip sensing of other materials at THz frequencies.

Keywords D-glucose, Guided wave, On-chip sensing, Coplanar strip (CPS), Terahertz (THz), Thin membrane, Silicon nitride

Glucose detection is important across various industries, including the food, beverage, and medical sectors[1]. The escalating consumption of sugar in diets has been linked to chronic health issues, notably cardiovascular diseases, diabetes, and obesity[2,3]. Given the importance of these health issues, accurate detection and monitoring of glucose both in the human body and food become imperative. In response to this need, researchers have been developing glucose-sensing technologies for blood glucose monitoring in the last couple of decades[4,5]. Also, industries such as food, beverage, and fermentation manufacturing are required to shrink and control sugar levels while ensuring the quality and safety of their products[1]. This necessitates continuous monitoring and measurement of various samples, including sugars, throughout the manufacturing process and in the final product. On the other hand, selective detection of glucose is essential for investigation in the food and beverage industry because natural glucose should not be entirely replaced with artificial sweeteners since they have other health side-effects such as sugar craving and mood disorders[6]. The necessity to either control excessive sugar levels or detect natural sugars from artificial sweeteners motivates researchers to explore advanced sugar-sensing methodologies. D-glucose is one of the main sugars that exist in food and the common naturally occurring simple sugar[7]. In the context of this paper, the term 'glucose' exclusively denotes anhydrous D-glucose[8].

The pursuit of glucose sensing methods aligns with the broader objective of promoting health and well-being, either glucose detection in food, or blood glucose monitoring. Glucose sensing methods have been reviewed in[4,5,9] from traditional enzymatic and electrochemical methods to optical and spectroscopic techniques. Regarding in-body glucose sensing, the category of optical sensors is favorable for their non-invasive nature and potential for continuous monitoring. These methods include fluorescence, Raman spectroscopy, near-infrared (NIR), mid-infrared (MIR), and far-infrared (FIR) spectroscopy[5]. However, optical methods face challenges due to scattering[4,9,10] with reduced scattering coefficient of 30–50 cm^{-1}[11], contributing to signal-to-noise ratio (SNR) reduction[12], relatively weak glucose absorption peaks especially in NIR range[13], and interference from surrounding light[1]. On the other hand, THz waves have less scattering compared to IR and optical beams[10,12] with estimated reduced scattering coefficient up to 1 cm^{-1} based on analysis in[11], and have strong glucose absorption peaks[8,14] which enables easier glucose detection with higher signla-to-noise ratios[9]. Moreover, THz waves penetrate into human tissue up to 300 μm[15], potentially reaching the dermis layer where blood and glucose are present whereas the MIR range only penetrates up to 100 μm, which corresponds to the thickness of the epidermis layer that lacks blood[13]. However, glucose can still be detected in the MIR and THz range within the

[1]Department of Electrical and Computer Engineering, University of Victoria, Victoria, BC V8P 5C2, Canada. [2]Centre for Advanced Materials and Related Technology (CAMTEC), University of Victoria, Victoria, BC V8W 2Y2, Canada. ✉email: levismith@uvic.ca

interstitial fluid (ISF) of the epidermis, where a slight concentration of glucose is present but blood capillaries are not reached at this depth[13]. Absorption coefficients extracted from THz time-domain spectroscopy (THz-TDS) measurements have shown a high sensitivity to the glucose level in blood samples[16]. Additionally, THz-TDS combined with weak value amplification was demonstrated to be sensitive to small changes in concentrations of glucose both in solid and liquid samples[17,18]. However, challenges remain in terms of miniaturization and cost-effectiveness of THz sensors[5], which can be addressed by on-chip THz sensors, that are the focus of this research.

Glucose absorbs electromagnetic radiation at certain frequencies in the THz band. The first peak of absorption spectra for glucose beyond 1 THz occurs in the range of 1.40–1.44 THz[8,14,19–22]. In literature, the majority of glucose sensing methods at THz frequencies involve directing a free-space THz beam towards a thin glucose sample[8], a metasurface[20,21,23–25], or nano-antennas (i.e., also a form of metasurface)[14] coated by sugar (glucose) then detecting the transmitted wave. Using metasurfaces results in strong subwavelength field concentration at a resonance frequency, making them sensitive to small features and slight variations in the nearby environment, thereby enhancing their overall sensitivity[23]. In[24,25] authors designed metasurface unit cells that have resonance frequencies below 0.5 THz and then measured the shift in resonance frequency in the presence of glucose or other materials. Others[14,20] have designed the metasurface unit cell so that it targets the first THz-band absorption frequency of glucose near 1.4 THz. In[14] the authors proposed a metasurface for THz transmission by nano-slot-antennas which increases the molecular absorption cross-sections, thereby enabling the detection of sugar molecules at low concentrations. Table 1 provides an overview of various THz sensing methods for sugar detection including key details such as the reference source, resonance frequency in THz, frequency range covered by the sensor, structural design, mechanism of wave transmission, spectral detection method employed, and the type of sugar targeted in the respective study. Our work, highlighted as 'This Work' in Table 1, proposes on-chip glucose sensing operating in the broad frequency range of 0.1–2.2 THz, employing guided waves which as previously mentioned, is the key difference from the other works.

The aforementioned studies use free-space THz radiation for sensing which offers simplicity and flexibility in accommodating various sample geometries and configurations; however, free-space methods suffer from path loss and require bulky THz optical components[26]. Alternatively, guided-wave methods are attractive because they are compact and do not require the alignment of a THz beam. Also, a guided-wave sensor can offer lower channel loss[26] and increased sensitivity by confining the electromagnetic field within the sample region making it suitable for on-chip integrated sensors in various applications[27]. Additionally, guided-wave methods are more resilient to sample roughness and heterogeneity owing to the guided propagation of electromagnetic waves.

There are several studies that use guided waves for sensing at THz frequencies. In[28] the authors reported high-loss liquid sensing including water using a coplanar waveguide (CPW) up to 1.1 THz where the signal decays below the noise floor. A similar approach is taken with microstrip lines (MSL) in[29] for liquid sensing (i.e., water), and authors mentioned that the experimental results for frequencies greater than 1 THz are close to the noise floor, although spectral data is reported up to 1.5 THz. This is mainly due to the high loss of MSL configuration at THz frequencies and also partly because of the thickness of the waveguide cover layer[29]. Similarly, a proof-of-concept on-chip planar Goubau line, integrated with a microfluidic channel is presented in[30] to measure the permittivity of liquids up to 0.8 THz and thereby sensing different types of alcohols. The aforementioned studies demonstrate experimental measurements up-to 1.5 THz which is suitable for many applications, but does not address the need to resolve signatures at 1.42 THz and 2.07 THz for label-free glucose sensing. Additionally, there are other THz dielectric waveguide approaches for sensing reported in[31,32] that do not use of metallic conductors. Though these approaches mitigate ohmic losses, they operate at sub-1 THz frequencies and are relatively narrow band (fractional bandwidths < 45 %) making them unsuitable for glucose detection.

This work explores a unique approach for on-chip glucose sensing using guided waves via coplanar stripline (CPS) on a thin silicon nitride (Si_3N_4) substrate which presents a platform that mitigates the limitations of standard THz waveguide systems for sensing applications. A CPS is commonly used in conjunction with photoconductive switches since they are compatible with two-terminal devices which allows for excitation and detection using the sliding-contact method[33]. Also, the CPS on a thin membrane enables the interaction of the electromagnetic field with materials (such as glucose) beneath the membrane (see Fig. 1). Our experiments show the prominent THz-band absorption frequency of 1.42 THz measured with the fabricated sensor, which aligns with the absorption frequency reported in Table 1. We note that label-free sensing involves the detection of the multiple characteristic absorption signatures which occur at different frequencies and the measurement of a

References	Resonance freq. (THz)	Freq. range (THz)	Structure	Wave transmission	Spectral detection method	Sugar type
[8]	1.43, 2.08	0.3–3.0	NA (direct exposure)	Free-Space	Absorption frequency	D-glucose
14	1.4, 1.7	0.5–2.5	Nano-slot antennas	Free-Space	Absorption frequency	D-glucose, Fructose, Sucrose
20	1.43	1.2–1.6	Metasurface	Free-Space	Absorption frequency	D-glucose
21	1.435	1.2–1.6	Metasurface	Free-Space	Absorption frequency	D-glucose
24	0.26	0.2–0.5	Metasurface	Free-Space	Resonance shift	D-glucose
25	0.32	0.2–0.5	Metasurface	Free-Space	Resonance shift	D-glucose
34	0.6	0.3–1.2	Meta-material absorber	Free-Space	Resonance shift	D-glucose
This work	1.42, 2.07	0.1–2.2	CPS	Guided-Wave	Absorption frequency	D-glucose

Table 1. Summary of experimental sugar sensing methods based on THz spectroscopy.

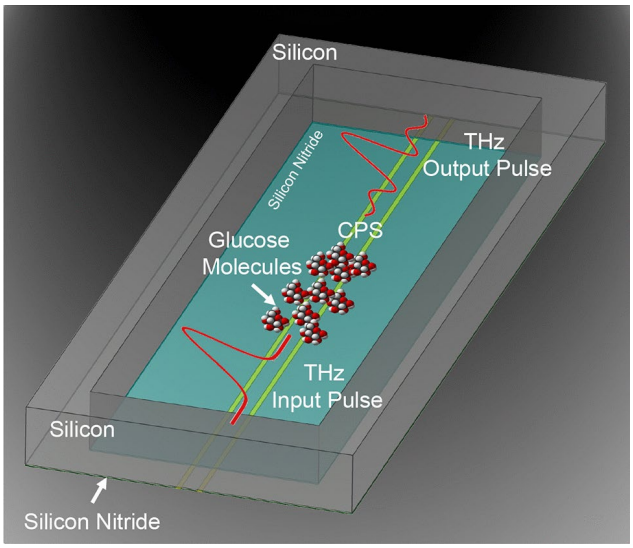

Figure 1. Illustration of glucose sensing by CPS waveguide on a thin Si_3N_4 membrane.

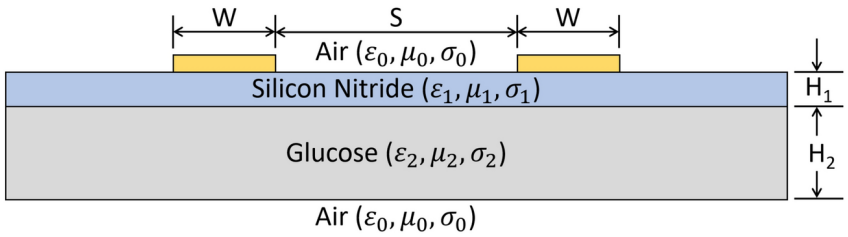

Figure 2. CPS sensor cross section.

broad spectrum facilitates this capability. To confirm label-free sensing, we simultaneously resolve the glucose absorption features at 1.42 THz and 2.07 THz.[8,19].

Results

Design, modeling, and simulation

The sensor presented in this work operates on the principle of frequency-dependent dielectric loss from a nearby material (i.e., glucose). Figure 2 illustrates a cross-section of the sensor geometry which is a CPS transmission line ($S = 130$ μm and $W = 30$ μm) on a suspended thin Si_3N_4 membrane ($H_1 = 1$ μm) which is in contact with a thin glucose layer ($H_2 \approx 10$ μm). The effective permittivity of the propagating wave, ε_{eff}, depends on the individual material parameters ($\varepsilon_{0,1,2}$, $\mu_{0,1,2}$, and $\sigma_{0,1,2}$) and the dimensions of the transmission line and substrate ($S, W, H_{1,2}$). Here, of primary concern, is detecting frequency-dependent variations in glucose permittivity, $\varepsilon_2(\omega)$, which can be achieved when the Si_3N_4 layer is thin $H_1 \approx 1$ μm.

The CPS sensor structure is fabricated by depositing a 1 μm Si_3N_4 layer on a 500 μm silicon substrate. Next, a rectangle of silicon with a dimension of 2 mm × 10 mm is etched under the structure where the sample material will be placed. Metallic conductors are placed using photolithography and metal deposition (Ti/Au: 10 nm/200 nm). The overall design of the is similar to our prior work[35]. The transmitter and receiver are photoconductive switches (PCSs) ($R_{dark} \approx 50\text{M}\Omega$) that are placed onto the CPSs to provide a low frequency bias for the transmitter and a method to sample the transmitted electric field at the receiver. The transmitter is directly connect to a DC voltage supply (24V). The receiver is directly connected to the current input of a lock-in amplifier (1 kHz reference to optical chopper, 300 ms integration time). Note that care must be taken to eliminate cavities, i.e, the bias lines bend to radiate undesired signals and mitigate resonances, and the receiving PCS is placed at a junction to ensure the reflections occurring from the separate conductor and substrate discontinues are not resolved.

In this study, we incorporate a frequency-dependent permittivity model for glucose[21] into the existing model of a CPS that is depicted in Fig. 2. Our objective is to obtain the attenuation coefficient of the CPS for glucose layers of varying thicknesses for frequencies ranging from 0.5 to 2.5 THz. The simulation was performed using ANSYS HFSS 2023 and characterizes the CPS behavior in the presence of glucose at different frequencies and thicknesses. The material properties of the model components include the Si_3N_4 substrate with 1 μm thickness and $\varepsilon_r = 7.6$, $\sigma_{Si_3N_4} = 0$, $\tan\delta_e = 0.00526$[36], and gold conductors with 200 nm thickness and the conductivity of $\sigma_{Au} = 4.1 \times 10^7$ S/m. The dielectric permittivity of the glucose layer with single resonance at THz frequencies

was previously modeled using the modified Lorentz model, which is widely used for modeling a single resonance in material's permittivity, as presented in[21].

Our work includes the second resonance of glucose to the glucose Lorentz model as observed in[14] and also our experiments. Equation (1) shows the relation of this permittivity model with two resonances:

$$\varepsilon(\omega) = \varepsilon_\infty + \frac{\omega_p^2}{\omega_{0,1}^2 - \omega^2 + i\gamma_1\omega} + \frac{\omega_p^2}{\omega_{0,2}^2 - \omega^2 + i\gamma_2\omega} \tag{1}$$

where $\varepsilon_\infty = 3.231$ is the dielectric coefficient at infinite frequency[21], $\omega_{0,1} = 2\pi(1.42\,\text{THz})$ is the first resonance frequency beyond 1 THz, $\omega_{0,2} = 2\pi(2.07\,\text{THz})$ is the first resonance frequency, $\omega_p = 2\pi(0.11\,\text{THz})$ is bulk plasma frequency of the dielectric for the thin film of glucose, $\gamma_1 = 2\pi(0.04\,\text{THz})$ and $\gamma_2 = 2\pi(0.08\,\text{THz})$ represents the corresponding damping constant at the resonance frequencies.

Next, we simulated the attenuation coefficient for the CPS illustrated in Fig. 3a with a glucose layer (ε_2 in Fig. 2) using (1) for several different glucose thicknesses ($H_2 = 5$, 10, 15 μm). The results of this simulation are plotted in Fig. 3b along with a reference without any glucose which has an attenuation of ≈ 0.6 dB/mm at 1.4 THz. As previously mentioned, the average thickness of glucose is ≈ 10 μm based on the average of the profile plot in Fig. 6 measured by a profilometer along the top CPS line depicted on the inset. According to Fig. 3b this thickness corresponds to an attenuation depth of ≈ 4.5 dB/mm which is the height of the absorption peak at 1.42 THz and attenuation of ≈ 2.2 dB/mm at 2.07 THz.

As observed in Fig. 6, there are step-like discontinuities in the thickness of the glucose layer. This nonideality will be mitigated in future works; however, the effect is investigated here. To quantify the impact, we performed full-wave simulations using ANSYS HFSS to obtain the S-parameters for step discontinuities for several glucose layer thicknesses ($H_2 = 0$, 5, 10, 15, 20 μm). The simulation data is found in the Supplementary Material S1. For a glucose layer thickness of 10 μm at 1.4 THz we found that the insertion loss is less than 0.7 dB and the return loss is greater than 22 dB which ensures the discontinuities will not drastically degrade the sensor performance.

Experimental results and discussion

The measurement results of unloaded (no glucose) and loaded sensor (with ≈ 10 μm glucose layer) are shown in Fig. 4. Note that the spectral amplitude decay with increasing frequency in the experimental results is an expected consequence of applying a THz finite duration pulse as an input signal rather than an ideal THz impulse with a flat spectral response[37]. From the simulations (Fig. 3b), the depth of peak absorption should be approximately 3 mm × 4.5 dB/mm = 13.5 dB which is observed in measurement results (spectral response in Fig. 4). We find our experimental peak absorption frequency (1.42 THz) lies within the range (1.40–1.435 THz) found in other literature (see Table 1).

The frequency-dependent absorption observed in experimental results demonstrates the sensor functionality. It is important to recognize that this work is primarily a proof-of-concept and that future methods will be developed to improve sensitivity through the optimization of sample distribution methodology and circuit topology. We note that glucose shows broad absorption starting from 1.10 THz up to around 1.28 THz[8,14,19]. This is observed in Fig. 4 as a minor depression before the main peak at 1.42 THz. Moreover, another THz

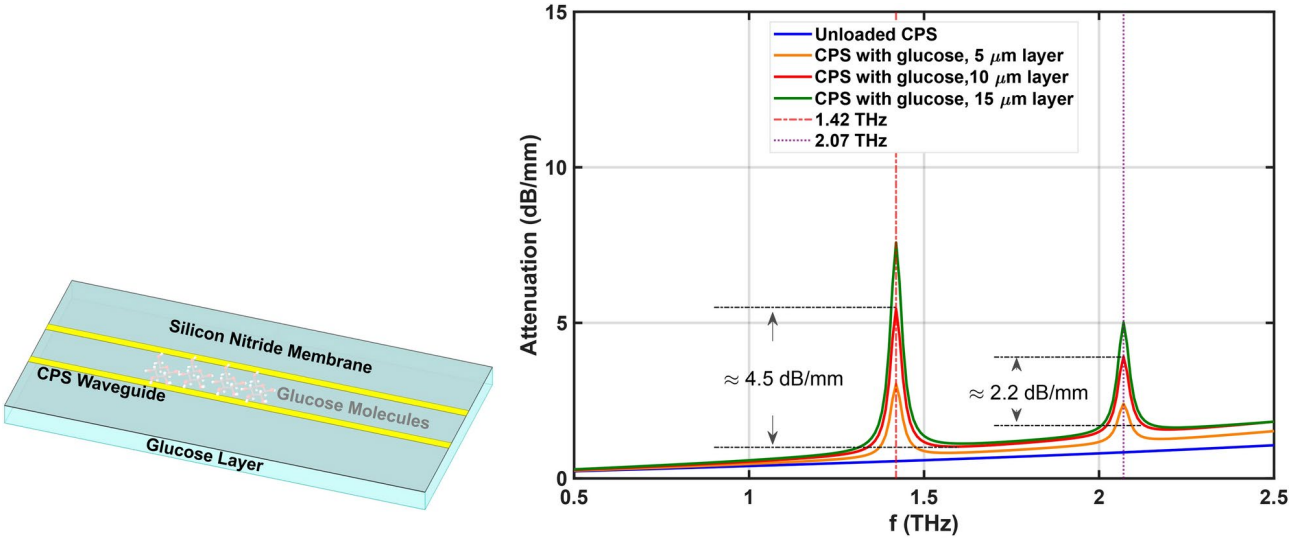

Figure 3. (**a**) CPS on the thin membrane with glucose layer. (**b**) Attenuation of CPS with modified Lorentz model for glucose layer with different thicknesses under the sensor's thin membrane.

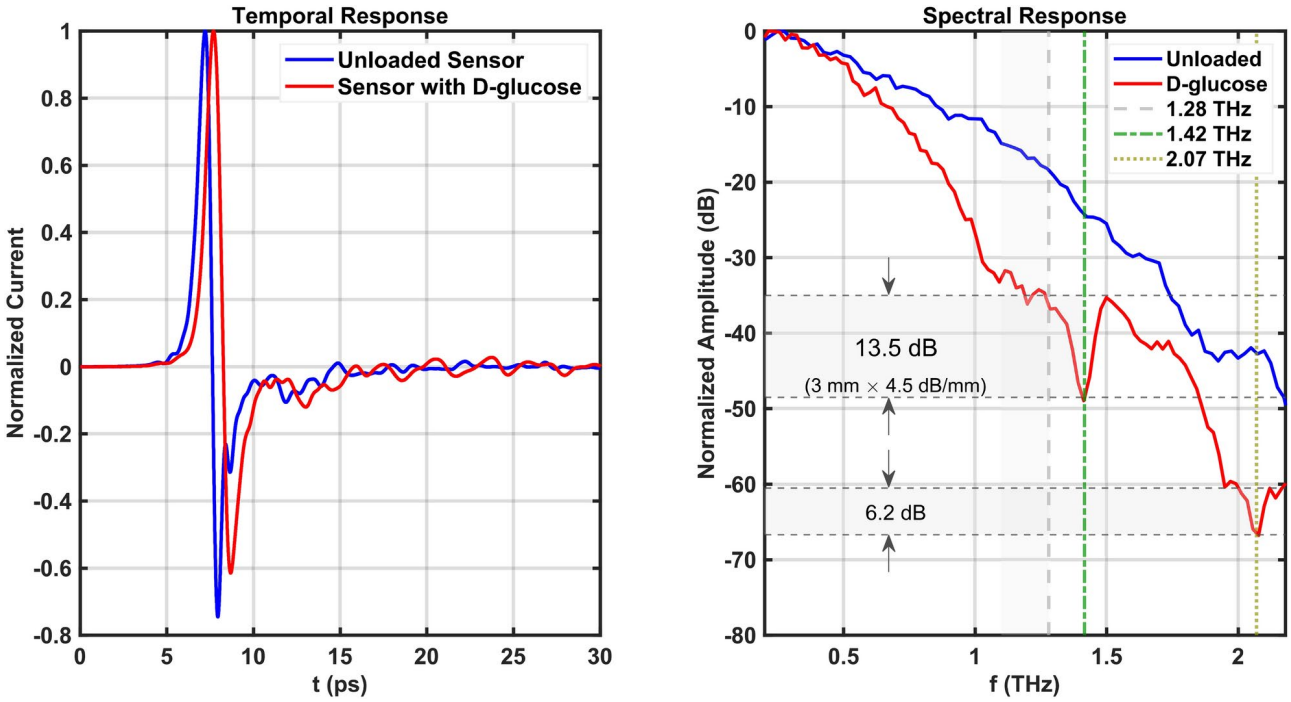

Figure 4. Measurement results of the proposed CPS-based glucose sensor.

absorption peak of glucose at 2.07 THz is observed in the measurement results and is expected to occur at 2.05–2.10 THz[8,14,19,20]. We predict the attenuation of the dip at 2.07 THz relative to the attenuation at 1.42 THz using the data from[14] which results in an expected attenuation of ≈ 5.8-6.6 dB at 2.07 THz. As shown in Fig. 4 the experimental results find a depth of absorption peak is ≈ 6.2 dB which is within reasonable agreement with the expected value.

It is important to consider practical aspects of sensors. The broadband nature of the received spectrum has several benefits which can reduce the probability of false positives and false negatives. First, the absorption at 1.42 THz can be measured relative to the adjacent region of the spectrum (i.e., 1.5 THz), but this method would be susceptible to false positives since other materials, such as sucrose, exhibit weak absorption characteristics near 1.4 THz. However, since the presented sensor is capable of resolving broad spectral information that corresponds to two signatures for glucose (1.42 THz and 2.07 THz) it becomes straightforward to reduce the probability of false positives by verifying that both signatures exist simultaneously with the appropriate relative magnitudes. Next, the sensor can exhibit false negatives if the glucose film is poorly distributed away from the CPS. Our proof-of-concept sensor is susceptible to this issue [see Fig. 5b] due to our current drop-coating method. After a precise method for uniformly distributing the glucose layer is developed, then it will become possible to determine the thickness of the glucose layer (without using a profilometer) by measuring the magnitude of attenuation at the absorption peaks. Also, we have begun investigating alternative microfluidic methods to address this issue and to develop a pathway towards measuring glucose level monitoring (in blood or aqueous solution) - both of which are beyond the scope of this work.

Conclusion

An on-chip glucose sensor is demonstrated using guided waves at THz frequencies on a thin Si_3N_4 membrane. The sensor is based on the interaction between the propagating electromagnetic waves at THz frequencies and a thin layer of glucose placed in close proximity to a transmission line which results in frequency-dependent notches in the received spectrum. Our experiments reveal a resonance at 1.42 THz and 2.07 THz which aligns with findings in existing literature. Our approach stands out for its guided-wave nature and on-chip microfluidic integration potential. This work demonstrates pathways towards on-chip label-free sensing of glucose and other materials with applications such as the food industry and healthcare.

Methods

Sample preparation

We made a mixture of glucose and isopropanol (5 g: 50 mL) and sonicated that in a beaker to reduce the grain size. Then, we placed drops of the liquid using a micropipette in steps of 10 µL on the backside of the membrane and waited for the isopropanol to evaporate. Figure 5 illustrates microscopic and close-up photos of the sensor with and without glucose on the backside of the membrane. The thickness of the resulting glucose layer was measured using a profilometer (Fig. 6) after placing 60 µL of the mix. It is important to note that with our current simple drop placement methodology precise control of the glucose distribution was not possible. Future work will address this limitation by the introduction of lithographically-defined microfluidic channels. For this

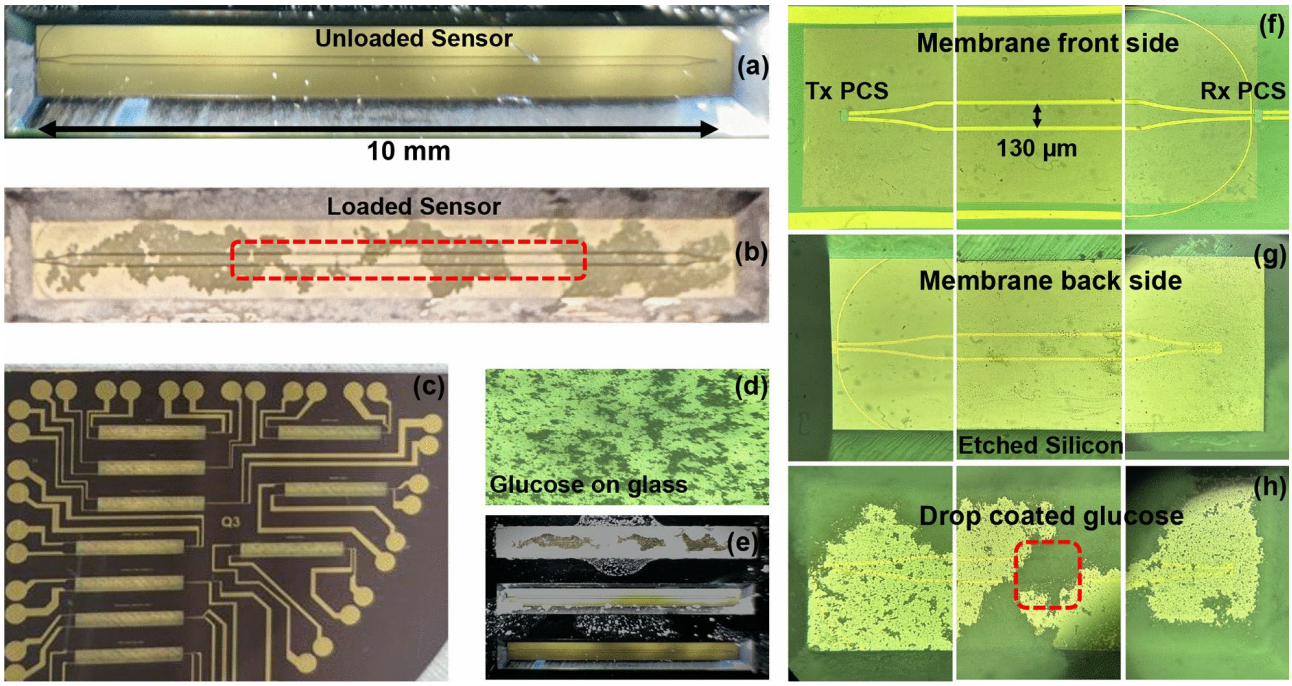

Figure 5. Sensor and membrane pictures. (**a**) Clean (unloaded) membrane back side. (**b**) Dehydrated glucose on the back side membrane (loaded sensor). (**c**) Fabricated wafer. (**d**) glucose grains on a glass after 10 min of sonication with isopropanol. (**e**) CPS sensor windows (wafer backside). (**f**) Membrane front: CPS side microscope image. (**g**) Membrane back: Material side microscope image. (**h**) Membrane back image with dried drop-coated glucose with a micropipette.

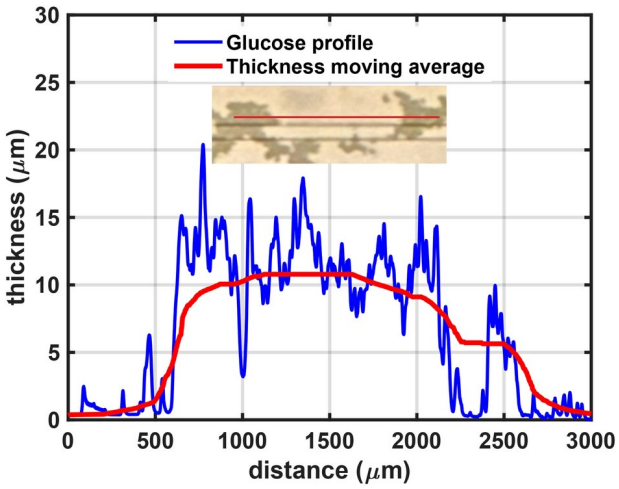

Figure 6. Thickness profile of the glucose layer, and back side of the Si_3N_4 membrane with non-uniform drop-coated glucose (inset).

specific experiment, the glucose film thickness is $H_2 \approx 10$ μm, and the glucose interaction length is $L \approx 3$ mm (Fig. 5b). We note that to avoid absorption saturation, a thin sample layer is desired[8].

Experimental setup

The experimental measurements were carried out using a modified THz-TDS setup that is in Fig. 7[37,38]. A femtosecond pulsed laser with a wavelength of 780 nm and average output power of 20 mW was split and directed towards thin-film low-temperature grown gallium arsenide (LT-GaAs) photo-conductive switches (PCS) placed on both sides of the tapered CPS to generate and detect a broadband THz pulse signal[37]. The fabrication of the LT-GaAs PCS devices is detailed in[38,39]. The transmitted signal was reconstructed by photo-conductive sampling of the output of the THz pulse, using the mechanical delay line and measuring the receiver

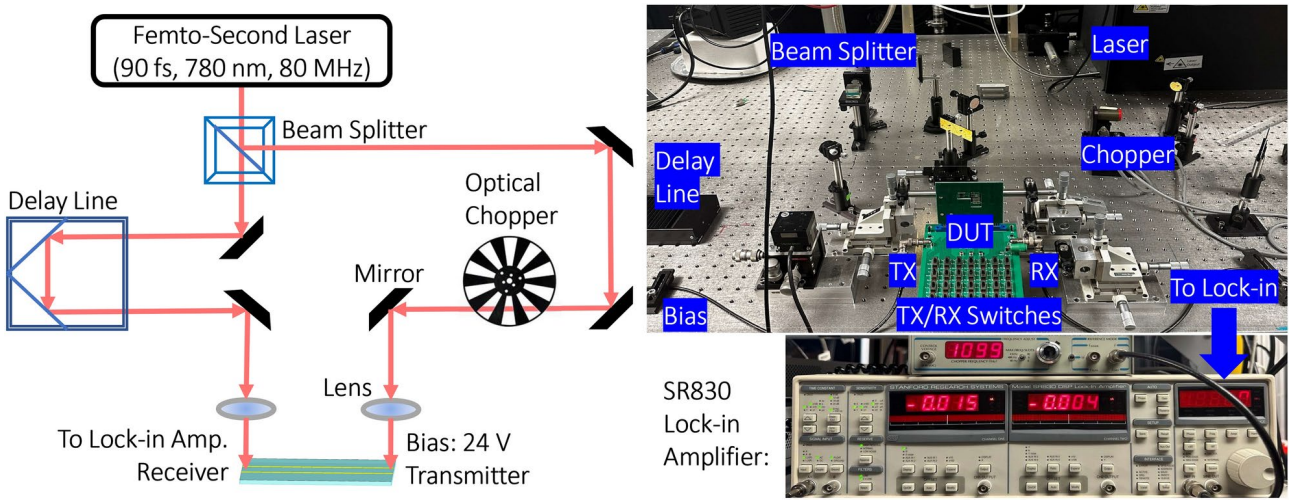

Figure 7. Measurement setup picture and diagram for glucose sensing.

current using a lock-in amplifier, similar to conventional THz-TDS techniques[40]. Other specific details about the experiment are the optical chopping frequency of 1 KHz and the bias voltage of transmitting PCS of 24 Volts.

Data availability

Data is provided within the supplementary information files.

Received: 8 July 2024; Accepted: 28 November 2024
Published online: 05 December 2024

References

1. Hassan, M. H., Vyas, C., Grieve, B. & Bartolo, P. Recent advances in enzymatic and non-enzymatic electrochemical glucose sensing. *Sensors* **21**. https://doi.org/10.3390/s21144672 (2021).
2. Mozaffarian, D. Dietary and policy priorities for cardiovascular disease, diabetes, and obesity. *Circulation* **133**, 187–225. https://doi.org/10.1161/CIRCULATIONAHA.115.018585 (2016).
3. Ventura, E. E., Davis, J. N. & Goran, M. I. Sugar content of popular sweetened beverages based on objective laboratory analysis: Focus on fructose content. *Obesity* **19**, 868–874. https://doi.org/10.1038/oby.2010.255 (2011).
4. Oliver, N. S., Toumazou, C., Cass, A. E. G. & Johnston, D. G. Glucose sensors: A review of current and emerging technology. *Diab. Med.* **26**, 197–210. https://doi.org/10.1111/j.1464-5491.2008.02642.x (2009).
5. Di Filippo, D., Sunstrum, F. N., Khan, J. U. & Welsh, A. W. Non-invasive glucose sensing technologies and products: A comprehensive review for researchers and clinicians. *Sensors* **23**. https://doi.org/10.3390/s23229130 (2023).
6. Choi, Y., Lee, S., Lee, S., Hong, S. & Kwon, H. W. Bioelectronic tongues mimicking insect taste systems for real-time discrimination between natural and artificial sweeteners. *ACS Sensors* **7**, 3682–3691. https://doi.org/10.1021/acssensors.2c01254 (2022).
7. American Chemical Society. D-glucose. https://www.acs.org/molecule-of-the-week/archive/g/d-glucose.html (2012).
8. Liu, H.-B. & Zhang, X.-C. Dehydration kinetics of d-glucose monohydrate studied using thz time-domain spectroscopy. *Chem. Phys. Lett.* **429**, 229–233. https://doi.org/10.1016/j.cplett.2006.07.100 (2006).
9. Li, Y. & Chen, Y. Review of noninvasive continuous glucose monitoring in diabetics. *ACS Sens.* **8**, 3659–3679. https://doi.org/10.1021/acssensors.3c01538 (2023).
10. Pickwell, E. & Wallace, V. P. Biomedical applications of terahertz technology. *J. Phys. D Appl. Phys.* **39**, R301. https://doi.org/10.1088/0022-3727/39/17/R01 (2006).
11. Jacques, S. L. Optical properties of biological tissues: a review. *Phys. Med. Biol.* **58**, R37. https://doi.org/10.1088/0031-9155/58/11/R37 (2013).
12. Truong, N. C. D., Shahdadian, S., Kang, S., Wang, X. & Liu, H. Influence of the signal-to-noise ratio on variance of chromophore concentration quantification in broadband near-infrared spectroscopy. *Front. Photon.* **3**. https://doi.org/10.3389/fphot.2022.908931 (2022).
13. Kottmann, J., Rey, J. M., Luginbühl, J., Reichmann, E. & Sigrist, M. W. Glucose sensing in human epidermis using mid-infrared photoacoustic detection. *Biomed. Opt. Express* **3**, 667–680. https://doi.org/10.1364/BOE.3.000667 (2012).
14. Lee, D. et al. Highly sensitive and selective sugar detection by terahertz nano-antennas. *Sci. Rep.* **5**. https://doi.org/10.1038/srep15459 (2015).
15. Vilagosh, Z., Lajevardipour, A. & Wood, A. W. Computational phantom study of frozen melanoma imaging at 0.45 terahertz. *Bioelectromagnetics* **40**, 118–127. https://doi.org/10.1002/bem.22169 (2019).
16. Chen, H. et al. Quantify glucose level in freshly diabetic's blood by terahertz time-domain spectroscopy. *J. Infrared Milli Terahz Waves* **39**, 399–408. https://doi.org/10.1007/s10762-017-0462-2 (2018).
17. Lu, X. et al. Weak value amplified precision terahertz spectroscopic detection of solid and liquid glucose samples. *ACS Photon.* **10**, 3149–3160. https://doi.org/10.1021/acsphotonics.3c00525 (2023).
18. Lykina, A. A. et al. Terahertz spectroscopy of diabetic and non-diabetic human blood plasma pellets. *J. Biomed. Opt.* **26**, 043006–043006 (2021).
19. Song, C. et al. Terahertz and infrared characteristic absorption spectra of aqueous glucose and fructose solutions. *Sci. Rep.* **8**. https://doi.org/10.1038/s41598-018-27310-7 (2018).
20. Jaber, A. et al. Hybrid architectures for terahertz molecular polaritonics. *Nat. Commun.* **15**. https://doi.org/10.1038/s41467-024-48764-6 (2024).

21. Lee, G., Cho, Y. & Ok, G. Improved analysis of thz metamaterials for glucose sensing based on modified lorentz dispersion model. *Spectrochim. Acta Part A Mol. Biomol. Spectrosc.* **293**, 122519. https://doi.org/10.1016/j.saa.2023.122519 (2023).
22. Huang, H., Shao, S., Wang, G., Su, B. & Zhang, C. Terahertz spectral properties of glucose and two disaccharides in solid and liquid states. *iScience* **25**, 104102. https://doi.org/10.1016/j.isci.2022.104102 (2022).
23. Beruete, M. & Jáuregui-López, I. Terahertz sensing based on metasurfaces. *Adv. Opt. Mater.* **8**. https://doi.org/10.1002/adom.201900721 (2019).
24. Yang, J. et al. A terahertz metamaterial sensor used for distinguishing glucose concentration. *Res. Phys.* **26**, 104332. https://doi.org/10.1016/j.rinp.2021.104332 (2021).
25. Serita, K., Murakami, H., Kawayama, I. & Tonouchi, M. A terahertz-microfluidic chip with a few arrays of asymmetric meta-atoms for the ultra-trace sensing of solutions. *Photonics* **6**, 12. https://doi.org/10.3390/photonics6010012 (2019).
26. Zeng, H. et al. A review of terahertz phase modulation from free space to guided wave integrated devices. *Nanophotonics* **11**, 415–437. https://doi.org/10.1515/nanoph-2021-0623 (2022).
27. Singh, S. P., Tiwari, N. K. & Akhtar, M. J. Spoof surface plasmon-based coplanar waveguide sensor for dielectric sensing applications. *IEEE Sens. J.* **20**, 193–201 (2020).
28. Cabello-Sánchez, J., Drakinskiy, V., Stake, J. & Rodilla, H. On-chip characterization of high-loss liquids between 750 and 1100 ghz. *IEEE Trans. Terahertz Sci. Technol.* **11**, 113–116. https://doi.org/10.1109/TTHZ.2020.3029503 (2021).
29. Ohkubo, T., Onuma, M., Kitagawa, J. & Kadoya, Y. Micro-strip-line-based sensing chips for characterization of polar liquids in terahertz regime. *Appl. Phys. Lett.* **88**, 212511. https://doi.org/10.1063/1.2207989 (2006).
30. Swithenbank, M. et al. On-chip terahertz-frequency measurements of liquids. *Anal. Chem.* **89**, 7981–7987. https://doi.org/10.1021/acs.analchem.7b01235 (2017).
31. Reck, T. J., Jung-Kubiak, C., Gill, J. & Chattopadhyay, G. Measurement of silicon micromachined waveguide components at 500–750 ghz. *IEEE Trans. Terahertz Sci. Technol.* **4**, 33–38. https://doi.org/10.1109/TTHZ.2013.2282534 (2014).
32. Farahabadi, S. A. H. et al. Sub-terahertz silicon-based on-chip absorption spectroscopy using thin-film model for biological applications. Sci. Rep. **12**. https://doi.org/10.1038/s41598-022-21015-8 (2022).
33. Grischkowsky, D. et al. Capacitance free generation and detection of subpicosecond electrical pulses on coplanar transmission lines. *IEEE J. Quant. Electron.* **24**, 221–225. https://doi.org/10.1109/3.116 (1988).
34. Hu, X. et al. Metamaterial absorber integrated microfluidic terahertz sensors. *Laser Photon. Rev.* **10**, 962–969. https://doi.org/10.1002/lpor.201600064 (2016).
35. Smith, L., Gomma, W., Esmaeilsabzali, H. & Darcie, T. Tapered transmission lines for terahertz systems. *Opt. Express* **29**, 17295–17303. https://doi.org/10.1364/OE.421008 (2021).
36. Cataldo, G. et al. Infrared dielectric properties of low-stress silicon nitride. *Opt. Lett.* **37**, 4200–4202. https://doi.org/10.1364/OL.37.004200 (2012).
37. Smith, L. & Darcie, T. Demonstration of a low-distortion terahertz system-on-chip using a cps waveguide on a thin membrane substrate. *Opt. Express* **27**, 13653–13663. https://doi.org/10.1364/OE.27.013653 (2019).
38. Haghighat, M., Darcie, T. & Smith, L. Demonstration of a terahertz coplanar-strip spoof-surface-plasmon-polariton low-pass filter. *Sci. Rep.* **14**. https://doi.org/10.1038/s41598-023-50599-y (2024).
39. Ríos, R. D. V., Bikorimana, S., Ummy, M. A., Dorsinville, R. & Seo, S.-W. A bow-tie photoconductive antenna using a low-temperature-grown gaas thin-film on a silicon substrate for terahertz wave generation and detection. *J. Opt.* **17**, 125802. https://doi.org/10.1088/2040-8978/17/12/125802 (2015).
40. Jepsen, P., Cooke, D. & Koch, M. Terahertz spectroscopy and imaging - modern techniques and applications. *Laser Photon. Rev.* **5**, 124–166. https://doi.org/10.1002/lpor.201000011 (2011).

Acknowledgements

This work was supported by an NSERC Discovery Grant. The authors thank 4D LABS at Simon Fraser University for the fabrication of the CPS waveguides and the thin membrane, and also the Centre for Advanced Materials and Related Technology (CAMTEC) at the University of Victoria for providing Nanofab facilities for the fabrication of the PCS devices. We thank Jean-Michel Ménard (and Ahmed Jaber) from the University of Ottawa for the inspiring discussions.

Author contributions

M.H. conducted the modeling and simulations, fabricated PCS devices, designed and performed the experiments, and prepared an early draft of the manuscript. T.D. provided guidance and advice on the concept and writing. L.S. offered insights on the main idea, theory, fabrication, and experiments, and revised the writing. All authors have reviewed the manuscript.

Declarations

Competing interests

The authors declare no competing interests.

Additional information

Supplementary Information The online version contains supplementary material available at https://doi.org/10.1038/s41598-024-81731-1.

Correspondence and requests for materials should be addressed to L.S.

Appendix F

On-Chip Guided-Wave THz SSPP Sensor with Absorption and Permittivity Sensing Mechanisms

On-Chip Guided-Wave Terahertz Spoof Surface Plasmon Polariton Sensor with Absorption and Permittivity Sensing Mechanisms

Mohsen Haghighat[1,2], Thomas Darcie[1], Levi Smith[1,2*]

[1]Department of Electrical and Computer Engineering, University of Victoria, 3800 Finnerty Rd, Victoria, V8P 5C2, BC, Canada.
[2]Centre for Advanced Materials and Related Technology (CAMTEC), University of Victoria, 3800 Finnerty Rd, Victoria, V8W 2Y2, BC, Canada.

*Corresponding author(s). E-mail(s): levismith@uvic.ca;

Abstract

This paper introduced a novel on-chip Terahertz (THz) sensor based on the Spoof Surface Plasmon Polariton (SSPP) waveguide. The proposed sensor shows a low-pass behavior with a band edge at 1.7 THz and strong field confinement in the 1.0-1.6 THz range. This confined field is capable of effectively interacting with surrounding materials. Absorption signatures in this frequency range sensitively absorb the power. We used Glucose as an example for a demonstration of this effect in which intermolecular resonances result in absorption at $\approx$ 1.4 THz. Using the same device, the thickness of the glucose film (or the effective mass of glucose at the sensing area) alters the permittivity of the dielectric, leading to a shift in the band edge of the spectrum. This change results in time-delay variations in the temporal response, which we demonstrate experimentally. Additionally, we employed another sensor with a band-edge frequency at 0.72 THz, where glucose exhibits a relatively constant permittivity, to examine the effect of band-edge variation with the material's average thickness, which is correlated to the effective permittivity. This work introduces the first THz sensing method based on SSPP, combining both resonance shift and absorption sensing mechanisms simultaneously.

Keywords: Terahertz (THz), Effective Permittivity, Sensor, Coplanar Strip (CPS), Spoof Surface Plasmon Polaritons (SSPP), CPS-SSPP, Field Confinement, Thin Membrane, Silicon Nitride

1 Introduction

Terahertz (THz) sensors have gained significant attention for their potential in highly sensitive non-invasive sensing applications based on THz spectroscopy [1, 2]. Among these, sensors based on spoof surface plasmon polaritons (SSPPs) offer unique advantages, including strong field confinement and enhanced interaction with the target analyte [3]. SSPPs enable the design of versatile and miniaturized THz systems, making them suitable for applications in healthcare, food safety, and chemical analysis. Several previous studies have investigated free space SSPP excitations or guided wave methods at the microwave range [1, 3–5]. Yet there is a gap in the investigation of on-chip guided-wave SSPP sensing methods. This work focuses on the development of SSPP-based on-chip THz sensors for glucose detection as a proof-of-concept material, which has not been investigated by SSPP-based sensors already proposed in the literature [2, 6].

Glucose sensing is essential in various industries, including the medical and food sectors. Escalating sugar consumption in modern diets has been linked to chronic health issues such as cardiovascular diseases, diabetes, and obesity [7, 8]. This necessitates accurate and reliable glucose detection methods. In this study, glucose is chosen as the model analyte due to its widespread significance in both health monitoring and food quality control.

Traditional glucose detection methods, including enzymatic and electrochemical techniques, have limitations such as short lifespan, complex handling, and limited portability [9]. Recent advancements have explored optical methods such as fluorescence, Raman spectroscopy, and infrared spectroscopy, which are non-invasive but face

challenges like scattering, weak absorption peaks, and interference from ambient light [10, 11]. THz sensing, particularly with SSPP structures, addresses these challenges by providing strong glucose absorption peaks and reduced scattering [12, 13].

SSPP-based sensors leverage the interaction between electromagnetic waves and engineered periodic structures to confine and enhance the electric field near the sensor surface. This feature makes SSPP structures highly sensitive to small variations in the dielectric properties of the target analyte, such as glucose [3]. Additionally, SSPP-based sensors are compatible with on-chip fabrication technologies, enabling integration with electronic systems for portable and real-time glucose monitoring.

Glucose serves as an ideal proof-of-concept material to validate the performance of SSPP-based sensors due to its well-characterized dielectric properties and strong absorption in the THz range [14]. In the THz domain, glucose exhibits distinct absorption peaks, facilitating its detection even at low concentrations [15]. Moreover, its relevance to both healthcare and food safety ensures the practical applicability of SSPP-based sensing technologies.

This paper presents the design and experimental validation of an SSPP-based on-chip THz sensor for glucose detection. The sensor demonstrates high sensitivity and selectivity, paving the way for broader applications in material sensing. Figure 1 shows the fabricated sensor structure, and Figure 2 depicts the filed plot of the structure indicating strong confined filed at the central area of the sensor, which is beneficial for effective interaction with surrounding materials.

2 Design

Two primary approaches can be employed for designing SSPP-based sensors. The first approach, which is relatively underexplored in the literature, involves leveraging the confined field within the transmission band of the structure to target the absorption frequency peak or vibrational resonance of the material. The second approach focuses

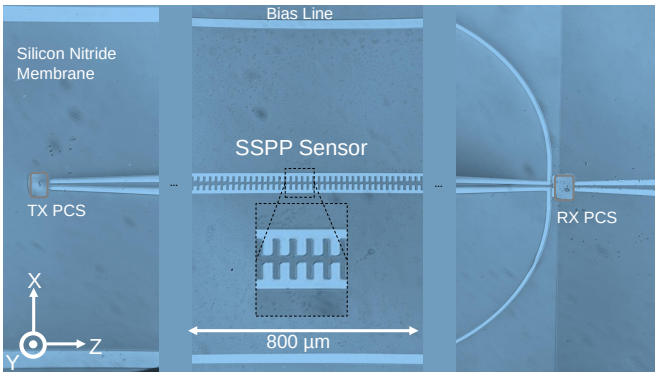

Fig. 1 Fabricated SSPP sensor based on CPS with internal corrugations

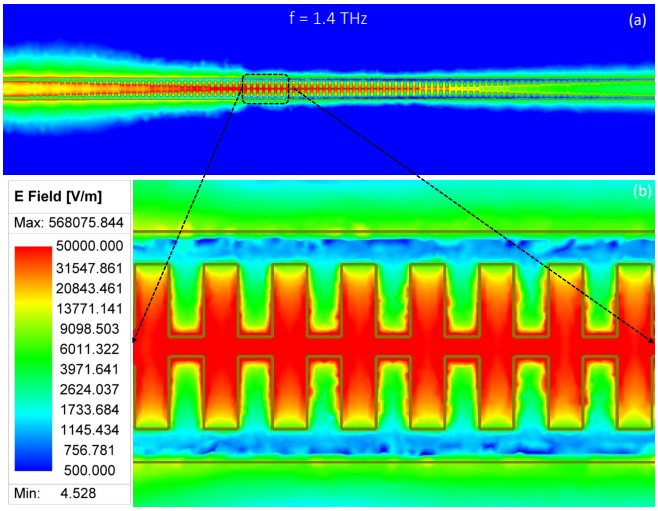

Fig. 2 Electric field plots of the structure showing strong field confinement at the central area of the SSPP sensor. (a) Entire structure. (b) Zoomed on the central area.

on identifying a frequency range where the permittivity of the sample remains relatively constant and detecting shifts in the band-edge frequency (resonance frequency) of the SSPP structure, which vary depending on the concentration or thickness of the target substance.

In order to seek the first approach, We design the proposed SSPP unit cell, such that it has a specific band-edge frequency as we know the field confinement is maximum at that frequency, depending on the material under test. This can be achieved using

the dispersion relation of the SSPP. As presented in [16, 17] the dispersion relation can be approximated by (for a surface wave propagating along the Z-direction): $k_z = k_{eff}\sqrt{1 + (a^2/d^2)\tan^2(k_{eff}H)}$, where H is the length of SSPP stubs inside of the CPS (i.e. depth of grooves), d is the period of corrugation, W_s is the width of the stubs, $a = d - W_s$ is the aperture or the width of grooves, $k_{eff} = \omega\sqrt{\varepsilon_{eff}}/c$ is the effective wavenumber, ε_{eff} is the effective relative permittivity (for the CPS feedlines on thin Silicon Nitride membrane $\varepsilon_{eff} \approx 1.9$ based on the simulations at THz frequencies), and c is the speed of light. This dispersion relation shows that the band-edge and asymptotic frequency of SSPP structures is mainly controlled by H and provides a reasonable approximation to the design of SSPP made by rectangular grooves [18, 19].

Now that we have an approximation of the dispersion relation at our disposal, suppose that we want the structure to have band-edge frequencies at about 1.7 THz for the first approach and 0.7 THz for the second approach, given the glucose permittivity model [20].

We fix the values of d = 20, 50 µm and a =10, 30 µm as they should be much smaller than the wavelength of operation [18, 21, 22]. Then, we numerically solve the dispersion relation to find the value of H. The calculation results in rounded values of H = 22 µm and 65 µm for the band-edge frequency at 1.7 THz and 0.7 THz, respectively. The gap between the internal stub tips is fixed to be 10 µm for both of the sensors. Smaller gaps can slightly affect the band edge as a result of creating shunt capacitance between the mutual stubs [16].

Based on the simulations, increasing the number of SSPP stubs, N, enhances the slope of the band-edge, however, there are only moderate improvements in roll-off rates for $N > 9$ [23]. Large N values can guarantee a sharp band-edge, but in practice, it can increase the insertion loss as the length of the SSPP waveguide increases. For the lower bound, $N < 5$ decreases the slope of roll-off and reduces the area with enhanced field confinement which are the primary benefits of SSPP [16, 24].

Table 1 Stub lengths for the TC (Units: µm), for the sensor with H= 20 µm

H	H_1	H_2	H_3	H_4	H_5	H_6	H_7
20	2.5	5.0	7.5	10.0	12.5	15.0	17.5

Table 2 Stub lengths for the TC (Units: µm), for the sensor with H= 65 µm

H	H_1	H_2	H_3	H_4	H_5	H_6
65	5.0	15.0	25.0	35.0	45.0	55.0

Next, we design a transition circuit (TC) to minimize the return loss and effectively convert the TEM mode in CPS to TM mode in SSPP. This is achieved by gradually increasing the stub length. Here we selected a linear growth of stubs. The values of stubs are shown in Table 1 and 2.

3 Simulations

ANSYS HFSS was used to perform eigenmode and frequency-domain (FD) simulations on the proposed structures. We aim to replicate the real devices in the simulations, hence, the model includes the Si_3N_4 substrate as 1 µm thick and $\varepsilon_r = 7.6$, $\sigma_{Si_3N_4} = 0$, and tan $\delta_e = 0.00526$ [25]. The gold (Au) thickness is 200 nm and the conductivity is $\sigma_{Au} = 4.1 \times 10^7$ S/m. All simulations use d =20, 50 µm, W_s =10, 20 µm, S_{CPS} =90, 140 µm, and W =10, 30 µm, where the first and second number are related to two different structures.

We use the eigenmode simulation to obtain the dispersion diagram and band-edge frequencies for the fabricated CPS-SSPP unit cells [16]. We also used FD simulation to study the transmission of the structure comparing unloaded and loaded conditions with glucose layer under the sensor's membrane. Figure 3 shows the S_{21} of the structure when the glucose layer thickness varies from 0 (unloaded) to 5µm, showing both absorption at 1.4 THz and band edge shift mechanism. Additionally, Fig. 4 illustrates a comparison between proposed SSPP sensor and CPS sensor presented in [20], with

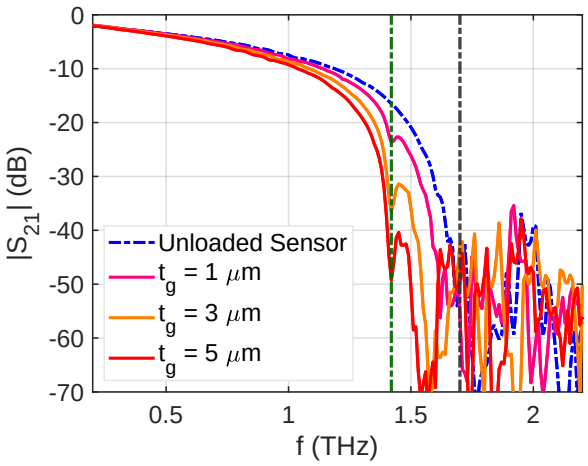

Fig. 3 Simulated S_{21} of the SSPP structure holding band-edge at 1.7 THz (dashed grey line) with different glucose thicknesses, showing both absorption at 1.42 THz (dashed green line, modeled) and band-edge frequency shift as a result of effective permittivity variation

the same glucose layer thickness when loaded. The comparison of the unloaded and loaded responses of each sensor at the absorption frequency of 1.4 THz shows a 25 dB difference which is significant in terms of sensitivity. Also, the depth of absorption is 2 dB higher in the SSPP case.

Regarding the SSPP sensing at lower frequencies (0.7 THz), where the permittivity of glucose is relatively constant, we performed an eigenmode simulation in Fig. 5 showing that effective permittivity of the dielectric directly affects the band edge frequency. From the Kraszewski [26] dielectric model, the effective permittivity of dielectric is also a function of the thickness of the material and is not merely limited to chemical properties. Therefore we can compare simulations, measurements, and modified Kraszewski model [26] in Fig. showing a good agreement.

The sensor's field plot is shown in Fig. 2, illustrating that this structure confines the field inside the corrugations and between the mutual stubs.

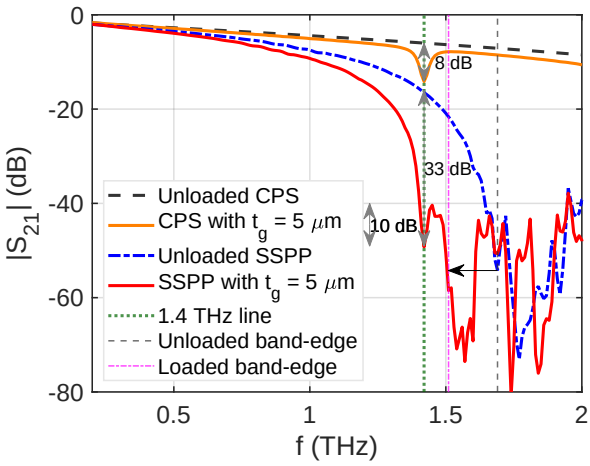

Fig. 4 Simulated S_{21} of the SSPP vs CPS sensors with the same glucose thickness, showing a significantly larger difference with the unloaded response at 1.4 THz for the SSPP sensor

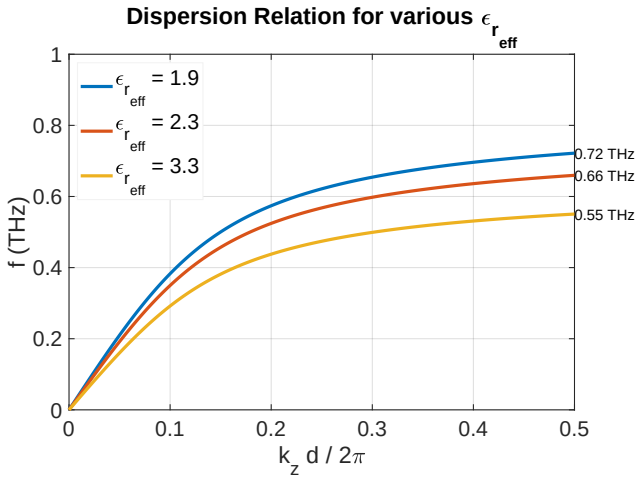

Fig. 5 Dispersion curves of the Proposed SSPP for the measured dimensions obtained from eigenmode simulation

4 Experimental Results and Discussion

The results from the SSPP sensor measurements for different glucose samples are presented and discussed in this section. The first measurement, shown in Figure 7,

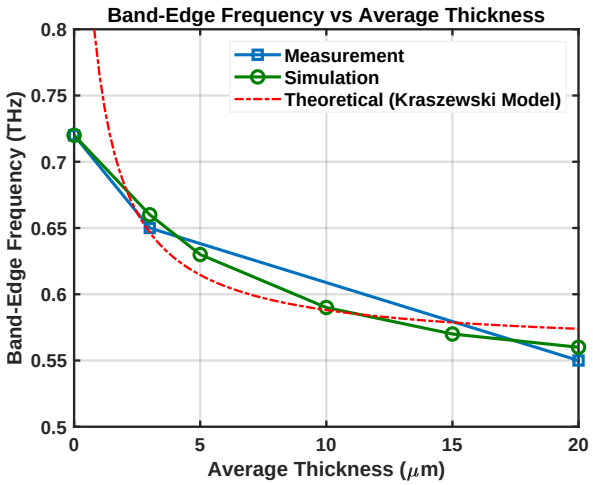

Fig. 6 Band-edge frequency variations (Simulated, Measured, Theoretical based on dispersion relation of SSPP and modified Kraszewski effective permittivity model) versus the thickness of the glucose layer with bulk permittivity of 3.2 at the frequency range of 0.5-0.8 THz.

depicts the sensor response for a dehydrated thin film of glucose powder. This measurement demonstrates the sensor's ability to detect absorption in the THz range, where a significant absorption peak appears around 1.4 THz, corresponding to the glucose intermolecular resonances. This observation highlights the sensor's sensitivity to material properties in the THz domain.

In Figure 8, the SSPP sensor response for a dried 250 mmol/L glucose solution is shown. Similar absorption behavior is observed, confirming the robustness of the sensor across different forms of glucose. The peak absorption shifts slightly due to the differences in the material's permittivity, but the sensor's ability to detect subtle variations in the glucose concentration is clearly evident, showcasing the potential of the SSPP sensor for quantitative analysis.

Further, Figure 9 presents the SSPP sensor measurements for glucose distribution and mass variations on the membrane of the sensor structure. The left column illustrates the different distributions of glucose, while the middle column shows the resulting time delays in the temporal pulse. The right column highlights the spectral

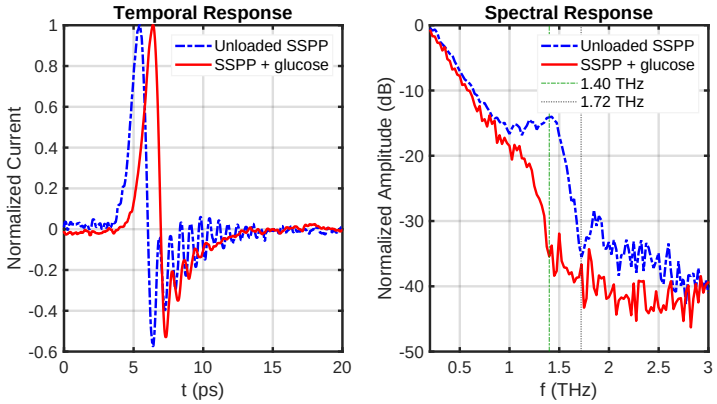

Fig. 7 SSPP Sensor Measurement Results for a dried thin film of glucose powder.

variations in the band edge location and the consistent absorption peak around 1.4 THz. These results emphasize the sensor's capability to measure the material's distribution and thickness, which directly influences the spectral response, including the shift in the band edge and the intensity of the absorption peak.

Finally, in Figure 10, the experimental measurement results are compared with simulation results for the SSPP sensor response. The comparison reveals excellent agreement between the measured and simulated data, with a slight offset in the spectral response due to experimental conditions. This validates the sensor's performance and demonstrates that the SSPP-based sensor can be accurately designed for different sensing applications.

Overall, the SSPP sensor shows significant potential to improve sensitivity to lower concentrations compared to the CPS-based sensor [20]. Also, the combination of absorption sensing and resonance shift detection mechanisms further enhances the sensor's sensitivity and also makes it a promising tool for label-free sensing applications in biomedical and material analysis.

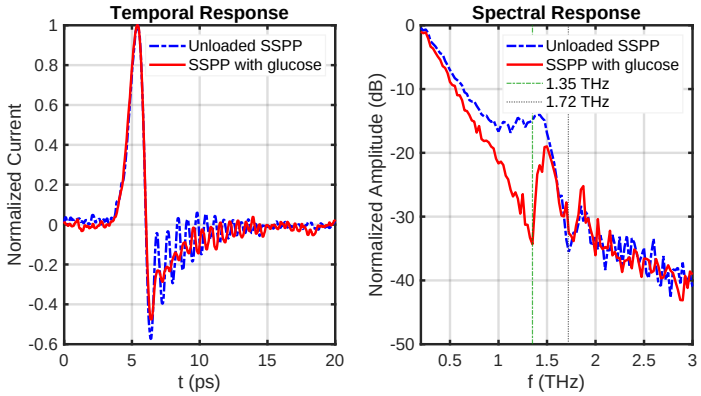

Fig. 8 SSPP Sensor Measurement Results for dried 250 mmol/L glucose solution.

5 Methods

Fabrication of PCS

In this section, we present the process of fabricating photo-conductive switches (PCSs) and conducting measurements. PCSs are utilized for the generation and detection of THz signals. To fabricate these components, a multi-step process was performed, involving photolithography, gold (Au) sputtering, and wet-etching. While the detailed process can be found in other references [27], we provide a summary here for completeness.

Firstly, a desired LT-GaAs layer is grown on a sacrificial AlAs layer situated on a semi-insulating GaAs substrate. The LT-GaAs surface is then patterned using standard photolithography to create Au contacts. Subsequently, each PCS region is masked and wet-etched using Citric Acid and Hydrogen Peroxide, which determines the thickness of the PCS. Next, the surface is cleaned and re-masked using an etch-resist wax. The LT-GaAs layer is then dissolved by immersing it in hydrofluoric acid (HF), detaching it from the AlAs layer. To disconnect the remaining LT-GaAs film, which interconnects a grid of PCSs, the LT-GaAs film is submerged again in Citric Acid and

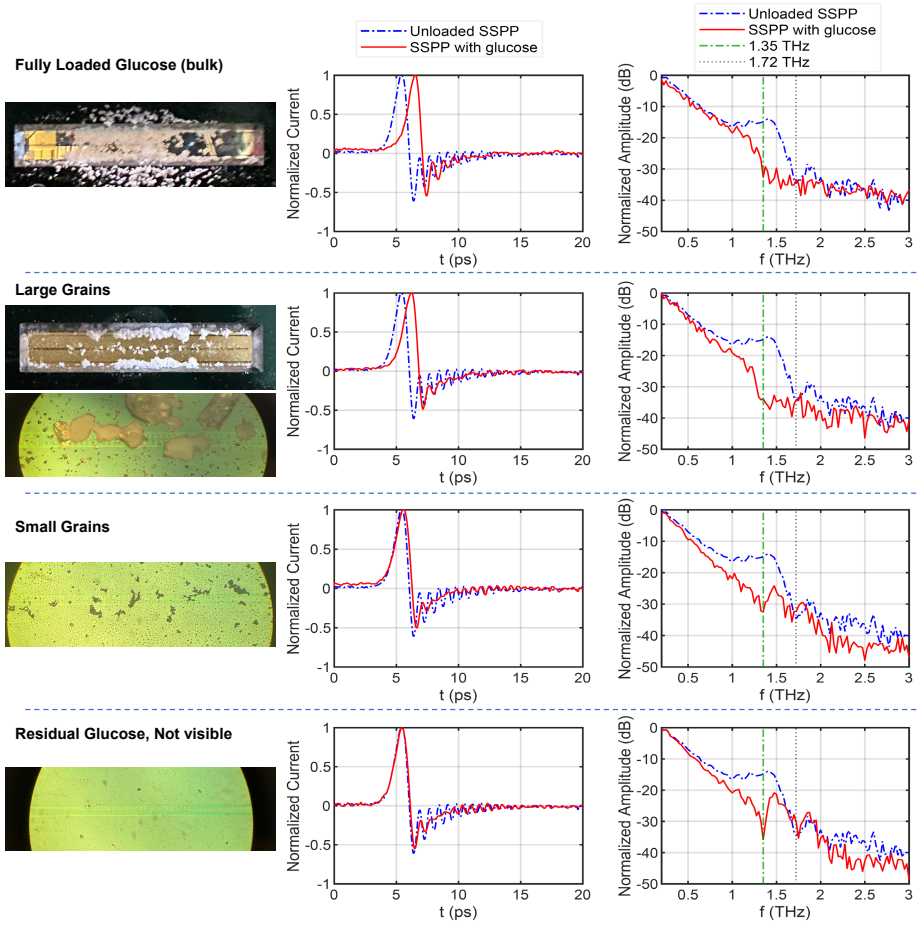

Fig. 9 SSPP Sensor Measurement Results for different distribution and mass of glucose on the membrane of the sensor structure (left column), showing the different delays in the temporal pulse (middle column) and spectral variations in the band edge location and also a consistent absorption peak (right column).

Hydrogen Peroxide. Finally, the etch-resistant wax is removed using trichloroethylene (TCE), resulting in numerous active regions of LT-GaAs PCSs.

Next, two PCSs are placed on the designated spots (transmitter and receiver) on the membrane (as shown in Fig. 1) and bonded using a droplet of water with the Van

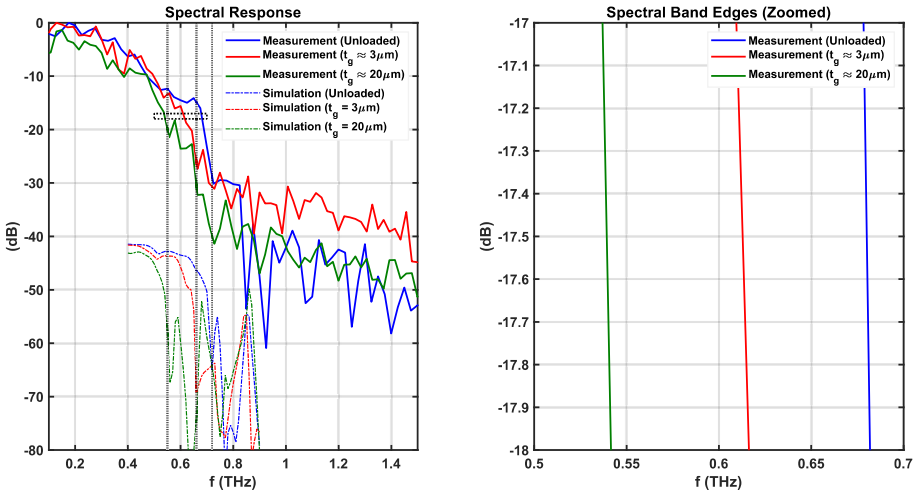

Fig. 10 SSPP Sensor Measurement Results along with simulation results for comparison (offset of -40 dB on the Spectral Response).

der Waals (VDW) forces, as explained in [28]. The dimensions of the fabricated PCS are 70 µm × 40 µm × 1.5 µm, with a 5 µm gap between the PCS metal (Gold) contacts.

Experimental Setup

The measurements are carried out using a modified THz Time-domain Spectroscopy (THz-TDS) setup [16, 29]. The experiment utilizes a femtosecond pulsed laser with a wavelength of 780 nm, a pulse width of 90 fs, a repetition rate of 80 MHz, and an average output power of 28 mW. The laser is focused onto PCSs positioned on the waveguide to generate and detect broadband THz pulse signals. The transmitted signal is reconstructed by adjusting a mechanical delay line and measuring the receiver current with a lock-in amplifier, following an approach similar to THz-TDS [29, 30].

6 Conclusion

This study presents a pioneering on-chip Terahertz (THz) sensor based on the Spoof Surface Plasmon Polariton (SSPP) waveguide, demonstrating its potential for highly

sensitive material characterization. By exploiting both resonance shifts and absorption mechanisms, the sensor effectively captures subtle changes in the dielectric properties of materials, such as glucose, in the THz frequency range. The observed shift in the band edge and its correlation with material thickness provides a novel approach for precise sensing and measurement. This work opens new avenues for THz sensing applications, offering enhanced sensitivity and versatility in detecting a wide range of substances, paving the way for future advancements in biomedical diagnostics and material analysis.

References

[1] Beruete, M. & Jáuregui-López, I. Terahertz sensing based on metasurfaces. *Advanced Optical Materials* **8** (2019).

[2] Tang, W. X., Zhang, H. C., Ma, H. F., Jiang, W. X. & Cui, T. J. Concept, theory, design, and applications of spoof surface plasmon polaritons at microwave frequencies. *Advanced Optical Materials* **7**, 1800421 (2019).

[3] Lee, D. *et al.* Highly sensitive and selective sugar detection by terahertz nano-antennas. *Scientific Reports* **5** (2015).

[4] Hu, X. *et al.* Metamaterial absorber integrated microfluidic terahertz sensors. *Laser Amp; Photonics Reviews* **10**, 962–969 (2016).

[5] Serita, K., Murakami, H., Kawayama, I. & Tonouchi, M. A terahertz-microfluidic chip with a few arrays of asymmetric meta-atoms for the ultra-trace sensing of solutions. *Photonics* **6**, 12 (2019).

[6] Singh, S. P., Tiwari, N. K. & Akhtar, M. J. Spoof surface plasmon-based coplanar waveguide sensor for dielectric sensing applications. *IEEE Sensors Journal* **20**, 193–201 (2020).

[7] Mozaffarian, D. Dietary and policy priorities for cardiovascular disease, diabetes, and obesity. *Circulation* **133**, 187–225 (2016).

[8] Ventura, E. E., Davis, J. N. & Goran, M. I. Sugar content of popular sweetened beverages based on objective laboratory analysis: Focus on fructose content. *Obesity* **19**, 868–874 (2011).

[9] Oliver, N. S., Toumazou, C., Cass, A. E. G. & Johnston, D. G. Glucose sensors: a review of current and emerging technology. *Diabetic Medicine* **26**, 197–210 (2009).

[10] Di Filippo, D., Sunstrum, F. N., Khan, J. U. & Welsh, A. W. Non-invasive glucose sensing technologies and products: A comprehensive review for researchers and clinicians. *Sensors* **23** (2023).

[11] Pickwell, E. & Wallace, V. P. Biomedical applications of terahertz technology. *Journal of Physics D: Applied Physics* **39**, R301 (2006).

[12] Liu, H.-B. & Zhang, X.-C. Dehydration kinetics of d-glucose monohydrate studied using thz time-domain spectroscopy. *Chemical Physics Letters* **429**, 229–233 (2006).

[13] Jacques, S. L. Optical properties of biological tissues: a review. *Physics in Medicine and Biology* **58**, R37 (2013).

[14] Chen, H., Chen, X., Ma, S. *et al.* Quantify glucose level in freshly diabetic's blood by terahertz time-domain spectroscopy. *J Infrared Milli Terahz Waves* **39**, 399–408 (2018). URL https://doi.org/10.1007/s10762-017-0462-2.

[15] Lu, X. *et al.* Weak value amplified precision terahertz spectroscopic detection of solid and liquid glucose samples. *ACS Photonics* **10**, 3149–3160 (2023). URL https://doi.org/10.1021/acsphotonics.3c00525.

[16] Haghighat, M., Dehghanian, A., Darcie, T. & Smith, L. Demonstration of terahertz spoof surface plasmon polariton waveguides using coplanar striplines with internal corrugations. *Optics Express* (2024).

[17] Haghighat, M., Darcie, T. & Smith, L. Demonstration of a terahertz coplanar-strip spoof-surface-plasmon-polariton low-pass filter. *Scientific Reports* **14** (2024).

[18] Shen, X., Cui, T. J., Martin-Cano, D. & Garcia-Vidal, F. J. Conformal surface plasmons propagating on ultrathin and flexible films. *Proceedings of the National Academy of Sciences* **110**, 40–45 (2013).

[19] Ma, H. F., Shen, X., Cheng, Q., Jiang, W. X. & Cui, T. J. Broadband and high-efficiency conversion from guided waves to spoof surface plasmon polaritons. *Laser Photonics Rev.* **8**, 146–151 (2014).

[20] Haghighat, M., Darcie, T. & Smith, L. On chip glucose sensing using guided waves at terahertz frequencies. *Scientific Reports* **14** (2024).

[21] Garcia-Vidal, F. J., Martín-Moreno, L. & Pendry, J. B. Surfaces with holes in them: new plasmonic metamaterials. *Journal of Optics A: Pure and Applied Optics* **7**, S97 (2005).

[22] Maier, S. A., Andrews, S. R., Martín-Moreno, L. & García-Vidal, F. J. Terahertz Surface Plasmon-Polariton Propagation and Focusing on Periodically Corrugated Metal Wires. *Physical Review Letters* **97**, 176805 (2006).

[23] Guo, Y. J., Da Xu, K. & Tang, X. Spoof plasmonic waveguide developed from coplanar stripline for strongly confined terahertz propagation and its application in microwave filters. *Optics Express* **26**, 10589 (2018).

[24] Haghighat, M., Darcie, T. & Smith, L. Demonstration of a terahertz coplanar-strip spoof-surface-plasmon-polariton low-pass filter. *Scientific Reports* **14** (2024).

[25] Cataldo, G. *et al.* Infrared dielectric properties of low-stress silicon nitride. *Optics Letters* **37**, 4200–4202 (2012).

[26] Kraszewski, A. Prediction of the dielectric properties of two-phase mixtures. *Journal of Microwave Power* **12**, 216–222 (1977).

[27] Ríos, R. D. V., Bikorimana, S., Ummy, M. A., Dorsinville, R. & Seo, S.-W. A bow-tie photoconductive antenna using a low-temperature-grown gaas thin-film on a silicon substrate for terahertz wave generation and detection. *Journal of Optics* **17**, 125802 (2015).

[28] Yablonovitch, E., Hwang, D. M., Gmitter, T. J., Florez, L. T. & Harbison, J. P. Van der Waals bonding of GaAs epitaxial liftoff films onto arbitrary substrates. *Applied Physics Letters* **56**, 2419–2421 (1990).

[29] Smith, L. & Darcie, T. Demonstration of a low-distortion terahertz system-on-chip using a cps waveguide on a thin membrane substrate. *Optics Express* **27**, 13653–13663 (2019).

[30] Gomaa, W., Smith, L., Shiran, V. & Darcie, T. Terahertz low-pass filter based on cascaded resonators formed by CPS bending on a thin membrane. *Optics Express* **28**, 31967 (2020).

This page intentionally left blank.